

Stochastic models for near-synchronous neuronal firing activity

Dissertation
zur Erlangung des Doktorgrades
der Naturwissenschaften

vorgelegt beim Fachbereich Informatik und Mathematik
der Johann Wolfgang Goethe-Universität
in Frankfurt am Main

von
Gaby Schneider
aus Frankfurt am Main

Frankfurt am Main 2006
(D 30)

vom Fachbereich Informatik und Mathematik
der Johann Wolfgang Goethe-Universität als Dissertation angenommen.

Dekan: Prof. Dr.-Ing. Detlef Krömker

Gutachter: Prof. Dr. Anton Wakolbinger
Prof. Dr. Reinhard Höpfner
Prof. Dr. Dirk Metzler

Datum der Disputation: 14. Juni 2006

Acknowledgements

I wish to express my deepest gratitude to my advisor Dr. Brooks Ferebee, whose extraordinary questions and ideas inspired me in many ways. During the last five years, I had the pleasure to profit from his brilliant and sharp-witted mind, his immense expertise, and above all, from his wise and ever kindhearted support. I am also very much obliged to Prof. Anton Wakolbinger for his interest in this interdisciplinary thesis, and for his constant availability and helpfulness.

Thanks are also due to Dr. Danko Nikolić for providing the neurophysiological and methodological questions which motivated this work. During many stimulating discussions, I could learn from his extensive knowledge and experience in the field of neuroscience. I wish to thank Martha N. Havenith for many valuable comments and for her bright enthusiasm. I am also indebted to Julia Biederlack for data acquisition and to Michael Stephan for his valuable support with data conversion.

This thesis was motivated and partially developed in a joint project with Danko Nikolić and Martha N. Havenith from the department of Neurophysiology at the Max-Planck-Institute for Brain Research. The neurophysiological data and question originate from the studies of D. Nikolić, and the mathematical approaches and results have been elaborated by the author of this thesis. The main results of the Parts I and II are published (Schneider and Nikolić, 2006) or have been accepted for publication (Schneider *et al.*, 2006).

Contents

1	Introduction	1
1.1	Motivation	1
1.2	Outline	2
I	Assessment of phase offsets	9
2	Introduction and Results	11
3	Measurement of phase offsets	13
3.1	Gabor function	13
3.2	Cosine function	15
3.2.1	Assumptions	15
3.2.2	Data Analysis	15
4	Precision of measurement	19
4.1	A formula for the variance of a phase estimate	20
4.1.1	Proof of Proposition 1	21
4.1.2	Formula asymptotic variance: Interpretation	27
4.1.2.1	Parameterization	27
4.1.2.2	The parameters of V	28
4.1.2.3	The parameters of G	30
4.1.3	Formula asymptotic variance: Implications for practical application	33
4.2	The scope of the formula	34
4.2.1	Simulations	35
4.2.1.1	Parameter ranges	35
4.2.1.2	Results for typical parameter values	35

4.2.1.3	Applicability of the formula	38
4.2.2	Binning	39
4.2.3	Comparison to experimental variability	41
4.3	Application: A significance test	42
5	Conclusion – Part I	45
II	The structure of phase offsets	47
6	Introduction and Results	49
6.1	Motivation	49
6.2	Results	51
7	Stochastic model	53
7.1	Framework and results	53
7.1.1	Proofs	55
7.1.2	The geometric perspective	57
7.2	Analysis of variance	59
7.2.1	Application: Differences between configurations	59
7.3	Model assumptions and model extensions	63
7.3.1	Missing data	65
7.3.1.1	Framework	65
7.3.1.2	Existence and uniqueness of estimates	66
7.3.1.3	ML-estimates	69
7.3.1.4	Global variance	72
7.3.2	Heteroscedasticity	73
7.4	Model summary	75
8	Data analysis	77
8.1	Positions of the units on the time axis	78
8.2	Investigation of linear configurations	81
8.2.1	Heteroscedasticity versus global variance	81
8.2.2	Permutation test	83
8.3	Differences between linear configurations	85
9	Conclusion – Part II	89

III	How spike train properties shape CCHs	91
10	Introduction and Results	93
10.1	Motivation	93
10.2	Results	95
11	A spike train model	99
11.1	Assumptions	99
11.2	The single spike train	101
11.3	Parallel spike trains	103
12	Auto and cross correlation	105
12.1	ACF & CCF in the spike train model	106
12.1.1	Proof of Theorem 2	107
12.1.1.1	Auto correlation function	107
12.1.1.2	Cross correlation function	111
12.1.1.3	Note: Distribution of IPIs	112
12.1.2	Practical remarks	112
12.2	Shape of ACF and CCF	114
12.2.1	Decomposition of a CCF	114
12.2.2	Interpretation of parameters	117
12.2.2.1	‘Strength of oscillation’	117
12.2.2.2	Central peak	118
12.2.2.3	Asymmetry	119
12.3	Summary	121
13	Practical usefulness	123
13.1	Investigation of model assumptions	124
13.1.1	Distribution and independence of IPIs	124
13.1.2	Distribution of spikes within packets	125
13.1.3	Stability of firing rates	127
13.2	Fitting ACFs to ACHs	127
13.3	Prediction of CCHs	134
13.3.1	Good fits	134
13.3.2	Suboptimal fits	135
13.3.3	Rate correction	137
13.4	Simulation of spike trains	139
13.4.1	Spike trains	139

13.4.2 Variability of counts in ACHs and CCHs	141
14 What then is a phase offset?	145
15 Discussion and outlook	151
A Neurophysiological Background	155
A.1 Neuronal information processing	155
A.2 ‘CCH’ - Terminology	158
A.3 The sample data set	159
Bibliography	164

Chapter 1

Introduction

1.1 Motivation

It is commonly agreed that cortical information processing is based on the electric discharges ('spikes') of special nerve cells, the neurons. To investigate the spiking activity of neuronal cells, their spike times are recorded in discrete time steps and represented in binary time series S ('spike trains'; Fig. 1.1):

$$S(j\delta) = \begin{cases} 1 & \text{if (at least) one spike was recorded in } [j\delta, (j+1)\delta), \\ 0 & \text{otherwise,} \end{cases}$$

where $j = 0, 1, \dots, T/\delta - 1$. The time resolution of the spike train is denoted by δ , and T is a multiple of δ and denotes the length of the analysis window.

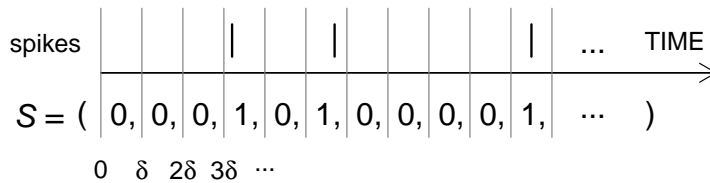


Figure 1.1: Formal representation of a spike train with time resolution δ . Recorded spike times are transformed into a binary time series in discrete time.

Complex information is assumed to be represented and processed in the combined activity of a large number of neurons in the highly connected network of cells. Therefore, many studies focus on the temporal interaction between the spike trains of multiple neurons obtained in parallel recordings. Evidence is

accumulating which suggests that this temporal interaction can take place with extremely high precision, indicating that the efficiency of cortical processing may depend crucially on the precise spike timing of many cells (The reader interested in the neurophysiological background can find a more detailed presentation of the research field in Appendix A.1).

This work focuses on two temporal properties of parallel spike trains that attracted growing interest in the recent years: In the first place, delays between the firing times of two spike trains are investigated. In particular, it is studied whether small temporal delays can be identified confidently between two spike trains that have the tendency to fire almost simultaneously. Second, the temporal relations between multiple spike trains are investigated on the basis of such small delays between pairs of processes. Since the analysis of all delays among the firing activity of n neurons is extremely complex, a method is required with which this highly dimensional information can be collapsed in a straightforward manner such that the temporal interaction among a large number of neurons can be represented consistently in a single temporal map. Finally, a stochastic model is presented that provides a framework to integrate and explain the observed temporal relations that result from the previous analyses.

1.2 Outline

The CCH In practice, temporal correlations between two spike trains S_1, S_2 with the same time resolution δ are often analyzed with the so-called cross-correlation histogram (CCH; Moore *et al.*, 1966; Perkel *et al.*, 1967b, for a discussion of the terminology see Appendix A.2). With a maximal delay $L > 0$, a set of lags

$$\mathfrak{L}_\delta^L := \{k\delta \mid k \in \mathbb{Z}, |k\delta| \leq L\}$$

is specified. For every delay $\ell \in \mathfrak{L}_\delta^L$, the number of spikes in S_2 is counted which occur ℓ time units after a spike in S_1 (see also App. A.2):

$$H_{S_1 S_2}(\ell) := \sum_j S_1(j\delta) S_2(j\delta + \ell) \quad (\text{Fig. 1.2}). \quad (1.1)$$

Since a delay ℓ between a spike pair in S_1 and S_2 is equivalent to a delay $-\ell$ between the same spike pair in S_2 and S_1 , the CCH between S_2 and S_1 is a mirror image of the CCH between S_1 and S_2 :

$$H_{S_2 S_1}(\ell) = H_{S_1 S_2}(-\ell). \quad (1.2)$$

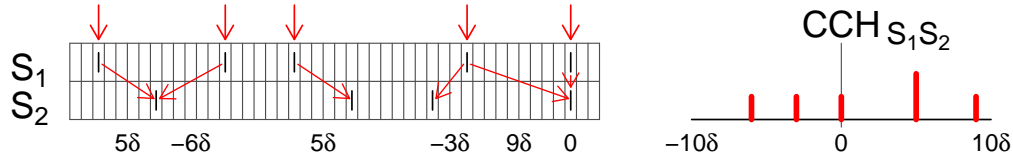


Figure 1.2: Schematic representation of the computation of a raw CCH for two spike trains S_1, S_2 with time resolution δ and maximal time lag $L = 10\delta$.

The CCH is central for the present work because it is a well-established method of analysis for the investigation of coordinated neuronal firing activity (e.g., Toyama *et al.*, 1981; Ts'o *et al.*, 1986; Gray *et al.*, 1989; Nowak *et al.*, 1995; Kreiter and Singer, 1996). Figure 1.3 shows an exemplary CCH for two spike trains obtained experimentally. As the counts in a CCH are usually noisy, they are often smoothed or fitted with a suitable function in order to estimate the relevant parameters.

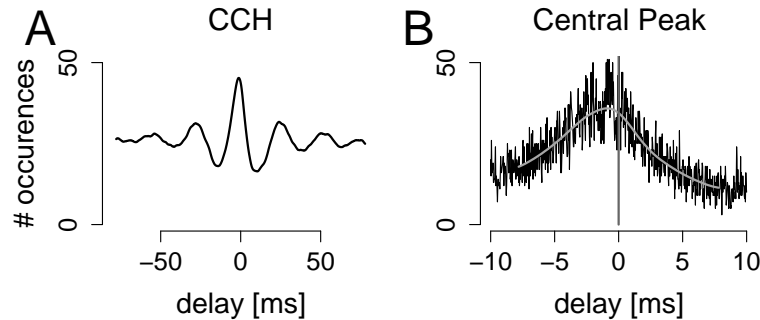


Figure 1.3: A: Smoothed shape of a CCH computed for two experimentally derived spike trains ($L = 80$ ms). The oscillatory shape indicates preferred delays at $\ell \approx 0, \pm 25$ ms, \dots , while intermediate delays are less frequent. B: Central region of the same CCH ($L = 10$ ms, $\delta = 1/32$ ms).

This work is motivated by the contrast provided between two different approaches. On the one hand, the widely used CCH technique is simple and provides detailed information about temporal relations but is restricted to pairwise analysis. On the other hand, highly elaborated approaches are available that deal with multiple spike trains but suffer from the complexity arising with a high number of processes (Perkel *et al.*, 1975; Gerstein *et al.*, 1985; Gerstein and Aertsen, 1985; Abeles and Gerstein, 1988; Kaluzny *et al.*, 1991; Martignon *et al.*,

1995; Baker and Lemon, 2000; Abeles and Gat, 2001; Grün *et al.*, 2002a,b; Amari *et al.*, 2003; Schneider and Grün, 2003, for a review see e.g., Brown *et al.* (2004)). Simple methods should be available to the experimenter with which additional information can be extracted from CCHs. Especially, it is investigated whether interactions between multiple neurons might be visible in CCHs.

Part I

The first part deals primarily with the identification of small temporal delays between the spike times of pairs of spike trains. As in Figure 1.3 A, many CCHs take their maximum close to zero, which indicates that the two spike trains tend to fire nearly simultaneously. However, panel B shows that the maximum of the peak may deviate slightly from $\ell = 0$. The exact position of the maximum - the ‘phase offset’ - is the central parameter investigated in Part I. Small phase offsets such as the one in Figure 1.3 B have not been analyzed in the past because they are usually considered negligible in comparison to the variability of counts in the CCH (e.g., Roelfsema *et al.*, 1997). However, since neuronal firing activity can take place with high temporal precision (e.g., Mainen and Sejnowski, 1995; Riehle *et al.*, 1997; Reinagel and Reid, 2002; Ikegaya *et al.*, 2004), also near-zero phase offsets might be relevant for information processing. In order to decide whether a near-zero phase offset can be considered a systematic deviation or whether it is caused by random fluctuations, it is important to assess the variance with which a phase offset can be estimated. To this end, a method is presented that can be used to estimate phase offsets and that allows also the assessment of the variability of these estimates.

The presented method assumes that the counts in the central peak of a CCH can be described with a cosine function with independent and normally distributed noise σZ_ℓ

$$H(\ell) = A \cos(\omega(\ell - \varphi)) + \beta_0 + \sigma Z_\ell, \quad \ell \in \mathfrak{L}_\delta^L.$$

With these assumptions, the variance of the phase estimate can be approximated with the δ -method (see Prop. 2 on page 22). The resulting formula (eq. (4.29)-(4.33)) is composed of two multiplicative terms, V and G . V indicates that the precision of the phase estimate increases with the oscillation frequency ω , with the quotient A/σ , and with the number of data points in the CCH, $N = 2L/\delta + 1$. The term G can be interpreted geometrically and depends essentially on the relation of data points at the edges of the cosine function as compared to the data points at the extremes (sect. 4.1.2).

The theoretical formula corresponds well to the variance of the phase estimate derived with simulations (sect. 4.2.1) and to the variability observed in a sample data set with $n = 14$ parallel spike trains obtained experimentally (sect. 4.2.3, details on stimuli and analysis window are provided in Appendix A.3). In the sample data set, the absolute value $|\hat{\varphi}|$ of most phase estimates was considerably larger than the standard deviation $\sigma_{\hat{\varphi}}$, indicating that deviations from zero are unlikely to be explained by random fluctuations.

Part II

The results obtained in Part I also suggest that near-zero phase offsets can vary systematically between different stimulation conditions (sect. 4.3). Therefore, it is investigated in Part II whether temporal relations among n spike trains can be extracted from the pairwise information given by the set of all $\binom{n}{2}$ phase offsets associated with these n processes. In particular, it is investigated to which degree a set of phase offsets can be represented in a lower dimensional structure with the help of the additivity assumption: If the phases computed among any triplet of spike trains S_i, S_j, S_k are perfectly additive, i.e., if $\varphi_{ik} = \varphi_{ij} + \varphi_{jk}$ (with $\varphi_{ik} = -\varphi_{ki}$), the set of phase offsets can be represented in an $(n - 1)$ -dimensional space. In this representation, each spike train S_i is assigned a value x_i on the real line such that every phase φ_{ij} equals the ‘model distance’ $\delta_{ij} = x_j - x_i$ (ch. 6, Fig. 6.1 B).

Part II investigates whether such an additive structure can represent important aspects of the information provided in a set of phase offsets - which are not necessarily additive. In the framework of a linear model, it is assumed that every phase φ_{ij} is a noisy measurement of the difference δ_{ij} between points in an additive, ‘linear configuration’ $\mathcal{C} = \{\hat{x}_1, \dots, \hat{x}_n\}$ (ch. 7):

$$\varphi_{ij} = \delta_{ij} + \sigma Z_{ij} \quad \forall i < j, \quad \text{with } Z_{ij} \sim \mathcal{N}(0, 1) \text{ and } (Z_{ij})_{i < j} \text{ independent.}$$

With these assumptions, the model distances δ_{ij} are estimated such that the phase offsets φ_{ij} are represented as closely as possible, i.e., that the error sum of squares $\sum (\varphi_{ij} - \hat{\delta}_{ij})^2$ is minimized. The resulting maximum-likelihood estimates of δ_{ij} are weighted sums of direct measurements φ_{ij} and indirect measurements of length 2, $\varphi_{il} + \varphi_{lj}$ (Corollary 3).

In the sample data set, the experimentally obtained phase offsets φ_{ij} could be represented to a high degree by the estimated model distances $\hat{\delta}_{ij}$ (Fig. 8.2 A). Thus, the presented method allows one to collapse the temporal relations between all units in a consistent way by estimating the linear configuration. In addition,

the linear model allows the application of an analysis-of-variance approach with which k linear configurations $\mathcal{C}_1, \dots, \mathcal{C}_k$ obtained under different stimulation conditions can be tested for differences (sect. 7.2). The resulting analysis suggests that linear configurations can vary systematically between different stimulation conditions, indicating a potential role of the extracted temporal maps in information processing.

Part III

The methods presented in the Parts I and II provide powerful tools in the analysis of neurophysiological data because they are based on the widespread CCH technique and because they allow the efficient analysis of temporal relations between a high number of parallel spike trains. However, since they are based only on special CCH parameters, their results do not provide direct information about the spiking characteristics of the underlying processes. In particular, it remains unclear which spike train properties are crucial for establishing the observed phenomena of small phase offsets and their linear structure. In order to investigate this issue, Part III discusses the relation between the properties of the underlying spike trains and central form parameters extracted from the CCHs. Among these form parameters, not only the position of the central peak is considered relevant, but also its height and width as well as the periodically occurring side peaks of decreasing height that can be observed in oscillatory CCHs (Fig. 10.1) and that are assumed to originate in spike trains with synchronized periodic spike packets (e.g., Singer and Gray, 1995).

In order to allow an adequate treatment of the problem, n spike trains S_1, \dots, S_n are modeled as parallel point processes X_1, \dots, X_n . A parametric stochastic model is introduced that can be used to investigate which spike train properties might be relevant for the emergence of the characteristic shape of oscillatory CCHs (ch. 11). In the doubly stochastic model, a single spike train is assumed to emerge as follows: A stationary point process $\mathbb{B} = (\dots, B_{-1}, B_0, B_1, \dots)$ with preferred interval length $\mathbb{E}(B_b - B_{b-1}) = \mu$ and variance $\text{Var}(B_b - B_{b-1}) = \sigma^2$ gives rise to independent Poissonian spike packets. For every packet, the firing intensity rises instantaneously at ‘packet onset’ B_b and then decays exponentially. Different processes may differ in the decay constant $\tau > 0$ but share the same ‘packet onset process’ \mathbb{B} , by which correlations are introduced. Thus, for given \mathbb{B} , n independent and inhomogeneous Poisson processes are generated

with firing intensities

$$\rho_{\mathbb{B}}^j(t) := \frac{\alpha_j}{\tau_j} \sum_{b \in \mathbb{Z}, B_b \leq t} e^{\frac{-(t-B_b)}{\tau_j}} + \beta_j, \quad j = 1, \dots, n. \quad (\text{Fig. 11.3, } n = 2)$$

Here, $\alpha_j \geq 0$ describes the expected number of spikes in a packet in process X_j , and $\beta_j \geq 0$ denotes a constant background firing intensity.

In the framework of this model, important geometric CCH properties of two processes X_i and X_j can be related to the parameters α, τ, μ and σ (sect. 12.2). The parameter μ mainly determines the position of the first side peak, while the speed with which the side peaks decrease in height depends on σ . The parameter τ determines both the height and width of the central peak, where the height increases and the width decreases with decreasing τ .

The spike train model suggests a precise relationship between different spike train statistics. Especially the relation between auto correlation histograms (ACHs), which are CCHs of two identical copies of a single spike train, and the corresponding CCHs is investigated. This theoretically predicted relation between ACHs and CCHs can also be found in the experimental data set. Various further comparisons also indicate that the experimental data set complies to a high degree with the model assumptions (ch. 13).

Finally, non-zero phase offsets between the processes X_i and X_j can be explained by a difference between the parameters τ_i and τ_j (ch. 14): If $\tau_i < \tau_j$, the intensity ρ^i decays faster with respect to each packet onset B_b than the intensity ρ^j . As a consequence, the spike times in process X_i tend to be earlier than the spike times of X_j , producing a positive phase offset in the CCH between X_i and X_j . In this framework, additivity of phase offsets can be explained directly by the linear relation of the values $\tau_i \in \mathbb{R}$.

In conclusion, the model offers a theoretical explanation for the phenomena observed in CCHs by providing a connection to the relevant spike train parameters. Since the model can be used to investigate temporal properties of single spike trains as well as correlations between processes, it can be highly useful in the analysis of temporal interactions between multiple parallel spike trains.

Part I

Assessment of phase offsets

Chapter 2

Introduction and Results

The first part is concerned with the measurement of phase offsets of central CCH peaks and with a method that can be used to determine the measurement error. As the number of phase offsets grows quadratically with the number of units, a technique is required which can be implemented easily and which also provides confidence intervals for individual estimates and for sets of measurements. In the same time, it should allow statistical inferences about differences between measurements or deviations from theoretical values, in particular from zero.

Chapter 3 is concerned with methods that can be used to measure phase offsets and with an exemplary analysis of the sample data set (see App. A.3). In chapter 4, an asymptotic formula with which this error can be quantified is derived and applied to the phase offsets estimated in the sample data set.

Model 1: Cosine function with random noise

Phase offsets are estimated here with the following stochastic model. Due to the oscillatory shape of many experimentally obtained CCHs, it is assumed that the counts $H(\ell)$ in the central peak of a CCH can be described with a cosine function with independent and normally distributed noise σZ_ℓ :

$$H(\ell) = A \cos(\omega(\ell - \varphi)) + \beta_0 + \sigma Z_\ell, \quad \ell \in \mathcal{L}_\delta^L \quad (\text{Figs. 3.1 D \& 3.2 A; cmp. p. 2}).$$

With these assumptions, a nonlinear least squares algorithm with standardized starting values is applied to the central CCH peak in order to estimate the parameters A , ω , β_0 and the phase offset φ . The 91 phase estimates resulting from the application to the sample data set of 14 parallel spike trains take very small values between +2 and -2 milliseconds (cf. Fig. 3.2 B).

Variance of $\hat{\varphi}$: Approximate formula In the given model, the δ -method implies that if ω is known, $\hat{\varphi}$ has asymptotic normal distribution with asymptotic variance

$$\hat{\sigma}_{\hat{\varphi}}^2 = V(\omega, A/\sigma, N) \cdot G(s, f), \quad (\text{eq. (4.29)-(4.33)})$$

where $N = 2L/\delta + 1$ is the number of data points in the CCH. V decreases monotone in each of its arguments and thus, the precision with which φ can be estimated increases with ω , A/σ and N . The term G depends on the shift $s = \varphi/p$ of the cosine as a fraction of the period p and on the fraction of the period $f = 2L/p$ to which the cosine is fitted. Most importantly, G implies that the data points at the edges of the cosine function, where the slope is maximal, contribute much information about φ , whereas points close to the extremes, where the slope is close to zero, are less important. Therefore, G depends crucially on the fraction of data points at the edges of the cosine in relation to the fraction at the extremes.

The scope of the formula In order to investigate whether the approximate formula yields useful estimates of $\hat{\sigma}_{\hat{\varphi}}$ when ω is unknown and for practically relevant values of N , cosine functions with independent and normally distributed noise have been simulated, and phase offsets have been estimated by fitting a cosine function to such simulated peaks. The resulting empirical standard deviation of $\hat{\varphi}$, $\sigma_{\hat{\varphi}}$, is compared to the distribution of standard deviations $\hat{\sigma}_{\hat{\varphi}}$ that have been estimated with the formula (Fig. 4.7 F). For a typical set of parameters, $\sigma_{\hat{\varphi}} \approx 0.2$ ms or 1% of a period. The root mean square (RMS) deviation of the approximate values $\hat{\sigma}_{\hat{\varphi}}$ from $\sigma_{\hat{\varphi}}$ was about 6.5% of $\sigma_{\hat{\varphi}}$. Both the RMS deviation and the empirical standard deviation $\sigma_{\hat{\varphi}}$ increase with σ/A . For all parameter sets, the normed phase estimate, $\hat{\varphi}/\hat{\sigma}_{\hat{\varphi}}$ was approximately normally distributed. As a consequence, each phase offset can be equipped with a 95%-confidence interval, which is smaller than one millisecond for the typical set of parameters. Thus, since the 91 phase estimates in the sample data set take values up to ± 2 ms, many among them are unlikely to be explained by measurement error.

In order to investigate whether the approximate formula can grasp the variability of phase offsets in the experimental data set, the data are divided, and two independent estimates $\hat{\varphi}_1, \hat{\varphi}_2$ are derived for every phase offset. The results suggest that the formula can describe the variability of these estimates because the distribution of normed differences $Z := (\hat{\varphi}_1 - \hat{\varphi}_2) \cdot (\hat{\sigma}_{\hat{\varphi}_1}^2 + \hat{\sigma}_{\hat{\varphi}_2}^2)^{1/2}$ does not show strong deviations from the standard normal distribution. Therefore, the formula is used to compare two sets of phase offsets. In the sample data set, phase offsets show systematic variations between different stimulation conditions.

Chapter 3

Measurement of phase offsets

As shown in Figures 1.3 & 3.1, the phase offset in a CCH may deviate from zero. However, due to the variability in the CCH, this phase offset cannot be obtained directly from the graph. Thus, a method is required with which the phase offset can be estimated and with which the precision of this estimate can be determined.

3.1 Gabor function

In order to estimate phase offsets, König (1994) proposed a method in which a damped cosine function (called Gabor function) is fitted to the CCH. The phase offset is directly available as the position of the maximum of the fitted function. The Gabor function $G(\ell)$ consists of three additive parts:

$$\begin{aligned} G(\ell) &:= O + \text{Gaussian} \cdot \text{Cosine} + \text{Central Gaussian} \\ &= O + \exp\left(-\left(\frac{|\ell - \varphi|}{\sigma_1}\right)^\lambda\right) \cdot A \cos(2\pi\omega(\ell - \varphi)) + B \exp\left(-\left(\frac{|\ell - \varphi|}{\sigma_2}\right)^2\right), \end{aligned}$$

where O describes the offset at the ordinate. Including O , the Gabor function depends on eight parameters: The cosine depends on the amplitude A , the oscillation frequency ω , and on φ , the phase offset. It is damped by a so-called generalized Gaussian with the three parameters φ , which denotes the shift of the maximum, $\sigma_1 > 0$, the standard deviation, and λ , which describes the shape of the peak and takes the value 2 for a usual Gaussian. Finally, the central and usually narrow Gaussian depends on the three parameters B , the amplitude, φ ,

the shift of the maximum, and $\sigma_2 > 0$, the standard deviation. The three additive parts of the Gabor function are shown in Figure 3.1 C together with the parameters A , B , O , ω , φ , σ_1 and σ_2 .

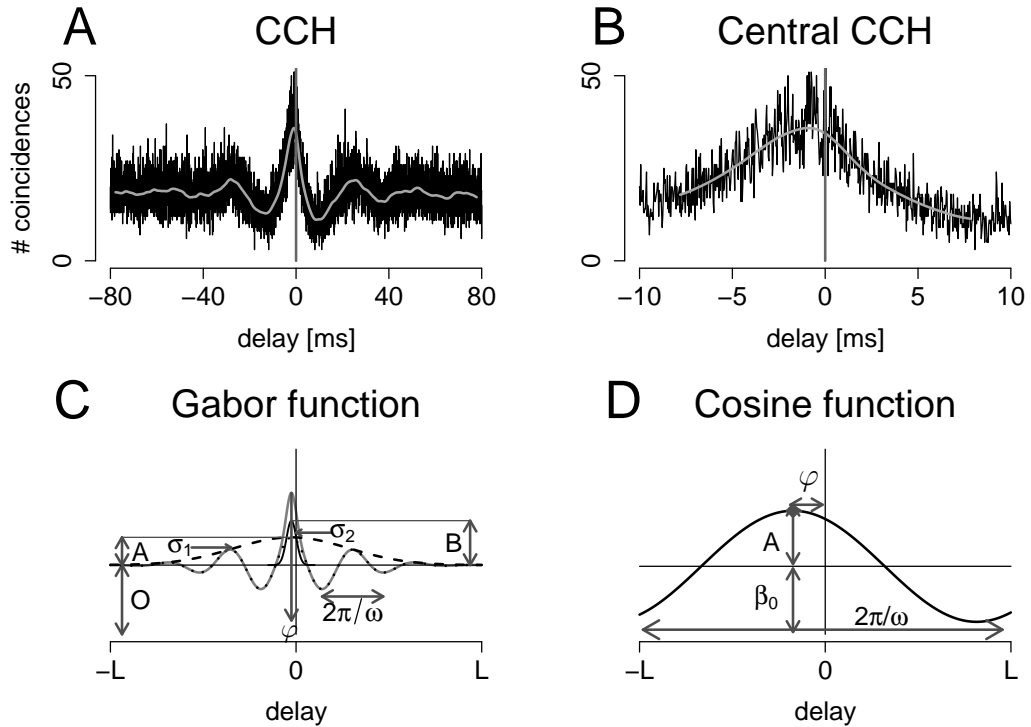


Figure 3.1: Example CCH and the parameters of a Gabor and a cosine function. A: CCH with $L = 80$ ms in the original time resolution ($\delta = 1/32$ ms, black) and smoothed with a Gaussian kernel with standard deviation 29δ (gray). B: CCH in A with $L = 10$ ms. C: Scheme of the components of a Gabor function. Black: Gaussian (dashed), damped cosine (dotted), central Gaussian (solid). Gray: Final Gabor function (solid). D: The parameters of a cosine function.

The high number of parameters of G yields very close fits of CCHs, and many parameters such as the oscillation frequency or the phase shift have a direct interpretation. On the other hand, this high number of parameters evokes computational difficulties. For example, if one wants to fit such a Gabor function to a CCH, all eight parameters have to be estimated in parallel. Often, several sets of starting values have to be chosen until the fitting procedure converges to a satisfactory result. This prevents a straightforward standardization of the fitting procedure and thus implies that the resulting estimates are not perfectly reproducible (cf. König, 1994). As a result, the measurement error of the estimated

parameters cannot be determined.

To resolve this issue, the fitted function is simplified. Since the main interest is the central peak, only the central part of the CCH is fitted, and the side peaks are excluded, which are unimportant and can differ in shift or frequency. The most simple function which can describe a central peak and has interpretable parameters for the phase offset as well as the oscillation frequency is a cosine function with the four parameters A , ω , φ and β_0 , where β_0 describes the offset at the ordinate (Fig. 3.1 D).

3.2 Cosine function

3.2.1 Assumptions

As shown in Figure 3.2 A, every data point in the CCH is assumed to be composed of a systematic component given by the cosine function and a nonsystematic error component. These errors are assumed to be independent across data points and normally distributed with variance σ^2 . Hence, every data point $H(\ell)$ in the CCH at time lag ℓ is described as

$$\begin{aligned} H(\ell) &= \text{Cosine} + \text{Noise} \\ &= A \cos(\omega(\ell - \varphi)) + \beta_0 + \sigma Z_\ell, \end{aligned} \quad (3.1)$$

where the $\{Z_\ell\}_{\ell \in \mathfrak{L}_\delta^L}$, are independent with $Z_\ell \sim \mathcal{N}(0, 1)$.

3.2.2 Data Analysis

According to the width of the central peaks of the CCHs in the sample data set, L was chosen to be 10 ms. The resulting window of 20 ms was big enough to cover the center peaks but sufficiently small to exclude the side peaks. With the time resolution of $\delta = 1/32$ ms, this yielded $N = 2L/\delta + 1 = 641$ data points, and

$$\mathfrak{L}_{1/32}^{10} = \{-320, -319, -318, \dots, -1, 0, 1, \dots, 318, 319, 320\} \cdot 1/32\text{ms}. \quad (3.2)$$

To find the cosine function that fits a given CCH best, the four parameters A , ω , φ and β_0 were estimated with the Gauss-Newton method implemented in the statistical analysis tool R¹. This iterative algorithm estimates the four

¹www.r-project.org

parameters in such a way that the sum of squares of the residuals between the CCH and the cosine function is minimized:

$$\sum_{\ell \in \mathcal{L}_\delta^L} \left(H(\ell) - [\hat{A} \cos(\hat{\omega}(\ell - \hat{\varphi})) + \hat{\beta}_0] \right)^2 \stackrel{!}{=} \min.$$

The Gauss-Newton algorithm requires appropriate starting values for the parameters. Due to the oscillatory shape of the CCHs, these starting values are easy to find. In the sample data set, all peaks were positioned close to zero and thus, the initial value of φ was also set to zero. The initial value of the oscillation frequency was chosen to correspond to the width of the center peaks in the set of analyzed CCHs, which was about 20 ms, yielding a frequency of about 50 Hz, or $\omega \approx 0.1\pi$ [ms⁻¹]. Since the analysis window covered about one cosine period, the initial value of the additive constant β_0 was set to the mean count in the analyzed CCH, and the initial value of A was always set to 1. This yielded the set S^* of standardized starting values

$$S^* := \{ \varphi^* := 0, \quad \omega^* := 0.3, \quad A^* := 1, \quad \beta_0^* := N^{-1} \sum_{\ell \in \mathcal{L}_\delta^L} H(\ell) \}. \quad (3.3)$$

This set S^* was used to fit all central CCH peaks in the sample data set. The resulting fitted functions agreed closely with the empirical CCHs, suggesting that the iterative algorithm found the global minimum.

The phase offset estimates that result from the application of this fitting procedure to all $91 = \binom{14}{2}$ CCHs of 14 analyzed channels in stimulation condition 1 are shown in Figure 3.2 B. As one can see, they range only up to about 2 ms, which is only 10% of the average peak width.

The results were highly robust against changes in individual starting parameters. Local minima with half the oscillation frequency and double amplitude were only obtained if either the additive constant β_0^* was too small (e.g. $\beta_0^* = \min_{\ell \in \mathcal{L}_\delta^L} H(\ell)$) or if the starting value ω^* was chosen too close to half the oscillation frequency. Additionally, local minima with double oscillation frequency may be returned if ω^* is too close to 2ω .

Justification of assumptions After the estimation of the parameters, it was investigated whether the assumptions presented in section 3.2.1 are suitable to describe the given data set. Figure 3.2 C shows one central CCH from the sample data set together with its fitted cosine function. The residuals plotted in Figure 3.2 D show no systematic trend, which suggests that the fitted cosine function essentially grasps the shape of the central peak. The distribution of the

residuals is shown in Figure 3.2 E and agrees well with the theoretically assumed normal distribution. Finally, the dependence between residuals was investigated by computing the serial correlations of the residuals at all time lags up to 10 ms. The resulting correlation between the original CCH and the CCH shifted by different lags is shown in Figure 3.2 F. For all lags $\tau \leq 10$ ms, the correlation between one residual and its τ -next neighbor is smaller than 0.1, suggesting that correlations between residuals can be considered close to zero for the presented CCH. Comparable results were obtained in most CCHs in the sample data set.

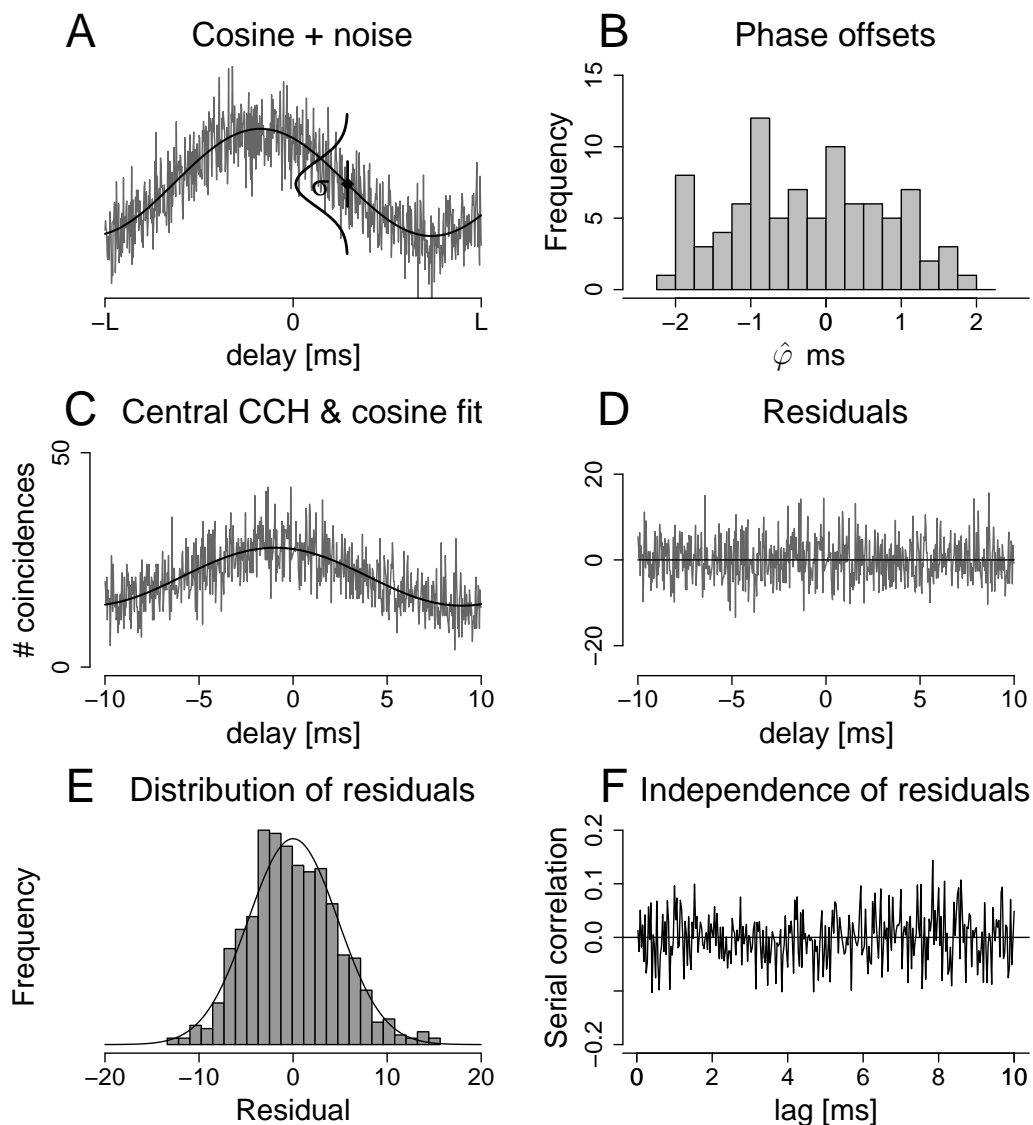


Figure 3.2: Analysis of residuals between central CCHs and fitted cosine functions. A: Theoretical assumption of independent and normally distributed noise added to the cosine function. B: Distribution of phase offset estimates obtained from fitting cosine functions to all 91 CCHs in stimulation condition 1. C: An example CCH obtained experimentally (gray). Counts between $-2/32$ ms and $2/32$ ms were excluded due to potential artifacts. Black: Cosine function fitted to the CCH. D: Residuals between the empirical CCH and the fitted cosine function in C as a function of the time lag. E: Distribution of the residuals in D (histogram) and normal distribution (curve). F: Temporal correlation of residuals in D expressed as the correlation between the vector of residuals and itself, shifted by lags up to 10 ms.

Chapter 4

Precision of measurement

Since phase offsets can be very small in relation to the cosine period length (Fig. 3.2 B), such small phase offsets are often considered equivalent to zero offsets (e.g., Toyama *et al.*, 1981; Gerstein *et al.*, 1985; Ts'o *et al.*, 1986; Gray *et al.*, 1989; Gochin *et al.*, 1991; Engel *et al.*, 1991; Gray *et al.*, 1992; Roelfsema *et al.*, 1997), and small deviations from zero are attributed to the variability of counts in the CCH. Additionally, there is evidence that non-zero phase offsets in periodic activity may play a role in information processing (König *et al.*, 1995; Traub *et al.*, 1997). Since recent findings suggest that neurons can coordinate their firing activity with high temporal precision, one should be able to determine also the measurement error of very small phase estimates as precisely as possible. This can be achieved by various methods.

First, one could measure phase offsets repeatedly under identical conditions. This investigation of the empirical variability allows a straightforward interpretation of the estimates in the analyzed data set because the approach is parameter free and can directly assess the variability of estimates between independent measurements. However, this comparison of independent measurements requires recording a high number of identical repetitions. Although this is advisable from the statistician's perspective, the number of replications may be limited by experimental constraints. Thus, only a splitting of the available data set is practicable for the statistical analysis. The resulting analysis performed on a smaller data set can only be done with lower precision. Additionally, a splitting and a separate analysis of data sets requires computational effort, and the results are only relevant for the data set under investigation and thus, hard to generalize.

Second, one could use simulated CCHs to study the variability of phase estimates between independent data sets obtained under identical conditions. As

an advantage, there is no limitation in the wealth of surrogate data, and they can be generated more easily than experimental CCHs. However, simulations require additional computational effort and are based on model assumptions which can only describe essential parts of the data and can never grasp all relations among the data points. Furthermore, the results of simulations can only be applied to data within the investigated parameter ranges and can thus also not be generalized without restrictions.

The third possibility to assess the precision of measurement is to provide a mathematical expression which can be used directly to estimate the variability of the phase estimate after the fitting procedure. This formula would avoid computational effort and should be applicable to a wide parameter range. However, the application of such a mathematical expression requires that the analyzed data set complies with the assumptions used in the derivation of the formula.

In the following subsections, the three described methods are combined to determine the variability of a phase estimate as precisely as possible. The main goal is to develop a formula with which this variability can be assessed directly. This formula should provide practical guidelines concerning the appropriate choice of the analysis window as well as theoretical insights into the relations between the cosine parameters and the estimation precision. The scope of the derived formula is investigated by simulations and by comparison to the empirical variability of phase estimates computed in independent trials of the same stimulation condition.

4.1 A formula for the variance of a phase estimate

To develop a formula for the approximate variance of the phase estimate, the starting point is equation (3.1), which describes the assumption that every data point in the CCH consists of a cosine component and a random error component:

$$H(\ell) = A \cos(\omega(\ell - \varphi)) + \beta_0 + \sigma Z_\ell \quad \forall \ell \in \mathcal{L}_\delta^L,$$

where all Z_ℓ are independent and $\mathcal{N}(0, 1)$ distributed.

The question approached here is the following. When cosine functions are fitted to different CCHs with identical parameters A , ω , φ , β_0 and σ , the estimated phase offsets vary due to different noise components. Additionally, the size of σ can affect this variability of the phase estimates in different ways, depending

on the other parameters of the cosine. For example, the same σ should have a bigger impact on the estimation precision if the amplitude A is small than when A is big.

The goal is to answer the following question: How does the variability of phase estimates depend on the cosine parameters A , ω , φ , β_0 and σ and on the number of data points, $N = 2L/\delta + 1$? This section approaches this question by the derivation of a mathematical formula, which is discussed and interpreted in section 4.1.2.

Proposition 1 (Asymptotic variance of the phase estimate) *For known ω , the phase estimate has asymptotic normal distribution with asymptotic variance*

$$\text{Var}(\hat{\varphi}) \doteq \widetilde{\text{Var}}(\hat{\varphi}) := V(\omega, N, \sigma, A) \cdot G(\omega, \varphi, L) \quad \text{as } N \rightarrow \infty \quad (4.1)$$

with

$$V(\omega, N, \sigma, A) := \frac{2}{\omega^2} \cdot \frac{1}{N} \cdot \frac{\sigma^2}{A^2} \quad (4.2)$$

$$G(\omega, \varphi, L) := \frac{\cos^2(\omega\varphi)}{D_1(\omega L)} + \frac{\sin^2(\omega\varphi)}{D_2(\omega L)}, \quad (4.3)$$

$$D_1(\omega L) := 1 - \frac{\sin(2\omega L)}{2\omega L} \quad (4.4)$$

$$D_2(\omega L) := 1 + \frac{\sin(2\omega L)}{2\omega L} + \frac{2\sin^2(\omega l)}{\omega^2 L^2}. \quad (4.5)$$

Since the symbol \sim is used here to describe equality in distribution, the symbol \doteq denotes asymptotic equivalence in the sense that $a_N \doteq b_N : \iff a_N/b_N \rightarrow 1$ as $N \rightarrow \infty$.

4.1.1 Proof of Proposition 1

To prove proposition 1, equation (3.1) is first transformed into a linear combination containing coefficients β_0 , β_1 and β_2 . This allows to express $\hat{\varphi}$ as a function of the estimates $\hat{\beta}_1$ and $\hat{\beta}_2$. After this, the main idea is based on the (multidimensional) δ -method with which one can derive the approximate variance of $\hat{\varphi}$ as a function of the variances of $\hat{\beta}_1$ and $\hat{\beta}_2$.

Transformation into a linear combination

$$\begin{aligned} A \cos(\omega(l - \varphi)) &= A[\cos(\omega\varphi) \cos(\omega l) + \sin(\omega\varphi) \sin(\omega l)] \\ &= \beta_1 \cos(\omega l) + \beta_2 \sin(\omega l) \end{aligned} \quad (4.6)$$

with

$$\beta_1 = A \cos(\omega\varphi) \quad \text{and} \quad \beta_2 = A \sin(\omega\varphi), \quad (4.7)$$

$$A^2 = A^2(\cos(\omega\varphi)^2 + \sin(\omega\varphi)^2) = \beta_1^2 + \beta_2^2, \quad (4.8)$$

$$\varphi = \omega^{-1} \arcsin\left(\beta_2/\sqrt{\beta_1^2 + \beta_2^2}\right) \quad \text{for } |\omega\varphi| < \frac{\pi}{2}, \quad (4.9)$$

$$\varphi = \text{sgn}(\varphi) \left(\pi - \omega^{-1} \arcsin\left(\beta_2/\sqrt{\beta_1^2 + \beta_2^2}\right) \right) \quad \text{for } |\omega\varphi| \in \left[\frac{\pi}{2}, \pi\right]. \quad (4.10)$$

Thus, equation (3.1) can be written as

$$H(\ell) = \beta_0 + \beta_1 \cos(\omega\ell) + \beta_2 \sin(\omega\ell) + \sigma Z_\ell, \quad (4.11)$$

where the phase estimate can be derived from the coefficients β_1 and β_2 according to equation (4.9) if $\beta_2 \geq 0$ and with equation (4.10) if $\beta_2 < 0$.

Multidimensional δ -method If the oscillation frequency, ω , is known, fitting a cosine function to the CCH is equivalent to estimating the coefficients β_0 , β_1 and β_2 with linear regression analysis. Thus, the phase estimate is a function of the coefficient estimates $\hat{\beta}_1$ and $\hat{\beta}_2$. Since the variances of the terms in (4.9) and (4.10) are identical, the variance of the term given in (4.9) is derived here with the multidimensional δ -method (e.g., Bishop *et al.*, 1975, p.493):

Proposition 2 Multidimensional δ -method Let $\theta := (\vartheta_1, \dots, \vartheta_d)$ be a d -dimensional parameter, and let $\hat{\theta}_N := (\hat{\vartheta}_{N,1}, \dots, \hat{\vartheta}_{N,d})$ be a d -dimensional random vector with the property

$$\mathcal{L} \left[\sqrt{N}(\hat{\theta}_N - \theta) \right] \xrightarrow{N \rightarrow \infty} \mathcal{N}(0, \Sigma(\theta)), \quad (4.12)$$

where $\Sigma(\theta)$ is the $d \times d$ asymptotic covariance matrix of $\hat{\theta}_N$. Let furthermore be $f : O \rightarrow \mathbb{R}$ a function defined on an open subset $O \subseteq \mathbb{R}^d$ which is differentiable at θ , i.e., f has the following expansion for x close to θ :

$$f(x) = f(\theta) + \sum_{i=1}^d (x_i - \vartheta_i) \frac{\partial f}{\partial x_i}(\theta) + o(\|x - \theta\|). \quad (4.13)$$

Then the asymptotic distribution of $f(\hat{\theta}_N)$ is given by

$$\mathcal{L} \left[\sqrt{N}(f(\hat{\theta}_N) - f(\theta)) \right] \xrightarrow{N \rightarrow \infty} \mathcal{N} \left(0, \left(\frac{\partial f}{\partial \theta} \right) \Sigma(\theta) \left(\frac{\partial f}{\partial \theta} \right)^T \right). \quad (4.14)$$

Thus, if $\sigma_{k\ell}(\theta)$ denotes the element of $\Sigma(\theta)$ in the k^{th} row and ℓ^{th} column, the asymptotic variance of $f(\hat{\theta}_N)$ is described by

$$\text{Var}(f(\hat{\theta}_N)) \doteq N^{-1} \sum_{k,\ell=1}^d \sigma_{k\ell}(\theta) \left(\frac{\partial f}{\partial \theta_k} \right) \left(\frac{\partial f}{\partial \theta_\ell} \right). \quad (4.15)$$

The δ -method will be used to compute the asymptotic variance of the phase estimate. Since $\hat{\varphi}$ is a function of the coefficient estimates $\hat{\beta}_1$ and $\hat{\beta}_2$, the asymptotic distribution of those estimates is needed for the application of Proposition 2 and will be derived in Lemmata 1 and 2.

Lemma 1 *The coefficient estimates $\hat{\beta}_1$ and $\hat{\beta}_2$ have asymptotic normal distributions with expectation β_1 and β_2 , respectively. Their variances are given by*

$$\sigma_1^2 := \text{Var}(\hat{\beta}_1) = \frac{\sigma^2 N}{N \sum \cos^2(\omega\ell) - (\sum \cos(\omega\ell))^2} \quad (4.16)$$

$$\sigma_2^2 := \text{Var}(\hat{\beta}_2) = \frac{\sigma^2}{\sum \sin^2(\omega\ell)}, \quad (4.17)$$

and their covariance $\text{Cov}(\hat{\beta}_1, \hat{\beta}_2) = 0$.

Proof.

Equation (4.11) reads in matrix notation

$$\begin{aligned} \begin{pmatrix} H(-L) \\ H(-L + \delta) \\ \vdots \\ H(L) \end{pmatrix} &= \begin{pmatrix} 1 & \cos(\omega(-L)) & \sin(\omega(-L)) \\ 1 & \cos(\omega(-L + \delta)) & \sin(\omega(-L + \delta)) \\ \vdots & \vdots & \vdots \\ 1 & \cos(\omega L) & \sin(\omega L) \end{pmatrix} \begin{pmatrix} \beta_0 \\ \beta_1 \\ \beta_2 \end{pmatrix} + \sigma \begin{pmatrix} Z_{-L} \\ Z_{-L+\delta} \\ \vdots \\ Z_L \end{pmatrix} \\ &=: X\beta + \sigma Z. \end{aligned}$$

As is known from linear regression analysis,

$$\hat{\beta} \sim \mathcal{N}(\beta, (X^T X)^{-1} \sigma^2). \quad (4.18)$$

Note that

$$\begin{aligned} \sum_{\ell \in \mathfrak{L}_\delta^L} 1 \cdot \sin(\omega\ell) &= \sum_{\ell \in \mathfrak{L}_\delta^L, \ell > 0} (\sin(\omega\ell) - \sin(\omega\ell)) = 0 \\ \sum_{\ell \in \mathfrak{L}_\delta^L, \ell > 0} \sin(\omega\ell) \cos(\omega\ell) &= \sum_{\ell \in \mathfrak{L}_\delta^L, \ell > 0} \cos(\omega\ell) (\sin(\omega\ell) - \sin(\omega\ell)) = 0. \end{aligned}$$

Therefore,

$$X^T X = \begin{pmatrix} N & \sum \cos(\omega\ell) & 0 \\ \sum \cos(\omega\ell) & \sum \cos^2(\omega\ell) & 0 \\ 0 & 0 & \sum \sin^2(\omega\ell) \end{pmatrix}. \quad (4.19)$$

Thus, $\hat{\beta}_1$ and $\hat{\beta}_2$ are uncorrelated, and the diagonal elements $(X^T X)_{(2,2)}^{-2}$ and $(X^T X)_{(3,3)}^{-2}$ are σ_1^2 and σ_2^2 as given in equations (4.16) and (4.17), respectively. \square

To simplify the formulas for σ_1^2 and σ_2^2 , the sums in equations (4.16) and (4.17) are approximated by their corresponding integrals, yielding the asymptotic formulas in Lemma 2.

Lemma 2 *For large N , σ_1^2 and σ_2^2 can be approximated by*

$$\sigma_1^2 \doteq \frac{2\sigma^2}{N} \left(1 + \frac{\sin(2\omega L)}{2\omega L} - \frac{2\sin^2(\omega L)}{\omega^2 L^2} \right)^{-1} = \frac{2\sigma^2}{N} \cdot \frac{1}{D_2(\omega L)} \quad (4.20)$$

$$\sigma_2^2 \doteq \frac{2\sigma^2}{N} \left(1 - \frac{\sin(2\omega L)}{2\omega L} \right)^{-1} = \frac{2\sigma^2}{N} \cdot \frac{1}{D_1(\omega L)} \quad (4.21)$$

Proof.

It suffices to show the asymptotic formulas for the following sums:

$$\sum_{\ell \in \mathfrak{L}_\delta^L} \cos^2(\omega\ell) \doteq \frac{N}{2} \left[1 + \frac{\sin(2\omega L)}{2\omega L} \right] \quad (4.22)$$

$$\sum_{\ell \in \mathfrak{L}_\delta^L} \cos(\omega\ell) \doteq N \cdot \frac{\sin(\omega L)}{\omega L} \quad (4.23)$$

$$\sum_{\ell \in \mathfrak{L}_\delta^L} \sin^2(\omega\ell) \doteq \frac{N}{2} \left[1 - \frac{\sin(2\omega L)}{2\omega L} \right] \quad (4.24)$$

Note first that

$$\begin{aligned}\int_{-L}^L \cos^2(\omega x) dx &= L + \frac{\sin(2\omega L)}{2\omega} \\ \int_{-L}^L \cos(\omega x) dx &= 2/\omega \cdot \sin(\omega L) \\ \int_{-L}^L \sin^2(\omega x) dx &= L - \frac{\sin(2\omega L)}{2\omega}.\end{aligned}$$

Approximating $\sum \cos^2(\omega \ell)$ with its corresponding integral yields

$$\begin{aligned}\sum_{\ell \in \mathfrak{L}_\delta^L} \cos^2(\omega \ell) &= \delta^{-1} \sum_{\ell \in \mathfrak{L}_\delta^L} \cos^2(\omega \ell) \cdot \delta \\ &= \delta^{-1} \left[\int_{-L}^L \cos^2(\omega x) dx + R \right] \\ &= \frac{N-1}{2} \left[1 + \frac{\sin(2\omega L)}{2\omega} \right] + \frac{R}{\delta},\end{aligned}$$

with

$$R \leq \delta(\cos^2(\omega L) + \omega L).$$

The term $\cos^2(\omega L) \cdot \delta$ is caused by the right border point, L , which adds an extra rectangle of size $\cos^2(\omega L) \cdot \delta$ that cannot be used to approximate the integral. The term

$$\omega L \cdot \delta = (\omega \delta) \cdot (\delta) \cdot 1/2 \cdot (N-1)$$

originates in the maximal approximation error in each of the $N-1$ summands: Since the maximal slope of $\cos^2(\omega x)$ is ω :

$$\max_x (\cos^2(\omega x))' = \max_x (-2 \cos(\omega x) \sin(\omega x) \omega) = \max_x (-\omega \sin(2\omega x)) = \omega,$$

the size of the rectangle originating from the maximal slope is $(1/2)\omega\delta^2$. Hence,

$$\sum_{\ell \in \mathfrak{L}_\delta^L} \cos^2(\omega \ell) = \frac{N}{2} \left[1 + \frac{\sin(2\omega L)}{2\omega} \right] + R_1$$

with

$$R_1 \leq \cos^2(\omega L) + \omega L + \frac{1}{2} + \frac{\sin(2\omega L)}{4\omega}.$$

R_1 does not depend on N and is thus neglected in equation (4.22). The approximations (4.23) and (4.24) can be derived analogously. \square

Corollary 1

$$\mathcal{L} \left[\sqrt{N} \begin{pmatrix} \hat{\beta}_1 - \beta_1 \\ \hat{\beta}_2 - \beta_2 \end{pmatrix} \right] \xrightarrow{N \rightarrow \infty} \mathcal{N} \left(0, \begin{pmatrix} 2\sigma^2/D_2(\omega L) & 0 \\ 0 & 2\sigma^2/D_1(\omega L) \end{pmatrix} \right) \quad (4.25)$$

Corollary 2

$$\text{Var}(\omega\hat{\varphi}) \doteq \frac{2}{N} \cdot \frac{\sigma^2}{A^2} \cdot \left(\frac{\cos^2(\omega\varphi)}{D_1(\omega L)} + \frac{\sin^2(\omega\varphi)}{D_2(\omega L)} \right). \quad (4.26)$$

Proof.

With Proposition 2 and Conclusion 1, with $d = 2$ and

$$\theta := \frac{\beta_2}{\sqrt{\beta_1^2 + \beta_2^2}}$$

$$f((\beta_1, \beta_2)) := \arcsin \left(\frac{\beta_2}{\sqrt{\beta_1^2 + \beta_2^2}} \right)$$

$$O := \left\{ (\beta_1, \beta_2) : \frac{\beta_2}{\sqrt{\beta_1^2 + \beta_2^2}} < \pi \right\},$$

it follows that

$$\begin{aligned} \text{Var}(\omega\hat{\varphi}) &= \text{Var} \left(\arcsin \left(\hat{\beta}_2 / \sqrt{\hat{\beta}_1^2 + \hat{\beta}_2^2} \right) \right) = \text{Var}(f(\hat{\theta})) \\ &\doteq N^{-1} \left(\frac{2\sigma^2}{D_2(\omega L)} \left(\frac{\partial f}{\partial \beta_1} \right)^2 + \frac{2\sigma^2}{D_1(\omega L)} \left(\frac{\partial f}{\partial \beta_2} \right)^2 \right) \\ &= \frac{2\sigma^2}{N(1 - \beta_2^2/(\beta_1^2 + \beta_2^2))} \left(\frac{\beta_1^2 \beta_2^2}{D_2(\omega L)(\beta_1^2 + \beta_2^2)^3} + \frac{(1 - \beta_2^2/(\beta_1^2 + \beta_2^2))^2}{D_1(\omega L)(\beta_1^2 + \beta_2^2)} \right) \\ &= \frac{2}{N} \cdot \frac{\sigma^2}{A^2} \left(\frac{\cos^2(\omega\varphi)}{D_1(\omega L)} + \frac{\sin^2(\omega\varphi)}{D_2(\omega L)} \right), \end{aligned}$$

which completes the proof of Proposition 1. \square

Thus, equation (4.1) approximates the variance of $\hat{\varphi}$ if N is large and if ω is known. Before the discussion of the practical usefulness of the formula, its formal and geometric implications are investigated more closely.

4.1.2 Formula asymptotic variance: Interpretation

4.1.2.1 Parameterization

To understand the derived formula for the approximate variance of phase offsets (4.1), note that the term $G = G(\omega, \varphi, L)$ in (4.3) depends on the two quantities $(\omega\varphi)$ and (ωL) . Therefore, the following parameterization is more suitable to describe G . Let

$$s := \frac{\varphi}{p} = \frac{\omega\varphi}{2\pi} \quad (4.27)$$

denote the shift of the cosine expressed as a proportion of one cosine period, p (Fig. 4.1 A), and let

$$f := \frac{2L}{p} = \frac{\omega L}{\pi} \quad (4.28)$$

denote the fitted part of the cosine, expressed as a fraction of p (Fig. 4.1 B). Since f and s describe geometric quantities, the term G is also referred to as the ‘geometric term’. The asymptotic formula now reads

$$\widetilde{\text{Var}}(\hat{\varphi}) = V(\omega, N, \sigma, A) \cdot G(f, s) \quad (4.29)$$

with

$$V(\omega, N, \sigma, A) = \frac{2}{\omega^2} \cdot \frac{1}{N} \cdot \frac{\sigma^2}{A^2} \quad (4.30)$$

$$G(s, f) = \frac{\cos^2(2\pi s)}{D_1(f)} + \frac{\sin^2(2\pi s)}{D_2(f)} \quad (4.31)$$

$$D_1(f) = 1 - \frac{\sin(2\pi f)}{2\pi f} \quad (4.32)$$

$$D_2(f) = 1 + \frac{\sin(2\pi f)}{2\pi f} + \frac{2 \sin^2(\pi f)}{\pi^2 f^2}. \quad (4.33)$$

Note that $\widetilde{\text{Var}}(\hat{\varphi})$ is defined unless one of the parameters ω , N , A or f equals zero. This is no restriction because trivially, without data points ($N = 0$), without oscillation ($\omega = 0$ or $A = 0$) or with an analysis window of size zero ($f = 0$), no cosine can be fitted.

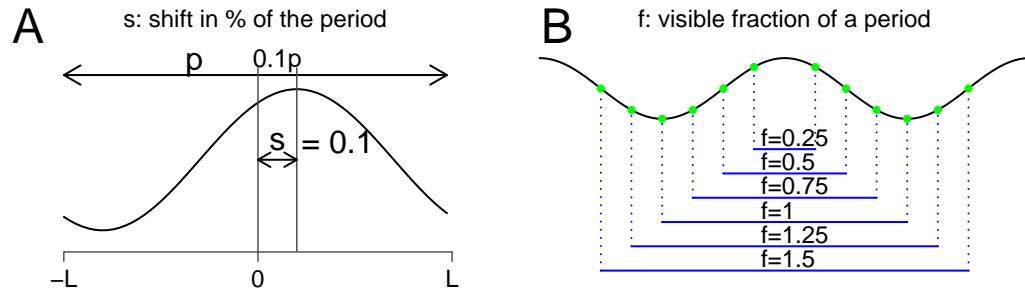


Figure 4.1: Illustration of the parameters s and f . A: An example with $s = 10\%$ of the cosine period. B: Visible fractions of a period for a centered cosine function ($s = 0$), depending on the window size.

4.1.2.2 The parameters of V

Most parameters of the term V are directly interpretable. Keeping all other parameters constant, an increase in the number of data points (Figs. 4.2 A & B) and a decrease in the relation of the noise σ to the amplitude A (Figs. 4.2 C & D) increase the precision of the estimate.

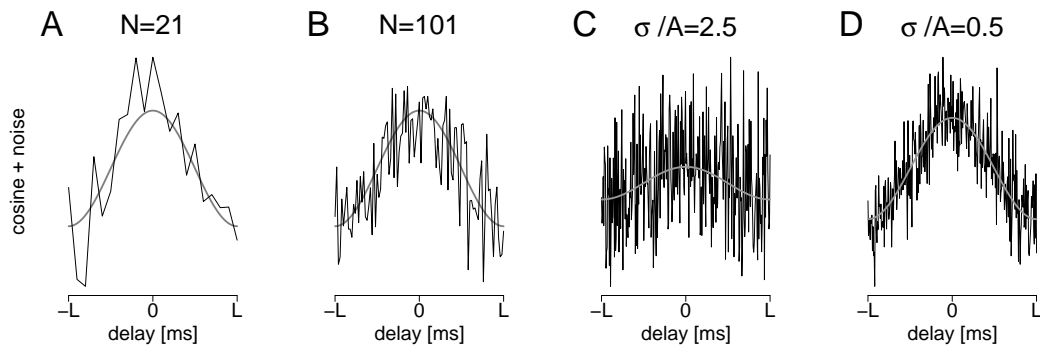


Figure 4.2: Influence of N and σ/A on the estimation precision of φ . Simulated noisy cosine functions with parameters $\varphi = 0$, $A = 1$, $f = 1$. A, B: For constant σ , the estimation precision increases with N ($\sigma = 0.55$). C, D: For constant N , the estimation precision decreases with growing σ/A ($N = 300$).

The number of data points In the preceding paragraph, the influence of the number of data points, N , was discussed independent of the parameter σ , i.e., the variability of data points around the cosine. However, for a given analysis window, N determines the time resolution, or ‘bin size’, and σ thus depends on

N . The following two paragraphs provide heuristic arguments for two claims: (i) Although the precision of the phase estimate is not affected by a change of the bin size, (ii) the variance of the phase estimate can be determined less precisely for a lower time resolution.

(i) If the bin size is increased by an integer factor k by averaging counts of k adjacent bins, the new values $\sigma_{N/k}^2$ and $N_{N/k}$ are given by

$$\sigma_{N/k}^2 = \text{Var}\left(\sigma^2/k \sum_{l=i_1}^{i_k} Z_l^2\right) = \sigma^2/k \quad \text{and} \quad N_{N/k} = N/k. \quad (4.34)$$

Thus, the quotient remains constant and does not depend on k :

$$\frac{\sigma_{N/k}^2}{N_{N/k}} = \frac{\sigma^2}{N} \quad \forall k \in \mathbb{N}, \quad (4.35)$$

which means that a change of the bin size should not affect the precision of $\hat{\varphi}$.

(ii) However, a decrease in N may affect the usefulness of the asymptotic approximation as well as the precision with which σ can be estimated. Again, a simplified computation shows:

Let Z_1, \dots, Z_N be independent and $\mathcal{N}(0, \sigma^2)$ -distributed, denoting the noise in the N bins. Estimating the variance with

$$\hat{\sigma}^2 := 1/N \sum_{i=1}^N Z_i^2 \quad \text{implies} \quad \text{Var}(\hat{\sigma}^2) = \sigma^4/N. \quad (4.36)$$

Thus, the difference $(\hat{\sigma}^2 - \sigma^2)$ is of the size σ^2/\sqrt{N} , or $1/\sqrt{N} \cdot 100\%$ of σ^2 . Let now be N a multiple of k and let the binned error counts be given by

$$Y_1 := 1/k \sum_{j=1}^k Z_j, \quad Y_2 := 1/k \sum_{j=k+1}^{2k} Z_j, \quad \dots$$

Then, $Y_j \sim \mathcal{N}(0, \sigma^2/k)$, $j = 1, \dots, N/k$.

The variance of $Y_1, \dots, Y_{N/k}$ is estimated with

$$\hat{\sigma}^2/k := \frac{1}{N/k} \sum_{j=1}^{N/k} Y_j^2, \quad \text{which yields} \quad \text{Var}(\hat{\sigma}^2/k) = \sigma^4/N \cdot 1/k. \quad (4.37)$$

Here, the difference $(\hat{\sigma}^2/k - \sigma^2/k)$ is of the size $\sqrt{k/N} \cdot 100\%$ of σ^2/k . Thus, the relative estimation error of the variability grows with \sqrt{k} , where k is the number of data points that are averaged.

The practical influence of the bin size on the variability of phase estimates as well as on its estimation precision will be investigated in practice in section 4.2.2.

The oscillation frequency, ω . Finally, V depends on ω . V increases with a decrease in the oscillation frequency because the precision decreases when the peak is broadened. In addition, since the geometric parameters s and f both depend on ω , the geometric term G is also affected. The next paragraph describes the dependence of the geometric term, G , on f and s .

4.1.2.3 The parameters of G

The dependence of G on f is first discussed for $s = 0$. In this case, G simplifies to

$$G(0, f) = D_1(f)^{-1} = \frac{1}{1 - \frac{\sin(2\pi f)}{2\pi f}}. \quad (4.38)$$

The graph of $G(0, f)$ is plotted in Figure 4.3 A. As one can see both in the graph and in equation (4.38),

$$\lim_{f \rightarrow \infty} G(0, f) = 1, \quad G(0, n/2) = 1 \quad \forall n \in \mathbb{N}, \quad \text{and} \quad \lim_{f \rightarrow 0} G(0, f) = \infty.$$

Thus, $G(0, f)$ tends to 1 and is close to 1 (i.e., $|G(0, f) - 1| < 0.2$) for $f > 0.5$. Clearly, G is large if the phase shift is estimated from a window that comprises less than half of the cosine period.

The oscillatory shape of G originates in the term $\sin(2\pi f)$. To understand this oscillation, consider the case where the parameters ω , A , σ and N are constant, in which the variance of the phase estimate depends only on G . In this case, the variance is minimal for $f^* \approx 0.72$ and has local minima that reoccur with a period of about 1. Vice versa, the maximal variance for $f > 0.5$ is obtained for $f^o \approx 1.23$, and G has local maxima that reoccur after about 1 unit of f . The corresponding analyzed data points (for $N = 25$) of the cosine for the minimal $f \in \{0.72, 1.74\}$ and the maximal $f \in \{1.23, 2.24\}$ are illustrated in the Figures 4.3 B & C, respectively. One can see that those constellations with minimal variance contain many data points at the ‘edges’ of the cosine function, i.e., at the points with maximal slope (Fig. 4.3 B). On the other hand, those f for

which the variance reaches local maxima are characterized by a high number of data points at the extremes, i.e., at the points with minimal slope (Fig. 4.3 C). Thus, the data points of the cosine function with maximal slope contribute more information about the phase offset than the data points with minimal slope.

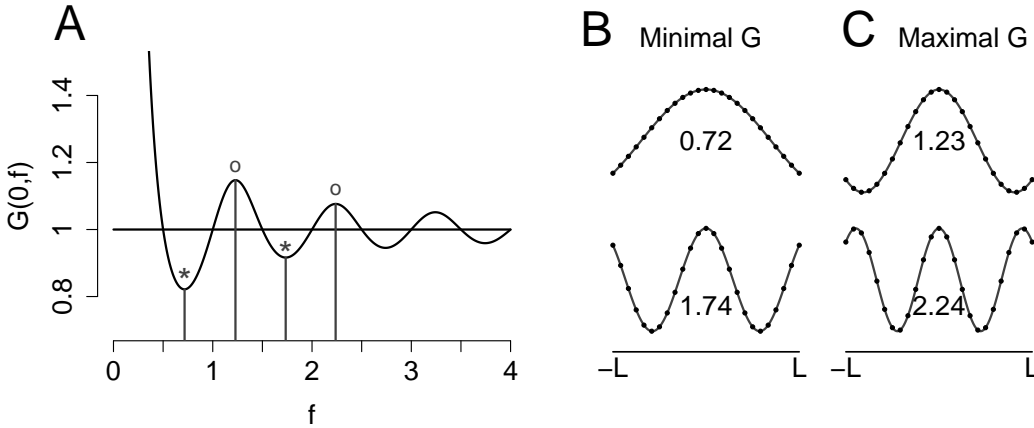


Figure 4.3: Geometric interpretation of the dependence of G on f for $s = 0$ and constant N . A: The curve of $G(0, f)$. Two local minima are indicated by stars, and the corresponding data points for $f = 0.72$ and $f = 1.74$ are illustrated in B ($N = 25$). Small circles in A indicate local maxima, and the corresponding data points for $f = 1.23$ and $f = 2.24$ are indicated in C ($N = 25$).

Given this key principle, one can conclude the following properties of the geometric term $G(s, f)$ for $s \neq 0$. These properties can also be observed in Figures 4.4 A-C, which show the graphs of $G(s, f)$ for the values $s \in \{0.06, 0.12, 0.2\}$.

1. For integer f , the data points are positioned equidistant and uniformly across the whole cosine period. Thus, no shift should affect the value of G . This can be confirmed by a simple computation: For all $n \in \mathbb{N}$, $D_1(n) = D_2(n) = 1$, implying

$$G(s, n) = \cos^2(2\pi s) + \sin^2(2\pi s) = 1 = G(0, n) \quad \forall n \in \mathbb{N}, \forall s \in \mathbb{R}.$$

2. For constant f , $G(s, f)$ is periodic in s with period $1/2$ because a shift of 50% of a cosine period results in an identical cosine function which is only multiplied with -1 .
3. For small f , i.e., $f < 0.5$, any shift should decrease G and thus improve the estimation precision because shifting includes additional data points at the edges and excludes data points at the maximum.

4. Similarly, at the f -values where $G(0, f)$ reaches local maxima, any shift $s \neq 0$ should decrease G , and the maximal decrease should be obtained for $s = 0.25$ because this exchanges the numbers of points at the edges and the extremes. The same holds true for the local minima of $G(0, f)$.

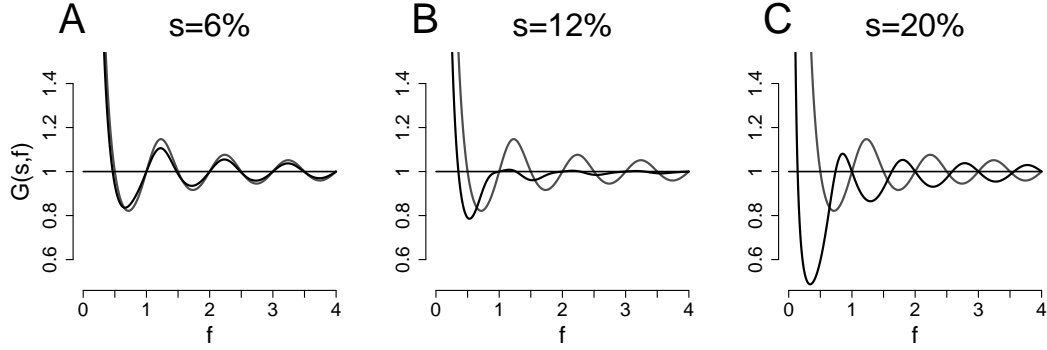


Figure 4.4: Dependence of G on the visible part of the period for $s \neq 0$. Graphs of $G(s, f)$ for $s = 0.06$ (A), $s = 0.12$ (B) and $s = 0.2$ (C). Gray curves indicate $G(0, f)$ (Fig. 4.3 A).

The window size In the preceding paragraph, the influence of f was discussed for constant V , i.e., N was kept constant. This led to important insights into the geometric properties of G . However, to investigate the practical influence of f on the variability of $\hat{\varphi}$, one has to take into account that in practice, the number of data points N increases with the size of the analysis window, which depends on f . Thus, not only G but also V depends on f . Writing N as a function of f , the variability of the phase estimate as a function of f can be described with the following expression if ω , σ , δ and A are kept constant:

$$\widetilde{\text{Var}}(\hat{\varphi}) = c \cdot \frac{1}{f \frac{2\pi}{\omega\delta} + 1} \cdot \left(\frac{\cos^2(2\pi s)}{D_1(f)} + \frac{\sin^2(2\pi s)}{D_2(f)} \right). \quad (4.39)$$

The graphs of this function are shown in Figures 4.5 A-C for different s . One can see that the variance of $\hat{\varphi}$ decreases constantly with f if the number of data points is increased with f . Thus, every data point adds information about the position of the peak. However, for a centered cosine (Fig. 4.5 A), the slope is zero for integer f , which means that the data points close to the maxima and minima of the cosine do not improve the phase estimate. This phenomenon does not occur for $s \neq 0$ because the windows are asymmetric with respect to the maximum.

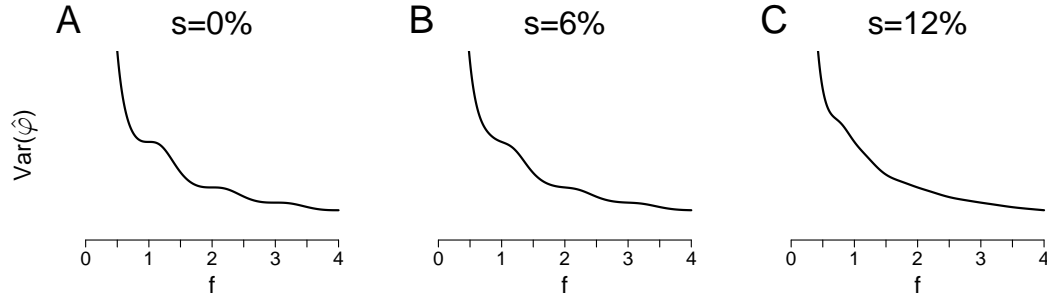


Figure 4.5: Decrease in the variance of $\hat{\varphi}$ as a function of f (equation (4.39)) for the parameters $s = 0$ (A), $s = 0.06$ (B) and $s = 0.12$ (C) and for constant A , σ , ω and δ . y-axis limits identical in all panels.

4.1.3 Formula asymptotic variance: Implications for practical application

The most important points discussed in sections 4.1.1 and 4.1.2 are summed up here with respect to the application of the formula to experimental data.

Choice of the analysis window The data points close to the maxima or minima of the cosine do not contribute much information about the position of the peak. In contrast, the data points located at the maximal slope of the cosine are highly informative. For a peak centered close to zero, one should use the maximal possible analysis window because every data point adds information about the position of the peak. In practice however, the cosine shape is not continued in a CCH for bigger time lags than $f \approx 1$, implying that the analysis window should not exceed the area of the center peak considerably.

Application of the approximate formula The variability of the phase estimate in an experimentally obtained CCH can be approximated as follows:

1. Choose a time resolution δ (as fine as possible) and an analysis window that contains slightly more than the central peak. This yields the maximal time lag L and the number of data points, $N = 2L/\delta + 1$.
2. Estimate the parameters ω , A , β_0 and φ by fitting a cosine function to the data points in the chosen analysis window.

3. From the fitted cosine function, estimate the standard deviation (σ) of the residuals between the cosine and the CCH.
4. Estimate the variance of the phase estimate by insertion of the estimated parameters into the formula given in (4.1), i.e.,

$$\hat{\sigma}_{\hat{\varphi}}^2 = \frac{2\hat{\sigma}^2}{\hat{\omega}^2 N \hat{A}^2} \cdot \left(\frac{\cos^2(\hat{\omega}\hat{\varphi})}{1 - \frac{\sin(2\hat{\omega}L)}{2\hat{\omega}L}} + \frac{\sin^2(\hat{\omega}\hat{\varphi})}{1 + \frac{\sin(2\hat{\omega}L)}{2\hat{\omega}L} + \frac{2\sin^2(\hat{\omega}L)}{\hat{\omega}^2 L^2}} \right). \quad (4.40)$$

5. If the theoretical formula yields reliable estimates of the variability of the phase estimate in the given CCH, then

$$[\hat{\varphi} - 2\hat{\sigma}_{\hat{\varphi}}, \hat{\varphi} + 2\hat{\sigma}_{\hat{\varphi}}]$$

should be an approximate 95% confidence interval for the phase estimate in the CCH.

6. As a rule of thumb, the measurement error of the phase estimate is relatively small if the variability of data points around the cosine is small compared to the amplitude and if the analysis window contains many data points in those areas of the cosine with high slope.

4.2 The scope of the formula

The existence of a mathematical expression for the measurement error of phase estimates has many advantages. For example, the computational effort can be reduced, and confidence intervals can be constructed in a straightforward manner. However, the derivation of the formula is based on several assumptions.

One of those assumptions states that the oscillation frequency, ω , is known before the cosine is fitted to the CCH. In practice, this is not the case, and ω needs to be estimated together with the other parameters φ , σ and A . It is thus necessary to investigate whether the formula also approximates the variance of the phase estimate if ω has to be estimated. Additionally, the formula is derived on the basis of the assumption that the number of data points is sufficiently large to neglect higher-order terms in the Taylor expansion. In practice, the number of data points is limited and thus, one should investigate whether N is sufficiently large to apply the asymptotic formula.

The two issues concerning the number of data points and the estimation of ω are investigated in section 4.2.1. After the extraction of the relevant parameter ranges from the experimental data, noisy cosine functions are simulated, and the estimated variance of the phase estimate is compared to the empirical variance observed in the simulations.

Finally, experimentally obtained CCHs do not have to comply with the assumptions in the cosine model. Therefore, the experimentally obtained variability of phase estimates is compared in section 4.2.3 to the variability predicted by the formula.

4.2.1 Simulations

4.2.1.1 Parameter ranges

The parameter ranges for which simulations are performed are extracted from the CCHs in the sample data set (see App. A.3) in order to ensure that the results are applicable to this data set. Figure 4.6 shows the empirical distributions of the parameter estimates $\hat{\sigma}/\hat{A}$, \hat{f} and \hat{s} obtained from fitting all 91= $\binom{14}{2}$ CCHs in stimulation condition 1. The mean estimated fraction σ/A was about 1.2, this quotient ranging up to 2.9. The mean fraction of the cosine period, f , was about 110%, ranging between 0.9 and slightly more than 1.3. The estimated phase shifts, s , were approximately uniformly distributed on the interval $[0, 0.1]$. Therefore, the parameter ranges used to simulate noisy cosine functions were

$$\sigma \in \{0.5, 1, 1.5, 2\}, \quad A = 1, \quad f \in \{0.9, 1, 1.1, 1.2\} \quad \text{and} \quad s \in \{0, 4\%, 8\% \}.$$

The simulations were performed for all combinations of these parameters. Detailed results are shown for the typical parameter set

$$A^t = 1, \quad \sigma^t = 1, \quad f^t = 1.1, \quad s^t = 0. \quad (4.41)$$

As described in section 3.2.2, the number of data points was $N = 641$.

4.2.1.2 Results for typical parameter values

For every parameter set $\{A, f, s, \sigma\}$, 10,000 surrogate CCHs were simulated by adding independent and normally distributed noise with variance σ^2 to each of the $N = 641$ data points of a cosine segment parameterized by A , f and s . After this, a cosine function was fitted to each of the noisy cosine segments as described in section 3.2.2. In a third step, the variability of the phase estimate

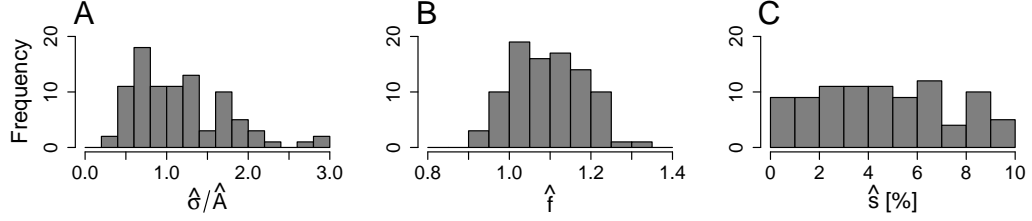


Figure 4.6: Distributions of parameter estimates $\hat{\sigma}/\hat{A}$ (A), \hat{f} (B), \hat{s} (C) obtained from fitting cosine functions to all 91 CCHs in stimulation condition 1.

was estimated for every simulated CCH by insertion of the parameter estimates into equation (4.1).

The distributions of the estimated parameters $\{A, \sigma, f, s\}$ are shown in Figures 4.7 A, B, D and E for the typical parameter set (4.41), the true parameter values being indicated by vertical lines. As one can see, the estimated phase shift (measured in percent of the period) typically deviates by less than 1% of the period from the true value zero. From the estimates of A and σ , the estimated signal-to-noise ratio, $\hat{\sigma}/\hat{A}$, is derived and shown in Figure 4.7 C. Additionally, the estimates of f and s are scaled in milliseconds for the analysis window given by $L = 10$ ms (Figs. 4.7 G & H, respectively). In this setting, the estimated phase shifts typically deviate from zero by less than 0.2 ms (empirical standard deviation $\sigma_{\hat{\varphi}} \approx 0.17$ ms indicated by arrow). This empirically derived value is used as a reference in Figure 4.7 F (indicated by black line), where it is compared to the distribution of estimated standard deviations of $\hat{\varphi}$ as computed with equation (4.40). As one can see, the distribution of the estimated standard deviations is very close to the empirically derived value. The root mean square (RMS) error measures the typical deviation of the estimates $\hat{\sigma}_{\hat{\varphi}}$ from the empirically derived value, $\sigma_{\hat{\varphi}}$. For convenience, it is expressed in % of $\sigma_{\hat{\varphi}}$:

$$\frac{100\%}{\sigma_{\hat{\varphi}}} \cdot \sqrt{\frac{\sum_i (\hat{\sigma}_{\hat{\varphi}}^i - \sigma_{\hat{\varphi}})^2}{10,000}}. \quad (4.42)$$

For the typical parameter set, the RMS deviation is only 6.5 % of $\sigma_{\hat{\varphi}}$ as indicated in Figure 4.7 F. Thus, equation (4.40) yields relatively precise estimates of the measurement error of $\hat{\varphi}$ in a CCH with the typical parameters.

Finally, it was investigated whether the standardized phase estimates are approximately standard normally distributed. The distribution of the values $\hat{\varphi}/\hat{\sigma}_{\hat{\varphi}}$ is shown in Figure 4.7 I together with the curve of the standard normal

distribution. The distribution of the standardized phase estimates is very close to the standard normal distribution for the typical parameter set, indicating that equation (4.40) can be used to build approximate confidence intervals for the phase shift. The results were comparable for all investigated parameter combinations.

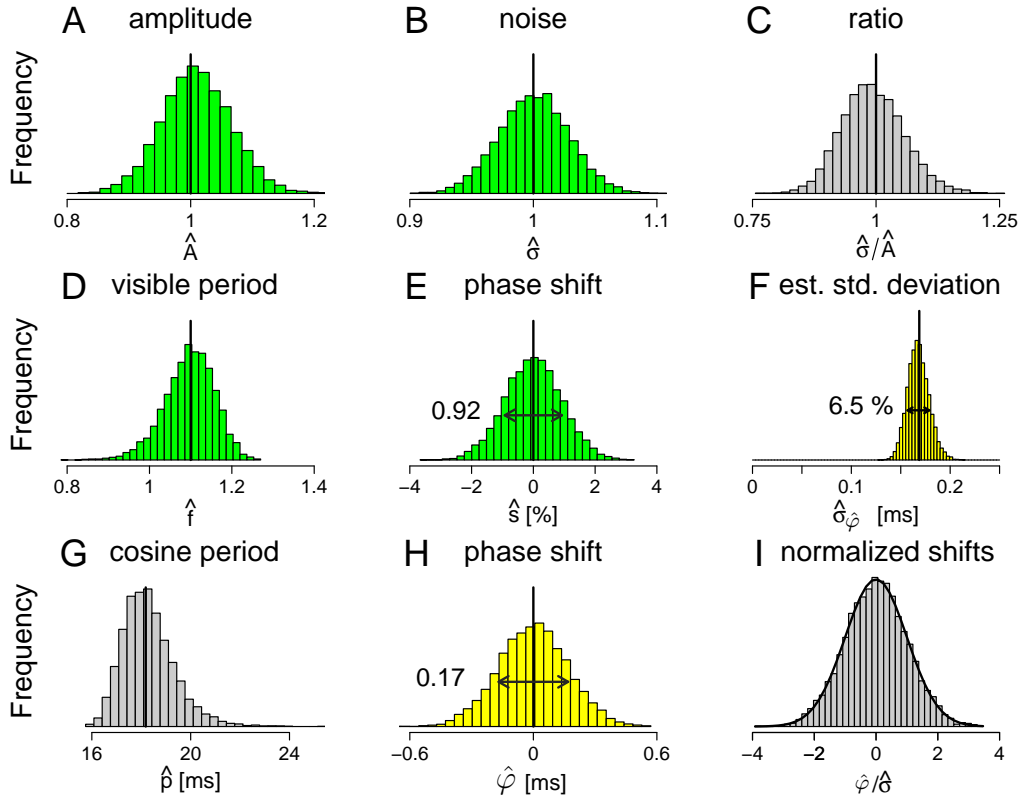


Figure 4.7: Distributions of estimates resulting from 10,000 simulations with the typical parameter set (4.41). A-D, G: Distributions of the estimates of A , σ , σ/A , f and p , respectively. Real parameters are indicated by vertical lines. E: Distribution of \hat{s} in % of a period with indicated empirical standard deviation. H: Distribution of $\hat{\varphi}$ in ms with indicated empirical standard deviation. F: Standard deviation of $\hat{\varphi}$ derived empirically (vertical line) and distribution of estimated standard deviations of $\hat{\varphi}$ computed with equation (4.40). Arrow indicates RMS deviation of the estimates $\hat{\sigma}_{\hat{\varphi}}$ from $\sigma_{\hat{\varphi}}$. I: Distribution of phase estimates normalized by their estimated standard deviations (histogram) and theoretical standard normal distribution (curve).

4.2.1.3 Applicability of the formula

After the discussion of the simulation results for the typical parameter set, three main issues are studied in this section for all simulated parameter combinations. First, the dependence of the empirical standard deviation, $\sigma_{\hat{\varphi}}$, on the variability of data points in relation to the amplitude, σ/A (compare Figs. 4.2 C & D), is investigated. Second, the dependence of the RMS deviation of $\hat{\sigma}_{\hat{\varphi}}$ from $\sigma_{\hat{\varphi}}$ on σ/A is investigated. In the third step, the usefulness of equation (4.40) is evaluated with respect to the construction of confidence intervals.

Empirical standard deviation of phase estimates, $\sigma_{\hat{\varphi}}$ For the typical parameter set (4.41), the standard deviation $\sigma_{\hat{\varphi}}$ is about 0.17 ms, or 0.92% of a period (indicated by arrows in Figs. 4.7 E & H and by the vertical line in Fig. 4.7 F). The dependence of $\sigma_{\hat{\varphi}}$ on σ/A is shown in Figure 4.8 A for $\sigma/A \in \{0.5, 1, 1.5, 2\}$, $f = 1.1$, $s = 0$, and $A = 1$. The right y-axis indicates units of milliseconds, while the left y-axis shows units of percent of a period. As predicted in the theoretical formula (4.1), the standard deviation of $\hat{\varphi}$ grows linearly with σ/A if all other parameters are kept constant. The slope depends on the parameter f but varies only slightly in the investigated parameter ranges. Likewise, small variations in s cause only negligible changes in the results.

The root mean square deviation of $\hat{\sigma}_{\hat{\varphi}}$ from $\sigma_{\hat{\varphi}}$ is indicated in Figure 4.8 A by vertical bars. The deviation of $\hat{\sigma}_{\hat{\varphi}}$ from the empirical standard deviation $\sigma_{\hat{\varphi}}$ also grows with σ/A , indicating that not only φ but also its variability, $\sigma_{\hat{\varphi}}$, are harder to estimate when the noise is big in relation to the amplitude. For the rightmost data point with $\sigma/A = 2$, the RMS error amounts to about 13% of $\sigma_{\hat{\varphi}}$, which is already twice as large as the value 6.5% obtained for $\sigma/A = 1$.

Confidence intervals Finally, the confidence intervals produced with the estimate $\hat{\sigma}_{\hat{\varphi}}$ from equation (4.40) are investigated. The points in Figure 4.8 B indicate the percentages of simulations in each parameter set in which

$$\varphi \in CI_1 := [\hat{\varphi} - \hat{\sigma}_{\hat{\varphi}}, \hat{\varphi} + \hat{\sigma}_{\hat{\varphi}}] \quad \text{and} \quad \varphi \in CI_2 := [\hat{\varphi} - 2\hat{\sigma}_{\hat{\varphi}}, \hat{\varphi} + 2\hat{\sigma}_{\hat{\varphi}}].$$

They match closely the theoretical percentages 68.3% and 95.4% indicated by horizontal lines. The empirical percentages tend to be slightly smaller than the theoretical values, which corresponds to an underestimation of $\sigma_{\hat{\varphi}}$ in the mean. This phenomenon can also be observed in Figure 4.7 F in which the mean of the

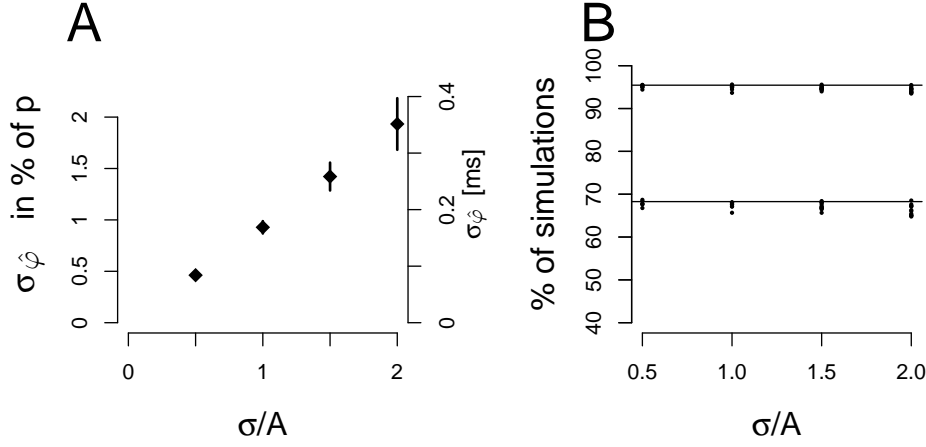


Figure 4.8: Usefulness of asymptotic formula for different parameter ranges and construction of confidence intervals. A: Dots indicate empirically derived standard deviation of phase estimates in 10,000 simulations for the parameters $s = 0, f = 1.1, N = 641$ and $\sigma/A \in \{0.5, 1, 1.5, 2\}$. Error bars indicate RMS error of $\hat{\sigma}_{\hat{\varphi}}$ from $\sigma_{\hat{\varphi}}$. Left y-axis shows units of % of a cosine period, right y-axis shows units of ms for $L = 10$ ms. B: empirically derived confidence intervals. Dots indicate percentages of simulations with $\varphi \in [\hat{\varphi} - \hat{\sigma}_{\hat{\varphi}}, \hat{\varphi} + \hat{\sigma}_{\hat{\varphi}}]$ and $\varphi \in [\hat{\varphi} - 2\hat{\sigma}_{\hat{\varphi}}, \hat{\varphi} + 2\hat{\sigma}_{\hat{\varphi}}]$ for all simulated parameter ranges. Horizontal lines indicate theoretical percentages.

distribution of $\hat{\sigma}_{\hat{\varphi}}$ is slightly smaller than the empirical value $\sigma_{\hat{\varphi}}$. However, this phenomenon is negligible compared to the RMS deviation of $\hat{\sigma}_{\hat{\varphi}}$ from $\sigma_{\hat{\varphi}}$. Thus, for CCHs that comply with the cosine assumption in the investigated parameter ranges, formula (4.1) can be used to approximate the variance of $\hat{\varphi}$ and to build confidence intervals for the phase shift.

4.2.2 Binning

‘Binning’ describes the reduction of the time resolution that is caused by merging adjacent data points, so-called ‘bins’. This reduces the computational effort but has well-known disadvantages because it also reduces the precision of the data. Since spike trains or CCHs are often binned to a time resolution of a few milliseconds, the effect of binning on the estimation precision of φ and of $\sigma_{\hat{\varphi}}$ is studied here for an exemplary set of parameters. Starting with the typical parameter set

$$A^t = 1, \sigma^t = 1, f^t = 1.1, s^t = 0, N = 641, \delta = 1/32 \text{ ms}, L = 10 \text{ ms},$$

the time resolution δ is reduced to the values $\{1/4, 1/2, 1, 2, 2.5, 5\}$ ms, resulting in $N \in \{81, 41, 21, 11, 9, 5\}$ and in a new variability of data points $\sigma_{new}^2 \in \{1/8, 1/16, 1/32, 1/64, 1/80, 1/160\}\sigma^2$. Note the side effect that due to the merging of bins, the set of new data points contains slightly more information because the borders, $-L$ and L , result from merging data points up to a lag of $|L + \delta/2|$. Again, 10,000 simulations are performed for each parameter set.

Analogous to Figure 4.7 F, the distribution of $\hat{\sigma}_{\hat{\varphi}}$ was compared to the empirical standard deviation, $\sigma_{\hat{\varphi}}$. The results for a bin size of $\delta \in \{0.5, 2.5\}$ ms are shown in Figures 4.9 A & B. First, one should note that the empirical standard deviation of $\hat{\varphi}$, indicated by thick vertical bars, does not change with the bin size. This can also be observed in Figure 4.9 C. The empirically obtained standard deviations of $\hat{\varphi}$ are indicated by dots and stay constant for all values of δ used in the simulation. However, the error with which $\sigma_{\hat{\varphi}}$ can be estimated grows with the bin size. This is indicated by the error bars in Figure 4.9 C and by the RMS errors shown in Figure 4.9 D. For $\delta = 0.5$ ms, the RMS deviation from the empirical standard deviation is about 13%, which is already twice as much as was observed for the original time resolution. For the broader time resolution of $\delta = 2.5$ ms, the RMS error amounts up to 32% of the empirical variability.

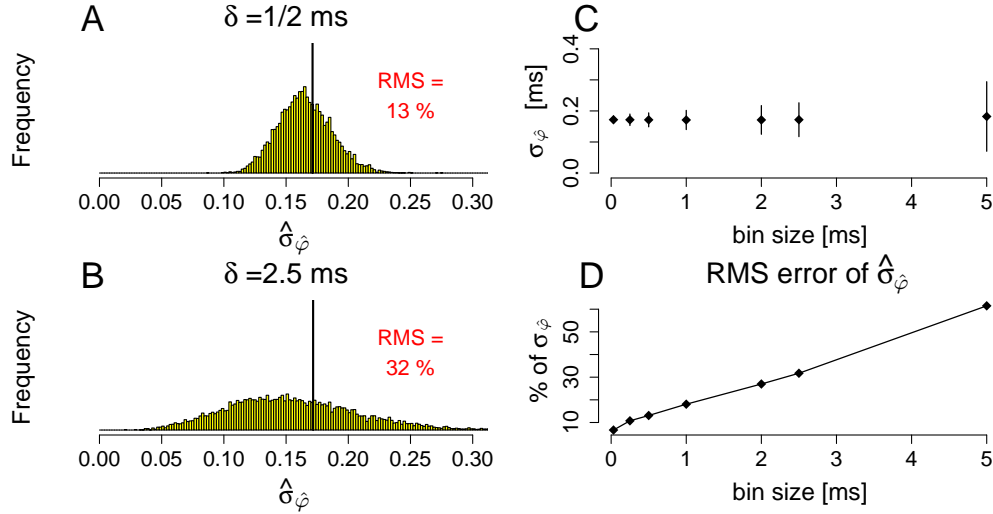


Figure 4.9: Application of the asymptotic formula (4.1) to binned data (10,000 simulations with parameters $A = 1, \sigma = 1, f = 1.1, s = 0, N = 641, L = 10$ ms and $\delta \in \{1/32, 1/4, 1/2, 1, 2, 2.5, 5\}$ ms). A, B: Distributions of $\hat{\sigma}_{\hat{\varphi}}$ in ms for $\delta = 1/2$ ms (A) and $\delta = 2.5$ ms (B). The empirical $\sigma_{\hat{\varphi}}$ is indicated by vertical bars. C: Points indicate empirical $\sigma_{\hat{\varphi}}$ as a function of the bin size. Error bars indicate RMS deviation of estimates from empirical $\sigma_{\hat{\varphi}}$. D: RMS deviation of $\hat{\sigma}_{\hat{\varphi}}$ from $\sigma_{\hat{\varphi}}$ in % of $\sigma_{\hat{\varphi}}$ as a function of the bin size.

Thus, although the precision of $\hat{\varphi}$ does not depend on the bin size, this precision is harder to estimate if the time resolution is decreased. As was described earlier, errors in the determination of the estimation precision can result in erroneous confidence intervals for the phase offset. One should thus use the original sampling frequency in which the data were recorded whenever possible.

4.2.3 Comparison to experimental variability

The studies in section 4.2.1 suggest that formula (4.1) can be used to estimate the variance of the phase estimate for data which (i) comply with the cosine assumption, i.e., cosine functions with independent and normally distributed random noise, and (ii) whose parameter values are within the investigated intervals. This also suggests that the formula is applicable to the experimentally obtained CCHs because (i) the data analysis in section 3.2.2 did not indicate deviations from the cosine assumption and because (ii) the investigated parameter ranges were derived from the empirical estimates. However, one cannot prove that the experimentally obtained CCHs comply with the cosine assumption. It is therefore necessary to investigate whether formula (4.1) can also grasp the variability of phase estimates obtained experimentally.

To approach this question, the spike trains that were used to compute one phase offset φ are divided into two independent sets of equal size. For each of the two sets, a CCH is computed and a cosine function is fitted separately. Thus, two estimates of φ are derived. To investigate whether the asymptotic formula can describe the variability between the two estimates, equation (4.1) is used to estimate the variance of $\hat{\varphi}$ in one half of the data. This theoretical variability is then compared to the empirical difference between the two estimates.

The assumptions are as follows. Let $\varphi_1, \dots, \varphi_n$ denote the phase offsets. Then, by splitting the data sets, one gets two sets of estimates

$$\mathcal{S}_1 := \{\hat{\varphi}_1^{(1)}, \dots, \hat{\varphi}_n^{(1)}\} \quad \text{and} \quad \mathcal{S}_2 := \{\hat{\varphi}_1^{(2)}, \dots, \hat{\varphi}_n^{(2)}\}.$$

Let the estimates $\hat{\varphi}_1^{(1)}, \dots, \hat{\varphi}_n^{(1)}, \hat{\varphi}_1^{(2)}, \dots, \hat{\varphi}_n^{(2)}$ be independent and

$$\hat{\varphi}_i^{(k)} \sim \mathcal{N}(\varphi_i, \sigma_{\hat{\varphi}_i}^2) \quad \forall k = 1, 2, \quad \forall i = 1, \dots, n.$$

A standardization of the difference of estimates yields standard normally distributed random variables

$$\frac{\hat{\varphi}_i^{(1)} - \hat{\varphi}_i^{(2)}}{\sqrt{2}\sigma_{\hat{\varphi}_i}} \sim \mathcal{N}(0, 1) \quad i = 1, \dots, n. \quad (4.43)$$

To investigate whether equation (4.1) can be used to estimate the variability of phase estimates, $\sigma_{\hat{\varphi}_i}$ is estimated with equation (4.1), and the distribution of the resulting values

$$Z_i := \frac{\hat{\varphi}_i^{(1)} - \hat{\varphi}_i^{(2)}}{\sqrt{2}\hat{\sigma}_{\hat{\varphi}_i}}, \quad (4.44)$$

which should be approximately $\mathcal{N}(0, 1)$ -distributed, is compared to the standard normal distribution.

In practice, the data analysis is performed as follows: From the 14 recorded channels, $n = 91$ pairwise CCHs and phase offsets are derived. Originally, every phase offset in stimulation condition 1 is computed from the responses to 20 identical presentations of the same stimulus (trials 1, ..., 20). These trials are divided into the two independent sets of odd and even trials ($\{1, 3, \dots, 19\}$ and $\{2, 4, \dots, 20\}$), and CCHs and phase offsets are derived separately. This results in the two sets of phase offsets \mathcal{S}_1 and \mathcal{S}_2 measured in the odd and even trials, respectively. The standard deviation of a single phase offset is then estimated from the CCH in the odd trials by application of formula (4.1). This yields $n = 91$ Z -values derived with equation (4.44). Since it is irrelevant whether Z_i is positive or negative and since there are only 91 values, the absolute values $|Z_i|$ are compared to the nonnegative part of the standard normal distribution. Figure 4.10 A shows that the distribution of the $|Z_i|$ -values is close to the standard normal distribution. Also the corresponding normal plot of Z_i -values in Figure 4.10 B shows high agreement between the sample and the theoretical quantiles. This indicates that the approximate formula (4.1) can describe the variability of phase estimates for noisy cosine functions as well as grasp the measurement error of phase shifts in experimentally obtained CCHs in the sample data set. Thus, the theoretical formula can be used for practical applications such as statistical decisions concerning deviations of single phase offsets from zero or statistical comparisons of sets of phase measurements. An exemplary analysis of the latter will be performed in the following section.

4.3 Application: A significance test

Chapter 4 showed that the measurement error of phase estimates in CCHs in the sample data set can be estimated quickly and precisely with formula (4.1). This allows answering the questions posed in the beginning of this chapter. One of the

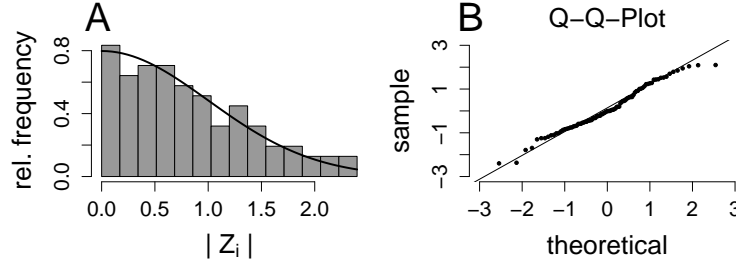


Figure 4.10: Comparison of the variability of phase offsets as derived experimentally and as estimated with the formula. A: Distribution of 91 absolute differences of phase offsets in odd and even trials in stimulation condition 1, standardized with the estimated standard deviation. The black curve indicates the theoretical standard normal distribution. B: Q-Q-plot of standardized phase offset differences from A.

most striking issues concerns the small size of measured phase offsets, which range only up to a few milliseconds. With the help of confidence intervals estimated with the theoretical formula (4.1), it is now possible to evaluate deviations of phase offsets from zero. As could be observed for the typical parameter set, 95 % confidence intervals can be smaller than one millisecond, which allows conclusions about phase offsets in the millisecond range.

Even more interesting is the question whether or not these small phase offsets might play a role in information processing. In order to investigate this issue, one needs to be able to study changes of sets of phase offsets across different stimulation conditions. To this end, a formula is proposed which allows the comparison of two sets of phase offsets by a simple test statistic and avoids multiple testing.

The null hypothesis of the statistical test is similar to the situation described on page 41. Consider two independent sets of n measurements, $\mathcal{S}_1 := \{\hat{\varphi}_1^{(1)}, \dots, \hat{\varphi}_n^{(1)}\}$ and $\mathcal{S}_2 := \{\hat{\varphi}_1^{(2)}, \dots, \hat{\varphi}_n^{(2)}\}$, which are paired such that for all $i = 1, \dots, n$,

$$\hat{\varphi}_i^{(k)} \sim \mathcal{N}(\varphi_i, (\hat{\sigma}_{\hat{\varphi}_i}^{(k)})^2), \quad k = 1, 2.$$

Note that according to this null hypothesis, two paired measurements do not necessarily have the same variance. The terms

$$Z_i := \frac{\hat{\varphi}_i^{(1)} - \hat{\varphi}_i^{(2)}}{\sqrt{(\hat{\sigma}_{\hat{\varphi}_i}^{(1)})^2 + (\hat{\sigma}_{\hat{\varphi}_i}^{(2)})^2}} \quad (4.45)$$

have an approximate standard normal distribution, where $(\hat{\sigma}_{\hat{\varphi}_i}^{(k)})^2$ denotes the estimated variance of $\hat{\varphi}_i^{(k)}$ in the set \mathcal{S}_k . Since the sum of squares of n stan-

standard normally distributed random variables has χ^2 -distribution with n degrees of freedom, we get an approximate $\chi^2(n)$ -distribution of the test statistic

$$S := \sum_{i=1}^n Z_i^2 \quad (4.46)$$

under the null hypothesis that differences between measurements in the sets \mathcal{S}_1 and \mathcal{S}_2 are only caused by measurement errors. If on the other hand differences between paired measurements are too big to be explained by measurement errors, the test statistic S grows, which yields smaller p -values.

Application of the test to the sample data set simply requires choosing the two sets of measurements \mathcal{S}_1 and \mathcal{S}_2 that are to be compared. For example, one can test sets of phase offsets derived from independent repetitions of the same stimulation condition to investigate differences of phase offsets across repeated presentations of the same stimulus. To this end, the 20 presentations of the same stimulus are again divided into the two sets of odd and even trials, the $2n$ phase offsets $(\hat{\varphi}_i^{(1)}, \hat{\varphi}_i^{(2)})_{i=1, \dots, n}$ and their approximate variances $\left((\hat{\sigma}_{\hat{\varphi}_i}^{(1)})^2, (\hat{\sigma}_{\hat{\varphi}_i}^{(2)})^2 \right)_{i=1, \dots, n}$ are estimated independently for each of the two sets of trials. From these estimates, the test statistic S is computed, and the corresponding probability that a $\chi^2(n)$ -distributed random variable is at least as big as S is derived from the χ^2 -distribution.

The results of this analysis applied to stimulation conditions 3 and 5 are presented in the rows 1 and 2 of Table 4.1. In row 3, phase offsets that were measured in stimulation conditions 3 and 5 are compared with the same technique. The big p -values in rows 1 and 2 are in agreement with the hypothesis that phase offsets stay stable across repeated measurements of stimulation conditions 3 and 5 in the sample data set. On the other hand, the changes in phase offsets between stimulation conditions 3 and 5 are unlikely to have occurred by chance, which is indicated by the small p -value in the last row.

<i>Comparison</i>	<i>S</i>	<i>p</i>
odd - even trials, cond. 3:	89.8	0.516
odd - even trials, cond. 5:	104.1	0.165
Cond. 3 - cond. 5	285.0	< 0.0001

Table 4.1: Application of the statistical test to two stimulation conditions from the sample data set; $n = 91$ phase offsets in each set of measurements.

Chapter 5

Conclusion – Part I

In summary, a method was presented with which the phase shift in a CCH can be estimated by fitting a cosine function to the central CCH peak. The presented technique is sufficiently simple to allow standardization of the starting parameters and of the estimation procedure. Therefore, a formula is derived which approximates the variance of the phase estimate as a function of the cosine parameters and additional geometric parameters. This formula describes the variability of phase offsets in simulations with parameter ranges similar to those in the experimental data set and predicted the variability obtained experimentally. It can thus be applied in the construction of confidence intervals for single phase offsets and in statistical tests of differences between sets of measurements.

As a limiting factor, the derived formula is based on the assumptions presented in section 3.2.1, i.e., that the counts in a CCH peak can be described with a cosine function with independent and normally distributed noise. Moreover, the formula has been tested here only for a limited set of parameters. For example, if CCHs are more noisy than those given in the sample data set - which may be the case in recordings of single units - it may be necessary to bin CCHs prior to further analysis. This increases the error with which σ can be estimated. Thus, an application of the derived formula should also consider the parameter range.

A central question concerns the interpretation of phase offsets in a formal and in a physiological sense. Formally, phase offsets can be interpreted as indicating the most frequent delay recorded between two units. However, this delay does not occur exclusively. In contrast, spike delays of two units are broadly jittered around this delay, which is reflected in the width of the central peak. Also, no conclusions are drawn about the source of correlation between two spike

trains that causes the peak. As discussed by several authors, CCHs can only be interpreted in a straightforward manner if the spike trains can be considered stationary in the sense that the joint distribution of the numbers of spikes in fixed intervals is invariant under translation (Cox and Lewis, 1966; Perkel *et al.*, 1967b)¹. If spike trains are not stationary in time, central peaks can be caused by a covariation of excitability such as a variability of response onset (‘latency variability’) or covariations in the firing rate (Perkel *et al.*, 1967a,b; Brody, 1999a,b; Baker and Gerstein, 2001; Ventura, 2004). On the other hand, central peaks can be caused by precisely coordinated synchronous discharges which occur within a few milliseconds and thus irrespective of a detectable increase in the firing rate. In the investigation of central CCH peaks performed in this part, the mechanism that causes a peak is irrelevant. In fact, the method is not restricted to CCHs but can be applied to any noisy and peak-shaped function that complies with the model assumptions given in section 3.2.1. Thus, the method of fitting a cosine function combined with the formula for the approximate variance of the phase estimate provides an analytic tool for the investigation of temporal properties in neuronal discharges.

Physiologically, it might be possible to encode additional information with the help of small phase offsets. Accordingly, Hopfield (1995) proposed a theoretical coding mechanism that requires oscillatory activity and uses the relative phase of firing as a carrier of information. Going one step further, it has been argued that information might be encoded in the relative temporal order of single spikes of different neurons within a population (Traub *et al.*, 1997; Van Rullen *et al.*, 1998; Delorme and Thorpe, 2001; Delorme, 2003). It is commonly agreed that this coding mechanism has great computational power and speed, providing efficient object representation and robustness against noise or a change of the stimulus (Van Rullen and Thorpe, 2001; Johansson and Birznieks, 2004).

Such approaches, which combine the relative phase of firing with a temporal order code, motivate the investigations in Part II. The phase offsets analyzed in this Part provide the basis for the further analysis of temporal relations between the discharge times in large networks.

¹This restriction gave rise to time-resolved extensions such as the joint peri-stimulus time histogram (JPSTH, Gerstein and Perkel, 1969, 1972; Aertsen *et al.*, 1989) with which dynamic temporal relations between pairs of units can be investigated.

Part II

The structure of phase offsets

Chapter 6

Introduction and Results

6.1 Motivation

This part deals with the analysis of temporal relations among the spike trains of different neurons in large networks. Many available methods face the problem of high computational effort since the number of possible temporal relations increases exponentially with the number of units. The approach described here circumvents this problem by restricting the investigation of temporal patterns to the predominant delays measured between pairs of units, i.e., phase offsets. On the basis of these pairwise measurements, temporal relations among all units are investigated. On the one hand, this restriction to pairwise analysis reduces the computational effort because among n units¹, only $\binom{n}{2}$ phase offsets are computed. On the other hand, this restricted but complex pairwise information has to be integrated in order to analyze temporal relations among all units.

The presented method is based on the idea that the preferred delays are additive. Figure 6.1 A shows three phase offsets φ_{12} , φ_{23} and φ_{13} between the units 1, 2 and 3. These are additive if the sum $\varphi_{12} + \varphi_{23}$ corresponds to the direct offset φ_{13} . If this condition is satisfied for all phase offsets computed among a set of n neurons, all phase offsets can be represented as differences between points on a line, which is referred to as the *time axis*. Accordingly, in Figure 6.1 B, six units are positioned on the time axis, and the difference between two units indicates the phase offset - or the ‘preferred spiking delay’ between these units. Therefore, the positions of the units on the time axis are called ‘preferred relative firing times’ (*PTs*). Note that preferred delays between two units can be positive or negative. In particular, $\varphi_{ij} = -\varphi_{ji}$.

¹Note that in Part II, n denotes the number of units, whereas the resulting number of phase offsets, $\binom{n}{2}$, was denoted by n in Part I.

If a set of phase offsets is completely additive, it is also highly redundant, and the units can be positioned easily on the time axis on the basis of only a few measurements. In practice, however, phase offsets are measured with an error and can thus never be completely additive. Therefore, it is necessary to develop a model with which the set of unit positions on the time axis can be estimated on the basis of additive but noisy phase offsets. The model should furthermore allow the estimation of the measurement error. In chapter 7, a model is presented with which the set of unit positions and the measurement error can be estimated. This allows the extraction of a simple and low-dimensional temporal structure for the firing activity of a large group of neurons if the set of phase offsets complies with the model assumption of additivity and unsystematic noise.

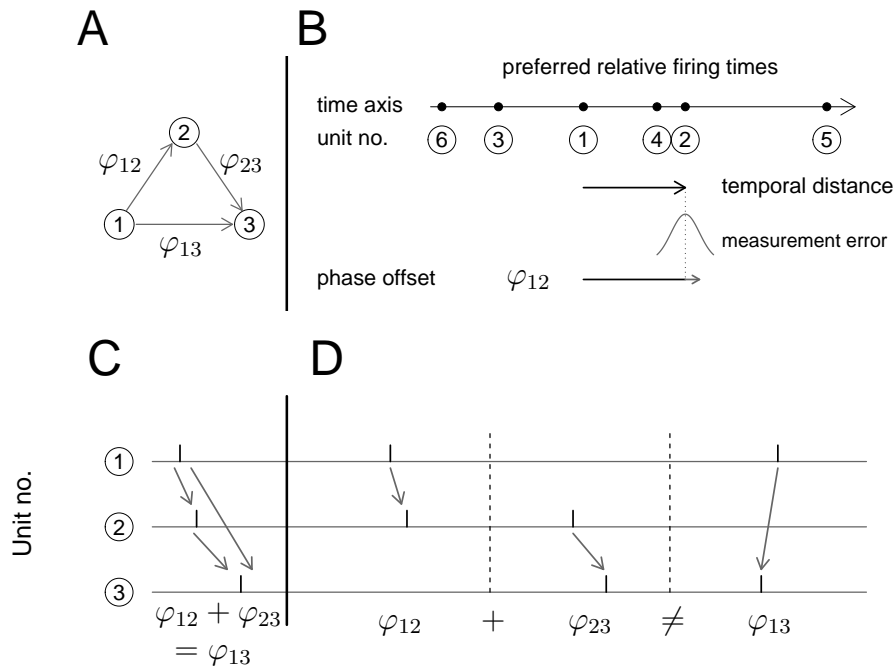


Figure 6.1: Structure in phase offsets. A: Three units and their phase offsets. B: Main model assumptions: Units are represented as points on the time axis, while pairwise phase offsets represent noisy measurements of differences between unit positions. C: Additivity of delays can arise when systematic delays between different units refer to identical spikes. D: If unit pairs fire at different times, additivity is not given by default.

However, phase offsets are not necessarily additive. While additivity can arise for example if every unit spikes once within a small time window (Fig. 6.1 C), additivity is not necessarily given if systematic delays between pairs of units occur in a temporally independent manner (Fig. 6.1 D). It is therefore necessary

to investigate whether the model can provide a reasonable representation of the structure given in a set of phase offsets. In chapter 8, the mathematical formulas and results are applied to the sample data set, and the applicability of the model to a set of experimentally obtained phase offsets is investigated.

6.2 Results

Model II: Noisy pairwise differences between points on the real line

In order to investigate the degree to which a set of $\binom{n}{2}$ phase offsets can be represented by additive distances between points on the real line, a linear model is used. It is assumed that every phase φ_{ij} represents the noisy measurement of the difference $\delta_{ij} = x_j - x_i$ between points $x_i, x_j \in \mathbb{R}$. All measurement errors are assumed to be independent and normally distributed with expectation 0 and variance² σ^2 :

$$\varphi_{ij} = \delta_{ij} + \sigma Z_{ij} \quad \forall 1 \leq i < j \leq n \quad (\text{Fig. 6.1 B}).$$

Since only distances are specified, the condition $\sum_i x_i = 0$ is required for uniqueness. A set of points $\mathcal{C} = \{x_1, \dots, x_n\}$ on the real line is called a ‘linear configuration’.

Estimates The maximum-likelihood estimate for the position x_k is given by

$$\hat{x}_k = \frac{1}{n} \sum_{i \neq k} \varphi_{ik}. \quad (\text{Lemma 3})$$

This estimate is unbiased also if several model assumptions are not satisfied, e.g. if phase offsets are not normally distributed or have different variances. The resulting estimates of the model distances δ_{ij} are derived as a weighted sum of direct measurements φ_{ij} and indirect measurements of length 2, $\varphi_{il} + \varphi_{lj}$:

$$\hat{\delta}_{ij} = \hat{x}_j - \hat{x}_i = \frac{1}{n} \left(2\varphi_{ij} + \sum_{\ell \neq i, j} (\varphi_{i\ell} + \varphi_{\ell j}) \right) \quad (\text{Corollary 3}).$$

These estimates minimize the error sum of squares, $Q := \sum_{i < j} (\varphi_{ij} - \hat{\delta}_{ij})^2$, with which the deviation from the optimal linear configuration is measured and with

²Note that in Part II, σ^2 denotes the measurement error of a phase estimate, which was denoted by σ_ϕ^2 in Part I.

which an unbiased estimate of σ can be derived as $\hat{\sigma} = Q/\binom{n-1}{2}$ (Lemma 4). In the geometric interpretation, the vector of estimated model distances $\hat{\Delta}$ represents the orthogonal projection of the vector of phase offsets, $\Phi \in \mathbb{R}^{\binom{n}{2}}$, onto an $(n-1)$ -dimensional model space \mathcal{M}_n . With this procedure, $\hat{\Delta}$ is estimated such that the squared distance $Q := \|\hat{\Delta} - \Phi\|^2$ is minimized. Application of the derived formulas to the set of 91 phase offsets measured in the sample data set yields a linear configuration in which the phase offsets can be represented to a high degree by the estimated model distances δ_{ij} (cf. Fig. 8.2 A, and Fig. 8.5 B for permuted phase offsets).

Analysis of variance In order to investigate whether differences between k linear configurations can be explained by random variations, the linear model is extended, and the vector of phase offsets, $(\Phi_1, \dots, \Phi_k) \in \mathbb{R}^{k\binom{n}{2}}$ is decomposed by two orthogonal projections. First, individual estimates $(\hat{x}_i^{(\ell)})_{\ell=1, \dots, k}$ are derived for each of the k configurations. Second, global estimates x_i are derived by projection onto the $(n-1)$ -dimensional model space which represents the null hypothesis that all k configurations $\mathcal{C}_1, \dots, \mathcal{C}_k$ are independent realizations of one and the same linear structure $\{x_1, \dots, x_n\}$ on \mathbb{R} . For the given linear model, the squared length of specific vectors is χ^2 -distributed, and their quotient is F -distributed. This can be used to investigate differences between the configurations. In the sample data set, differences between linear configurations that result from repeated presentation of the same stimulus are small, whereas big differences can be observed between configurations obtained in different stimulation conditions. This suggests that a linear configuration extracted from near-zero phase offsets can vary systematically between different stimulation conditions.

In addition to the model extension used for the statistical analysis, another model extension is presented in which maximum-likelihood estimates of the unit positions are derived for incomplete sets of phase offsets in which not all unit pairs (i, j) are assigned a measurement φ_{ij} . This case is of special importance in practice if some phase offsets cannot be estimated. A necessary and sufficient condition is provided for the uniqueness of ML-estimates (Thm. 1).

Chapter 7

Stochastic model

In this chapter, the mathematical framework is provided for the model illustrated in Figure 6.1 B. Section 7.1 describes the basic form of the model. Formulas are derived for the estimation of the preferred firing times of the units as well as for the measurement error. The presented linear model allows the application of analysis of variance, which is discussed in section 7.2. Section 7.3 provides extensions of the basic model that deal with heteroscedasticity and incomplete data sets. The results provided in section 7.3 can be useful in the analysis of experimental data in which the general assumptions of the basic model are not given as well as in the investigation of the impact that these assumptions have on the resulting linear configuration. Finally, section 7.4 provides a summary of the basic model and its extensions as well as references to all results presented in this chapter that may be important for data analysis.

7.1 Framework and results

The basic model Let $n \in \mathbb{N}$ be the number of units, $x_1, \dots, x_n \in \mathbb{R}$ be their positions on the time axis, also called *PTs*. Since only the distances between the units are specified, let $\sum_{i=1}^n x_i = 0$.

The set $\mathcal{C} := \{x_1, \dots, x_n\}$ of PTs on the time axis is called a (*linear*) *configuration*. Define the *model distance* δ_{ij} between the PTs of units i and j as

$$\delta_{ij} := x_j - x_i \quad \forall 1 \leq i, j \leq n, \quad \text{which implies} \quad (7.1)$$

$$\delta_{ij} = -\delta_{ji} \quad \text{and} \quad \delta_{ii} = 0. \quad (7.2)$$

A phase offset is assumed to be composed of the corresponding model distance and random measurement error:

$$\varphi_{ij} := \delta_{ij} + \sigma Z_{ij} \quad \forall 1 \leq i < j \leq n, \quad (7.3)$$

where $\sigma \in \mathbb{R}_+$ and $\{Z_{ij}\}_{1 \leq i < j \leq n}$ are independent and $\mathcal{N}(0, 1)$ -distributed random variables. Since only one phase offset can be computed for each pair of units, let

$$\varphi_{ji} := -\varphi_{ij} \quad \forall 1 \leq i < j \leq n \quad \text{and} \quad \varphi_{ii} := 0 \quad \forall i = 1, \dots, n.$$

The estimates In this setting, the preferred firing times x_1, \dots, x_n , the model distances, δ_{ij} , and the measurement error, σ , are to be estimated from the set of measured phase offsets, $\{\varphi_{ij}\}_{1 \leq i < j \leq n}$. The following formulas are directly applicable to experimentally derived phase offsets:

Lemma 3 *The maximum-likelihood estimate of the vector of PTs $\mathbf{x} := (x_1, \dots, x_n)$ is given by*

$$\hat{x}_k = \frac{1}{n} \sum_{i=1}^n \varphi_{ik} \quad \forall k = 1, \dots, n.$$

Corollary 3 *The maximum-likelihood estimate $\hat{\Delta}$ of the vector of model distances, $\Delta = (\delta_{12}, \dots, \delta_{n-1,n})$, is given by*

$$\hat{\delta}_{ij} = \frac{1}{n} \left(2\varphi_{ij} + \sum_{\substack{\ell=1 \\ \ell \neq i, j}}^n (\varphi_{i\ell} + \varphi_{\ell j}) \right) \quad \forall 1 \leq i < j \leq n.$$

Corollary 4 *The position x_k of unit k can be estimated with variance*

$$\sigma_{\hat{x}}^2 := \text{Var}(\hat{x}_k) = \frac{n-1}{n^2} \sigma^2 \quad \forall 1 \leq k \leq n.$$

Lemma 4 *An unbiased estimate of the measurement error σ^2 is given by*

$$\hat{\sigma}^2 = \frac{1}{\binom{n-1}{2}} \sum_{1 \leq i < j \leq n} (\varphi_{ij} - \hat{\delta}_{ij})^2.$$

7.1.1 Proofs

Proof of Lemma 3 To derive the likelihood function, note that according to equation (7.3), the vector of phase offsets,

$$\Phi := (\varphi_{12}, \dots, \varphi_{n-1,n}),$$

is assumed to be normally distributed in $\mathbb{R}^{\binom{n}{2}}$, with

$$\begin{aligned} \mathbb{E}(\varphi_{ij}) &= x_j - x_i, & \text{Var}(\varphi_{ij}) &= \sigma^2 \quad \forall 1 \leq i, j \leq n, & \text{and} & & (7.4) \\ \text{Cov}(\varphi_{ij}, \varphi_{i'j'}) &= 0 & & \forall (i, j) \neq (i', j'), (i, j) \neq (j', i'). \end{aligned}$$

Thus, the likelihood function is

$$L(\mathbf{x}, \sigma) = \frac{1}{(2\pi\sigma^2)^{\frac{1}{2}\binom{n}{2}}} \cdot \exp\left(-\frac{1}{2\sigma^2} \sum_{1 \leq i < j \leq n} (\varphi_{ij} - (x_j - x_i))^2\right). \quad (7.5)$$

Maximizing the likelihood function for constant σ is equivalent to minimizing the error sum of squares,

$$Q(\mathbf{x}) := \sum_{1 \leq i < j \leq n} (\varphi_{ij} - (x_j - x_i))^2 = \sum_{1 \leq i < j \leq n} (\varphi_{ij} - (x_j - x_i))^2. \quad (7.6)$$

The partial derivatives of $Q(\mathbf{x})$ are

$$\frac{\partial Q(\mathbf{x})}{\partial x_k} = 2 \sum_{i=1}^n (\varphi_{ki} - x_i + x_k) = 2 \sum_{i=1}^n \varphi_{ki} - 2 \sum_{i=1}^n x_i + 2nx_k.$$

With the constraint $\sum_{i=1}^n x_i = 0$, the gradient of $Q(\mathbf{x})$ equals zero for the estimates given in Lemma 3. The second partial derivatives of $Q(\mathbf{x})$ are given by

$$\frac{\partial^2 Q(\mathbf{x})}{\partial x_k \partial x_l} = \begin{cases} 0 & k \neq l, \\ 2n & k = l, \end{cases}$$

which implies that the estimates in Lemma 3 minimize $Q(\mathbf{x})$ and thus maximize the likelihood function $L(\mathbf{x}, \sigma)$ for constant σ . Corollary 3 follows by insertion of Lemma 3 into equation (7.1), and Corollary 4 can be computed directly with Lemma 3 and the assumptions in (7.4). \square

Proof of Lemma 4 To prove $\mathbb{E}[\hat{\sigma}^2] = \sigma^2$, the expectation of one summand of $Q(\hat{\mathbf{x}})$, $\mathbb{E}[(\varphi_{ij} - (\hat{x}_j - \hat{x}_i))^2] = \mathbb{E}[(\varphi_{ij} - \hat{\delta}_{ij})^2]$, is computed first. For any pair (i, j) with $1 \leq i, j \leq n$,

$$\varphi_{ij} - \hat{\delta}_{ij} = \frac{1}{n} \left[(n-2)\varphi_{ij} - \sum_{\ell \neq i, j} (\varphi_{i\ell} + \varphi_{\ell j}) \right] = \frac{1}{n} \sum_{\ell \neq i, j} (\varphi_{ij} + \varphi_{j\ell} + \varphi_{\ell i}).$$

Thus,

$$\mathbb{E}[\varphi_{ij} - \hat{\delta}_{ij}] = \frac{1}{n} \mathbb{E} \left(\sum_{\ell \neq i, j} (x_j - x_i) + (x_\ell - x_j) + (x_i - x_\ell) \right) = 0$$

$$\mathbb{E}[(\varphi_{ij} - \hat{\delta}_{ij})^2] = \text{Var}[\varphi_{ij} - \hat{\delta}_{ij}] = \frac{\sigma^2}{n^2} [(n-2)^2 + 2(n-2)] = \frac{n-2}{n} \sigma^2.$$

Therefore,

$$\begin{aligned} \mathbb{E}[\hat{\sigma}^2] &= \frac{1}{\binom{n-1}{2}} \cdot \binom{n}{2} \cdot \mathbb{E}[(\varphi_{ij} - \hat{\delta}_{ij})^2] \\ &= \frac{2}{(n-1)(n-2)} \cdot \frac{n(n-1)}{2} \cdot \frac{(n-2)}{n} \sigma^2 = \sigma^2. \end{aligned}$$

□

Note: The Maximum Likelihood estimate of σ^2 , $\hat{\sigma}_{\text{ML}}^2$, differs from the estimate given in Lemma 4: Computing the log-likelihood and its derivative,

$$\log L(\hat{\mathbf{x}}, \sigma) = -\binom{n}{2} \log(\sqrt{2\pi}) - \binom{n}{2} \log(\sigma) - 0.5\sigma^{-2}Q(\hat{\mathbf{x}})$$

$$\frac{\partial \log L(\hat{\mathbf{x}}, \sigma)}{\partial \sigma} = \sigma^{-1} \left(-\binom{n}{2} + \sigma^{-2}Q(\hat{\mathbf{x}}) \right),$$

one can see that the derivative equals zero only for

$$\hat{\sigma}_{\text{ML}}^2 = \frac{1}{\binom{n}{2}} Q(\hat{\mathbf{x}}) = \frac{1}{\binom{n}{2}} \sum_{1 \leq i < j \leq n} (\varphi_{ij} - (\hat{x}_j - \hat{x}_i))^2, \quad (7.7)$$

where the second derivative is negative:

$$\frac{\partial^2 \log L(\hat{\mathbf{x}}, \hat{\sigma}_{\text{ML}}^2)}{\partial^2 \sigma^2} = \hat{\sigma}_{\text{ML}}^{-2} \left(\binom{n}{2} - 2\hat{\sigma}_{\text{ML}}^{-2}Q(\hat{\mathbf{x}}) \right) = -\binom{n}{2}^2 (Q(\hat{\mathbf{x}}))^{-1}.$$

Thus, the ML-estimate $\hat{\sigma}_{\text{ML}}^2$ differs from the unbiased estimate by the factor $\binom{n-1}{2} / \binom{n}{2}$.

7.1.2 The geometric perspective

In this subsection, the additivity model and its estimates are interpreted in a geometric way. The presented model is a linear model of the form

$$\Phi = \Delta + \sigma \mathfrak{Z}, \quad (7.8)$$

where Φ is the vector of phase offsets, Δ contains the corresponding model distances, and $\mathfrak{Z} = (Z_{12}, \dots, Z_{n-1,n}) \sim \mathcal{N}(0, I_{\binom{n}{2}})$ is a vector of independent and standard normally distributed random variables (I_n denotes the $n \times n$ -identity matrix). According to the additivity assumption, all model distances δ_{ij} are additive, i.e., the vector Δ is assumed to be an element of the $(n-1)$ -dimensional model space $\mathcal{M}_n \in \mathbb{R}^{\binom{n}{2}}$

$$\mathcal{M}_n := \left\{ (c_2 - c_1, c_3 - c_1, \dots, c_n - c_1) \mid c_1, \dots, c_n \in \mathbb{R}, \sum_{i=1}^n c_i = 0 \right\}. \quad (7.9)$$

To estimate the vector of model distances, Δ , the vector of phase offsets, Φ , is decomposed by orthogonal projection onto \mathcal{M}_n :

$$\Phi = \mathcal{P}_{\mathcal{M}_n} \Phi + \mathcal{P}_{\mathcal{M}_n^\perp} \Phi =: \hat{\Delta} + R,$$

where $\hat{\Delta} := \mathcal{P}_{\mathcal{M}_n} \Phi$ represents the orthogonal projection of Φ onto \mathcal{M}_n , and $R := \mathcal{P}_{\mathcal{M}_n^\perp} \Phi$ is the residual component, i.e., the orthogonal projection of Φ onto the orthogonal complement of \mathcal{M}_n . According to the orthogonal projection, the length of R is the minimal distance between Φ and \mathcal{M}_n :

$$\min_{v \in \mathcal{M}_n} \|\Phi - v\|^2 = \|R\|^2 = \sum_{1 \leq i < j \leq n} (\varphi_{ij} - \hat{\delta}_{ij})^2 = Q(\hat{\mathbf{x}}).$$

Thus, the estimate $\hat{\Delta}$ resulting from orthogonal projection is also the ML-estimate that results from Corollary 3 because it minimizes the error sum of squares. Therefore, the decomposition $\Phi = \hat{\Delta} + R$ reads componentwise

$$\begin{aligned} \varphi_{ij} &= \hat{\delta}_{ij} + (\varphi_{ij} - \hat{\delta}_{ij}) = \hat{\delta}_{ij} + r_{ij} \\ &= \frac{1}{n} \left(2\varphi_{ij} + \sum_{\ell \neq i, j} (\varphi_{i\ell} + \varphi_{\ell j}) \right) + \frac{1}{n} \sum_{\ell \neq i, j} (\varphi_{ij} + \varphi_{j\ell} + \varphi_{\ell i}). \end{aligned}$$

The model distances δ_{ij} are estimated by a linear combination of the direct measurement, φ_{ij} , and all indirect measurements of size two, $\varphi_{i\ell} + \varphi_{\ell j}$ (cf. Fig. 7.1).

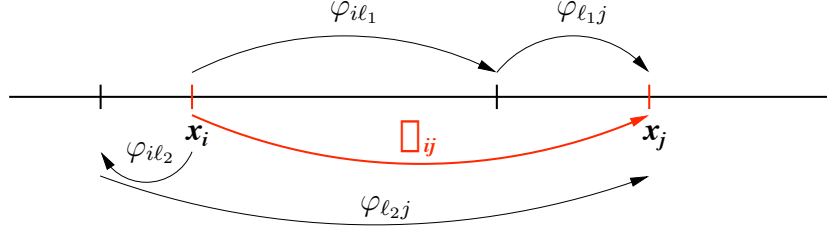


Figure 7.1: Estimation of model distances by the direct distance and all indirect measurements of size two.

In this linear combination, the direct distance is counted twice because it is only affected by one error of measurement, while the indirect distance is affected by two measurement errors: $\text{Var}(\varphi_{il} + \varphi_{lj}) = 2\sigma^2 = 2\text{Var}(\varphi_{ij})$.

The residual component, R , is estimated by ‘circles’ of phase offsets, $\varphi_{ij} + \varphi_{jl} + \varphi_{li}$, which are zero for additive phase offsets. In the linear model where phase offsets are additive apart from a measurement error of size σ^2 , this error is estimated according to Lemma 4 with:

$$\hat{\sigma}^2 = \frac{1}{\binom{n-1}{2}} Q(\hat{\mathbf{x}}) = \frac{1}{\binom{n-1}{2}} \cdot \|R\|^2.$$

As shown with elementary calculations in section 7.1.1, $\binom{n-1}{2}^{-1} \|R\|^2$ is an unbiased estimate of σ^2 . Geometrically, unbiasedness of $\hat{\sigma}^2$ can be concluded easily from the dimension of the subspace \mathcal{M}_n :

$$\text{Recall: } \Phi = \Delta + \sigma\mathfrak{Z}, \quad \Phi \in \mathbb{R}^{\binom{n}{2}}, \quad \Delta \in \mathcal{M}_n, \quad \mathfrak{Z} \sim \mathcal{N}(0, I_{\binom{n}{2}}).$$

Since $\Delta \in \mathcal{M}_n$, $R = \mathcal{P}_{\mathcal{M}_n^\perp} \Phi = \mathcal{P}_{\mathcal{M}_n^\perp} \sigma\mathfrak{Z}$. Hence,

$$\sigma^{-2} \|R\|^2 = \sigma^{-2} \|\mathcal{P}_{\mathcal{M}_n^\perp} \sigma\mathfrak{Z}\|^2 \sim \chi^2(\dim(\mathcal{M}_n^\perp)) = \chi^2\left(\binom{n}{2} - \dim(\mathcal{M}_n)\right).$$

This implies

$$\mathbb{E}(\|R\|^2) = \sigma^2 \cdot \binom{n-1}{2}, \quad \text{which yields } \mathbb{E}[\hat{\sigma}^2] = \sigma^2.$$

The framework of this linear model and the homoscedasticity assumption that every phase offset is measured with the same variance σ^2 allows the application of analysis of variance.

7.2 Analysis of variance

To apply analysis of variance to the linear model described in section 7.1.2, the framework is extended by introduction of an additional hypothesis space H . Consider the more general model

$$\Phi = \mu + \sigma\mathfrak{Z},$$

where $\Phi \in \mathbb{R}^m$, \mathcal{M} is a subspace of \mathbb{R}^m and denotes the model space with $\mu \in \mathcal{M}$, and $\mathfrak{Z} \sim \mathcal{N}(0, I_m)$. To test the null hypothesis $H_0 : \mu \in H$, where H is a subspace of \mathcal{M} and denotes the hypothesis space, against the alternative $H_1 : \mu \in \mathcal{M}$, the vector Φ is decomposed by orthogonal projection onto H and \mathcal{M} :

$$\Phi = \mathcal{P}_H\Phi + \mathcal{P}_E\Phi + \mathcal{P}_{M^\perp}\Phi,$$

where E denotes the orthogonal complement of H in \mathcal{M} , i.e., $\mathcal{M} = H \oplus E$ (cf. Fig. 7.2). Then, the lengths of $\mathcal{P}_E\Phi$ and $\mathcal{P}_{M^\perp}\Phi$ are compared. Under both H_0 and H_1 , $\mu \in \mathcal{M}$ and thus, $\mathcal{P}_{M^\perp}\mu = 0$. Therefore,

$$\mathcal{P}_{M^\perp}\Phi = \mathcal{P}_{M^\perp}\sigma\mathfrak{Z} \implies \sigma^{-2}\|\mathcal{P}_{M^\perp}\Phi\|^2 \sim \chi^2(\dim(M^\perp)).$$

$$\text{Under } H_0 : \mathcal{P}_E\Phi = \mathcal{P}_E\sigma\mathfrak{Z} \implies \sigma^{-2}\|\mathcal{P}_E\Phi\|^2 \sim \chi^2(\dim(E)),$$

$$\text{and under } H_1 : \|\mathcal{P}_E\Phi\|^2 = \|\mathcal{P}_E\mu + \mathcal{P}_E\sigma\mathfrak{Z}\|^2 > \|\mathcal{P}_E\sigma\mathfrak{Z}\|^2.$$

Thus, under H_0 ,

$$F = \frac{\|\mathcal{P}_E\Phi\|^2 / \dim(E)}{\|\mathcal{P}_{M^\perp}\Phi\|^2 / \dim(M^\perp)} \quad (7.10)$$

has Fisher distribution with $\dim(E)$ and $\dim(M^\perp)$ degrees of freedom, whereas F is increased systematically under H_1 .

The application of this result to specific problems only requires choosing the appropriate model space, \mathcal{M} , and the hypothesis space, H . As an example, analysis of variance is used here to investigate differences between linear configurations derived under different experimental conditions.

7.2.1 Application: Differences between configurations

Analysis of variance is applied to investigate differences between k linear configurations, denoted by

$$\mathcal{C}_1 := \{x_1^{(1)}, \dots, x_n^{(1)}\}, \quad \dots, \quad \mathcal{C}_k := \{x_1^{(k)}, \dots, x_n^{(k)}\},$$

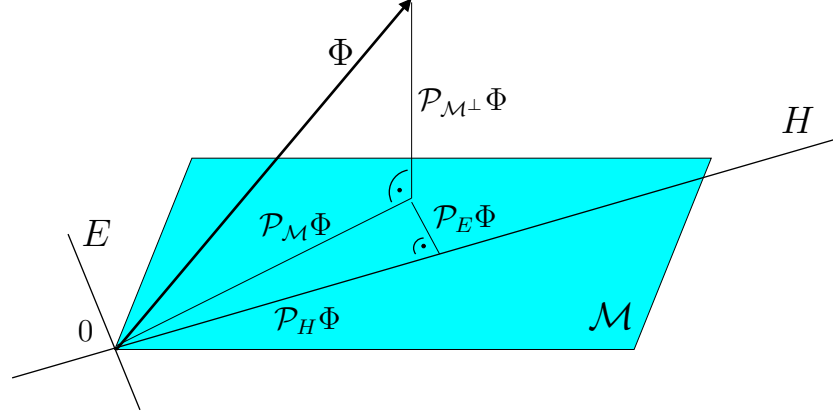


Figure 7.2: Decomposition of Φ by orthogonal projection onto the model space, \mathcal{M} , and the hypothesis space, H .

that originate from k sets of measurements, $\{\varphi_{ij}^{(1)}\}_{1 \leq i < j \leq n}, \dots, \{\varphi_{ij}^{(k)}\}_{1 \leq i < j \leq n}$. The null hypothesis states that phase offsets $\varphi_{ij}^{(\ell)}$ between the same pair of units (i, j) but from different measurements $\ell = 1, \dots, k$ are random copies of the same distance $\delta_{ij} = x_j - x_i$ between the units i and j :

$$H_0 : \quad \varphi_{ij}^{(\ell)} \sim \mathcal{N}(x_j - x_i, \sigma^2), \quad \sum x_i = 0 \quad \begin{array}{l} \forall 1 \leq i < j \leq n, \\ \forall \ell = 1, \dots, k. \end{array} \quad (7.11)$$

The alternative hypothesis is represented by

$$H_1 : \quad \varphi_{ij}^{(\ell)} \sim \mathcal{N}(x_j^{(\ell)} - x_i^{(\ell)}, \sigma^2), \quad \sum x_i^{(\ell)} = 0 \quad \begin{array}{l} \forall 1 \leq i < j \leq n, \\ \forall \ell = 1, \dots, k, \end{array} \quad (7.12)$$

and not all $(x_i^{(\ell)})$, $\ell = 1, \dots, k$, are equal. H_1 states that the phase offsets obtained from different measurements ℓ represent noisy pairwise distances in different linear configurations $\mathcal{C}_1, \dots, \mathcal{C}_k$. In this case, we have

$$\Phi = \Delta + \sigma \mathfrak{Z},$$

where $\Phi \in \mathbb{R}^{k \binom{n}{2}}$ is the merged vector of phase offsets in k independent measurements. The model space

$$\mathcal{M} = \underbrace{\mathcal{M}_n \times \dots \times \mathcal{M}_n}_k = \{(v_1, \dots, v_k) \mid v_1, \dots, v_k \in \mathcal{M}_n\}$$

represents the assumption that phase offsets of different measurements are additive but may belong to different linear configurations. Note that $\dim(\mathcal{M}_n) = n - 1$ and therefore, $\dim(\mathcal{M}) = k(n - 1)$ and $\dim(\mathcal{M}^\perp) = k\binom{n-1}{2}$. The hypothesis space is given by

$$H = \{(v_1, \dots, v_k) \mid v_1 = \dots = v_k \in \mathcal{M}_n\}$$

and represents the assumption that phase offsets of different sets of measurements are additive and originate from the *same* linear configuration, i.e., $\mathcal{C}_1 = \dots = \mathcal{C}_k$. Obviously, $\dim(H) = n - 1$ and $\dim(E) = (k - 1)(n - 1)$.

Projection onto H : The orthogonal projection of Φ onto H is given by the components

$$(\mathcal{P}_H \Phi)_{ij}^{(\ell)} = \frac{1}{k} \sum_{\ell=1}^k \hat{\delta}_{ij}^{(\ell)}, \quad (7.13)$$

$$\text{with } \hat{\delta}_{ij}^{(\ell)} = \frac{1}{n} \left(2\varphi_{ij}^{(\ell)} + \sum_{\substack{r=1 \\ r \neq i,j}}^n (\varphi_{ir}^{(\ell)} + \varphi_{rj}^{(\ell)}) \right). \quad (7.14)$$

Thus, if all configurations are identical, the estimated model distances are averages of the estimated model distances in the separate measurements. The proof is analogous to the computations in section 7.1.1: The error sum of squares,

$$Q_H(\mathbf{x}) = \sum_{\ell=1}^k \sum_{i < j} (\varphi_{ij}^{(\ell)} - (x_j - x_i))^2,$$

is minimized by the estimates given in equation (7.13).

Projection onto \mathcal{M} : The orthogonal projection of Φ onto \mathcal{M} is given by the components

$$(\mathcal{P}_{\mathcal{M}} \Phi)_{ij}^{(\ell)} = \hat{\delta}_{ij}^{(\ell)}. \quad (7.15)$$

This means that if phase offsets are additive but if different measurements belong to different linear configurations, model distances are estimated separately for every set of measurements. Again, this can be shown directly with the ML method using

$$Q_{\mathcal{M}}(\mathbf{x}) = \sum_{\ell=1}^k \sum_{i < j} (\varphi_{ij}^{(\ell)} - (x_j^{(\ell)} - x_i^{(\ell)}))^2.$$

Sums of squares From equations (7.13) and (7.15) we get

$$(\mathcal{P}_E \Phi)_{ij}^{(\ell)} = \hat{\delta}_{ij}^{(\ell)} - \frac{1}{k} \sum_{r=1}^k \hat{\delta}_{ij}^{(r)} \quad \text{and} \quad (7.16)$$

$$\|(\mathcal{P}_E \Phi)_{ij}^{(\ell)}\|^2 = \sum_{\ell=1}^k \sum_{i < j} \left(\hat{\delta}_{ij}^{(\ell)} - \frac{1}{k} \sum_{r=1}^k \hat{\delta}_{ij}^{(r)} \right)^2, \quad (7.17)$$

i.e., the nominator of the test statistic F represents the deviations of single linear configurations from the global linear configuration. The sum of squares in the denominator is given by

$$(\mathcal{P}_{\mathcal{M}^\perp} \Phi)_{ij}^{(\ell)} = \varphi_{ij}^{(\ell)} - \hat{\delta}_{ij}^{(\ell)} \quad (7.18)$$

$$\implies \|(\mathcal{P}_{\mathcal{M}^\perp} \Phi)_{ij}^{(\ell)}\|^2 = \sum_{\ell=1}^k \sum_{i < j} (\varphi_{ij}^{(\ell)} - \hat{\delta}_{ij}^{(\ell)})^2, \quad (7.19)$$

i.e., the denominator represents the deviations between raw phase offsets and estimated model distances computed separately for each data set.

The statistic F can be derived now with the provided components. To construct a short representation, let $\hat{\sigma}_\ell^2$ denote the estimated variance in measurement ℓ :

$$\hat{\sigma}_\ell^2 = \binom{n-1}{2}^{-1} \sum_{i < j} (\varphi_{ij}^{(\ell)} - \hat{\delta}_{ij}^{(\ell)})^2.$$

F can be simplified to

$$\begin{aligned} F &= \frac{\sum_{\ell=1}^k \sum_{i < j} \left(\hat{\delta}_{ij}^{(\ell)} - \frac{1}{k} \sum_{r=1}^k \hat{\delta}_{ij}^{(r)} \right)^2 / (k-1)(n-1)}{\sum_{\ell=1}^k \sum_{i < j} (\varphi_{ij}^{(\ell)} - \hat{\delta}_{ij}^{(\ell)})^2 / k \binom{n-1}{2}} \\ &= \frac{1}{\sum_{\ell} \hat{\sigma}_\ell^2} \cdot \frac{k}{(k-1)(n-1)} \cdot \sum_{\ell} \sum_{i < j} \left(\hat{\delta}_{ij}^{(\ell)} - \frac{1}{k} \sum_r \hat{\delta}_{ij}^{(r)} \right)^2 \quad (7.20) \\ &\sim \text{Fisher} \left((k-1)(n-1), k \binom{n-1}{2} \right). \end{aligned}$$

Thus, to test differences between k linear configurations, one has to compute separate model distances, $\hat{\delta}_{ij}^{(\ell)}$, the measurement errors, $\hat{\sigma}_\ell^2$, and to compare the value resulting from equation (7.20) with a Fisher-distributed random variable with $(k-1)(n-1)$ and $k \binom{n-1}{2}$ degrees of freedom.

7.3 Model assumptions and model extensions

The general framework of a linear model presented in the previous section can be useful for further data analysis because it provides easy and straightforward formulas with which linear structure inherent in sets of measured phase offsets can be investigated. However, when interpreting the results of such an analysis, the special properties of the model have to be taken into account.

Linear configurations are not necessarily stable Most importantly, the presented model can be used to investigate whether a set of measured phase offsets is inherently consistent and additive in such a way that a linear configuration can be estimated with the results provided in section 7.1. However, this linear configuration is not necessarily stable throughout the analysis window. Consider the following example: Let $\mathcal{C}_1 := \{x_1^{(1)}, \dots, x_n^{(1)}\}$ be the linear configuration in the first half of each trial, and let $\mathcal{C}_2 := \{x_1^{(2)}, \dots, x_n^{(2)}\}$ be a different linear configuration in the second half of each trial. Then, by dividing the spike trains accordingly, one could get pairwise measurements of distances between unit pairs

$$m_{ij}^{(1)} = x_j^{(1)} - x_i^{(1)} + \sigma_1 Z_{ij}^{(1)} \quad \text{and} \quad m_{ij}^{(2)} = x_j^{(2)} - x_i^{(2)} + \sigma_2 Z_{ij}^{(2)}$$

that belong to \mathcal{C}_1 and to \mathcal{C}_2 , respectively. In this case, every global value φ_{ij} represents a combination of the separate measurements $m_{ij}^{(1)}$ and $m_{ij}^{(2)}$. If φ_{ij} is simply the average of $m_{ij}^{(1)}$ and $m_{ij}^{(2)}$, φ_{ij} can again be divided into an additive component and measurement error:

$$\begin{aligned} \varphi_{ij} &= \frac{1}{2}(m_{ij}^{(1)} + m_{ij}^{(2)}) \\ &= \left(\frac{1}{2}(x_j^{(1)} + x_j^{(2)}) - \frac{1}{2}(x_i^{(1)} + x_i^{(2)}) \right) + \frac{1}{2} \left(\sigma_1 Z_{ij}^{(1)} + \sigma_2 Z_{ij}^{(2)} \right). \end{aligned}$$

As a consequence, the set of phase offsets $\{\varphi_{12}, \dots, \varphi_{n-1,n}\}$ is assigned the linear configuration

$$\mathcal{C} = \left\{ \frac{1}{2}(x_1^{(1)} + x_1^{(2)}), \dots, \frac{1}{2}(x_n^{(1)} + x_n^{(2)}) \right\}, \quad \text{with} \quad \sigma = \frac{1}{2} \sqrt{\sigma_1^2 + \sigma_2^2}.$$

Thus, the linear configuration estimated on the basis of this set of phase offsets is only the mean linear configuration in which every unit is assigned its average

position within the two configurations \mathcal{C}_1 and \mathcal{C}_2 . Consequently, any linear configuration may represent only an average of different configurations that emerge throughout the analysis window. Systematic variations in the unit positions should then be investigated with the analysis-of-variance approach presented in section 7.2.

Assumptions on measurement errors Another important aspect that concerns the interpretation of a linear configuration is related to violations of the model assumptions with respect to measurement errors. In the linear model, measurement errors are assumed to be independent and normally distributed and to have the same variance σ^2 . Violations of these model assumptions may affect the estimates of the unit positions in Lemma 3, the estimated precision of a unit position in Corollary 4, and the results of the statistical analysis when comparing linear configurations.

Since expectation is linear, the unit positions derived with Lemma 3 remain unbiased even if all three assumptions concerning measurement errors are violated. However, the estimates can no longer be called Maximum-Likelihood estimates. If only the homoscedasticity assumption is violated, one can use the estimates of the measurement errors of single phase offsets as described in Part I to derive Maximum-Likelihood estimates of the unit positions. The respective formula is provided in section 7.3.2.

In addition, the variance of a unit position may differ from the value given in Corollary 4 if measurement errors are dependent or if their variances are unequal. In the latter case, every phase offset φ_{ij} is affected by a measurement error with variance σ_{ij}^2 , and the variance of the estimated unit position \hat{x}_k is

$$\text{Var}(\hat{x}_k) = \frac{1}{n^2} \sum_{i \neq k} \sigma_{ik}^2 \quad \forall 1 \leq k \leq n \quad (\text{see Lemma 3}).$$

Application of this equation requires the estimation of individual measurement errors σ_{ij}^2 from an independent source such as formula (4.1) provided in Part I.

Effects of dependent measurement errors cannot be discussed in general but are of special importance for the situation described on page 63, namely when different linear configurations exist within the analysis window. In this case, the configurations that exist during the trial deviate from the final average linear configuration, which could be interpreted as measurement error. Since these deviations originate from linear configurations, they are additive and therefore, dependent. However, the estimate of σ^2 as derived with Lemma 4

only takes into account the agreement between measured phase offsets and model distances and thus, only measures the deviation of phase offsets from the closest linear structure. Therefore, σ^2 does not incorporate the variability of the unit positions across the analysis window and thus, this source of dependence is not considered a measurement error. As a consequence, also Corollary 4 cannot take into account the variability of a unit position across different configurations that may evolve during the analysis window but can only describe the precision of a unit with respect to the internal additivity of the data set. Analogously, when linear configurations that originate from different data sets are compared with the analysis-of-variance approach, differences between configurations are only measured in terms of the internal additivity in each of the two data sets.

Finally, application of the presented model requires that phase offsets have been measured for all pairs of units. If this is not possible, the estimates of the unit positions and the variance provided in Lemmata 3 and 4 are no longer applicable. Moreover, additional requirements are needed to ensure that the parameters can be estimated at all. These issues are discussed in section 7.3.1.

7.3.1 Missing data

7.3.1.1 Framework

The model described in section 7.1 is modified here such that also incomplete sets of phase offsets can be investigated. Let

$$P_n := \{\{i, j\} \mid 1 \leq i < j \leq n\}$$

denote the set of all unit pairs, $|P_n| = \binom{n}{2}$. Let further

$$E \subset P_n \quad \text{and} \quad M := P_n \setminus E$$

denote the set of pairs with measured distances (*Edges*) and the set of pairs with missing data (*Missing edges*), respectively. The basic model is restricted to the subset of unit pairs of which phase offsets were measured:

$$\varphi_{ij} = \delta_{ij} + \sigma Z_{ij} \quad \forall \{i, j\} \in E.$$

If $\{i, j\} \in E$, the units i and j are called *directly connected*, i.e., they *share an edge*. Let furthermore denote

$$E_k := \{i \mid \{i, k\} \in E\}$$

the set of all units which share an edge with unit k . The set of edges, E , is called *connected on* $\{1, \dots, n\}$ if between any two units $i, j \in \{1, \dots, n\}$ there exists at least one path of edges:

Definition 1 E is called **connected on** $\{1, \dots, n\}$ if $\forall (i, j)_{1 \leq i < j \leq n}$

$$\exists w \in \{2, \dots, n\} \quad \text{and} \quad \exists k_1 = i, k_2, \dots, k_{w-1}, k_w = j \in \{1, \dots, n\}$$

$$\text{with} \quad \{k_r, k_{r+1}\} \in E \quad \forall r = 1, \dots, w - 1.$$

If E is not connected, then $\{1, \dots, n\}$ can be partitioned into disjoint subsets U_1 and U_2 such that no edge connects units of different subsets, i.e., $(u_1, u_2) \in M \forall u_1 \in U_1, u_2 \in U_2$.

Unique ML-estimates of the units' positions do not exist for all subsets $E \subset P_n$. In fact, the connectedness of E on the set $\{1, \dots, n\}$ is a necessary and sufficient condition for both existence and uniqueness of the ML-estimates of the units' positions. This will be shown in Theorem 1.

7.3.1.2 Existence and uniqueness of estimates

The function to be minimized by the ML-estimates is

$$Q_E(\mathbf{x}) = \sum_{\{i,j\} \in E} (\varphi_{ij} - (x_j - x_i))^2, \text{ again with } \sum_{i=1}^n x_i = 0.$$

Theorem 1 *The minimum of the function Q_E exists and is unique for $\sum_{i=1}^n x_i = 0 \iff E$ is connected on $\{1, \dots, n\}$.*

The proof makes use of the following observations

- The quadratic function Q_E has an extremum.
- If E is connected, one can define a compact set C outside of which the function is bigger than inside and thus conclude that the extremum is a minimum, m . As the area is compact, there is an $\mathbf{x}^m \in C$ with $Q_E(\mathbf{x}^m) = m$. (Lemma 5)
- The uniqueness of \mathbf{x}^m is proven by contradiction. Any pair $\mathbf{x}^{(1)} \neq \mathbf{x}^{(2)}$ with $Q_E(\mathbf{x}^{(1)}) = Q_E(\mathbf{x}^{(2)}) = m$ is located on a straight line, g , crossing C . Since $Q_E(\mathbf{x}) > m \forall \mathbf{x} \notin C$, $Q_E|_g$ is a parabola in \mathbb{R}^2 , which has a unique minimum, leading to a contradiction. (Lemma 5)

- If E is not connected, divide the set $\{1, \dots, n\}$ into disjoint components U_1, \dots, U_k such that there is no edge connecting any two units from different subsets. Q_E can be split up accordingly into sums of squares $Q_{E,1}, \dots, Q_{E,k}$. Together with the constraints $\sum_{i \in U_\ell} x_i = 0 \forall \ell = 1, \dots, k$, there is a unique solution for every $Q_{E,\ell}$, and as $Q_E = \min \iff Q_{E,\ell} = \min \forall \ell = 1, \dots, k$, this is also a global solution. It is then used to give all possible solutions. (Lemma 6)

Lemma 5 *Let E be connected, and let $T := \max_{\{i,j\} \in E} |\varphi_{ij}|$. Let C denote the compact set*

$$C := \left\{ \mathbf{x} \in \mathbb{R}^n \mid \max_{(i,j) \in E} |x_j - x_i| \leq (n^2 - 1)T \wedge \sum x_i = 0 \right\}.$$

Then,

(i) Q_E has a global minimum, m , on C .

(ii) Within C , this minimum is unique, i.e., if $\mathbf{x}^{(1)}, \mathbf{x}^{(2)} \in C$ with $Q_E(\mathbf{x}^{(1)}) = Q_E(\mathbf{x}^{(2)}) = \min_{\mathbf{x} \in C} Q_E(\mathbf{x})$, then $\mathbf{x}^{(1)} = \mathbf{x}^{(2)}$.

Proof.

(i). Since Q_E is a quadratic function, it must have an extremum. If it can be shown that $\exists \mathbf{x}^* \in C$ with $Q_E(\mathbf{x}^*) < Q_E(\mathbf{x}) \forall \mathbf{x} \notin C$, then Q_E must have a global minimum in C .

Take $\mathbf{x}^* := \mathbf{0} \in C$ and note that $Q_E(\mathbf{0}) = \sum_{\{i,j\} \in E} \varphi_{ij}^2 < \binom{n}{2} T^2$. For any $\mathbf{x} \notin C \exists \{i, j\}$ with $|x_j - x_i| > (n^2 - 1)T$. Due to the connectedness of E , there is a path connecting the two units i and j , given by a length $w \in \{2, \dots, n\}$ and units $k_1 = i, \dots, k_w = j$ with edges $\{k_r, k_{r+1}\} \in E \forall r = 1, \dots, w - 1$, and $\exists \ell$ denoting the longest edge on this path:

$$|x_{k_{\ell+1}} - x_{k_\ell}| > \frac{(n^2 - 1)T}{w - 1} \geq \frac{(n^2 - 1)T}{(n - 1)} = (n + 1)T.$$

According to the definition of $T := \max_{\{i,j\} \in E} |\varphi_{ij}|$, it follows

$$|\varphi_{k_\ell k_{\ell+1}} - (x_{k_{\ell+1}} - x_{k_\ell})| \geq nT \quad \text{and thus,} \quad Q_E(\mathbf{x}) \geq n^2 T^2 > Q_E(\mathbf{0}) \quad \forall \mathbf{x} \notin C.$$

Thus, as C is compact and Q_E is continuous, Q_E has a global minimum m inside C , i.e., $\exists \mathbf{x}^m \in C$ with $Q_E(\mathbf{x}^m) = m$, and $\forall \mathbf{x} \notin C, Q_E(\mathbf{x}) > m$.

(ii) Suppose the minimum is not unique, i.e., $\exists \mathbf{x}^{(1)} \neq \mathbf{x}^{(2)} \in C$ with

$Q_E(\mathbf{x}^{(1)}) = Q_E(\mathbf{x}^{(2)}) = m$. Then consider the straight line connecting $\mathbf{x}^{(1)}$ and $\mathbf{x}^{(2)}$:

$$g(\lambda) := \lambda \mathbf{x}^{(1)} + (1 - \lambda) \mathbf{x}^{(2)}, \quad \lambda \in \mathbb{R}.$$

As C is compact, it is also bounded, and $\exists \lambda_1 < 0, \lambda_2 > 1$ with $g(\lambda_1) \notin C$ and $g(\lambda_2) \notin C$,

$$Q_E(g(\lambda_1)) > m = Q_E(\mathbf{x}^{(1)}) = Q_E(\mathbf{x}^{(2)}) = m < Q_E(g(\lambda_2)).$$

Therefore, $Q_E(g(\lambda))_{\lambda \in \mathbb{R}}$ describes a parabola that has its minimum inside C . Hence, $\mathbf{x}^{(1)} \neq \mathbf{x}^{(2)}$ implies that

$$Q_E(g(1/2)) = Q_E(1/2(\mathbf{x}^{(1)} + \mathbf{x}^{(2)})) < m,$$

which is a contradiction to the fact that m is the global minimum of Q_E . \square

Lemma 6 *If E is not connected, the solution to $Q_E(\mathbf{x}) \stackrel{!}{=} \min$ is not unique.*

Proof.

If E is not connected, the set of edges can be split into disjoint subsets which are connected on subcomponents of $\{1, \dots, n\}$. The units of every connected subcomponent can be positioned in a unique way relative to each other but not relative to other subcomponents. Thus, the unit positions of every subcomponent can be shifted on the real axis without increasing the error sum of squares, yielding multiple solutions.

If E is not connected, the set $\{1, \dots, n\}$ can be split into disjoint subsets U_1, \dots, U_k of $\{1, \dots, n\}$ with $\cup_{\ell=1}^k U_\ell = \{1, \dots, n\}$ such that the subsets are connected and that no edge connects units from different subsets.

Thus, E can be split into disjoint subsets

$$F_\ell := \{\{i, j\} \in E \mid i, j \in U_\ell\}$$

of edges between units in U_ℓ such that $E = \cup_{\ell=1}^k F_\ell$ and every F_ℓ is connected on U_ℓ . This implies a corresponding decomposition of the error sum of squares:

$$Q_E(\mathbf{x}) = \sum_{\ell=1}^k \sum_{\{i,j\} \in F_\ell} (\varphi_{ij} - (x_j - x_i))^2 = \sum_{\ell=1}^k Q_{F_\ell}(\mathbf{x}),$$

with

$$Q_{F_\ell}(\mathbf{x}) := \sum_{\{i,j\} \in F_\ell} (\varphi_{ij} - (x_j - x_i))^2.$$

Note that $Q_{F_\ell}(\mathbf{x})$ depends only on the components x_i with $i \in U_\ell$. Therefore, the notation is simplified by defining a vector of unit positions

$$\mathbf{x}^\ell := (x_{\ell_1}, \dots, x_{\ell_{n_\ell}}) \text{ for each connected subset } U_\ell := \{\ell_1, \dots, \ell_{n_\ell}\}$$

and identifying $Q_{F_\ell}(\mathbf{x})$ with $Q_{F_\ell}(\mathbf{x}^\ell)$. The joint vector of all unit positions is denoted by

$$\mathbf{x} := (\mathbf{x}^1, \dots, \mathbf{x}^k).$$

Since $Q_E(\mathbf{x}) = \sum_{\ell=1}^k Q_{F_\ell}(\mathbf{x}^\ell)$ and F_1, \dots, F_k are disjoint,

$$Q_E(\mathbf{x}) = \min \iff Q_{F_\ell}(\mathbf{x}^\ell) = \min \quad \forall \ell = 1, \dots, k.$$

As F_ℓ is connected on U_ℓ , $Q_{F_\ell}(\mathbf{x}^\ell) \stackrel{!}{=} \min$ has a unique solution $\mathbf{x}^{\ell,0}$ under the restriction $\sum_{i \in U_\ell} x_i = 0$. Since $Q_{F_\ell}(\mathbf{x})$ depends only on distances between units, Q_{F_ℓ} stays minimal also when $\mathbf{x}^{\ell,0}$ is translated such that the mean of the units in U_ℓ equals $c_\ell \neq 0$. In this case, $Q_{F_\ell}(\mathbf{x}^\ell) \stackrel{!}{=} \min$ has the unique solution

$$\mathbf{x}^{\ell,c_\ell} = \mathbf{x}^{\ell,0} + c_\ell, \quad \text{with} \quad |U_\ell|^{-1} \sum_{i \in U_\ell} x_i = c_\ell \quad \forall c_\ell \in \mathbb{R},$$

and the minimum of Q_{F_ℓ} stays invariant: $Q_{F_\ell}(\mathbf{x}^{\ell,0}) = Q_{F_\ell}(\mathbf{x}^{\ell,c_\ell}) \quad \forall c_\ell \in \mathbb{R}$.

Thus, the global solutions to $Q_E(\mathbf{x}) = \min$ under the restriction $0 = \sum_{i=1}^n x_i = \sum_{\ell=1}^k \sum_{i \in U_\ell} x_i = \sum_{\ell=1}^k |U_\ell| c_\ell$ are given by

$$(\mathbf{x}^{1,c_1}, \mathbf{x}^{2,c_2}, \dots, \mathbf{x}^{k,c_k}) \quad \text{with} \quad \sum_{\ell=1}^k |U_\ell| c_\ell = 0.$$

□

Thus, if E is connected, $Q_E(\mathbf{x})$ has a unique solution under $\sum x_i = 0$, and if E is not connected, one can find multiple minima of $Q_E(\mathbf{x})$ under $\sum x_i = 0$, which proves Theorem 1. □

7.3.1.3 ML-estimates

The ML-estimates resulting from a connected set of edges E are characterized in Lemma 7 with a system of linear equations. Applications to simple examples are discussed in Corollaries 5-7.

Lemma 7 *Let E be connected on $\{1, \dots, n\}$, let $\mathbf{x}^m \in \mathbb{R}^n$ with $\sum_i x_i^m = 0$ and $Q_E(\mathbf{x}^m) = \min_{\mathbf{x} \in \mathbb{R}^n} Q_E(\mathbf{x})$. Then, the following relations hold:*

$$\sum_{i \in E_k} (x_k^m - x_i^m) = \sum_{i \in E_k} \varphi_{ik}, \quad \forall k = 1, \dots, n. \quad (7.21)$$

Thus, for every unit k , the sum of all measured distances φ_{ik} must be represented exactly by the sum of all corresponding model distances $\delta_{ik} = (x_k - x_i)$ with $i \in E_k$.

Proof.

As shown in Lemma 5, \mathbf{x}^m satisfies

$$\frac{\partial Q_E(\mathbf{x}^m)}{\partial x_k} = 0 \quad \forall k = 1, \dots, n.$$

The computation of the partial derivatives directly yields the claim:

$$\frac{\partial Q_E(\mathbf{x})}{\partial x_k} = 2 \left(- \sum_{i \in E_k} \varphi_{ik} + \sum_{i \in E_k} (x_k - x_i) \right).$$

□

This result is used in the following to investigate the estimates of the unit positions and the model distances in specific cases.

Corollary 5 *Let $|M| = 1$, i.e., one edge is missing. That means $\exists \ell_1 \neq \ell_2 : M = \{\{\ell_1, \ell_2\}\}$. Then, the ML-estimates for the distances are*

$$\hat{\delta}_{\ell_1 \ell_2} = \hat{x}_{\ell_2} - \hat{x}_{\ell_1} = \frac{1}{n-2} \left(\sum_{\substack{i=1 \\ i \notin \{\ell_1, \ell_2\}}}^n (\varphi_{\ell_1 i} + \varphi_{i \ell_2}) \right) \quad (7.22)$$

$$\hat{\delta}_{\ell_1 r} = \frac{1}{n} \left(2\varphi_{\ell_1 r} + \sum_{\substack{i=1 \\ i \notin \{\ell_1, \ell_2\}}}^n (\varphi_{\ell_1 i} + \varphi_{i r}) + \hat{\delta}_{\ell_1 \ell_2} + \varphi_{\ell_2 r} \right) \quad \text{for } r \neq \ell_2 \quad (7.23)$$

$$\delta_{rs} = \frac{1}{n} \left(2\varphi_{rs} + \sum_{\substack{i=1 \\ i \notin \{r, s\}}}^n (\varphi_{ri} + \varphi_{is}) \right) \quad \text{for } \{r, s\} \cap \{\ell_1, \ell_2\} = \emptyset. \quad (7.24)$$

Proof.

For $k \notin \{\ell_1, \ell_2\}$, equation (7.21) reads as in the case with complete data sets:

$$\sum_{i \in E_k} \varphi_{ik} = \sum_{\substack{i=1 \\ i \neq k}}^n (x_k - x_i) = \sum_{\substack{i=1 \\ i \neq k}}^n x_k - \sum_{\substack{i=1 \\ i \neq k}}^n x_i \stackrel{\sum x_i=0}{=} (n-1)x_k + x_k = nx_k.$$

Thus, the position of any unit k with $|E_k| = n-1$ is computed as usual (Lemma 3). To estimate δ_{ℓ_1, ℓ_2} , note that $E_{\ell_1} = \{1, \dots, n\} \setminus \{\ell_1, \ell_2\} = E_{\ell_2}$. Hence,

$$\left. \begin{aligned} (n-1)x_{\ell_1} &= \sum_{i \in E_{\ell_1}} (\varphi_{i\ell_1}) - x_{\ell_2} \\ (n-1)x_{\ell_2} &= \sum_{i \in E_{\ell_1}} (\varphi_{i\ell_2}) - x_{\ell_1} \end{aligned} \right\} (n-2)(x_{\ell_2} - x_{\ell_1}) = \sum_{i \notin \{\ell_1, \ell_2\}} (\varphi_{\ell_1 i} + \varphi_{i\ell_2}),$$

which gives equation (7.22). The proof of equation (7.23) is analogous. \square

Corollary 5 says that if only one edge (ℓ_1, ℓ_2) is missing, the corresponding distance δ_{ℓ_1, ℓ_2} is estimated by the average of all indirect distances of length 2. Furthermore, to estimate distances $\delta_{\ell_1 r}$, we usually use the direct distance $\varphi_{\ell_1 r}$ and all indirect distances with two steps. One of these indirect distances has not been measured and is therefore replaced by its ML-estimate. Distances between units r, s with full measurements, $|E_r| = |E_s| = (n-1)$, remain unaffected and are estimated as usual.

Corollary 6 *Let $|M| = 2$ with adjacent edges, i.e. wlog $\exists \ell_1 < \ell_2 < \ell_3 : M = \{\{\ell_1, \ell_2\}, \{\ell_2, \ell_3\}\}$. Then*

$$\hat{\delta}_{\ell_1 \ell_3} = \frac{1}{(n-1)} \left(2\varphi_{\ell_1 \ell_3} + \sum_{i \notin \{\ell_1, \ell_2, \ell_3\}} (\varphi_{\ell_1 i} + \varphi_{i\ell_3}) \right) \quad (7.25)$$

$$\hat{\delta}_{\ell_2 \ell_3} = \frac{1}{(n-3)} \left(\sum_{i \notin \{\ell_1, \ell_2, \ell_3\}} (\varphi_{\ell_1 i} + \varphi_{i\ell_3}) + \varphi_{\ell_1 \ell_3} - \hat{\delta}_{\ell_1 \ell_3} \right) \quad (7.26)$$

Proof.

Solve the system of equations (7.21) for the given M . \square

Corollary 6 states that whenever exactly two adjacent edges $\ell_1 \rightarrow \ell_2 \rightarrow \ell_3$ are missing, the distance $\delta_{\ell_1 \ell_3}$ is estimated as usual, only the indirect distance

$(\varphi_{\ell_1\ell_2} + \varphi_{\ell_2\ell_3})$ is left out because neither $\varphi_{\ell_1\ell_2}$ nor $\varphi_{\ell_2\ell_3}$ were measured. Equation (7.26) can be read as follows: Estimate the distance $\delta_{\ell_2\ell_3}$ by the mean of all indirect distances of length 2, of which both parts have been measured, add the existing part $(\varphi_{\ell_1\ell_3})$ of the indirect distance $(\varphi_{\ell_2\ell_1} + \varphi_{\ell_1\ell_3})$ and subtract its estimate $\hat{\delta}_{\ell_1\ell_3}$.

The last example deals with a minimal data case where $|E| = n - 1$.

Corollary 7 *Let E be connected on $\{1, \dots, n\}$ with $|E| = (n - 1)$ such that the units can be renumbered such that $E = \{\{1, 2\}, \{2, 3\}, \dots, \{n - 1, n\}\}$. Then*

$$\hat{\delta}_{i,i+1} = \varphi_{i,i+1} \quad \forall i = 1, \dots, n - 1. \quad (7.27)$$

Proof.

For the borders 1 and n the claim is trivial, as $|E_1| = |E_n| = 1$, and equations (7.21) yields the result. Induction from the first or from the last edge yields: If $(x_k - x_{k-1}) = \varphi_{k-1,k}$, the $(k - 1)^{th}$ component of equation (7.21) yields

$$\begin{aligned} (x_{k-1} - x_k) + (x_{k-1} - x_{k-2}) &= \varphi_{k,k-1} + \varphi_{k-2,k-1} \\ \iff (x_{k-1} - x_{k-2}) &= \varphi_{k-2,k-1} \end{aligned}$$

□

In the minimal data case, every measured distance is exactly represented by the corresponding model distance. Therefore, all measurements are needed to position the units, and the measurement error σ cannot be estimated. In general, the formula for the estimation of the measurement error in the case with missing data is analogous to the full data case:

7.3.1.4 Global variance

Lemma 8 *Let E be connected on $\{1, \dots, n\}$, and let $\hat{\mathbf{x}} = (\hat{x}_1, \dots, \hat{x}_n)$ be the ML-estimates of the unit positions under E . As usual, the error sum of squares is given by*

$$Q_E(\hat{\mathbf{x}}) = \sum_{\{i,j\} \in E} (\varphi_{ij} - (\hat{x}_j - \hat{x}_i))^2.$$

Then,

$$\hat{\sigma}^2 := \frac{1}{|E| - (n - 1)} \cdot Q_E(\hat{\mathbf{x}}) \quad (7.28)$$

is an unbiased estimate of σ^2 .

Proof.

The argument is analogous to the one used in the geometric interpretation in section 7.1.2: To determine the ML-estimate $\hat{\mathbf{x}}$ of the unit positions, the vector $\Phi \in \mathbb{R}^{|E|}$ is split by orthogonal projection. The resulting vector $\hat{\Delta}$ has components $\hat{\delta}_{ij} = \hat{x}_j - \hat{x}_i$ and lies in the $(n-1)$ -dimensional subspace \mathcal{M}_n , and for the residual $R = \Phi - \hat{\Delta}$, $\|R\|^2 = Q_E(\hat{\mathbf{x}})$ holds. Under the model assumptions

$$\Phi = \Delta + \sigma \mathfrak{Z}, \quad \Delta \in \mathcal{M}_n, \quad \mathfrak{Z} \sim \mathcal{N}(0, I_{|E|}),$$

$$\sigma^{-2} Q_E(\hat{\mathbf{x}}) = \sigma^{-2} \|R\|^2 = \sigma^{-2} \|\mathcal{P}_{\mathcal{M}_n^\perp} \Phi\|^2 = \|\mathcal{P}_{\mathcal{M}_n^\perp} \mathfrak{Z}\|^2 \sim \chi^2(|E| - (n-1)).$$

Hence,
$$\mathbb{E} \left(\frac{Q_E(\hat{\mathbf{x}})}{|E| - (n-1)} \right) = \sigma^2.$$

□

Thus, in a situation in which not all phase offsets can be measured, Lemma 7 can be applied to compute the ML-estimates of the unit positions, and Lemma 8 can be applied to estimate the measurement error, σ^2 .

7.3.2 Heteroscedasticity

The assumption of homoscedasticity, i.e., that every phase offset φ_{ij} is measured with the same measurement error, σ^2 , leads to simple formulas both for the positions of the units on the time axis and for the model distances. It further allows application of analysis of variance. However, homoscedasticity does not need to be given in experimentally obtained phase offsets. If measurement errors do not have equal variances, ML-estimates of the unit positions can be obtained with the following model:

$$\varphi_{ij} = (x_j - x_i) + \sigma_{ij} Z_{ij} \quad \forall 1 \leq i < j \leq n,$$

with independent and standard normal random variables Z_{ij} . The vector of variances of measurement errors is denoted by $\vec{\sigma} := (\sigma_{12}, \dots, \sigma_{n-1,n})$.

Position estimates To estimate the unit positions under heteroscedasticity, the likelihood function from equation (7.5) is modified to

$$L(\mathbf{x}, \vec{\sigma}) = \frac{1}{(\sqrt{2\pi})^{\binom{n}{2}} \prod_{i < j} \sigma_{ij}} \cdot \exp \left(-\frac{1}{2} \sum_{1 \leq i < j \leq n} \frac{1}{\sigma_{ij}^2} (\varphi_{ij} - (x_j - x_i))^2 \right).$$

One thus needs to minimize the term

$$Q_{\vec{\sigma}}(\mathbf{x}) := \sum_{1 \leq i < j \leq n} \frac{1}{\sigma_{ij}^2} (\varphi_{ij} - (x_j - x_i))^2$$

for constant $\vec{\sigma}$. The partial derivatives

$$\frac{\partial Q_{\vec{\sigma}}(\mathbf{x})}{\partial x_k} = -2 \sum_{i \neq k} \frac{\varphi_{ik}}{\sigma_{ik}^2} + 2 \sum_{i \neq k} \frac{x_k - x_i}{\sigma_{ik}^2} \quad (7.29)$$

characterize the minimum. Together with $\sum_{i=1}^n x_i = 0$, the system of equations given by (7.29) can be solved by any statistical package if all φ_{ij} and σ_{ij}^2 are given.

In practice, phase offsets and variances of measurement errors can be estimated with the methods described in part I. With the estimates from equation (7.29), the linear configuration resulting from the homoscedasticity assumption can be compared to the linear configuration obtained from the analogous model which incorporates different measurement errors. Furthermore, the distribution of the variances σ_{ij}^2 can be compared to the estimate of the global variance σ^2 derived under the homoscedasticity assumption because both the global $\hat{\sigma}^2$ and the separate σ_{ij}^2 represent independent estimates of the same quantity. In fact, if homoscedasticity is not fulfilled but the homoscedasticity assumption is used to estimate the unit positions and the global variance σ^2 (Lemma 4), the expectation of the global $\hat{\sigma}^2$ is simply the mean of the individual variance estimates,

$$\mathbb{E}(\hat{\sigma}^2) = \frac{1}{\binom{n}{2}} \sum_{i < j} \sigma_{ij}^2. \quad (7.30)$$

Proof.

With the estimates \hat{x}_k from Lemma 3,

$$\begin{aligned} \varphi_{ij} - (\hat{x}_j - \hat{x}_i) &= \frac{1}{n} \left((n-2)\varphi_{ij} + \sum_{\ell \neq i,j} (\varphi_{j\ell} + \varphi_{\ell i}) \right) \\ \implies \mathbb{E}(\varphi_{ij} - (\hat{x}_j - \hat{x}_i)) &= \frac{1}{n} \mathbb{E} \sum_{\ell \neq i,j} (\varphi_{ij} + \varphi_{j\ell} + \varphi_{\ell i}) = 0 \\ \implies \mathbb{E}((\varphi_{ij} - (\hat{x}_j - \hat{x}_i))^2) &= \text{Var}(\varphi_{ij} - (\hat{x}_j - \hat{x}_i)) \\ &= \frac{1}{n^2} \left((n-2)^2 \sigma_{ij}^2 + \sum_{\ell \neq i,j} (\sigma_{j\ell}^2 + \sigma_{\ell i}^2) \right). \end{aligned}$$

Thus,

$$\begin{aligned}\mathbb{E}(\hat{\sigma}^2) &= \frac{1}{\binom{n-1}{2}} \cdot \frac{1}{n^2} \cdot \sum_{i < j} \left\{ (n-2)^2 \sigma_{ij}^2 + \sum_{\ell \neq i, j} (\sigma_{j\ell}^2 + \sigma_{\ell i}^2) \right\} \\ &= \frac{1}{\binom{n}{2}} \cdot \frac{1}{n(n-2)} \sum_{i < j} \sigma_{ij}^2 [(n-2)^2 + 2(n-2)] = \frac{1}{\binom{n}{2}} \sum_{i < j} \sigma_{ij}^2.\end{aligned}$$

□

7.4 Model summary

Chapter 7 was concerned with the development of a stochastic model with which an additive set of phase offsets can be represented. The main idea was to reduce the set of $\binom{n}{2}$ phase offsets to an $(n-1)$ -dimensional representation by positioning n units on the time axis such that pairwise distances represent phase offsets as closely as possible and that the mean of the positions is zero.

The basic model uses the assumptions presented in section 7.1:

$$\varphi_{ij} = (x_j - x_i) + \sigma Z_{ij} = \delta_{ij} + \sigma Z_{ij} \quad \forall 1 \leq i < j \leq n$$

with $x_1, \dots, x_n \in \mathbb{R}$ and $\sum x_i = 0$. This model assumes homoscedasticity, i.e., that the measurement errors of all phase offsets have the same variance σ^2 . Measurement errors are furthermore assumed to be independent and normally distributed. Lemma 3, Corollary 3 and Lemma 4 provide ML-estimates of the unit positions x_k , of the model distances δ_{ij} and an unbiased estimate of the measurement error σ^2 . The estimates are relatively robust against violations of the model assumptions that concern the measurement errors. The basic model yields parameter estimates that are relatively simple and directly interpretable. Furthermore, the homoscedasticity assumption allows the application of analysis of variance as discussed in section 7.2.

An interpretation of the resulting linear configuration has to take into account that unit positions are not necessarily stable across the analysis window because a configuration extracted from a set of pairwise measurements only represents the average unit positions in the analyzed period. The measurement

error only takes into account the deviations of the data set from the closest linear structure and does not include the variability of the unit positions across the analysis window.

Missing data The most important model extension concerns the situation in which not all phase offsets can be measured (section 7.3.1). If phase offsets are assumed to be missing due to an unsystematic, purely random cause, Theorem 1 states that ML-estimates of the unit positions exist if and only if each pair of units is connected by a path of non-missing phase measurements. The estimates are provided by the system of equations given in Lemma 7. The global variance can be estimated with Lemma 8 but requires a higher number of non-missing phase offsets.

In the following chapter, the theoretical results are applied to the sample data set. The basic model is of major interest, and extensions are only considered as far as the investigation of model assumptions of the basic model are concerned.

Chapter 8

Data analysis

The linear model presented in chapter 7 is applied here to the sample data set. As described in Appendix A.3, spiking activity of 14 units was recorded in 20 repetitions of each of six stimulation conditions with single and conflicting moving bars. In the exemplary analysis, three comparable stimuli with conflicting bars (conditions 1, 3 and 5) are investigated.

In section 8.1, the additivity model discussed in section 7.1 is applied to the phase offsets obtained from the CCHs in stimulation condition 1. This results in a linear configuration of the 14 units on the time axis together with an estimate of the error with which phase offsets were measured. The linear configuration is investigated more closely in order to evaluate whether the model assumptions can be used to represent the data set.

In section 8.2.1, the homoscedasticity assumption is investigated by a comparison of the global estimate $\hat{\sigma}^2$ to the measurement errors of individual phase offsets derived in part I. To this end, the distribution of individual measurement errors is compared to the global variance derived with the homoscedasticity assumption. Furthermore, the linear configuration obtained under the homoscedasticity assumption is compared to the ML-estimates derived under the assumption of inequality of variances. Finally, it is investigated whether the global variance represents only measurement error or whether it has an additional component which indicates deviations from the additivity assumption.

Section 8.2 investigates whether the additivity model provides a reasonable description of the data structure. To this end, the configuration resulting from experimentally derived phase offsets is compared to the configuration obtained from randomly permuted phase offsets.

Finally, section 8.3 approaches the crucial question whether the configurations

that can be extracted with the presented method may be related to information processing. To this end, linear configurations extracted from independent sets of trials are compared with the help of analysis of variance as shown in section 7.2.

8.1 Positions of the units on the time axis

With the help of the formulas presented in section 7.1, the set of temporal positions of the units on the time axis can be estimated easily. Starting with a set of phase offsets measured for all 91 pairs of units in stimulation condition 1, the ML-estimate of unit k 's position, x_k , is estimated with Lemma 3:

$$\hat{x}_k = \frac{1}{n} \sum_{i=1}^n \varphi_{ik} \quad \forall k = 1, \dots, n.$$

These ML-estimates of the preferred firing times, which are chosen such that they have mean zero, are represented as big gray points in Figures 8.1 A and B. In order to get an idea of the precision with which each unit's position is estimated, Figure 8.1 A also shows normal density functions which have a standard deviation of $\hat{\sigma}_{\hat{x}} \approx 0.05$ ms (derived with Lemma 4) and indicate the estimated variability of each position estimate. One can see that the PTs can be determined with an error that is much smaller than one millisecond.

To get a more detailed impression of the precision of one unit's position estimate, Figure 8.1 B shows the residuals between measured phase offsets and model distances, $\varphi_{ij} - \hat{\delta}_{ij}$. This representation can be used to investigate whether some phase offsets disagree with the linear structure given by all phase offsets. If this is the case, single residuals deviate remarkably from zero because the corresponding phase offset cannot be represented as closely by its model distance as the other phase offsets. Figure 8.1 B shows that the phase offsets from stimulation condition 1 yield residuals which are smaller than 0.5 ms and relatively homogeneous. Additionally, close vertical clustering of residuals (e.g. around unit 1) indicates that there is high agreement about the position of this unit among the phase offsets between the respective unit and all other units.

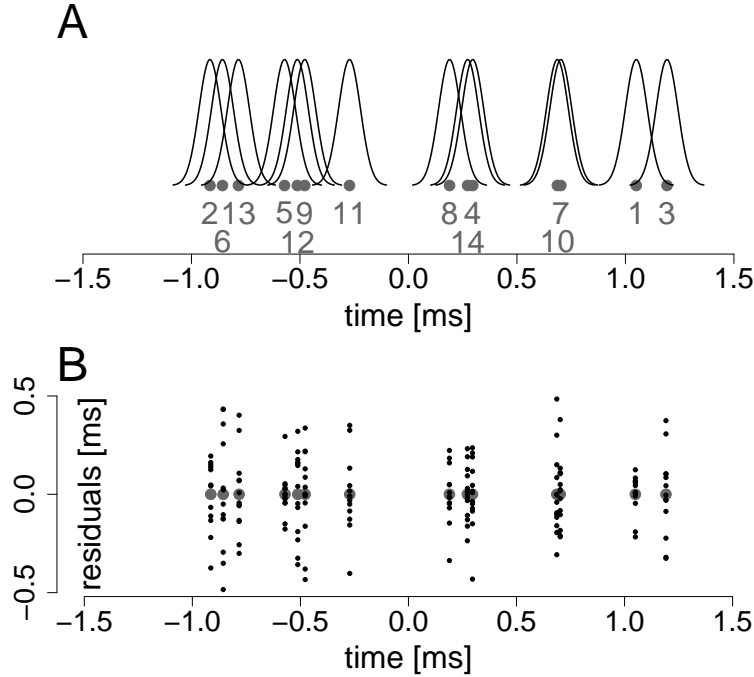


Figure 8.1: Linear configuration of units in stimulation condition 1. A: Numbers indicate temporal positions of units estimated with Lemma 3. Normal density functions indicate the variance of the position estimates (Corollary 4). B: Gray points indicate the same unit positions as in A. For every unit, the black points above and below its temporal position indicate the differences between measured phase offsets and the corresponding model distances.

The residuals between phase offsets and model distances can be compared to investigate the extent to which phase offsets can be represented in the model. Recall that the unit positions minimize the error sum of squares (equation (7.6))

$$Q(\hat{\mathbf{x}}) = \sum_{1 \leq i < j \leq n} (\varphi_{ij} - \hat{\delta}_{ij})^2.$$

Thus, the units are positioned such that phase offsets are represented as closely as possible by model distances. Therefore, the agreement between these quantities is a useful criterion for the suitability of the model. Figure 8.2 A shows a scatter plot of phase offsets and model distances. The close clustering of the points at the main diagonal and the high correlation of $r = 0.98$ indicate that the model distances extracted with the additivity model mirror the set of measured phase offsets to a high degree. One reason for this close correspondence is the high

agreement between direct phase offset measurements, φ_{ij} , and corresponding indirect measurements of length two, $\varphi_{il} + \varphi_{lj}$ (shown in Fig. 8.2 B), because these quantities provide the data basis with which the model distances δ_{ij} are estimated (cf. Corollary 3).

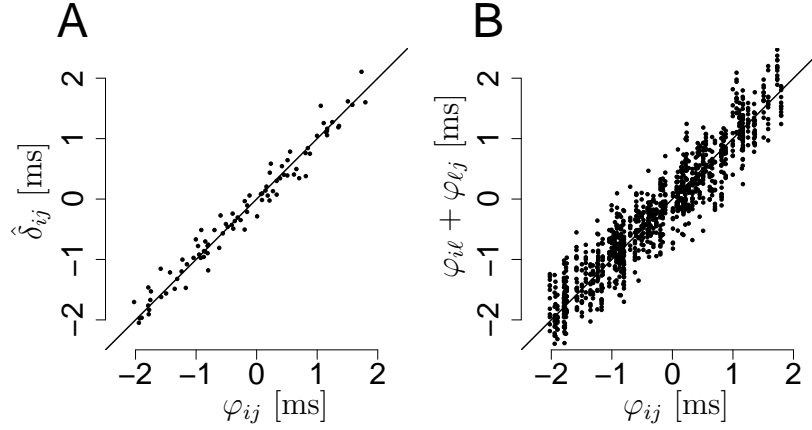


Figure 8.2: Representation of phase offsets by model distances in stimulation condition 1. A: Every measured phase offset φ_{ij} is plotted against the corresponding model distance $\hat{\delta}_{ij}$. B: Every direct phase measurement, φ_{ij} , is plotted against all indirect measurements with two components, $(\varphi_{il} + \varphi_{lj})_{l \neq i, j}$.

This internal consistency of the data set can also be observed in the following. To investigate the degree to which subsets of phase offsets agree about the global linear configuration, the set of units is split into a target set, $\mathcal{T} := \{1, 2, \dots, 6\}$ that is to be positioned on the time axis and two reference sets, $\mathcal{R}_1 := \{7, 8, 9, 10\}$ and $\mathcal{R}_2 := \{11, 12, 13, 14\}$, with which the positions of the targets are determined. The ML-estimates of Lemma 3 are modified to estimate the unit positions for all units $t \in \mathcal{T}$:

$$\hat{x}_t^{(1)} = \frac{1}{|\mathcal{R}_1| + 1} \sum_{r \in \mathcal{R}_1} \varphi_{rt} \quad \text{as seen from } \mathcal{R}_1, \quad (8.1)$$

$$\hat{x}_t^{(2)} = \frac{1}{|\mathcal{R}_2| + 1} \sum_{r \in \mathcal{R}_2} \varphi_{rt} \quad \text{as seen from } \mathcal{R}_2. \quad (8.2)$$

Thus, for each reference set, the position of unit t is estimated only on the basis of those phase offsets given between the units in the reference set and unit t . This does not result in position estimates with mean zero because positions are shifted according to the perspective of the reference set. Therefore, the estimates are

re-centered at zero, and the resulting position estimates are shown in Figure 8.3. One can see that although each position is estimated on the basis of only four measurements, the temporal order and the positions of the target units extracted from the two sets \mathcal{R}_1 and \mathcal{R}_2 are nearly identical. Thus, already small fractions of the given set of phase offsets yield reliable and consistent estimates of the global linear structure.

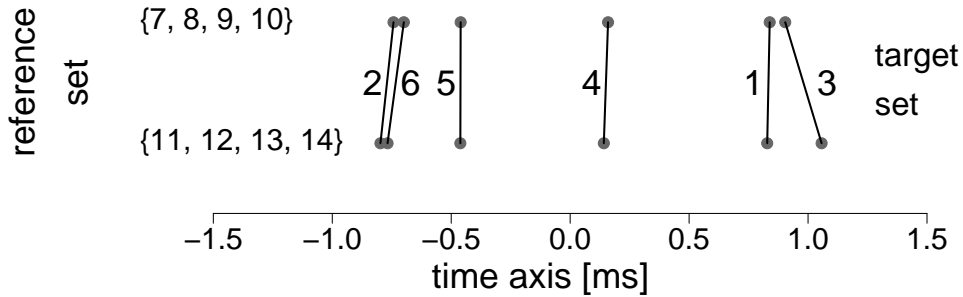


Figure 8.3: Linear configurations of target units extracted from independent reference sets \mathcal{R}_1 (top) and \mathcal{R}_2 (bottom) according to equations (8.1) and (8.2) after centering at zero.

8.2 Investigation of linear configurations

8.2.1 Heteroscedasticity versus global variance

The preceding analysis is based on the homoscedasticity assumption, i.e., every phase offset is assumed to be distorted by a measurement error with the same variance σ^2 . This assumption is now examined in more detail. The results from Part I are important in this analysis because approximations of the true measurement errors of single phase offsets are provided there and can be compared to the global variance σ^2 estimated with the linear model from section 7.1.

First, although the estimates of the unit positions from Lemma 3 are unbiased even if the variances of the measurement errors differ across phase offsets (p. 64), it is interesting to investigate the size of the differences between the linear configurations derived under homo- and under heteroscedasticity. To this end, the results of section 7.3.2 are applied to the phase offsets by making use of their individual variances $\sigma_{\hat{\phi}_{ij}}^2$ estimated in part I, which are denoted here by σ_{ij}^2 . Figure 8.4 A shows the temporal maps derived under homoscedasticity

(Lemma 3) and under heteroscedasticity (linear system of equations given by eq. (7.29) and $\sum x_i = 0$). The temporal order of units is identical, and also the distances between the positions do not change considerably. In particular, the unit positions under heteroscedasticity do not deviate more from the original positions than is allowed by the estimation imprecision indicated in Figure 8.1. Thus, for the given data set, the homoscedasticity assumption yields a sufficiently accurate representation of the unit positions. Therefore, the global variance is used in the following since it provides straightforward position estimates and allows application of analysis of variance.

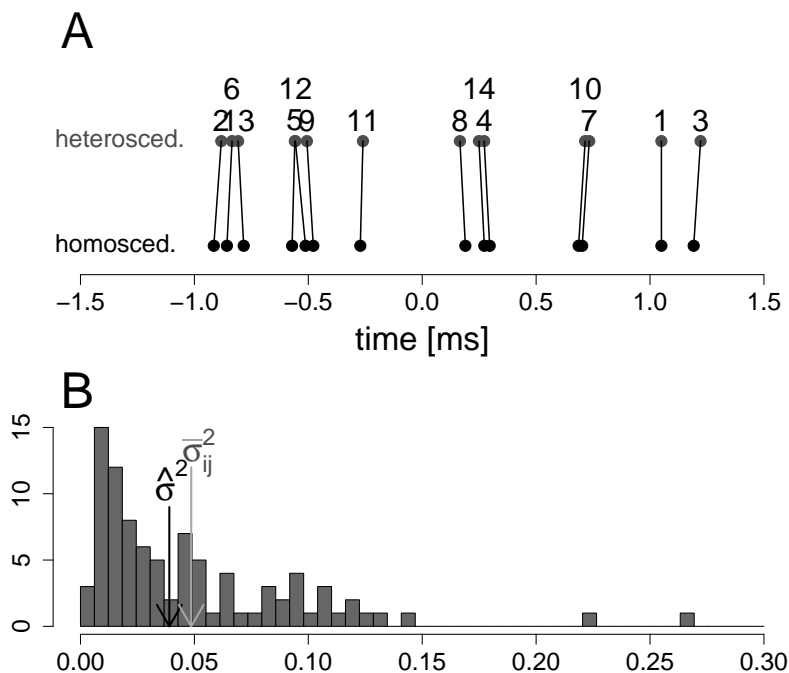


Figure 8.4: Results of model extension under heteroscedasticity. A: Linear configurations derived under homoscedasticity (bottom) and under heteroscedasticity (top). B: Distribution of individual phase offset variances, σ_{ij}^2 . Mean $\bar{\sigma}_{ij}^2$ indicated by gray arrow. The global variance estimated in the linear model under homoscedasticity assumption is indicated by black arrow.

The second issue which has to be considered when using the global variance deals with confounded errors. The global variance is assumed to represent pure measurement error of additive phase offsets but can be increased further if phase offsets are not additive. Thus, it confounds measurement error and deviations

from the additivity assumption. In order to investigate whether the global variance is increased by deviations from additivity, the distribution of individual measurement errors derived in Part I is compared to the estimate of the global variance. Figure 8.4 B shows the distribution of individual measurement errors of phase offsets together with the mean, $\bar{\sigma}_{ij}^2$, and the global variance estimate, $\hat{\sigma}^2$. According to equation (7.30), $\hat{\sigma}^2$ has expectation $\bar{\sigma}_{ij}^2$ if phase offsets are additive. For non-additive phase offsets, $\hat{\sigma}^2$ is increased because it does not only contain the measurement error but also the error caused by the lack of additivity. In the data analyzed here, the global variance is even smaller than the mean measurement error and thus, there is no indication of deviations from the model assumptions as far as the variance estimate is concerned.

8.2.2 Permutation test

In the previous paragraph, it was hypothesized implicitly that the analyzed set of phase offsets has an additive structure and that non-additive phase offsets cannot be represented in a similar manner by model distances on the time axis. This hypothesis is plausible, especially since the agreement between direct and indirect phase offsets in Figure 8.2 B is unlikely to be observed for non-additive phase offsets. Yet, it remains to be investigated to which extent the linear model can represent non-additive data sets in a pseudo-linear structure. To this end, the 91 phase offsets from stimulation condition 1 are permuted randomly and thus assigned to random pairs of units. Then, the units are positioned on the time axis according to Lemma 3. The results of one such permutation are shown in Figures 8.5 A & B, which are analogous to Figures 8.1 A & 8.2 A. One can see that the temporal positions of the units are clustered much closer around zero because the positions are estimated by a sum of certain phase offsets (Lemma 3), which is close to zero for random phase offsets because randomly assigned positive and negative values tend to average out.

As a consequence, phase offsets with a high absolute value cannot be represented by model distances because the distances between the units are too small. This can be observed in Figure 8.5 B in which the permuted phase offsets are plotted against the model distances derived from the permuted data set. The model distances are smaller than 1 ms and cannot represent bigger phase offsets. Additionally, the correlation between model distances and phase offsets is only 0.26, and the cloud of points is horizontal instead of being clustered at the main diagonal.

Comparable results were obtained for 10,000 analogous permutations. The distribution of correlation coefficients between phase offsets and model distances is shown in Figure 8.5 C. The arrow indicates $r = 0.98$ obtained for the original set of phase offsets. One can see that the experimentally obtained set of phase offsets yields a linear configuration which represents the original phase offsets much more closely than all permuted data sets. Thus, it is highly unlikely that a temporal map comparable to the one observed for the experimental data set is obtained by chance.

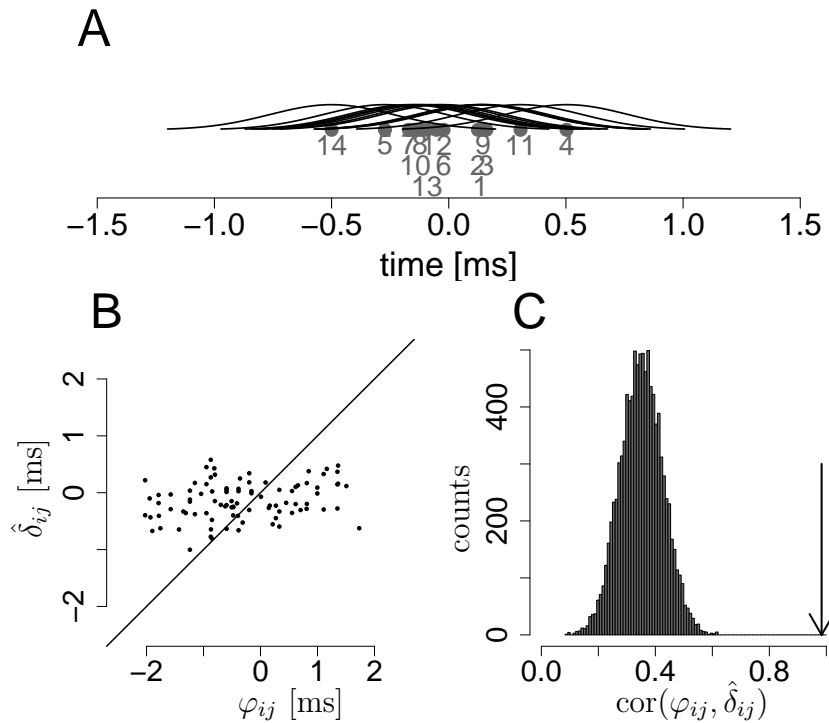


Figure 8.5: Application of the linear model to randomly permuted phase offsets. A: Estimated positions of the units on the time axis with normal density functions (cf. Fig. 8.1 A). B: Scatter plot of phase offsets and model distances (cf. Fig. 8.2 A). C: Distribution of correlation coefficients of permuted phase offsets and model distances in 10,000 permutations. The arrow indicates $r = 0.98$ obtained in the original data set.

8.3 Differences between linear configurations

The previous section was concerned with the investigation of the suitability of the model assumptions. The recorded units were positioned on the time axis according to their temporal order of firing given by the measured phase offsets. The resulting model distances could represent the measured phase offsets with a correlation of 0.98, a much larger value than those obtained from permuted data sets. Thus, the described model seems to be suitable to describe an important aspect of the data structure in the given set of phase offsets.

In this section, the analysis-of-variance approach presented in section 7.2.1 is applied to the sample data set to investigate changes across linear configurations. Moreover, an additional graphical method is used which provides information about the identity of units which change their temporal position.

Two linear configurations on the time axis,

$$\mathcal{C}_1 := \left\{ \hat{x}_1^{(1)}, \dots, \hat{x}_n^{(1)} \left| \sum_i x_i^{(1)} = 0 \right. \right\} \quad \text{and} \quad \mathcal{C}_2 := \left\{ \hat{x}_1^{(2)}, \dots, \hat{x}_n^{(2)} \left| \sum_i x_i^{(2)} = 0 \right. \right\}$$

that are extracted from two sets of phase offsets,

$$\mathcal{S}_1 := \{\varphi_{12}^{(1)}, \varphi_{13}^{(1)}, \dots, \varphi_{n-1,n}^{(1)}\} \quad \text{and} \quad \mathcal{S}_2 := \{\varphi_{12}^{(2)}, \varphi_{13}^{(2)}, \dots, \varphi_{n-1,n}^{(2)}\},$$

are to be tested for differences. To this end, the results of section 7.2.1 are specified for $k = 2$. The test statistic F from equation (7.20) requires the estimation of the model distances for both data sets,

$$\hat{\delta}_{ij}^{(1)} = \hat{x}_j^{(1)} - \hat{x}_i^{(1)} \quad \text{and} \quad \hat{\delta}_{ij}^{(2)} = \hat{x}_j^{(2)} - \hat{x}_i^{(2)},$$

and of the variances,

$$\hat{\sigma}_1^2 = \binom{n-1}{2}^{-1} \sum_{i<j} (\varphi_{ij}^{(1)} - \hat{\delta}_{ij}^{(1)})^2 \quad \text{and} \quad \hat{\sigma}_2^2 = \binom{n-1}{2}^{-1} \sum_{i<j} (\varphi_{ij}^{(2)} - \hat{\delta}_{ij}^{(2)})^2.$$

Then, under the null hypothesis that \mathcal{C}_1 and \mathcal{C}_2 are identical, the test statistic

$$\begin{aligned} F &= \frac{2}{(\hat{\sigma}_1^2 + \hat{\sigma}_2^2)(n-1)} \cdot \sum_{\ell=1,2} \sum_{i<j} (\hat{\delta}_{ij}^{(\ell)} - \frac{1}{2} \sum_{r=1,2} \hat{\delta}_{ij}^{(r)})^2 \\ &= \frac{1}{n-1} \cdot \frac{1}{\hat{\sigma}_1^2 + \hat{\sigma}_2^2} \cdot \sum_{i<j} (\hat{\delta}_{ij}^{(1)} - \hat{\delta}_{ij}^{(2)})^2 \end{aligned}$$

is Fisher-distributed with $(n-1)$ and $2\binom{n-1}{2}$ degrees of freedom.

As in Part I, the phase offsets extracted in stimulation conditions 1, 3 and 5 are analyzed here. Note again that the linear configuration extracted for one stimulation condition can represent only an average set of unit positions if these positions change during the recorded period. Therefore, this linear configuration is not necessarily stable across time. However, for a linear configuration to be relevant for information processing, it should replicate with repeated presentations of the same stimulus. In order to minimize other sources of variability, the 20 trials of one stimulation condition are divided into the two sets of odd and even trials. Comparisons between responses to different stimuli are based on all 20 trials in each stimulation condition. Since $n = 14$ units are analyzed, the degrees of freedom are $n - 1 = 13$ and $2^{\binom{n-1}{2}} = 156$ (cmp. (7.20) on p. 62).

Table 8.1 shows F -values and corresponding p -values for responses to identical and to different stimuli. As indicated by the small p -values on the right, differences between linear configurations derived under different stimulation conditions are highly unlikely to be observed by chance. On the left hand side, the p -values are much bigger. However, the comparisons within stimulation conditions 1 and 5 indicate that the changes observed across odd and even trials are slightly bigger than is accounted for by the deviations from additivity within the two data sets. This suggests that an additional source of variability affects the unit positions and produces changes across repeated measurements of the same stimulation condition.

The variability of the unit positions is, however, relatively small, as can be seen in the graphical representation of the data. Figure 8.6 shows scatter plots of unit positions in odd and even trials in stimulation condition 1 (panel A) and a comparison of stimulation conditions 1 and 3 (panel B). To measure the difference between two temporal positions of the same unit k , $\hat{x}_k^{(1)} - \hat{x}_k^{(2)}$, the variance of the latter term is estimated as

$$\hat{\sigma}_D^2 := \text{Var}(\hat{x}_k^{(1)} - \hat{x}_k^{(2)}) = \frac{n-1}{n^2} \cdot (\hat{\sigma}_1^2 + \hat{\sigma}_2^2), \quad (\text{see Cor. 4 on p. 54}) \quad (8.3)$$

and the borders of $\pm 2\hat{\sigma}_D$ are drawn around the main diagonal. Numbers outside of this error band indicate a change in the position of the respective unit.

One can see in Figure 8.6 that for identical stimuli, all units except for one remain inside of the $\pm 2\hat{\sigma}_D$ -borders, while eight out of 14 units show a considerable change between stimulation conditions 1 and 3. Thus, the graphical method indicates that in the sample data set, changes of linear configurations across stimulation conditions are bigger than differences between repeated presentations of the same stimulus.

<i>Identical stimuli</i>			<i>Different stimuli</i>		
<i>condition</i>	<i>F</i>	<i>p</i>	<i>condition</i>	<i>F</i>	<i>p</i>
1 vs. 1	2.0	0.03	1 vs. 3	22.5	$< 10^{-16}$
3 vs. 3	1.2	0.28	1 vs. 5	26.7	$< 10^{-16}$
5 vs. 5	1.9	0.03	3 vs. 5	6.7	$< 10^{-9}$

Table 8.1: Results of analysis of variance applied to investigate changes in temporal maps in stimulation conditions 1, 3 and 5.

One should keep in mind that the graphical analysis cannot be used as rigorous statistical tool because it does not correct for multiple testing and disregards covariances between the unit positions. Therefore, analysis of variance and graphical method should be combined when comparing linear configurations. In particular, the graphical approach is required for the interpretation of differences that are detected by the analysis of variance. It also provides supplementary information by identifying specific units that change their positions.

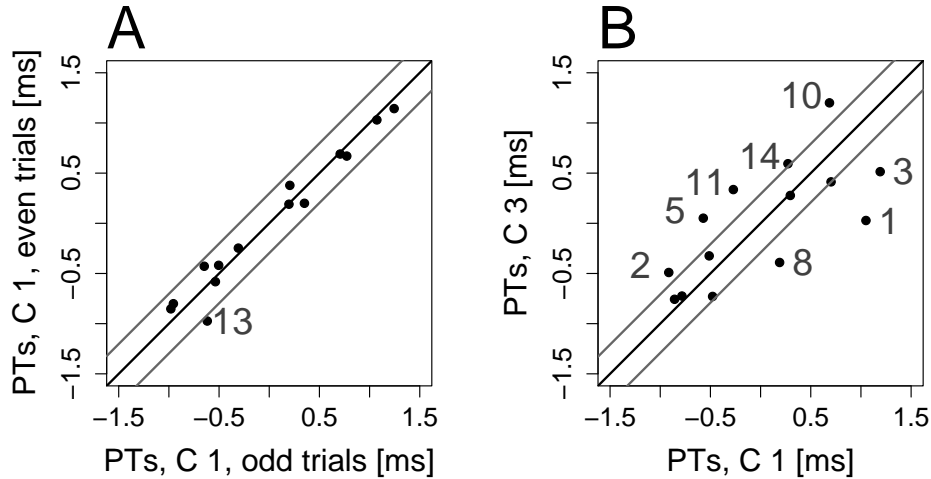


Figure 8.6: Graphic comparison of configurations. Scatter plot of preferred firing times ('PTs') of 14 units (indicated by numbers) obtained from independent sets of phase offsets. Gray lines indicate $\pm 2\sigma_D$ -borders computed with equation (8.3). A: Comparison of odd and even trials, stimulation condition 1. B: Comparison of stimulation conditions 1 & 3.

Chapter 9

Conclusion – Part II

Part II was concerned with the extraction of a spatiotemporal structure from raw phase offsets that were measured among a large group of neurons. A method was presented that makes use of a linear model to determine a specific temporal pattern, a linear configuration. This pattern is considered predominant among the recorded set of neurons because it reflects phase offsets, i.e., the predominant firing delays observed between pairs of units.

The present method is based on the assumptions that phase offsets are additive and that measurement errors are independent, normally distributed and have equal variance σ^2 . If the method is to be applied to experimentally obtained data sets, the suitability of these assumptions has to be investigated in order to ensure a reasonable interpretation of the resulting linear configuration. One should also keep in mind that the application to a non-additive data set also results in a linear configuration, in which, however, the data set is represented poorly (cf. sect. 8.2.2). It is therefore necessary to determine the degree with which the measured phase offsets can be represented by ‘model distances’. Although the existence of additive structure cannot be supported rigorously due to the lack of a sufficiently general alternative hypothesis, high agreement between phase offsets and model distances ensures that the additivity assumption renders a faithful image of the data structure.

Plausible coding mechanisms related to this data structure have been proposed recently and assume that the temporal order of firing may be relevant for stimulus encoding (Hopfield, 1995; Van Rullen *et al.*, 1998). In particular, a lead in phase is considered an indication of optimal activation of the respective cells (Hopfield, 1995; König *et al.*, 1995; Traub *et al.*, 1997; Wennekers and Palm, 2000). The data analysis performed here cannot provide sufficient information

about the role of additive near-zero phase offsets in the coding of stimulus properties, which would require further investigations as well as single-unit analysis. Instead, the application of the linear model to the sample data set was presented to illustrate the method's practical use in the study of spatiotemporal patterns.

One of the most important advantages of the method is its compatibility with analysis of variance. Among other issues, this allows studying the relevance of temporal maps by investigating differences between configurations. Second, the fact that the widely applied cross-correlation technique is used to determine phase offsets is another advantage of the method because CCHs, which have been restricted to the analysis of pairwise interactions, can now be used to analyze interactions among a high number of units. Finally, the equations provided in the methods section can be applied easily, and the resulting linear configuration yields a straightforward $(n - 1)$ -dimensional representation of a large set of pairwise measurements. Thus, data complexity is reduced without computational effort by cutting down the temporal relations to the predominant firing pattern indicated by pairwise phase offsets.

Interestingly, such a predominant firing pattern can be determined with extremely high precision ($\sigma_{\hat{x}} \approx 0.05$ ms, compare to section 8.1). This is a consequence of both the high redundancy of additive phase offsets and the high precision with which phase delays can be measured (cf. Part I). However, this precise determination of the linear configuration is not necessarily reflected in repetitive and precise firing patterns in the respective spike trains (e.g., Abeles *et al.*, 1993). In contrast, measuring phase offsets with a cosine function even requires firing delays to jitter around a preferred delay. Therefore, the role of phase offsets as small as one millisecond remains largely unclear, in particular because they originate in spiking delays that may jitter by a few milliseconds. Moreover, not only the connection of phase offsets to spiking delays but also the origin of their potential additive structure remains unexplained. It is therefore the goal of the following part to develop a stochastic model of synchronous oscillatory firing activity with which near-zero phase offsets and other essential CCH features can be explained and related to spike train properties.

Part III

How spike train properties shape CCHs

Chapter 10

Introduction and Results

10.1 Motivation

This part is concerned with essential properties of an oscillatory CCH and with the development of a model which can describe how these properties arise in terms of spike train statistics. The question concerning the way in which near-zero phase offsets and their additive structure might be reflected in the underlying spike trains is first formulated in a more fundamental way: What are the relevant parameters with which spike trains should be described in order to predict the shape of an oscillatory CCH? Or vice versa: Which spike train properties can be inferred from the geometric parameters of a CCH? Among the principal CCH features one usually distinguishes between properties related to the central peak and properties arising with oscillatory activity (called e.g. primary and secondary effects by Moore *et al.*, 1970). Figure 10.1 illustrates these principal features in an example CCH from the sample data set. Both panels show the same smoothed CCH, and in panel A, the raw counts obtained in the original time resolution of 1/32 ms are depicted additionally.

Features in a CCH Oscillatory activity is indicated in Figure 10.1 A by arrows. These arrows point out a pattern of re-occurring peaks whose height decreases with increasing delay. In experimentally obtained CCHs, the ‘strength of oscillation’ has been quantified on the basis of the number and height of these side peaks (Gray *et al.*, 1989, 1992; Karmon and Bergman, 1993; König, 1994; Nowak *et al.*, 1995).

The center peak can be characterized by its height and width marked by

the two arrows in Figure 10.1 B. For quantification purposes, the peak height is usually related to a baseline value (horizontal line in Fig. 10.1) (Aertsen and Gerstein, 1985; Melssen and Epping, 1987; König, 1994; Nowak *et al.*, 1995). The width of the peak has been quantified by fitting a Gaussian to the peak region and determining its standard deviation or its width at half height (Nowak *et al.*, 1995). Other approaches focus on the peak area, also quantified as the relative number of counts in a pre-defined peak region (Wiegner and Wierzbicka, 1987; Usrey and Reid, 1999).

Further properties associated with the shape of the center peak are illustrated in the central triangle of Figure 10.1 B. This triangle is asymmetric with respect to zero delay. Its tip is slightly shifted to the left, the counts decrease faster on the right than on the left and take smaller values in the right side valley. Finally, the variability of counts is another property of a CCH, which is indicated by the rightmost arrow in Figure 10.1 A.

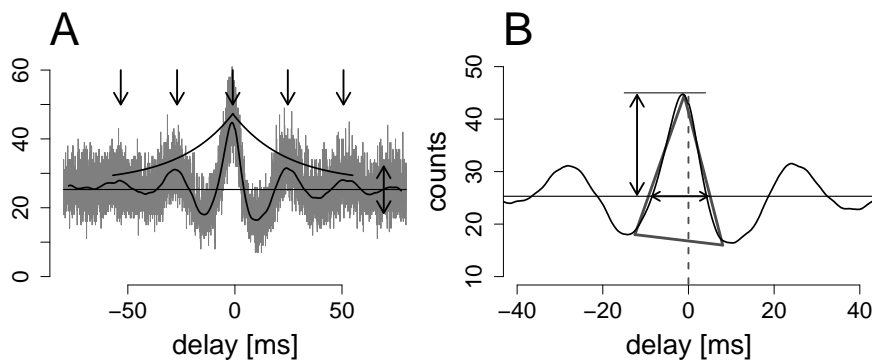


Figure 10.1: Features of oscillatory CCHs. A: CCH computed from the sample data set. Gray: original time resolution of $\delta = 1/32$ ms. Black: smoothed with a Gaussian kernel with a standard deviation of 1 ms. Arrows indicate oscillatory peaks of decreasing height (illustrated by peak-shaped curve). Rightmost arrow indicates variability of data points. B: Smoothed CCH from A. Peak asymmetry is indicated by the central triangle. Dashed gray line marks zero delay. Arrows indicate peak height and peak width at baseline.

Approaches for analysis Early approaches of statistical analysis of these CCH features used the null hypothesis of independent and stationary Poisson processes to determine the significance of the described CCH features.¹ Oscillatory peaks are interpreted as indicating a common oscillatory spiking rhythm,

¹In many cases, CCHs have been used to investigate the physiological connectivity (e.g., Abeles, 1982a; Aertsen and Gerstein, 1985). However, the connectivity structure is not directly

where the decrease in the peak height is assumed to originate in a varying period length. The central peak is taken as an indicator of near-coincident firing. Its height is used to measure the ‘strength of synchrony’, and its width has been considered related to bursting (Gochin *et al.*, 1991; Eggermont *et al.*, 1993). In addition, suitable verbal descriptions of spike trains are available with which the central peak and the oscillatory behavior of CCHs is commonly associated. Singer and Gray (1995) write e.g. “The spike trains consist of repetitive burst discharges at semiregular 15- to 30- ms intervals”. Analogously, Engel *et al.* (1992) speak of “... recurrent synchronous bursting [...], with a fluctuation of the burst frequency over a broad range [...]”

Program Such verbal descriptions provide useful insights into the significance of these CCH features for raw spike trains but represent only qualitative descriptions. Additionally, the spike train models used for statistical analysis are usually renewal processes such as Poisson processes² (e.g., Moore *et al.*, 1966; Perkel *et al.*, 1967b; Abeles, 1982a, 1991; Grün *et al.*, 2002a) or more regular processes in which inter spike intervals are the waiting times until the k th event of a Poisson process³ (Baker and Gerstein, 2000; Ventura, 2004) or other generalizations (Bair *et al.*, 1994; Kass and Ventura, 2001). These spike train models cannot be considered sufficient to model and quantify oscillatory bursting behavior. It is therefore the aim of this part to develop a model which describes oscillatory firing properties and with which one can explain and quantify the described CCH features.

10.2 Results

ACHs Since CCHs can primarily describe interactions between pairs of processes, they only provide indirect information about the properties of individual

related to the shape of a CCH because CCH peaks can be caused by several mechanisms and can vary with the stimulus (König, 1994; Vaadia *et al.*, 1995; Pauluis, 2000). Therefore, CCH properties are usually interpreted as indicating functional interactions.

²The modeling of spike trains by renewal processes is motivated by the mechanism that each spike resets the membrane potential. Since renewal processes can be characterized with the distribution of their inter spike intervals, many spike train analyses focus on interval statistics (Gerstein, 1960; Gerstein and Kiang, 1960; Rodieck *et al.*, 1962; Wyman, 1965; Tam *et al.*, 1988).

³Due to the resulting Gamma distribution of inter arrival times, such processes are also called ‘Gamma processes’.

spike trains. Therefore, the analysis is extended onto the auto correlation histograms ('ACHs'; Perkel *et al.*, 1967a), which are CCHs of two identical copies of a single spike train and thus describe properties of a single process. In contrast to a CCH, the peak of an ACH cannot be asymmetric because the ACH is necessarily symmetric with respect to zero. However, ACHs of processes which show oscillatory CCHs when paired with suitable other spike trains usually also show prominent peaks close to $\ell = 0$ and periodically occurring side peaks of decreasing height (Fig. 13.4). The central peak suggests that spikes tend to occur in packets because small intervals are preferred. Furthermore, the regular side peaks indicate that packet intervals tend to take values close to a preferred interval, and the decrease in height shows a certain variability in the inter packet intervals. These properties can also be observed qualitatively in the raw spike trains (Fig. A.1).

Model III: Doubly stochastic point processes

In order to describe the observed properties of processes with semiperiodically occurring spike packets, a doubly stochastic model is used (ch. 11). Spike trains S_1, \dots, S_n are modeled as discrete time versions of continuous time point processes X_1, \dots, X_n . Each point process X is assumed to emerge in two steps: A random walk on \mathbb{R} with independent and $\mathcal{N}(\mu, \sigma^2)$ -distributed intervals ($\sigma > 0$) produces a stationary point process $\mathbb{B} := (\dots, B_{-1}, B_0, B_1, \dots)$. Every point B_b gives rise to an independent Poissonian spike packet with exponentially decreasing firing intensity. Thus, for given \mathbb{B} , $X_{\mathbb{B}}$ is an inhomogeneous Poisson process with intensity

$$\rho_{\mathbb{B}}(t) := \frac{\alpha}{\tau} \sum_{b \in \mathbb{Z}, B_b \leq t} e^{-\frac{(t-B_b)}{\tau}} + \beta.$$

The correlation between n parallel point processes X_1, \dots, X_n is caused by the assumption that all processes share the same packet onset process \mathbb{B} (Fig. 11.3, $n = 2$). As a consequence, the parameters μ and σ are global parameters, whereas α , τ and β may differ between processes but are assumed to stay constant across time. The parameter α_j denotes the expected number of spikes in a packet of process X_j , τ_j denotes the speed of the exponential decay as well as the mean interval between the packet onset B_b and a spike of that packet in X_j , and β_j describes the background firing intensity. It should be noted that \mathbb{B} is the only source of correlation between the processes.

ACF and CCF In the framework of this model, a formula is derived for the intensity of spike pairs with delay $s \in \mathbb{R}$ (eqs. (12.1) & (12.2), ch. 12). Analogous to the terminology used for the CCH of discrete time spike trains, this value is called the auto (or cross) correlation function (‘ACF/CCF’) at shift s . The ACF of a process X is derived as the normed distribution of spikes in X , conditioned on the event to observe a spike at time t , which is equivalent to the normed Palm distribution of the process X . For the given doubly stochastic processes, the ACF can be decomposed into different summands (curves in Fig. 12.2), which reflect the intensity of spike pairs that originate in packets with a specific position relative to each other.

Interpretation of parameters The derived formula is used to investigate the dependence of the shape of ACF and CCF on the different parameters (sect. 12.2). The parameter μ describes the approximate position of the first side peak, and the strength of oscillation decreases with increasing σ . Both the height and width of the central peak depend on τ , and the width increases and the height decreases with increasing τ . In addition, differences between τ_i and τ_j provide the only source of asymmetry in the CCF between the processes X_i and X_j : If $\tau_i < \tau_j$, the peak decays faster on the left than on the right and reaches smaller counts in the respective side valley. Thus, it is possible to explain the central properties of a CCH and to relate them to the characteristics of the underlying processes on the basis of only a few parameters, which have a direct interpretation.

Data analysis (ch. 13) In order to find out whether the proposed doubly stochastic model can be used for the description and analysis of experimentally obtained data sets, theoretical ACFs are fitted to the experimentally derived ACHs. All ACHs can be fitted very closely with the theoretical functions, with global parameters μ and σ . With the parameters estimated from the fitted ACFs, the CCFs, which depend on the same sets of parameters, are predicted on the basis of the model and compared to the empirically derived CCHs. The CCFs between those units for which the parameters have been estimated with high precision can be predicted very precisely with the model assumption that all processes share the same packet onset process \mathbb{B} . In addition, parallel processes simulated with the model assumptions are highly comparable to experimentally derived spike trains, and the variability of data points in simulated CCHs agrees closely with the variability found in the experimental CCHs. These results sug-

gest that the doubly stochastic model can render a faithful description of essential characteristics of the observed point processes and CCHs.

Conclusion: Small additive phase offsets in the spike train model The proposed model allows one to relate the results from the Parts I and II to properties of the underlying spike trains (ch. 14). If a cosine function was fitted to the central peak of a CCH of two processes X_i and X_j that comply with the model assumptions, the resulting phase offset differs from zero if and only if $\tau_i \neq \tau_j$. In particular, the difference $\tau_j - \tau_i$ is directly related to the phase φ_{ij} : First, due to the asymmetric central peak, φ_{ij} is positive if and only if $\tau_i < \tau_j$, i.e., $\tau_j - \tau_i > 0$. Second, τ_i is the expected delay between a packet onset and a spike in process X_i and thus, the expected difference between a spike in X_i and a spike in X_j is related to the difference $\tau_i - \tau_j$. Assigning such a ‘preferred firing time’ τ_i to every process X_i yields a temporal map that is comparable to the linear configuration derived in Part II. With this heuristic interpretation, additivity of pairwise differences $\tau_j - \tau_i$ results canonically from the linear structure of the real line, \mathbb{R} .

With the given interpretation, small phase offsets between pairs of processes result from differences in the speed of decay of the firing intensity, which cannot be observed in small analysis windows but become visible only in the long run. Therefore, efficient coding mechanisms, which are assumed to work within a single oscillation cycle, are unlikely to use differences in the τ_i as central parameters in information processing. However, the structure of the model might be used more efficiently in the framework of large neuronal networks, in which a high number of parallel processes needs to be integrated.

Chapter 11

A spike train model

In this chapter, a model is presented with which spike trains with ‘repetitive, semiregular synchronous burst discharges’ (Singer and Gray, 1995) can be described, quantified and replicated. Similar to other characterizations by Smith and Smith (1965); Kaneoke and Vitek (1996) and Bair *et al.* (1994), the model in its basic form contains a characterization of two components: clusters of events (which are referred to as ‘packets’) and inter packet intervals (‘IPIs’). Mathematically, a doubly stochastic model is used to describe the two components. In the first step, a stationary packet onset process (‘POP’) is produced, and every packet onset gives rise to a Poissonian cluster with exponentially decaying firing intensity.

11.1 Assumptions

Packet onset process (‘POP’) When IPIs have a preferred length, packets reoccur in a regular, periodic manner. Therefore, the POP is assumed here to be a stationary point process with expected interarrival time μ . Here, this process is modeled as a random walk on the real line with independent and normally distributed increments with variance σ^2 . This assumption evokes pseudo-oscillatory activity with period μ and ‘semiregular’ IPIs. Finally, packet onsets are assumed to occur simultaneously across all units.

All assumptions are motivated by observations in experimental data. The position of the first side peak of a CCH is often interpreted as indicating a (dominant) oscillation frequency, which is modeled here by the preferred IPI length. Next, the variability of IPIs can be a plausible cause of the decrease in

the height of the side peaks. Finally, the center peak indicates that spikes tend to occur simultaneously across units. All model assumptions are investigated when applying the model to experimental data in chapter 13.

Packets In addition to the IPIs, it is necessary to describe the model assumptions concerning the spike packets. A packet can be characterized by the number of spikes, the time from the first to the last spike or the distribution of spikes in that interval (see e.g., Smith and Smith, 1965; Legendy and Salcman, 1985). Thus, to describe the firing activity in a packet, one parameter, $\alpha \geq 0$, is required for the number of spikes and one parameter, $\tau > 0$, for the length of the packet. To characterize the distribution of spikes in a packet only with these two parameters, an exponentially decaying function is chosen here, which causes the density of spikes in the beginning of the packet to be higher than in the end:

$$f(x) = \frac{\alpha}{\tau} e^{-\frac{x}{\tau}} \quad (\text{cf. Fig. 11.1}).$$

This assumption is in accordance with experimental findings that inter spike intervals increase during a packet (Eggermont *et al.*, 1993; Reinagel *et al.*, 1999), which was also found to be reflected in recurring spatio-temporal spiking patterns (see e.g., Abeles and Gerstein, 1988; Lestienne and Tuckwell, 1998). On different time scales, exponentially decaying functions have been used successfully to study the effect of excitatory post synaptic potentials on the firing rate of the subsequent neuron (Abeles, 1982a) or in single trial rate estimation (Nawrot *et al.*, 1999).

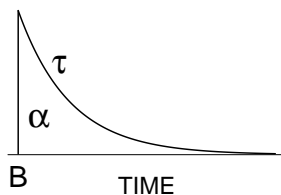


Figure 11.1: The firing intensity within a packet is assumed to decrease exponentially from the time B of the packet onset. The parameter α determines the expected number of spikes in each packet, and τ determines the speed of decay, or the ‘length’ of the packet.

11.2 The single spike train

Mathematically, a spike train is modeled as a cluster point process, or a doubly stochastic Poisson process (Cox process) in three steps as follows (Figure 11.2):

The first step produces the POP, which is modeled as a random walk \mathbb{B} on the real line with independent and normally distributed IPIs:

$$\mathbb{B} := (\dots, B_{-1}, B_0, B_1, \dots), \quad \text{with } B_{b+1} - B_b \sim \mathcal{N}(\mu, \sigma^2) \quad \forall b \in \mathbb{Z}.$$

One should note that the normal distribution of IPIs can only be a first approximation because negative IPIs do not occur in practice but have a positive probability in any normal distribution. However, the normal distribution has two important advantages. First, it allows straightforward computation of statistics related to the CCH, as is shown in chapter 12. Second, its mode μ allows for the production of pseudo-oscillatory activity with preferred IPI μ . Furthermore, negative IPIs are virtually ruled out if $\sigma \ll \mu$.

The second step Starting from the stationary point process \mathbb{B} , an exponentially decaying firing intensity f of the form

$$f_{B_b} = \begin{cases} \frac{\alpha}{\tau} e^{-\frac{(t-B_b)}{\tau}} & t \geq B_b \\ 0 & t < B_b \end{cases} \quad (\text{cf. Fig. 11.1})$$

is attached to each packet onset $B_b \in \mathbb{B}$. The overall firing intensity $\rho_{\mathbb{B}}$ is then defined as the sum of all f_{B_b} :

$$\rho_{\mathbb{B}} := \sum_{b \in \mathbb{Z}} f_{B_b} \quad (\text{cf. Fig. 11.2}).$$

In the third step, an inhomogeneous Poisson process with intensity $\rho_{\mathbb{B}}$ is constructed such that the expected number of spikes in every interval $[a, b]_{a < b}$ is given by

$$E_{a,b} := \int_a^b \rho_{\mathbb{B}} dt. \quad (11.1)$$

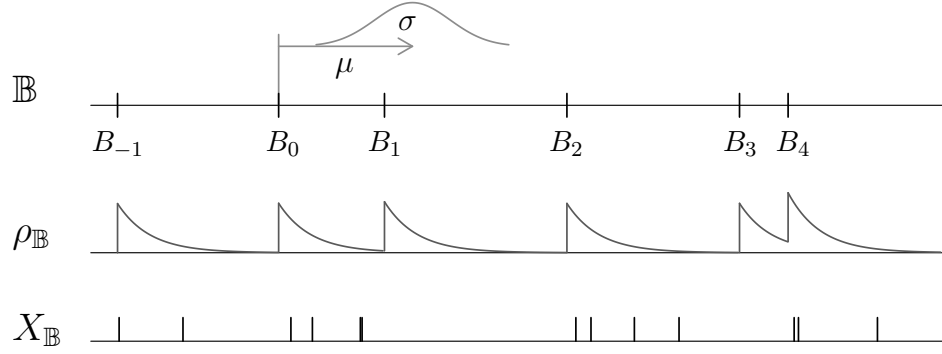


Figure 11.2: Doubly stochastic construction of a single spike train: A random walk produces a stationary point process, \mathbb{B} , on the real line. Every $B_b \in \mathbb{B}$ gives birth to a $\text{Poisson}(\alpha)$ -distributed number of children N_b whose times $(Y_j^{(b)})_{j=1, \dots, N_b}$ are $\text{Exp}(\tau)$ -distributed with respect to the packet start B_b .

The resulting process $X_{\mathbb{B}}$ has a random intensity measure $\rho_{\mathbb{B}}$, and for given \mathbb{B} , $X_{\mathbb{B}}$ is an inhomogeneous Poisson process. Thus, $X_{\mathbb{B}}$ is a Cox process (e.g., Stoyan *et al.*, 1987). It can be formalized as

$$X_{\mathbb{B}} = \sum_{b \in \mathbb{Z}} \sum_{j=1}^{N_b} \delta_{B_b + Y_j^{(b)}},$$

where all $Y_j^{(b)}$ are independent and $\text{Exp}(\tau)$ -distributed, and N_b is an independent random variable describing the number of spikes in packet b . N_b is $\text{Poisson}(\alpha)$ -distributed because α describes the expected number of spikes in each packet:

$$\frac{\alpha}{\tau} \int_0^{\infty} e^{-\frac{x}{\tau}} dx = \alpha.$$

The parameter τ determines the maximal intensity at packet onset and the speed of the decay. Both increase with decreasing τ :

$$f_0(0) = \frac{\alpha}{\tau} \quad \text{and} \quad f_0(\log(2) \cdot \tau) = \frac{1}{2} \cdot \frac{\alpha}{\tau} = \frac{1}{2} \cdot f_0(0).$$

Additionally, the parameter τ determines the center of mass of the exponential distribution, as

$$\int_0^{\infty} \frac{x}{\tau} e^{-\frac{x}{\tau}} dx \stackrel{y:=x/\tau}{=} \tau \int_0^{\infty} y e^{-y} dy = \tau.$$

Thus, a spike occurs in expectation τ time units after packet onset.

11.3 Parallel spike trains

To describe parallel spike trains, the model assumes that packet onsets occur simultaneously across all units. Thus, all spike trains are assumed to share the same POP. As a consequence, the parameters μ and σ are defined globally. In contrast, the parameters α and τ may differ across units and describe special firing characteristics of the different units.

In addition to the spikes in the packets, a constant background firing intensity $\beta \geq 0$ is introduced, which may also differ across units. The parameters of unit j ($j = 1, \dots, n$) are denoted by α_j , β_j and τ_j . Different levels of activation are described by the parameters α_j and β_j , and different decay constants τ_j account for more or less bursty firing.

Table 11.1 shows a summary of all introduced parameters. To make sure that the firing intensity of the preceding packet is low at the onset of the next packet, $\exp(-x/\tau)$ should be small for $x = \mu$. Thus, reasonable values of τ are smaller than $\mu/2$ because $\exp(-\mu/(\mu/2)) = \exp(-2) \approx 0.14$. Another constraint concerns the relation between the mean IPI μ and its standard deviation σ . Since negative IPIs cannot be observed, σ should be smaller than $\mu/2$.

Model part	parameter	range	meaning	defined
Periodicity	μ	$\in \mathbb{R}^+$	mean osc. period	global
	σ	$\in \mathbb{R}_0^+, \sigma < \frac{\mu}{2}$	std. dev. of IPIs	global
Packets	α_j	$\in \mathbb{R}_0^+$	spikes per packet	unit j
	τ_j	$\in \mathbb{R}^+, \tau < \frac{\mu}{2}$	'length' of packet	unit j
	β_j	$\in \mathbb{R}_0^+$	background intensity	unit j

Table 11.1: Summary of model parameters.

Model summary The firing intensity of unit j at time t is described by

$$\frac{\alpha_j}{\tau_j} \sum_{b=-\infty}^{n_t} e^{-\frac{(t-B_b)}{\tau_j}} + \beta_j, \quad (11.2)$$

where B_{n_t} denotes the last packet onset before t . Figure 11.3 illustrates the firing intensities of two units as described with the model. For packet onset times $\dots, B_1, B_2, B_3, \dots$, the firing intensity rises at packet onset according to equation (11.2) and decreases exponentially. Potential processes X_1, X_2 belonging to the plotted intensities are shown below the horizontal arrows.

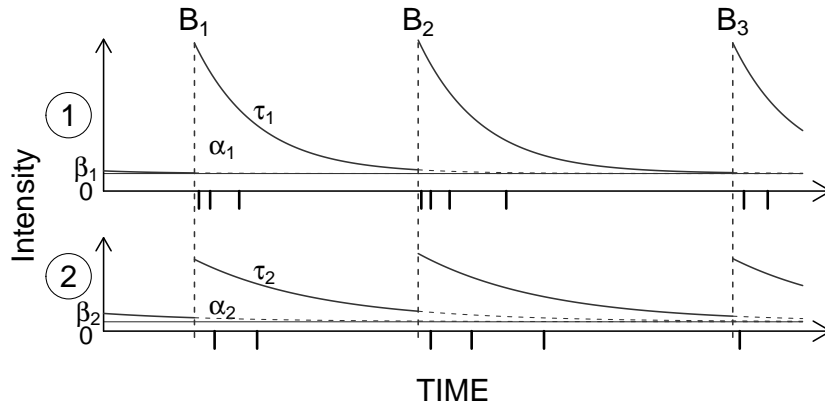


Figure 11.3: Summary of spike train model for two units. Packet onset times $\dots, B_1, B_2, B_3, \dots$ occur simultaneously across units and define the time of an instantaneous increase in firing intensity, followed by an exponential decay. Packet and background intensities may differ across units but are assumed to stay constant over time. Black vertical bars below horizontal arrows indicate potential spikes belonging to the intensity curves.

Chapter 12 shows how ACHs and CCHs of spike trains that comply with the assumptions presented in this chapter can be derived and how their shapes depend on the parameters.

Chapter 12

Auto and cross correlation

In this chapter, auto and cross correlation functions are discussed that result from processes that comply with the model assumptions in chapter 11. In section 12.1, formulas are derived that describe the expected shape of ACHs and CCHs as a function of the parameters μ , σ , α_j , β_j and τ_j . This shape is investigated in section 12.2, which yields an interpretation of the parameters with respect to several properties such as the height and width of the central peak, the decay in height of the side peaks or the cause of asymmetry.

Recapitulation: ACHs & CCHs Recall that for two spike trains $(S_1(j\delta))_j$ and $(S_2(j\delta))_j$ in discrete time with the same time resolution δ , the CCH at lag $\ell \in \mathfrak{L}_\delta^L = \{\ell : |\ell| \leq L, \ell/\delta \in \mathbb{Z}\}$ indicates the number of spikes in S_1 that are followed by a spike in S_2 with delay ℓ , i.e., after ℓ/δ bins (cf. eq. (1.1)):

$$CCH_{S_1 S_2}(\ell) := H_{S_1 S_2}(\ell) := \sum_j S_1(j\delta) S_2(j\delta + \ell).$$

Accordingly, the ACH counts the number of spike pairs in S_1 with delay ℓ :

$$ACH_{S_1}(\ell) := H_{S_1 S_1}(\ell) := \sum_j S_1(j\delta) S_1(j\delta + \ell).$$

These quantities are derived from two finite, binary processes S_1 and S_2 in discrete time. Therefore, they cannot be compared directly to statistics of cluster point processes of infinite length and in continuous time as have been described in chapter 11. For the latter, a concept analogous to the ACH is available.

12.1 ACF & CCF in the spike train model

For a single point process X that has a point at time t , consider the intensity of events on $\mathbb{R} \setminus \{t\}$. This distribution of points on $\mathbb{R} \setminus \{t\}$, given a point at time t , is the reduced Palm distribution, $P_0^!$ (Stoyan *et al.*, 1987).

For a stationary point process X , the intensity of spike pairs (x_t, x_{t+s}) with delay s is the product of the intensity λ of X and the Palm intensity of X . This intensity of spike pairs is closely related to the ACF and is therefore called here the *auto correlation function* (ACF) of the process X .

Analogous to the ACF, the *cross correlation function* of two processes X_1 and X_2 is the product of the intensity of X_1 and the intensity of points in X_2 , given a point in X_1 at time t . Theorem 2 provides formulas with which the ACF and the CCF can be computed for processes that comply with the model assumptions in chapter 11. Since the ACF is symmetric and the CCF between X_1 and X_2 is the mirror image of the CCF between X_2 and X_1 , the computations are restricted to nonnegative delays $s \geq 0$. In the following,

$$\Phi(x) := \int_{-\infty}^x \frac{1}{\sqrt{2\pi}} e^{-\frac{t^2}{2}} dt$$

denotes the standard normal distribution function,

$$\mu_i := i \cdot \mu \quad \text{and} \quad \sigma_i^2 := |i| \cdot \sigma^2.$$

Theorem 2 *Let X_1, X_2 be two Cox processes as specified in chapter 11: For a random walk \mathbb{B} with independent and $\mathcal{N}(\mu, \sigma^2)$ -distributed increments $B_{i+1} - B_i$ between the packet onsets, the firing intensity of X_j is described by*

$$\frac{\alpha_j}{\tau_j} \sum_{i=-\infty}^{n_t} e^{-\frac{(t-B_i)}{\tau_j}} + \beta_j \quad j = 1, 2.$$

Then, the ACF at shift $s \geq 0$ of X_j , $j = 1, 2$, is given by

$$\begin{aligned} F_{X_j X_j}(s) = & \frac{2\alpha_j \beta_j}{\mu} + \beta_j^2 + \frac{\alpha_j^2}{2\tau_j \mu} \left\{ e^{-\frac{s}{\tau_j}} + \sum_{i \in \mathbb{Z} \setminus \{0\}} e^{\frac{s - \mu_i}{\tau_j} + \frac{\sigma_i^2}{2\tau_j^2}} \Phi\left(\frac{\mu_i - s - \sigma_i^2/\tau_j}{\sigma_i}\right) \right. \\ & \left. + \sum_{i \in \mathbb{Z} \setminus \{0\}} e^{\frac{\mu_i - s}{\tau_j} + \frac{\sigma_i^2}{2\tau_j^2}} \Phi\left(\frac{s - \mu_i - \sigma_i^2/\tau_j}{\sigma_i}\right) \right\}. \end{aligned} \quad (12.1)$$

The CCF at shift $s \geq 0$ between X_1 and X_2 is

$$\begin{aligned}
 F_{X_1 X_2}(s) &= \frac{\alpha_1 \beta_2}{\mu} + \frac{\alpha_2 \beta_1}{\mu} + \beta_1 \beta_2 \\
 &+ \frac{\alpha_1 \alpha_2}{\mu(\tau_1 + \tau_2)} \left\{ e^{-\frac{s}{\tau_1}} + \sum_{j \in \mathbb{Z} \setminus \{0\}} e^{\frac{s - \mu_j}{\tau_1} + \frac{\sigma_j^2}{2\tau_1^2}} \Phi\left(\frac{\mu_j - s - \sigma_j^2/\tau_1}{\sigma_j}\right) \right. \\
 &\quad \left. + \sum_{j \in \mathbb{Z} \setminus \{0\}} e^{\frac{\mu_j - s}{\tau_2} + \frac{\sigma_j^2}{2\tau_2^2}} \Phi\left(\frac{s - \mu_j - \sigma_j^2/\tau_2}{\sigma_j}\right) \right\}.
 \end{aligned} \tag{12.2}$$

For $s < 0$, $F_{X_j X_j}(s) = F_{X_j X_j}(-s)$ and $F_{X_1 X_2}(s) = F_{X_2 X_1}(-s)$.

12.1.1 Proof of Theorem 2

Although equation (12.1) follows directly from (12.2), the ACF is derived first to explain the main computational steps. In the first step, β is set to zero.

12.1.1.1 Auto correlation function

The ACF of a process X with parameters α , $\beta = 0$, τ , μ and σ is derived by decomposition into the intensity and the reduced Palm distribution. The latter is computed in three steps:

1. Starting from a spike at time t , the packet onset B_0 of the corresponding packet is constructed by backward integration over

$$1/\tau \cdot e^{-\frac{t-b}{\tau}} db. \quad (\text{cf. Fig. 12.1, step 1})$$

2. For a given B_0 , the random walk \mathbb{B} is constructed forward and backward in time starting from B_0 such that the distribution of intervals between B_0 and all other packet onsets B_i is given by

$$(B_i - B_0) \sim \mathcal{N}(\mu_i, \sigma_i) \quad \forall i \in \mathbb{Z} \setminus \{0\} \quad (\text{cf. Fig. 12.1, step 2})$$

3. For the given stationary point process \mathbb{B} , spike times are constructed according to an inhomogeneous Poisson process with intensity

$$\rho_{\mathbb{B}} = \frac{\alpha}{\tau} \sum_{i \in \mathbb{Z}, i \leq n_t} e^{-\frac{(t-B_i)}{\tau}}. \quad (\text{cf. Fig. 12.1, step 3})$$

Thus, the underlying ‘family structure’ of the process (cf. Liemant *et al.*, 1988, sect. 1.9) is used in the computation, where spikes that originate in the same packet are referred to as ‘sister points’, while spikes that originate in different packets are called ‘cousin points’.

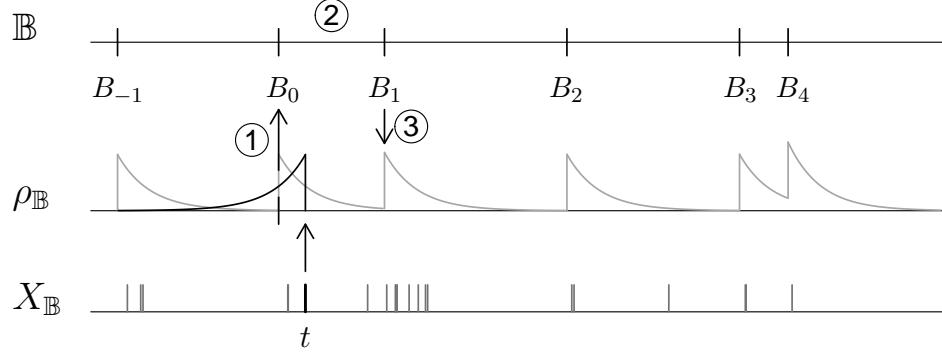


Figure 12.1: Derivation of the Palm distribution of a Cox process from chapter 11. Given a spike at time t , the respective packet onset B_0 is constructed backwards in time (1). Starting from B_0 , a random walk is performed in both directions (2). With the resulting stationary process \mathbb{B} , a Poisson process with firing intensity $\rho_{\mathbb{B}}$ is constructed (3).

In the following computations, $D_{0i}(s) := D_{B_0 B_i}(s)$ denotes the density of spikes in a packet with onset B_i that occur at $s + t$, given a spike in a packet with onset B_0 at time t . Obviously, step 2 is not necessary for the derivation of D_{00} , i.e., for the sister spikes that originate in the same packet as the spike at t . Thus, the computation can be split up into the density of sister points, D_{00} , and the density of cousin points that belong to different packets, $D_{(0i)_{i \neq 0}}$:

$$p_0^{\dagger}(s) = D_{00}(s) + \sum_{i \in \mathbb{Z} \setminus \{0\}} D_{0i}(s), \quad (12.3)$$

where p_0^{\dagger} is the density of the intensity measure of the Palm distribution P_0^{\dagger} . An analogous decomposition of the reduced Palm distribution by the use of the Palm distribution of the mother process can be found in Møller and Torrisi (2005).

Sister points According to the steps 1 and 3, the distribution of sister points is computed by construction of the packet onset, B_0 , followed by the creation of the Poisson process with intensity $\alpha/\tau \cdot \exp(-(t + s - B_0)/\tau)$:

$$D_{00}(s) = \int_{-\infty}^t \frac{1}{\tau} e^{-\frac{t-b}{\tau}} \cdot \frac{\alpha}{\tau} e^{-\frac{t+s-b}{\tau}} db = \frac{\alpha}{\tau^2} e^{-\frac{2t+s}{\tau}} \int_{-\infty}^t e^{-\frac{2b}{\tau}} db = \frac{\alpha}{2\tau} e^{-\frac{s}{\tau}}. \quad (12.4)$$

Cousin points - Fixed distance u To construct the distribution of cousin points in one packet with onset B_i , all three steps must be performed. The derivation can be simplified by first fixing $B_i := B_0 + u$, $u \in \mathbb{R}$, and by thus leaving out step 2 in the first place. The computation is then analogous to the one for the sister points, with the following modifications: Since the second packet does not start at B_0 but at $B_0 + u$, the delay s may also be smaller than u . Therefore, the latest possible time for the first packet B_0 is $t + s - u$ because otherwise, the spike at $t + s$ would occur before the packet at $B_0 + u$, which is impossible. Thus, it is necessary to distinguish between $s < u$ and $s \geq u$:

$$D_{0u}^{s < u}(s) = \int_{-\infty}^{t+s-u} \frac{1}{\tau} e^{-\frac{t-b}{\tau}} \cdot \frac{\alpha}{\tau} e^{-\frac{(t+s)-(b+u)}{\tau}} db = \frac{\alpha}{2\tau} e^{-\frac{u-s}{\tau}}. \quad (12.5)$$

$$D_{0u}^{s \geq u}(s) = \int_{-\infty}^t \frac{1}{\tau} e^{-\frac{t-b}{\tau}} \cdot \frac{\alpha}{\tau} e^{-\frac{(t+s)-(b+u)}{\tau}} db = \frac{\alpha}{2\tau} e^{-\frac{s-u}{\tau}}. \quad (12.6)$$

Cousin points - Random distance Finally, step 2 is incorporated by accounting for the fact that the distance U between B_0 and B_i is $\mathcal{N}(\mu_i, \sigma_i)$ -distributed. For $U > s$, the integration starts at s :

$$\begin{aligned} D_{0i}^{U > s}(s) &= \int_s^\infty \left(\int_{-\infty}^{t+s-u} \frac{1}{\tau} e^{-\frac{t-b}{\tau}} \cdot \frac{\alpha}{\tau} e^{-\frac{(t+s)-(b+u)}{\tau}} db \right) \cdot \frac{1}{\sqrt{2\pi}\sigma_i} e^{-\frac{(u-\mu_i)^2}{2\sigma_i^2}} du \\ &\stackrel{(12.5)}{=} \int_s^\infty \frac{\alpha}{2\tau} e^{-\frac{u-s}{\tau}} \frac{1}{\sqrt{2\pi}\sigma_i} e^{-\frac{(u-\mu_i)^2}{2\sigma_i^2}} du \\ &= \frac{\alpha}{2\tau} e^{\frac{s-\mu_i}{\tau} + \frac{\sigma_i^2}{2\tau^2}} \int_s^\infty \frac{1}{\sqrt{2\pi}\sigma_i} e^{-\frac{(u-(\mu_i - \frac{\sigma_i^2}{\tau}))^2}{2\sigma_i^2}} du. \end{aligned} \quad (12.7)$$

Substitution $y := \frac{1}{\sigma_i}(u + \sigma_i^2/\tau - \mu_i)$ yields

$$D_{0i}^{U > s}(s) = \frac{\alpha}{2\tau} e^{\frac{s-\mu_i}{\tau} + \frac{\sigma_i^2}{2\tau^2}} \int_{\frac{s-\mu_i + \sigma_i^2/\tau}{\sigma_i}}^\infty \frac{1}{\sqrt{2\pi}} e^{-\frac{y^2}{2}} dy = \frac{\alpha}{2\tau} e^{\frac{s-\mu_i}{\tau} + \frac{\sigma_i^2}{2\tau^2}} \Phi\left(\frac{\mu_i - s - \sigma_i^2/\tau}{\sigma_i}\right).$$

$U \leq s$ is computed analogously:

$$D_{0i}^{U \leq s}(s) = \frac{\alpha}{2\tau} e^{\frac{\mu_i - s}{\tau} + \frac{\sigma_i^2}{2\tau^2}} \Phi\left(\frac{s - \mu_i - \sigma_i^2/\tau}{\sigma_i}\right).$$

Therefore,

$$\begin{aligned} D_{0i}(s) &= D_{0i}^{U > s}(s) + D_{0i}^{U \leq s}(s) \\ &= \frac{\alpha}{2\tau} e^{\frac{\sigma_i^2}{2\tau^2}} \left\{ e^{\frac{s - \mu_i}{\tau}} \Phi\left(\frac{\mu_i - s - \sigma_i^2/\tau}{\sigma_i}\right) + e^{\frac{\mu_i - s}{\tau}} \Phi\left(\frac{s - \mu_i - \sigma_i^2/\tau}{\sigma_i}\right) \right\}. \end{aligned} \quad (12.8)$$

This yields the expressions for the terms in equation (12.3). Note in addition that the intensity of $X_{\mathbb{B}}$ is α/μ because the POP is a random walk without memory that can take any value $b \in \mathbb{R}$ since the normal distribution of increments is continuous and non-lattice as long as $\sigma^2 > 0$ (general renewal theorem, Feller, 1971, p. 381). Thus, with equation (12.3) and the consideration that the ACF is the product of the intensity α/μ and the reduced Palm intensity, this yields

$$F_{XX}(s) = \frac{\alpha}{\mu} \cdot \left(D_{00}(s) + \sum_{i \in \mathbb{Z} \setminus \{0\}} D_{0i}(s) \right), \quad (12.9)$$

which equals the result given in (12.1) for $\beta = 0$.

Background In the last step, background is added to the computation. Each of the two spikes in a pair with delay s may also belong to the background. Since the point process is an independent superposition of a stationary Poisson process with constant rate β and an inhomogeneous Poisson process with packet intensity α/μ , the intensity of spike pairs of which at least one spike originates in background is

$$\frac{2\alpha\beta}{\mu} + \beta^2 \quad \forall s \geq 0.$$

Thus, equation (12.1) results from

$$F_{XX}(s) = \frac{\alpha}{\mu} \cdot \left(D_{00}(s) + \sum_{i \in \mathbb{Z} \setminus \{0\}} D_{0j}(s) \right) + \frac{2\alpha\beta}{\mu} + \beta^2, \quad (12.10)$$

which yields the first part of Theorem 2. \square

12.1.1.2 Cross correlation function

To compute the CCF for two processes X_1 and X_2 , all computations are analogous because both processes are assumed to be based on the same packet onset process \mathbb{B} . Again, the computation is restricted to non-negative shifts s because the CCF of X_1 and X_2 is the mirror image of the CCF of X_2 and X_1 . Here, the term $D_{0i}(s) := D_{B_0 B_i}(s)$ denotes the density of spikes in X_2 in a packet with onset B_i at time $t + s$, given a spike in X_1 in a packet with onset B_0 at time t .

Sister points Analogous to equation (12.4), the distribution of sister points is given by

$$D_{00}(s) = \int_{-\infty}^t \frac{1}{\tau_1} e^{-\frac{t-b}{\tau_1}} \cdot \frac{\alpha_2}{\tau_2} e^{-\frac{t+s-b}{\tau_2}} db = \frac{\alpha_2}{\tau_1 \tau_2} e^{-\frac{t}{\tau_1} - \frac{t+s}{\tau_2}} \int_{-\infty}^t e^{\left(\frac{1}{\tau_1} + \frac{1}{\tau_2}\right) \cdot b} db = \frac{\alpha_2}{\tau_1 + \tau_2} e^{-\frac{s}{\tau_2}}.$$

Cousin points For the cousin points, the computation is analogous to the one given in (12.7):

$$\begin{aligned} D_{0i}^{U>s}(s) &= \int_s^\infty \left(\int_{-\infty}^{t+s-u} \frac{1}{\tau_1} e^{-\frac{t-b}{\tau_1}} \cdot \frac{\alpha_2}{\tau_2} e^{-\frac{(t+s)-(b+u)}{\tau_2}} db \right) \cdot \frac{1}{\sqrt{2\pi}\sigma_i} e^{-\frac{(u-\mu_i)^2}{2\sigma_i^2}} du \\ &= \frac{\alpha_2}{\tau_1 + \tau_2} \cdot \frac{1}{\sqrt{2\pi}\sigma_i} \int_s^\infty e^{-\frac{u-s}{\tau_1}} e^{-\frac{(u-\mu_i)^2}{2\sigma_i^2}} du \\ &= \frac{\alpha_2}{\tau_1 + \tau_2} e^{\frac{s-\mu_i}{\tau_1} + \frac{\sigma_i^2}{2\tau_1^2}} \Phi\left(\frac{\mu_i - s - \sigma_i/\tau_1}{\sigma_i}\right). \end{aligned} \quad (12.11)$$

The formula analogous to equation (12.8) thus reads for two processes

$$D_{0i}(s) = \frac{\alpha_2}{\tau_1 + \tau_2} \left\{ e^{\frac{s-\mu_i}{\tau_1} + \frac{\sigma_i^2}{2\tau_1^2}} \Phi\left(\frac{\mu_i - s - \sigma_i^2/\tau_1}{\sigma_i}\right) + e^{\frac{\mu_i-s}{\tau_2} + \frac{\sigma_i^2}{2\tau_2^2}} \Phi\left(\frac{s - \mu_i - \sigma_i^2/\tau_2}{\sigma_i}\right) \right\}.$$

Thus, the CCF can be computed as

$$F_{X_1 X_2}(s) = \frac{\alpha_1}{\mu} \cdot \left(D_{00}(s) + \sum_{i \in \mathbb{Z} \setminus \{0\}} D_{0i}(s) \right) + \frac{\alpha_1 \beta_2}{\mu} + \frac{\alpha_2 \beta_1}{\mu} + \beta_1 \beta_2, \quad (12.12)$$

where background activity has been included as in equation (12.10). This concludes the proof of Theorem 2. \square

12.1.1.3 Note: Distribution of IPIs

In Theorem 2, IPIs are assumed to be independent and normally distributed with expectation μ and variance σ^2 . Thus, also sums of intervals are normally distributed, and expectations and variances add up. Therefore, $\mu_i = i \cdot \mu$ and $\sigma_i^2 := |i| \cdot \sigma^2$ describe the relevant parameters for sums of IPIs, which are required in equations (12.1) and (12.2).

This model can be extended easily by changing the distribution of IPIs as long as IPIs remain normally distributed. For example, packets in different units might not start exactly at the global onset times but might vary around the global packet onset. In this case, one additional parameter, σ_D , is required, which defines the standard deviation with which individual packet onsets vary around the global onsets. Then, the packet onset times $(O_i^{(k)})_{i \in \mathbb{Z}}$ in unit k relative to the global onsets $(B_i)_{i \in \mathbb{Z}}$ are shifted by adding another independent and normally distributed random variable with variance σ_D^2 :

$$O_i^{(k)} = B_i + \sigma_D Z_i^{(k)}, \quad \text{with } Z_i^{(k)} \sim \mathcal{N}(0, 1) \text{ and } \{B_i, Z_i^{(k)}\}_{i \in \mathbb{Z}} \text{ independent.}$$

In this exemplary case, sums of IPIs are still normally distributed, with

$$\begin{aligned} \mu_i &= i \cdot \mu \quad \forall i \in \mathbb{Z} \quad \text{and} \quad \sigma_i^2 = |i| \cdot \sigma^2 + 2\sigma_D^2 \quad \text{for } i \in \mathbb{Z} \setminus \{0\}, \\ \sigma_0^2 &= 0 \quad \text{in equation (12.1)} \quad \text{and} \quad \sigma_0^2 = 2\sigma_D^2 \quad \text{in equation (12.2)}. \end{aligned}$$

Thus, model extensions that affect the mean and variance of sums of IPIs can be incorporated easily in the formulas presented in Theorem 2.

12.1.2 Practical remarks

Spike trains in discrete time Theorem 2 describes the density of spike pairs with distance $s \in \mathbb{R}$ for Cox processes that comply with the spike train model from chapter 11. In practice, spike trains can only be recorded in discrete time with time resolution δ . As a consequence, the analysis is restricted to spike pairs separated by ℓ bins, with $\ell \in \mathbb{Z}$. Conditioning on the event to observe a spike at time t , the expected number of spikes in the interval $[t + s, t + s + \delta)$ is given by

$$\int_s^{s+\delta} F(x) dx,$$

which is approximated here by the box area $\delta \cdot F(s)$. Thus, the ACFs and CCFs of spike trains in discrete time with time resolution δ are approximated by multiplying the formulas given in Theorem 2 with the bin size δ .

Nonstationary firing rates In Theorem 2, it is assumed that both the background rate and the firing intensity of packets remain constant throughout the process. In practice, however, firing rates can vary in time, and it is therefore investigated how the ACF and the CCF are affected by changes in the firing rate.

For technical reasons, it is assumed here that firing rates change according to a step function, which stays constant except for m_T equidistant jumps. Thus, let $0 = J_0 < J_1 < \dots < J_{m_T-1} < J_{m_T} = T$ denote the jump times at which either the background rate or the packet intensity change, and let α_{kj} and β_{kj} denote the packet and the background intensity of unit j , $j = 1, 2$, in the interval (J_k, J_{k-1}) , where $J_k - J_{k-1} \equiv c \forall k$. If spike pairs that cross jumps are neglected, the ACF of unit j can be approximated by the mean of the ACFs in the periods (J_k, J_{k-1}) of constant rate:

$$m_T^{-1} \left(\frac{\sum_k \alpha_{kj}^2}{\mu} \cdot \left(D_{00}(s) + \sum_{i \in \mathbb{Z} \setminus \{0\}} D_{0i}(s) \right) + \frac{2 \sum_k \alpha_{kj} \beta_{kj}}{\mu} + \sum_k \beta_{kj}^2 \right).$$

The corresponding CCF is given by

$$m_T^{-1} \left(\frac{\sum_k \alpha_{k1} \alpha_{k2}}{\mu} \left(D_{00}(s) + \sum_{i \in \mathbb{Z} \setminus \{0\}} D_{0i}(s) \right) + \frac{\sum_k \alpha_{k1} \beta_{k2} + \alpha_{k2} \beta_{k1}}{\mu} + \sum_k \beta_{k1} \beta_{k2} \right).$$

As a consequence, the relation between the height of the ACF and the height of the CCF is affected. Consider for example the case $\beta_{kj} = 0 \forall k, j$. When predicting the CCF with the parameters estimated from the ACF and the assumption of constant rate, the true term $\sum_{k=1}^{m_T} \alpha_{k1} \alpha_{k2}$ would be estimated erroneously as $(\sum_{k=1}^{m_T} \alpha_{k1}^2 \sum_{k=1}^{m_T} \alpha_{k2}^2)^{1/2}$. Due to the Cauchy-Schwarz inequality,

$$\sum_{k=1}^{m_T} \alpha_{k1} \alpha_{k2} \leq \left(\sum_{k=1}^{m_T} \alpha_{k1}^2 \sum_{k=1}^{m_T} \alpha_{k2}^2 \right)^{1/2},$$

and the CCF is reduced in height unless the covariance of the rates equals 1.

12.2 Shape of ACF and CCF

After the presentation of the formulas which describe the ACF and CCF of point processes that comply with the model assumptions presented in chapter 11, this section deals with the shape of these functions and its dependence on the parameters. Since the ACF is a special case of a CCF for $\alpha_1 = \alpha_2$, $\tau_1 = \tau_2$ and $\beta_1 = \beta_2$, only the shape of CCFs is discussed here. Furthermore, the background intensities β_1 and β_2 only increase the height of the CCF by an additive constant. Therefore, the background is set to zero in this section, the investigation focussing on that part of the CCF which consists of spike pairs originating exclusively in the packet process.

12.2.1 Decomposition of a CCF

Recall that with $\beta_1 = \beta_2 = 0$, equation (12.2) states that the CCF of X_1 and X_2 at shift $s \geq 0$ is described by

$$F_{X_1 X_2}(s) = \frac{\alpha_1}{\mu} \cdot \left(D_{00}(s) + \sum_{i \in \mathbb{Z} \setminus \{0\}} D_{0i}(s) \right),$$

$$\text{where } D_{00}(s) = \frac{\alpha_2}{\tau_1 + \tau_2} e^{-\frac{s}{\tau_2}}$$

$$\text{and } D_{0i}(s) = \frac{\alpha_2}{\tau_1 + \tau_2} \left\{ e^{\frac{s - \mu_i}{\tau_1} + \frac{\sigma_i^2}{2\tau_1^2}} \Phi \left(\frac{\mu_i - s - \sigma_i^2/\tau_1}{\sigma_i} \right) + e^{\frac{\mu_i - s}{\tau_2} + \frac{\sigma_i^2}{2\tau_2^2}} \Phi \left(\frac{s - \mu_i - \sigma_i^2/\tau_2}{\sigma_i} \right) \right\}.$$

In this decomposition, D_{00} describes the spike pairs which originate in packets that start at the same time. D_{0i} describes the spike pairs whose second spike belongs to the i^{th} -next packet after the packet of the first spike.

Figure 12.2 A illustrates this decomposition for one set of parameters. To get results that are comparable to experimentally obtained CCHs, μ is set to 25 ms, which corresponds to an oscillation frequency of 40 Hz. The parameters τ and σ are adjusted in relation to μ . In Figure 12.2, $\tau_1 = \tau_2 = 0.2\mu$, i.e., the packets are relatively short compared to the mean IPI, and $\sigma = 0.24\mu = 6$ ms. The parameters $\alpha_1 = \alpha_2 = 2$ affect the shape of the CCF only by multiplication with a scalar.

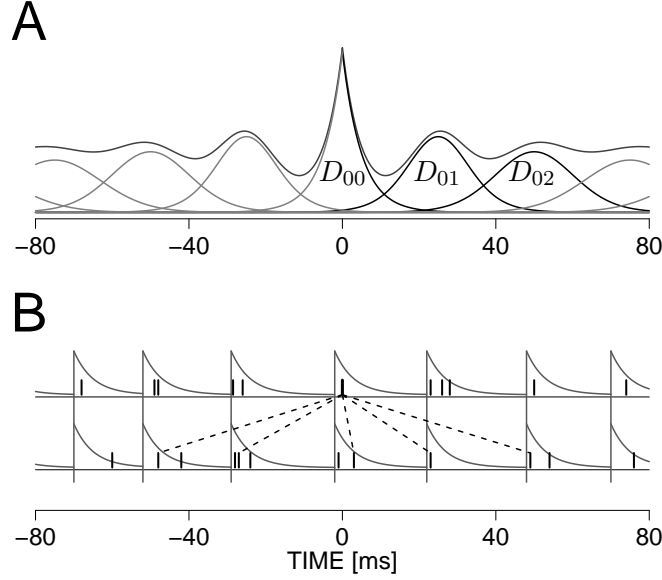


Figure 12.2: Decomposition of a CCF with parameters $\alpha_1 = \alpha_2 = 2$, $\tau_1 = \tau_2 = 5$ ms, $\beta_1 = \beta_2 = 0$, $\mu = 25$ ms, $\sigma = 6$ ms. A: Graph of the CCF (medium gray), single summands D_{00} , D_{01} and D_{02} (black), and other summands (light gray). B: Illustration of the computation of a CCH. Each summand in panel A counts the delays from the reference spike in the reference packet to spikes in one specific packet.

Maxima of summands The graphs of D_{00} , D_{01} and D_{02} are plotted in black in Figure 12.2 A. Given a spike at $t = 0$, the density of spikes that originate in the same packet, D_{00} , is maximal at $s = 0$ and decreases fast with s . This holds for the ACF as well as for the CCF because the packet onset process $\mathbb{B} = (\dots, B_{-1}, B_0, B_1, \dots)$ is assumed to be the same for all units.

The density of spike pairs which originate in successive packets, D_{01} , is maximal at $s = \mu$. In fact, the maximum of D_{0i} is $\mu_i = i\mu$ for all $i \in \mathbb{Z}$ if $\tau_1 = \tau_2$:

$$\frac{\partial D_{0i}(s)}{\partial s} = \frac{\alpha_1 \alpha_2}{\tau_1 + \tau_2} \left\{ e^{\frac{s-\mu_i}{\tau_1} + \frac{\sigma_i^2}{2\tau_1^2}} \Phi\left(\frac{\mu_i - s - \sigma_i^2/\tau_1}{\sigma_i}\right) \frac{1}{\tau_1} - e^{\frac{\mu_i - s}{\tau_2} + \frac{\sigma_i^2}{2\tau_2^2}} \Phi\left(\frac{s - \mu_i - \sigma_i^2/\tau_2}{\sigma_i}\right) \frac{1}{\tau_2} \right\}$$

Thus, for $\tau_1 = \tau_2 = \tau$, the partial derivative equals zero for $s = \mu_i$:

$$\frac{\partial D_{0i}(s)}{\partial s} = \frac{\alpha_1 \alpha_2}{2\tau^2} e^{\frac{\sigma_i^2}{2\tau^2}} \left\{ e^{\frac{s-\mu_i}{\tau}} \Phi\left(\frac{-\sigma_i}{\tau}\right) - e^{\frac{\mu_i - s}{\tau}} \Phi\left(\frac{-\sigma_i}{\tau}\right) \right\} \stackrel{s=\mu_i}{=} 0.$$

The maximum of D_{01} at $s = \mu$ is lower than the maximum of D_{00} at $s = 0$, and the distribution is broader. The reason for this effect is the parameter σ , the

variance of IPIs. Therefore, in contrast to D_{00} , in which the packet onsets of the corresponding spikes are simultaneous, the IPIs between successive packets have variance σ^2 . The maximum of D_{02} is even lower because the variance of the sum of two independent IPIs is $2\sigma^2$, i.e., twice the variance of one IPI.

Symmetry properties of summands On the left side of Figure 12.2 A, the graphs of D_{00} , D_{01} and D_{02} are plotted for $s < 0$, i.e., for the reverse CCF. Since the parameters α , β and τ do not differ between the units in this example, the curves are symmetric with respect to $s = 0$. Moreover, due to the symmetry in equation (12.2), the term $(D_{0i})^{X_1 X_2}(s)$ from the CCF between X_1 and X_2 equals $(D_{0(-i)})^{X_2 X_1}(-s)$ from the CCF between X_2 and X_1 :

$$\begin{aligned}
& (D_{0i})^{X_1 X_2}(s) \cdot \frac{\tau_1 + \tau_2}{\alpha_1 \alpha_2} = \\
& = e^{\frac{s-i\mu}{\tau_1} + \frac{|i|\sigma^2}{2\tau_1^2}} \Phi\left(\frac{i\mu - s - |i|\sigma^2/\tau_1}{\sqrt{|i|\sigma}}\right) + e^{\frac{i\mu-s}{\tau_2} + \frac{|i|\sigma^2}{2\tau_2^2}} \Phi\left(\frac{s - i\mu - |i|\sigma^2/\tau_2}{\sqrt{|i|\sigma}}\right) \\
& = e^{\frac{-s+i\mu}{\tau_2} + \frac{|i|\sigma^2}{2\tau_2^2}} \Phi\left(\frac{-i\mu + s - |i|\sigma^2/\tau_2}{\sqrt{|i|\sigma}}\right) + e^{\frac{-i\mu+s}{\tau_1} + \frac{|i|\sigma^2}{2\tau_1^2}} \Phi\left(\frac{-s + i\mu - |i|\sigma^2/\tau_1}{\sqrt{|i|\sigma}}\right) \\
& = (D_{0(-i)})^{X_2 X_1}(-s) \cdot \frac{\tau_1 + \tau_2}{\alpha_1 \alpha_2}.
\end{aligned}$$

Thus, every curve $D_{0i}(s)$ is continued also for $s < 0$, where it reflects the term $D_{0(-i)}(|s|)$ for the reversed CCF.

Figure 12.2 B illustrates how the delays between a spike in one spike train (located at shift $s = 0$) and the spikes in the other spike train are counted in the CCF. Delays to spikes in the same packet are likely to be counted in the central peak, whereas delays to spikes in succeeding and preceding packets are reflected in the side peaks on the right and on the left.

The whole CCF is summed over all D_{0i} , $i \in \mathbb{Z}$ and plotted in gray in Figure 12.2 A above the decomposed summands. In addition to the properties mentioned above, one should note that the maximum of the first side peak occurs at a slightly bigger shift than at $s = \mu$ because D_{02} is broader than D_{00} and thus contributes more density around $s = \mu$. Furthermore, the CCF approaches a limit value for growing s . This limit value is also called ‘baseline’-level and can

be computed as the product of the firing intensities of the two involved units:

$$\text{baseline: } \left(\frac{\alpha_1}{\mu} + \beta_1 \right) \left(\frac{\alpha_2}{\mu} + \beta_2 \right) = \frac{\alpha_1 \alpha_2}{\mu^2} + \frac{\alpha_1 \beta_2}{\mu} + \frac{\alpha_2 \beta_1}{\mu} + \beta_1 \beta_2. \quad (12.13)$$

The shape of the CCF is similar to the experimentally derived CCHs (e.g., Fig. 10.1). Before the model is compared to experimental data, the dependence of the CCF shape on the parameters is investigated in more detail.

12.2.2 Interpretation of parameters

12.2.2.1 ‘Strength of oscillation’

To illustrate the dependence of the CCF shape on the parameter σ , Figure 12.3 shows three decomposed CCFs which differ only in the parameter σ (all other parameters as in Fig. 12.2). In panel A, $\sigma = 0$, i.e., the spike train is fully periodic, and the length of all IPIs equals μ . In this case, D_{0B_i} has the same shape as D_{00} and is only shifted by $i\mu$ for all $i \in \mathbb{Z}$. Therefore, the peak height of the side peaks does not decrease with increasing s , and spike delays at $s = i\mu$ are just as likely for all $i \in \mathbb{Z}$ as they are for $s = 0$. Thus, the CCF is fully periodic with period μ .

If the variability σ of IPIs increases (panel B, $\sigma = 0.25\mu$), the length of IPIs varies and thus, the graphs of D_{0j} decrease in height, the maxima getting smaller with increasing number of IPIs. Again, the maxima of D_{0i} ($i > 0$) are located at $i\mu$, but the maxima of the side peaks of the CCF occur at slightly bigger shifts because the D_{0i} on the right contribute more density than the summands on the left. This effect is even more pronounced in panel C, where the curves of D_{02} and $D_{0(-2)}$ are so broad that the second side valleys nearly disappear. One can also see that the speed with which the CCF approaches the baseline level increases with σ because adjacent summands D_{0i} overlap to a higher extent.

The broadness of the side summands also causes the central peak to increase in height because, if σ is big enough, not only the term D_{00} is relevant for small s . This effect is, however, relatively small even for a big value of $\sigma = 0.5\mu$.

In conclusion, the parameter σ mainly determines the speed of decay of the side peaks and valleys towards the baseline level. This speed of decay, i.e., the number of visible side peaks, has also been called the ‘strength of oscillation’ (Gray *et al.*, 1989; Karmon and Bergman, 1993; König, 1994; Nowak *et al.*, 1995). For $\sigma = 0$, no decay occurs, while for $\sigma = 0.5\mu$, the decay is so fast that only one side valley and half a side peak can be observed.

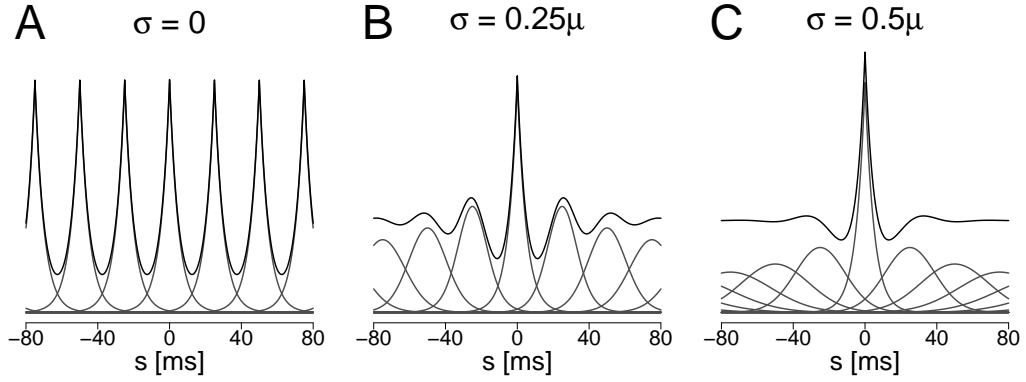


Figure 12.3: Dependence of the CCF shape on σ . Decomposed CCFs for the parameters $\alpha_1 = \alpha_2 = 2$, $\tau_1 = \tau_2 = 5$ ms, $\beta_1 = \beta_2 = 0$, $\mu = 25$ ms, and (A) $\sigma = 0$ ms, (B) $\sigma = 10$ ms, (C) $\sigma = 20$ ms. y-axis limits identical for all panels.

12.2.2.2 Central peak

The dependence of the CCF shape on the parameter $\tau = \tau_1 = \tau_2$ is illustrated in Figure 12.4, which shows the decomposed CCFs for the values $\tau \in \{2.5, 6.25, 12.5\}$ ms ($\sigma = 7.5$ ms, other parameters as in Figure 12.3). The most pronounced effect of τ concerns the height of the central peak. Obviously, the peak increases with decreasing τ/μ . This can be explained formally. As a first approximation, consider the height of the central term, D_{00} , at $s = 0$, which approximates the value of the CCF at $s = 0$ unless τ or σ are too close to 0.5μ :

$$\frac{\alpha_1}{\mu} D_{00}(0) = \frac{\alpha_1 \alpha_2}{\mu(\tau_1 + \tau_2)} \stackrel{\substack{\alpha_1 = \alpha_2 \\ \tau_1 = \tau_2}}{=} \frac{\alpha^2}{2\mu\tau}$$

Obviously, this value decreases with increasing τ , but also with decreasing α . More important in this context is the height of the peak relative to the baseline level. According to equation (12.13), this index can be approximated in the model by

$$\frac{\alpha_1 \alpha_2 / \mu(\tau_1 + \tau_2)}{\alpha_1 \alpha_2 / \mu^2} = \frac{\mu}{\tau_1 + \tau_2} \stackrel{\tau_1 = \tau_2}{=} \frac{\mu}{2\tau}, \quad (12.14)$$

if the central peak is approximated by D_{00} .

The peak width is also increased with τ . This can be quantified with the shift $s_{1/2}$ at which the term D_{00} reaches half height:

$$e^{-\frac{s_{1/2}}{\tau}} = 1/2 \quad \iff \quad s_{1/2} = \tau \log 2.$$

Thus, the smaller τ , the smaller $s_{1/2}$, and the earlier the peak reaches half height. The slope is thereby simply characterized by the function $e^{-s/\tau}$. Similarly, a decrease in τ increases the height of the side peaks and the depth of the side valleys relative to baseline.

Thus, a decrease of the parameter τ has two main effects on the central peak. It increases its height and decreases its width because the spikes of the packets are concentrated more densely at the packet onsets. This can be interpreted as a higher degree of synchronous firing. One should note, however, that the only coordination across units is caused by the global POP and that precise spike timing is not assumed to be additionally synchronized.

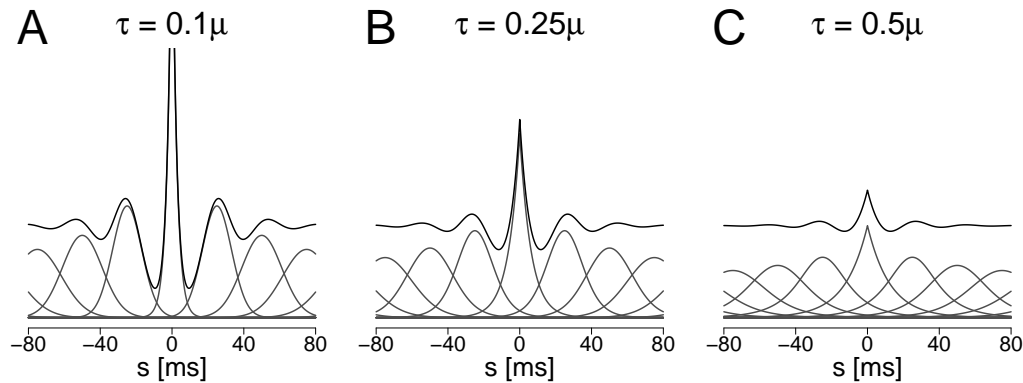


Figure 12.4: Dependence of the CCF shape on τ . Decomposed CCFs for the parameters $\alpha_1 = \alpha_2 = 2$, $\beta_1 = \beta_2 = 0$, $\mu = 25$ ms, $\sigma = 7.5$ ms = 0.3μ , and $\tau_1 = \tau_2 = 0.1\mu = 2.5$ ms (A), $\tau_1 = \tau_2 = 0.25\mu = 6.25$ ms (B), $\tau_1 = \tau_2 = 0.5\mu = 12.5$ ms (C). Y-axis limits are identical for all panels.

12.2.2.3 Asymmetry

As explained above, the CCF for two units with the same parameters $\tau_1 = \tau_2$, $\alpha_1 = \alpha_2$ and $\beta_1 = \beta_2$ is symmetric. Furthermore, equation (12.2) shows that the parameters $\alpha_1, \alpha_2, \beta_1$ and β_2 cannot affect the symmetry because the formula remains unchanged by exchanging α_1 and α_2 as well as β_1 and β_2 . Thus, only differences in the parameters τ_1 and τ_2 can affect the symmetry of a CCF in the present model.

Figure 12.5 A shows a CCF for the parameters $\tau_1 = 3$ ms and $\tau_2 = 7.5$ ms (all other parameters as in Figure 12.4). One can see that the difference in the parameters τ_1 and τ_2 has several consequences concerning the asymmetric shape

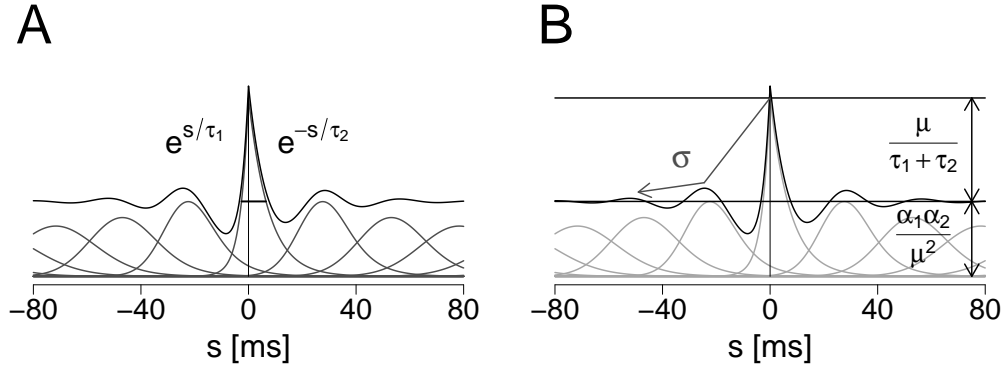


Figure 12.5: Asymmetric shape of CCFs. Decomposed CCF for the parameters $\alpha_1 = \alpha_2 = 2$, $\beta_1 = \beta_2 = 0$, $\mu = 25$ ms, $\sigma = 7.5$ ms, $\tau_1 = 3$ ms, and $\tau_2 = 7.5$ ms. A: Function for left and right side of central peak indicated by formulas, width of peak at baseline indicated in black. B: Baseline and peak height relative to baseline indicated by vertical arrows and formulas on the right. Decrease in height of side peaks indicated by left arrow.

of the CCF. First, the slope of the central peak differs on the right and on the left hand side. On the side with the smaller τ , the peak is steeper, the side valley is deeper, and the width of the peak is smaller. Taking again the term D_{00} as an approximation of the central peak, the asymmetry concerning width and slope of the peak can be explained with the following computation (cf. Fig. 12.5 A):

$$\text{For } s \geq 0, \text{ the central term is described by } \frac{\alpha_1\alpha_2}{\tau_1 + \tau_2} \cdot e^{-\frac{|s|}{\tau_2}},$$

$$\text{while for } s < 0, \text{ the respective term is } \frac{\alpha_1\alpha_2}{\tau_1 + \tau_2} \cdot e^{-\frac{|s|}{\tau_1}}.$$

Thus, the right and the left side of the central peak differ only in the exponent. As a consequence, the speed of decay is faster and the width is smaller on the side with the smaller τ . In fact, the ratio between the width s_1 on the left and the width s_2 on the right equals τ_1/τ_2 for any height if only the term D_{00} is taken into account:

$$\text{Let } s_1 \text{ and } s_2 \text{ be such that } e^{-\frac{s_1}{\tau_1}} = e^{-\frac{s_2}{\tau_2}}. \quad \text{This implies } \frac{s_1}{s_2} = \frac{\tau_1}{\tau_2}.$$

The horizontal line in the peak area of Figure 12.5 A indicates this quotient.

The summands D_{0i} with $i \neq 0$ have a similar shape as D_{00} , i.e., their slopes on the left and on the right hand side show the same asymmetry as D_{00} . As described

earlier, they are broadened by the variability σ^2 of IPIs. As a consequence of the combination of the normal distribution with the asymmetric shape, the maximum of D_{0i} is not necessarily at $i\mu$ but can be shifted to the right or left, depending on the parameters σ , μ , τ_1 and τ_2 .

Three quantities that remain largely unaffected by the asymmetry are the height of the central peak, the decay of the side peaks and the baseline level (indicated in Fig. 12.5 B). The peak height relative to baseline is described by $\mu/(\tau_1 + \tau_2)$ (equation (12.14)), and the baseline level is $\alpha_1\alpha_2/\mu^2$.

12.3 Summary

In this chapter, formulas for the ACF and CCF of processes that conform with the model from chapter 11 were derived, and the shape of ACFs and CCFs was discussed with respect to the relevant parameters. Section 12.2 shows that variations in very few parameters can account for a high variability in the shape of these functions. For example, the parameter τ influences both the height and width of the central peak as well as the slope of its flanks. As a consequence, differences between τ_1 and τ_2 produce all aspects of asymmetry discussed in chapter 10: different slopes, different depths of the side valleys as well as different widths with respect to zero delay. Furthermore, the parameter σ determines the speed of decay of the side peaks towards baseline level, and μ corresponds roughly to the position of the first side peak and thus to the dominant oscillation period. As a further advantage, the model allows the approximation of important quantities by simple formulas, including the baseline level or the peak height relative to baseline.

After the presentation of the model on a theoretical basis, the following chapter deals with practical issues. In order to investigate whether the model can be useful for the description of experimental data, the parameters are estimated on the basis of ACHs of the sample data set, and theoretically predicted properties are compared to experimentally obtained quantities. In this respect, it is particularly interesting that a single parameter can determine multiple aspects of the CCF simultaneously. Thus, a good agreement between the theoretical model and experimental data can be obtained only if the variability of shapes that can be treated theoretically corresponds to the shapes observed in experimental data.

Chapter 13

Practical usefulness

In order to investigate whether the model presented in chapter 11 and the corresponding formulas for the theoretical ACFs and CCFs from chapter 12 can be useful in the analysis of experimental data, the model is applied to the sample data set. In the first place, section 13.1 investigates whether independence and normal distribution of IPIs and exponentially decaying firing intensity are plausible candidates for the description of the spike trains in the sample data set. In section 13.2, the parameters α , τ , β , μ and σ are estimated for all units by simultaneously fitting theoretical ACFs to the empirically derived ACHs. The goodness of fit of these ACFs can indicate the degree to which the theoretical model can describe the experimentally observed variability of ACH shapes. As a next step, section 13.3 deals with the relation between the fitted ACHs and the CCHs computed across pairs of units. Since the model assumes that packets occur simultaneously across units, predictions can be derived about the shape of the CCHs, and the suitability of such predictions can be investigated by a comparison to experimentally obtained CCHs. Both agreement and disagreement of the predictions with the empirical CCHs can lead to important insights into interactions between different units. Finally, it is important whether, in addition to describing only the shapes of ACHs and CCHs, the model can also be used to simulate data that are comparable to experimental recordings. Section 13.4 therefore deals with a comparison of raw spike trains obtained from simulations and from experimental recordings. In addition, it is investigated whether the variability of counts in a CCH can be replicated by artificial spike trains that comply with the model assumptions.

13.1 Investigation of model assumptions

Concerning the appropriateness of the model assumptions, three main aspects have to be considered. First, IPIs are assumed to be independent and normally distributed. Although, as described in section 11.1, the normal distribution is motivated by the experimental observation that packets reoccur with a preferred interval, the mechanism of ‘pseudo-oscillation’ introduced by independent and normally distributed IPIs may differ from ‘real’ oscillatory activity. For example, independence of IPIs is not necessarily granted in oscillatory activity. On the one hand, successive IPIs might be positively correlated due to an increase or decrease in the oscillation frequency in time. On the other hand, IPIs might also be negatively correlated because a shift in one cycle increases the preceding while decreasing the succeeding IPI, or vice versa. Therefore, independence and normal distribution of IPIs is investigated in section 13.1.1. Second, the spike intensity within packets is assumed to decay exponentially with respect to packet onset. This assumption is motivated by the observation that inter spike intervals increase during packets, and it makes use of a suitable decaying function that can be described with two parameters. However, firing intensities do not have to decay exponentially. Therefore, this assumption is investigated in section 13.1.2. Finally, since the relation between ACFs and CCFs may deviate from the theoretical prediction if the firing rates of the units vary in time (cf. sect. 12.1.2), the variability of firing rates across time is studied in section 13.1.3.

13.1.1 Distribution and independence of IPIs

The distribution of IPIs is investigated by estimating packet onset times with the algorithm illustrated in Figure 13.1. For each time step, spikes are summed across all units, and the resulting time series is smoothed several times with a Gaussian kernel (curve plotted below dot display in Figure 13.1). The smoothed curve is used to define maxima as points after an increase of at least 3 ms and before a decrease of at least 3 ms duration. With this restriction, tiny peaks could be ignored in the sample data set, while the fraction of undetected packet onsets remained relatively small¹. To determine the packet onset as precisely as possible, these maxima are not used directly as onset times because they are less well defined than points with higher slope. Therefore, the time when

¹Since the erroneous identification of a non-existing packet falsely produces two small IPIs, while a packet that is not detected produces only one big IPI, the algorithm primarily decreases the number of falsely detected packet onsets.

the function reaches 60% of the maximum within a window of 10 ms before the identified maximum is defined as packet onset (vertical lines in Fig. 13.1). Although packet onsets are detected too early with this method, IPIs can be estimated more precisely than only on the basis of the maxima.

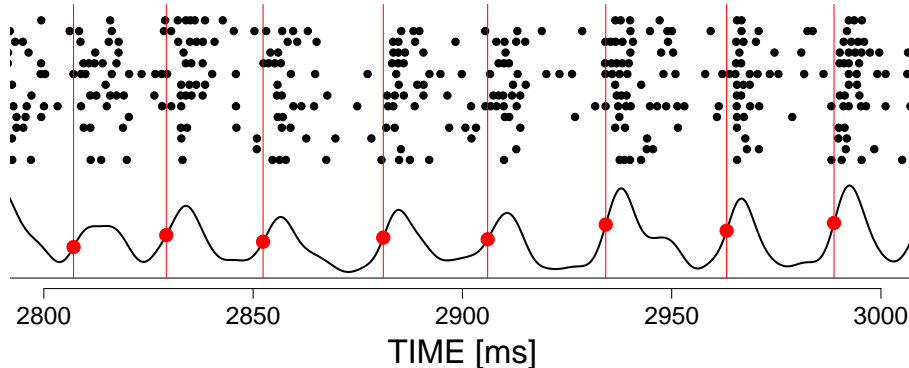


Figure 13.1: Estimation algorithm for IPIs. Spikes of different units are shown as dots in different lines. Spikes are cumulated across all units, and the resulting function is smoothed several times with a Gaussian kernel (smoothed function plotted below). ‘Maxima’ are defined as points between at least 3 ms increase and 3 ms decrease, and packet onset times are determined as the points at which 60% of the maximum is reached within a window of 10 ms before the maximum (packet onset times indicated by vertical lines).

The distribution of IPIs derived with this method is plotted in Figure 13.2 A for stimulation condition 1. One can see that the empirical distribution is far enough from zero, such that the theoretical fraction of negative IPIs can be neglected. Moreover, some packets are not detected by the algorithm, mostly because the criterion of at least 3 ms increase before and 3 ms decrease after the maximum is too strict. Therefore, an unexpectedly high number of large intervals (i.e., larger than 50 ms) are counted. If these are ignored, the mean IPI is $\hat{\mu} = 24.8$ ms, and the standard deviation is $\hat{\sigma} = 8.1$ ms. The density of the corresponding normal distribution is added to the plot and agrees relatively well with the empirical histogram. Finally, the correlation between successive IPIs is $r = 0.03$, which is in accordance with the assumption that successive IPIs are independent.

13.1.2 Distribution of spikes within packets

In order to investigate whether the assumption that the firing intensity decays exponentially from the time of the packet onset can be considered plausible, the

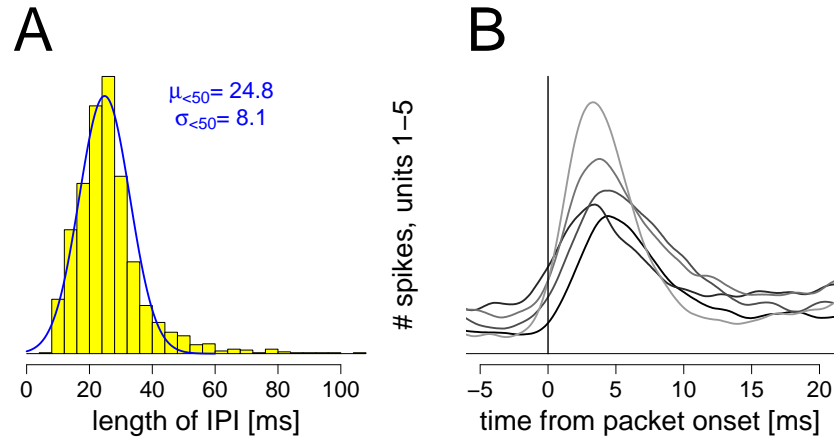


Figure 13.2: Distributions of IPIs and of spikes in packets in stimulation condition 1. A: Distribution of IPIs determined with the algorithm described in Figure 13.1. Normal distribution curve with $\mu = 24.8$ ms and $\sigma = 8.1$ ms added to the histogram. B: Smoothed distribution of spikes of units 1-5 relative to the packet onsets determined with the algorithm in Figure 13.1. Units 1-5 are colored from black to light gray.

spikes in each unit are counted relative to the packet onset times estimated in section 13.1.1. The resulting smoothed spike distributions are shown in Figure 13.2 B for the units 1-5. The curves correspond reasonably well to the assumed exponentially decaying firing intensity. As described above, the identified packet onsets are earlier than the onset of the firing activity, and accordingly, the main mass of the curves is located about 4 ms after the identified onsets. Furthermore, the plotted functions resemble more a smoothed exponential decay than a sharply defined onset. Thus, the function from equation (11.2) might be replaced by a less sharp function, e.g., by a sum of two exponentials. However, since packet onsets cannot be identified precisely by the described algorithm, even a steep increase in the firing intensity may be blurred by the imprecision with which packet onsets are determined. Therefore, the curves in Figure 13.2 B do not clearly indicate deviations from the assumed exponentially decaying intensity.

In addition, Figure 13.2 B shows a high accordance with the model assumption that the decay in the firing rate differs across units. In particular, one can see that the curves differ in their ‘burstiness’, i.e., in the tendency of spikes to be clustered in short time windows. For example, the spikes of unit 5 are closer together than the spikes of the other units. Also, the intensity of unit 3 decays more slowly than the intensity of the units 1 or 5.

13.1.3 Stability of firing rates

Finally, it is investigated whether firing rates can be considered stable both across trials and within trials. The changes in the firing rate *across* trials are shown in the first panel of Figure 13.3 in which every curve represents the spikes counted in one particular unit. Each curve shows only small changes across trials, except for trial 15 in which the firing rate is enhanced. However, these changes across trials are comparable in all units and thus, as discussed in section 12.1.2, they do not affect the predicted relation between the ACF and the CCF.

In contrast, the changes in the firing rate *within* trials differ across units, as is shown in the other panels of Figure 13.3. In each panel, the 20 gray curves indicate the spikes counted in one particular unit in each of the 20 trials. For every unit, these fluctuations are comparable across trials. Therefore, the average is plotted in black and indicates the mean rate change of this unit within each trial. For example, unit 2 has an increased firing rate at the end of each trial, while in unit 5, more spikes are observed at the beginning, and unit 3 fires more spikes in the middle of each trial.

In summary, rate covariations *across* trials are similar in all units and should not affect the direct applicability of the model, whereas rate covariations *within* trials differ across units and should therefore be taken into account when applying the model to the sample data set (cf. sect. 12.1.2).

13.2 Fitting ACFs to ACHs

Fitting procedure and estimates To investigate whether the described model can be useful in the representation of a data set, the ACHs derived from stimulation condition 1 of the sample data set are normed (i.e., divided by the length of the recording, 40,000 ms) to represent the number of coincidences per ms while keeping the original time resolution of $\delta = 1/32$ ms. Then, the ACF from equation (12.1) with the norming for spike trains in discrete time is fitted to these normed ACHs with the nonlinear least squares algorithm described in section 3.2.2. In order to get simultaneous estimates of the global parameters μ and σ across all units, all 14 ACHs were first fitted simultaneously. Thus, estimates of μ , σ , τ_1, \dots, τ_{14} , $\alpha_1, \dots, \alpha_{14}$ and $\beta_1, \dots, \beta_{14}$ were obtained. Among the estimates of the background intensity, only $\beta_2, \beta_3, \beta_6$ and β_9 deviated more

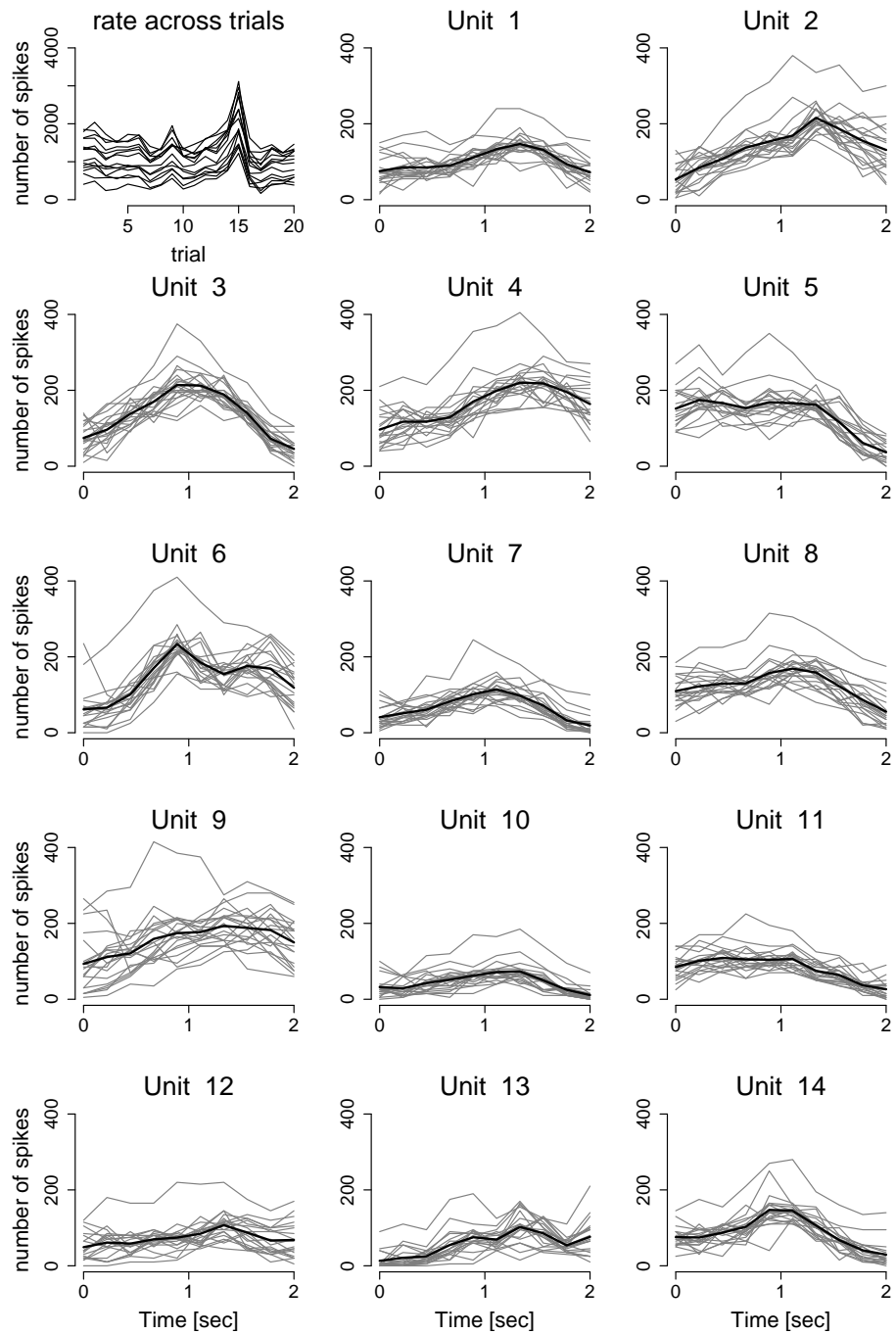


Figure 13.3: Number of spikes in each unit in stimulation condition 1. The first panel shows the overall number of spikes in each trial. Each unit is indicated by one curve. The other panels show rates within trials for each unit. For each trial, the number of spikes is counted in windows of 200 ms and plotted as a gray curve. The mean number of spikes is shown in black.

from zero than expected on the basis of their variance.² Among those, only the estimate of β_3 was negative, and it showed the smallest deviation from zero. Therefore, in a second step, all ACHs were fitted again simultaneously, while only the background intensities for the units 2, 6 and 9 were estimated, and all others were set to zero.

The resulting curves and parameter estimates are shown in Figure 13.4. The first panel illustrates the implications that the estimated parameters $\hat{\mu} \approx 25.3$ ms and $\hat{\sigma} \approx 7.2$ ms have on the distribution of IPIs. Given a packet at time 0, the densities of the three successive packets is drawn on the time axis. The parameter $\hat{\mu} \approx 25$ ms indicates that the predominant oscillation frequency is close to 40 Hz. The estimate of σ , 7.2 ms, is nearly 0.3μ , which yields curves comparable to the CCFs plotted in Figures 12.4 & 12.5. In the other panels, the raw ACH counts are plotted in light gray. Note that due to the spike detection algorithm, spikes occurring within a window of 1.2 ms after a detected spike are ignored. Thus, the counts in the ACH start at a delay of 1.2 ms. The black curves in Figure 13.4 show the smoothed counts, and the fitted curve is plotted in medium gray. One can hardly distinguish the black smoothed curve and the fitted ACF, which indicates that they agree closely and thus, that the theoretical ACFs can describe well the shapes of the empirically derived ACHs.

A high variability of ACH shapes is taken into account simultaneously. While for example unit 5 fires relatively regularly with dense packets, unit 6 shows nearly no oscillatory behavior at all, which is indicated by the high difference in the respective estimates of τ . For those ACHs without background, the parameter estimates of τ vary between $\hat{\tau}_5 = 4.0$ ms and $\hat{\tau}_{12} = 8.8$ ms. The estimates for the units with background are bigger and take values up to $\hat{\tau}_9 = 12.5$ ms. All estimates of τ stay in the range up to $\hat{\mu}/2$, most estimates being much smaller and taking values around $\hat{\mu}/4$ (cf. Fig. 12.4 B).

The estimates of the packet intensity α vary between $\hat{\alpha}_{10} = 1.4$ and $\hat{\alpha}_4 = 4.4$ spikes per packet. To make the background intensity comparable to $\hat{\alpha}$, $\hat{\beta}$ is multiplied by $\hat{\mu}$, yielding the expected number of spikes in the background in one packet. The estimates of $\beta\mu$ stay below $\hat{\alpha}$ and take the values 1.8, 1.7 and 1.3 spikes for the units 2, 6 and 9, respectively.

The total estimated firing intensity, $(\hat{\alpha}_i + \hat{\beta}_i\hat{\mu}) \cdot T/\hat{\mu}$, is comparable to the observed number of spikes in each unit (data not shown). However, the theoret-

²The variability of the parameters was estimated on the basis of their approximate variances as derived by the nonlinear least squares algorithm implemented in R. The algorithm returns a numerical estimate of the standard error of every parameter estimate on the basis of which deviations from zero are evaluated.

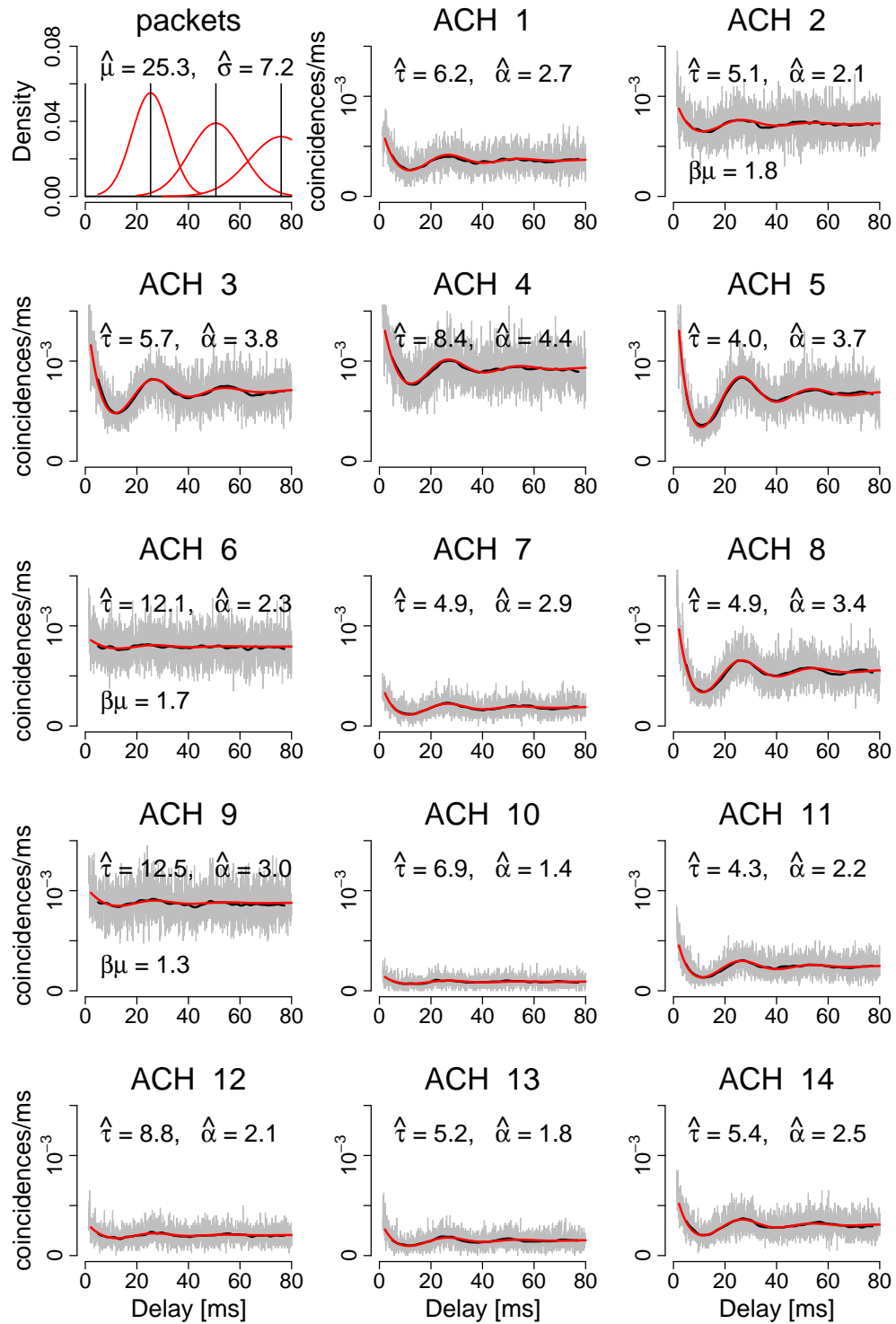


Figure 13.4: Theoretical ACFs fitted to experimental ACHs. Upper left: distribution of three successive packets following a packet at zero with $\hat{\mu} = 25.3$ ms and $\hat{\sigma} = 7.2$ ms. Panels 2-15: Gray: normed ACHs obtained from stimulation condition 1 in the sample data set. Black: Counts smoothed with a Gaussian kernel with a standard deviation of 1 ms. Medium gray: theoretical ACF fitted to the ACH.

ical firing intensity overestimates the number of spikes by about 10%. This can be explained by the spike detection algorithm which ignores spikes that follow within 1.2 ms after a detected spike. Thus, the deviation between the theoretical firing intensity and the empirical number of spikes is not in conflict with the model assumptions. However, one should note that the model assumes that a relatively high number of spikes, most of them occurring within the packets, has not been detected.

Residual analysis The last paragraph shows that all parameter estimates meet the restrictions in Table 11.1. In addition, the assumption of independence and normal distribution of the residuals should be investigated because it provides a basis for the nonlinear least squares algorithm. Since the residuals represent simple counts of coincidences, the normal distribution is highly likely to approximate the distribution of the residuals. Nevertheless, the distribution and the serial correlation of the residuals are investigated here. All units yield comparable results, and the analysis of unit 5 is presented in Figure 13.5. Panel A shows the distribution of the residuals between the fitted ACF and the empirical ACH together with the normal distribution fitted to the data. One can see that the empirical distribution agrees closely with the theoretical Gaussian distribution. Panel B shows that the serial correlation of the residuals of unit 5 stay below 0.1 up to a lag of 50 ms and that they do not show an apparent temporal structure. These results are in agreement with the model assumption of independence and normal distribution of residuals.

Precision of parameter estimates In order to investigate the precision with which the parameters can be estimated, two different procedures are performed. First, every estimate is equipped with its standard deviation as estimated by the algorithm (see footnote 2 on page 129). On the other hand, the parameter estimates derived independently in the ACHs obtained from the odd and from the even trials are compared. According to the two procedures with which the variability of a parameter estimate is approximated, Figure 13.6 shows two vertical lines for each parameter estimate. The left line indicates the interval of ± 2 standard deviations around the global estimate, and the right line connects the two estimates obtained in odd and even trials. One can see that both estimates of the variability agree to a high degree. This allows a rough evaluation of the precision with which a parameter can be estimated. However, one should keep in mind that each of the two estimates is affected by different variables. On the one

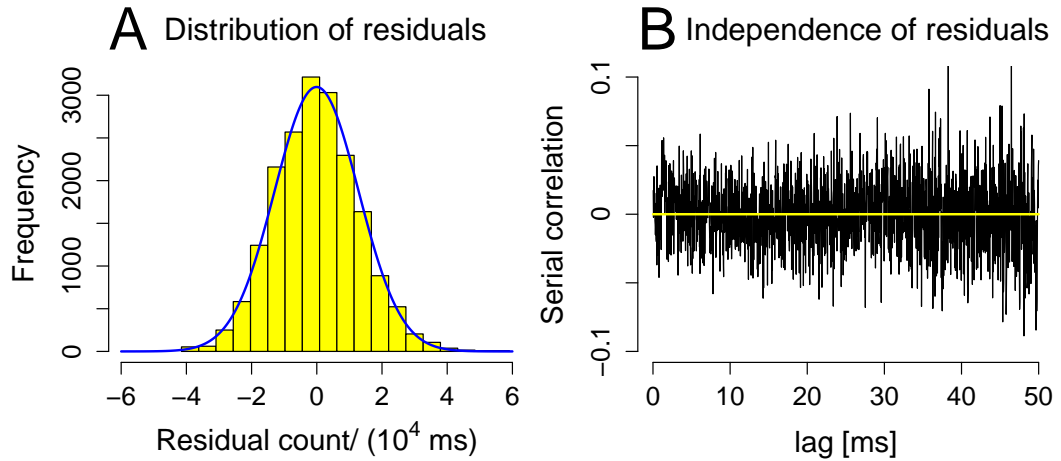


Figure 13.5: Analysis of residuals between the fitted ACF and the normed ACH of unit 5 in stimulation condition 1 of the sample data set. A: Distribution of residuals and curve of normal distribution. B: Serial correlation of residuals. The correlation between the vector of residuals and the shifted vector is plotted for time lags between 1/32 ms and 50 ms.

hand, the standard deviation estimated by the algorithm can only approximate the real variability because it is based on numerical approximations and on theoretical assumptions. On the other hand, the difference obtained between odd and even trials represents only a simple estimate of the variability, and it may also represent real variability in the parameters. For example, the high firing rate in trial 15 is likely to be reflected in consistently higher estimates of α in the odd trials. Nevertheless, Figure 13.6 indicates that the parameters μ and σ as well as most of the τ_i are estimated with a precision higher than 1 ms. The fact that the imprecision of τ_i is bigger for the units 2, 6 and 9 can be explained by the additional parameter β . This can also be observed in the high variability of α_2 , α_6 and α_9 in panel D. One should keep in mind that parameters that cannot be estimated precisely enough can yield suboptimal fits. Therefore, the following investigations will also take into account the precision with which the parameters have been estimated.

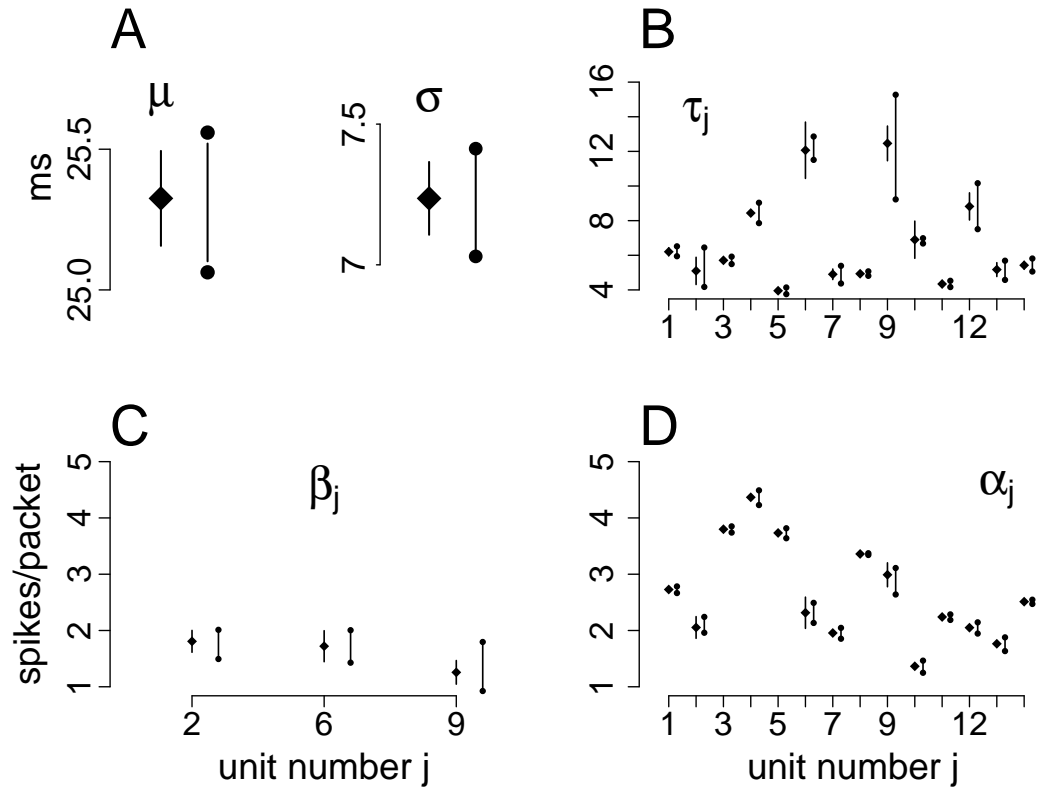


Figure 13.6: Variability of estimated parameters in the simultaneous fit of the normed ACHs in stimulation condition 1. For every parameter, the diamond on the left indicates its global estimate, and the vertical line shows the interval of ± 2 standard deviations as estimated numerically with the nonlinear least squares algorithm. On the right, the two points indicate the parameter estimates derived in odd and even trials. A: Estimated mean IPI, μ , and standard deviation σ . B: Estimated decay constants τ_j for the units $j = 1, \dots, 14$. C: Estimated background firing intensities β_j for the units 2, 6 and 9. D: Estimated packet intensities $\alpha_1, \dots, \alpha_{14}$.

13.3 Prediction of CCHs

The results presented in the previous section indicate a good correspondence between the model and the experimentally obtained ACHs. However, to show that the model provides an adequate description of the data set, also the CCFs have to agree with the empirical CCHs. In this respect, one should note that all free parameters have been estimated in section 13.2 and thus, that the theoretical CCFs can be computed on the basis of the derived parameter estimates and do not have to be fitted to the CCHs. The comparison between these predicted CCFs and the empirical counts can show whether the model can predict interactions between units on the basis of statistics of single spike trains. It can serve to investigate whether the model assumption that packet onsets occur simultaneously across units yields an adequate description of the interaction and thus, whether the model as a whole can provide a suitable representation of the data set.

To investigate whether the CCHs can be predicted from the shapes of the ACFs, the empirical CCHs are compared to the theoretical CCFs. The latter are derived with equation (12.2) (and norming for discrete time spike trains) by insertion of the parameters estimated from the ACHs. In addition, as mentioned in section 12.1.2, the height of each CCH is corrected with respect to the variability in the firing rates. Since the firing rates of all units covary across trials but change from the beginning to the end of every trial, the height of each CCF is corrected on the basis of the rate estimation performed in section 13.1.3. Mathematical details and effects of the rate correction can be found in section 13.3.3.

13.3.1 Good fits

Among all 91 CCHs, all 36 between the units 1,3,5,7,8,10,11 and 14 agree well with the theoretically predicted CCFs. Three of these are shown in Figure 13.7. One can see that the black smoothed curve and the theoretical CCFs plotted in medium gray agree to a high degree. Obviously, many different shapes can be represented very closely by the CCFs, including differences in the baseline level, variability in the height and width of the central peak as well as asymmetry with respect to zero lag.

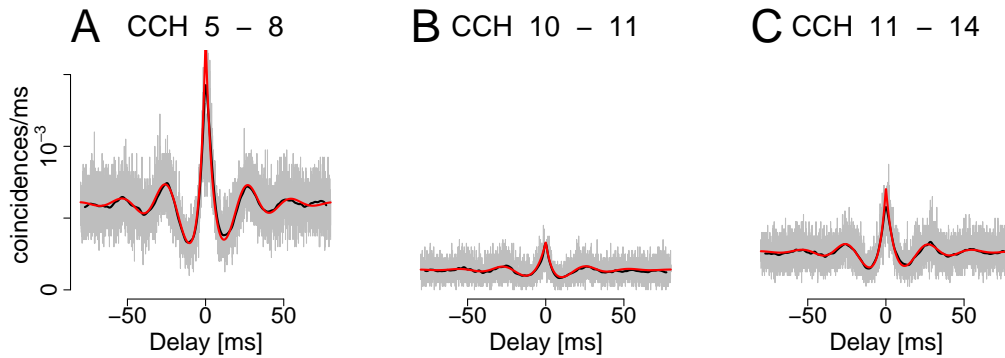


Figure 13.7: Comparison of empirically obtained CCHs and theoretically predicted CCFs for three unit pairs within the group 1,3,5,7,8,10,11,14. Empirical counts are plotted in light gray. The black curve shows counts smoothed with a Gaussian kernel with a standard deviation of 1 ms, and the theoretical CCF is plotted in medium gray.

13.3.2 Suboptimal fits

Among the remaining 55 unit pairs, not all predicted CCFs agree as nicely with the empirical CCHs as those in Figure 13.7. As can be seen in panels A-D of Figure 13.8, lack of agreement can have different forms.

First, the asymmetric shape of the central peak may not be described exactly (e.g., panels A & D). Since the asymmetry is reflected in the parameter τ , estimation imprecision of this parameter may cause such effects. This corresponds to the finding that the variability of the estimate $\hat{\tau}$ is smaller for the units with the good predictions, 1,3,5,7,8,10,11 and 14.

As a second effect, the height of the CCH can differ from the height of the CCF (panels B & D). In fact, all CCHs involving unit 6 are higher than predicted, suggesting that the rate variation is overestimated in this unit.

Finally, also the strength of oscillation can differ between the theoretical and the empirical CCH, as can be observed in CCHs that include unit 13 (Fig. 13.8 C). This may be caused by a suboptimal estimation of σ , which is in disagreement with the model assumption that σ is a global parameter. Therefore, differences with respect to the strength of oscillation cannot be accounted for in the present model but may therefore indicate possible modifications of the model and thus, provide additional information about the temporal interaction of the units.

In spite of the fact that some CCHs between units of the ‘good’ group $\{1,3,5,7,8,10,11,14\}$ and the remaining units $\{2,4,6,9,12,13\}$ show suboptimal fits, other CCHs between the remaining units can be predicted relatively well.

In particular, all CCHs between the units 2,9,12 and 13 agree well with the theoretical predictions (Figs. 13.8 E & F).

In summary, many CCHs can be predicted well with the parameters estimated only on the basis of spike characteristics of single units, while some CCHs differ from the theoretically derived CCFs. In the sample data set, these differences are usually small. Although some of these differences cannot be accounted for in the model, in most cases, disagreement between the predicted CCF and the empirical counts may be caused by suboptimal estimation of the parameters.

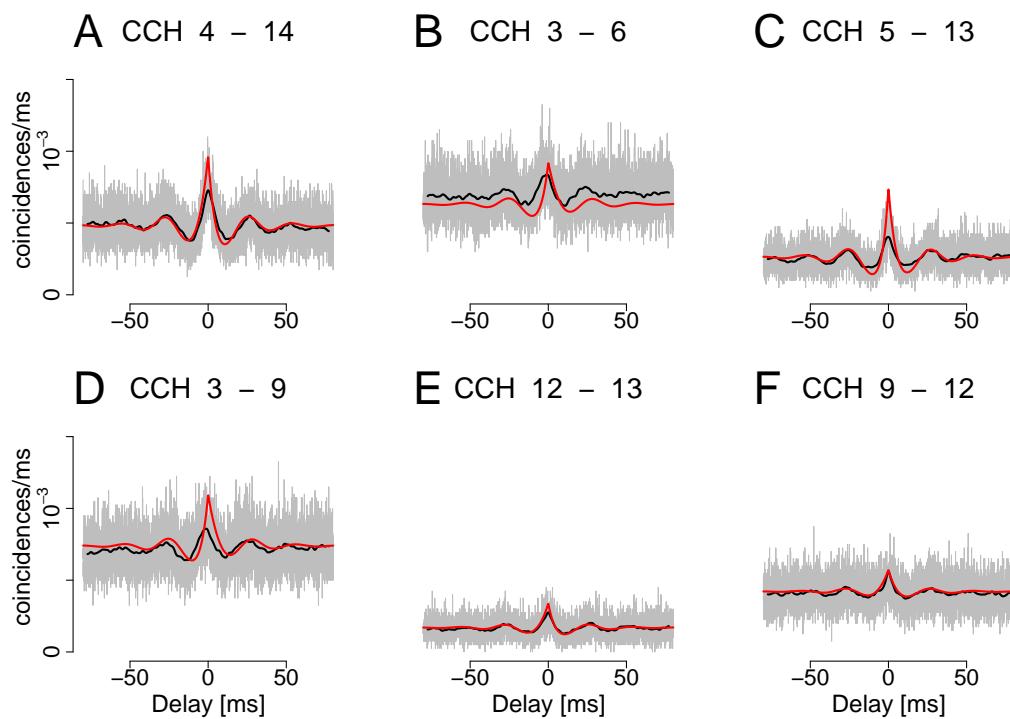


Figure 13.8: Comparison of empirically obtained CCHs and theoretically predicted CCFs for six unit pairs. Conventions as in Figure 13.7.

13.3.3 Rate correction

To correct the height of each CCF with respect to the rate variation across units, it is assumed that the firing rates of every unit change according to a step function that is given by the black curve in the panel of Figure 13.3 which belongs to this unit. Thus, the firing rate of each unit is assumed to be stable across trials, and the firing rate within all trials is approximated by a step function that jumps every 200 ms. This rather large distance between jump times was chosen to counteract random variations in the number of spikes. However, the abrupt changes of the step function might also overestimate the variability in the firing rate. Therefore, the assumed step function can only provide a rough approximation of the underlying changes in the firing rate.

For technical reasons, the packet intensity α and the background intensity β are assumed to covary because background and packets cannot be distinguished on the basis of raw spike events. The overall firing intensity is denoted by λ . The correction factor is computed according to the derivation in section 12.1.2. If the intensity of unit k , λ_k , can be described by a step function with equidistant jumps and values $\lambda_{1,k}, \dots, \lambda_{m_T,k}$, the estimate of the intensity λ_k that results from the fit of the ACHs is given by

$$\hat{\lambda}_k = \sqrt{\sum_{i=1}^{m_T} \hat{\lambda}_{i,k}^2}.$$

Thus, the estimate $\hat{\lambda}_{k_1} \hat{\lambda}_{k_2}$ for the CCF in equation (12.2) is computed as

$$\hat{\lambda}_{k_1} \hat{\lambda}_{k_2} = \sqrt{\sum_{i=1}^{m_T} \hat{\lambda}_{i,k_1}^2 \sum_{i=1}^{m_T} \hat{\lambda}_{i,k_2}^2}.$$

However, the estimated factor in the CCF should instead be

$$\sum_{i=1}^{m_T} \hat{\lambda}_{i,k_1} \hat{\lambda}_{i,k_2},$$

which is smaller or equal to the previous term according to the Cauchy-Schwartz inequality. To correct for this effect, the estimated firing rates $\hat{\lambda}_{i,k}$ from section 13.1.3 are used to compute the following correction term for each CCF:

$$c_{k_1 k_2} = \frac{\sum_{i=1}^{m_T} \hat{\lambda}_{i,k_1} \hat{\lambda}_{i,k_2}}{\sqrt{\sum_{i=1}^{m_T} \hat{\lambda}_{i,k_1}^2 \sum_{i=1}^{m_T} \hat{\lambda}_{i,k_2}^2}}. \quad (13.1)$$

The correction factors resulting from equation (13.1) are plotted in Figure 13.9 A. As one can see, the correction reduces the height of a CCF only by about 5% in the mean. However, this effect can be crucial for the agreement between the predicted CCF and the empirical CCH, as can be seen in panels B & C. The black curve shows the smoothed CCH between the units 4 and 5. In panel B, the uncorrected CCF is added in medium gray. The difference between the two curves is obvious, and the uncorrected height evokes the impression that the theoretical curve might be shifted to the left. However, after a simple multiplication with the correction factor $c_{45} = 0.89$, the theoretical curve matches nicely the empirical CCH (panel C). This effect can be observed in most of the CCHs.

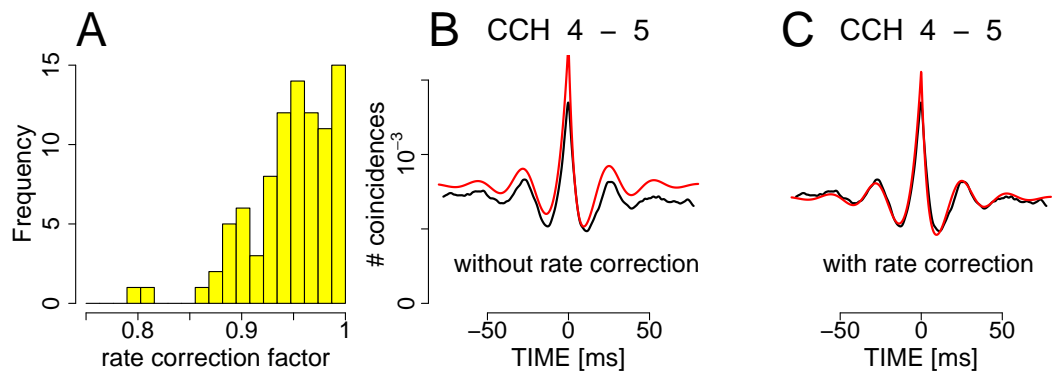


Figure 13.9: Effect of rate correction on the agreement between the theoretically predicted CCF and the empirically derived CCH. A: Histogram of rate correction factors derived with equation (13.1) for all 91 unit pairs in stimulation condition 1 of the sample data set. B: Smoothed CCH between units 4 and 5 (black) and theoretical CCF (gray) before rate correction. C: Gray curve shows theoretical CCF after rate correction.

13.4 Simulation of spike trains

In the previous sections, application of the present model to experimentally derived ACHs and CCHs showed that the model can be useful for the description and quantification of several properties concerning the shape of both ACHs and CCHs. Furthermore, the data were consistent with the model assumptions in so far as CCHs, i.e., pairwise interactions across units, could be predicted on the basis of parameters estimated from the ACHs, i.e., from single spike trains.

In addition, it remains to be investigated whether the model can also be used to represent and simulate raw spike trains. Section 13.4.1 shows an example in which spike trains recorded experimentally are compared to artificial data obtained by simulation. Closely related to the issue whether raw spike trains produced by the model are comparable to experimentally obtained spike times, the variability of coincidence counts in ACHs and CCHs represents the final parameter mentioned in chapter 10 with which a principal feature of an ACH or a CCH can be described. The question whether the variability of counts can be represented and reproduced in the present model is addressed in section 13.4.2.

13.4.1 Spike trains

In this section, spike trains that originate in processes which conform with the model assumptions are compared to experimentally recorded spike trains. To this end, parallel point processes are simulated in two steps: First, the POP is produced by simulation of a random walk with independent and $\mathcal{N}(\mu, \sigma^2)$ -distributed increments. For the given POP, parallel, independent Poisson processes with firing intensities as in equation (11.2) are generated. In the last step, the point processes in continuous time are converted into spike trains in discrete time with time resolution δ by

$$S(j) = I_{\{X_{([j, j+\delta])} \geq 1\}}, \quad j = 0, \delta, \dots, \delta \cdot (T - \delta) / \delta.$$

Figure 13.10 A shows real spike trains of the units 5, 8 and 11 recorded in stimulation condition 1. As one can see, every spike train consists of reoccurring packets with 1-5 spikes, IPIs ranging between 10 and 40 ms. Although packets occur roughly at the same time across the three units, packet times are not obvious only on the basis of the raw spike trains. The same behavior can be observed in panel B. It shows artificial spike trains S_5, S_8, S_{11} simulated with the parameters $\mu = 25.3$, $\sigma = 7.2$, $\alpha_5 = 3.7$, $\alpha_8 = 3.4$, $\alpha_{11} = 2.2$, $\tau_5 = 4.0$, $\tau_8 = 4.9$, $\tau_{11} = 4.3$, and $\beta_5 = \beta_8 = \beta_{11} = 0$ in the original time resolution of $\delta = 1/32$ ms.

To account for the spike detection algorithm in which spikes occurring up to 1.2 ms after a detected spike are ignored, such spikes which would be ignored by the algorithm are plotted only in light gray. The simulated spike trains show a pattern very similar to the recorded spike trains: Packets reoccur with a variable IPI length, and packet onset times are hard to identify only on the basis of the spike trains. Also the variability in the number of spikes across packets is comparable to the one in the recorded spike trains.

Thus, the spike train model can not only describe special interval statistics such as ACHs and CCHs but can also be used to generate spike trains that are comparable to those recorded experimentally. It should be noted, however, that the conclusions concerning Figure 13.10 are only based on visual examination. Comparability in this respect does not imply that the present model can describe the recorded spike trains in every aspect, including all inter spike interval statistics or the variability of spike numbers across different packets. However, spike trains simulated with the present model can be used to investigate any of these aspects. One of the most interesting issues concerns the variability of counts of coincidences in ACHs and CCHs. This is investigated in the following section.

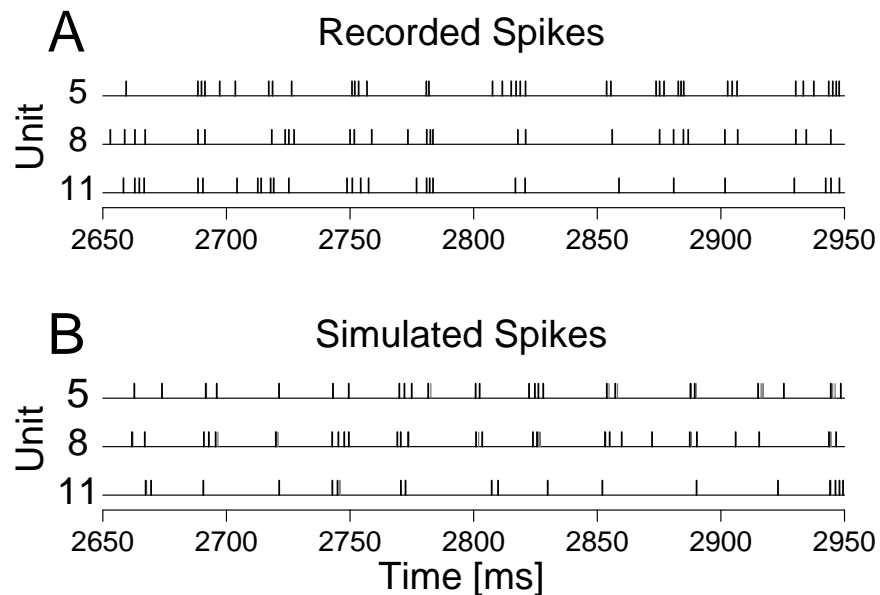


Figure 13.10: Comparison of recorded and simulated spike trains of the units 5, 8 and 11. A: Spikes obtained experimentally. B: Spikes obtained by simulation according to the model with the original time resolution of $\delta = 1/32$ ms. Spikes following an earlier spike more closely than 1.2 ms are plotted in light gray.

13.4.2 Variability of counts in ACHs and CCHs

In this section, experimentally obtained ACHs and CCHs are compared to ACHs and CCHs that result from simulated spike trains obtained from point processes that comply with the model assumptions. The most important issue in this respect concerns the investigation of whether the variability of coincidence counts is accounted for in the present model. In other words, the parameters α , β , τ , μ and σ are sufficient to describe the theoretical AC- and CC-functions that are obtained if ideal spike trains of infinite length were recorded. However, it is not clear whether such spike trains which are simulated in the original time resolution and with the given length and number of trials also result in a comparable variability of counts around the theoretical functions.

To investigate whether the variability of coincidence counts is accounted for in the present model, spike trains are simulated with the same time resolution and for the same duration as in the real data. For the simulated spike trains, ACHs and CCHs are computed. To allow a direct comparison, the units illustrated in Figures 13.4 & 13.7, which showed a high correspondence with the model assumptions, are chosen here. The three panels in the first row of Figure 13.11 show ACHs of spike trains simulated with the parameters of the units 5, 8 and 11. The comparison with Figure 13.4 shows that the variability of counts agrees closely with the one obtained from experimentally recorded spike trains. The same holds true for the CCHs between the unit pairs 5-8, 10-11 and 11-14 in the second row, which are highly comparable to the experimentally obtained CCHs shown in Figure 13.7.

For quantification purposes, the sum of squares of residuals of the raw counts and the theoretical functions are shown in Table 13.1 for every graph in Figure 13.11 and for the respective ACHs and CCHs obtained from the sample data set. One can see from the sums of squares that for every comparison, the variability of counts obtained in the artificial spike trains agrees closely with the variability obtained in the experimental data set. Thus, the present model can not only describe the theoretical shape of both ACHs and CCHs that is obtained for theoretical spike trains of infinite length, but it can also be used to simulate spike trains such that the variability of coincidence counts in ACHs and CCHs is replicated accurately.

In conclusion, chapters 12 and 13 show that the model presented in chapter 11 meets the requirements necessary for the description and representation of experimental data in the sample data set. The model can be used to describe and quantify various principal properties of ACHs and CCHs, and changes in a

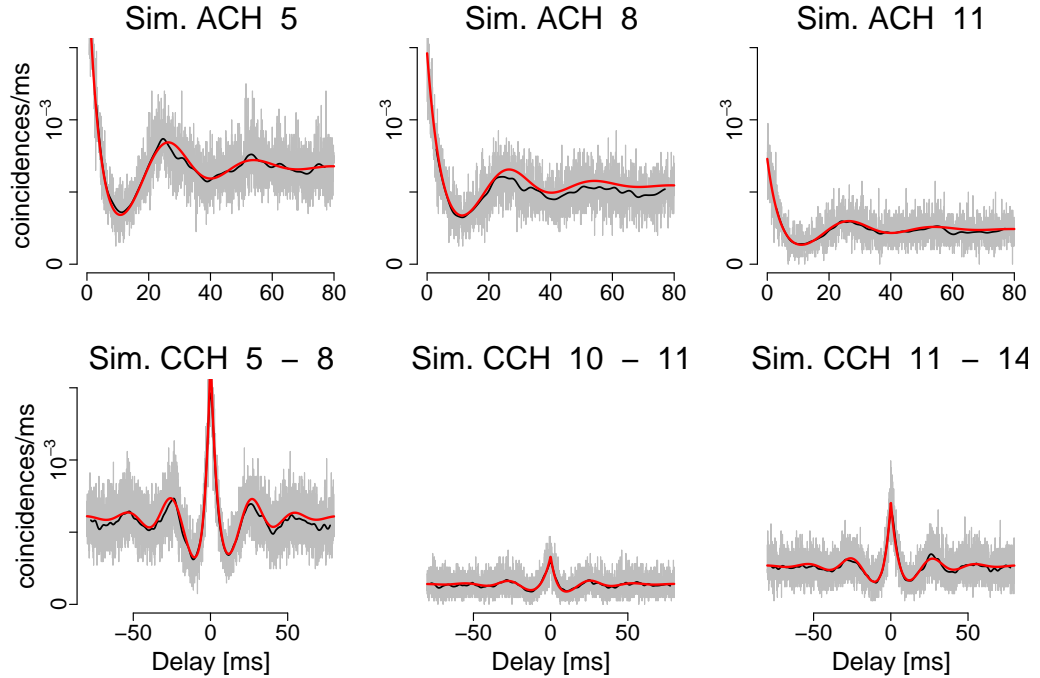


Figure 13.11: Normed ACHs and CCHs derived from simulated spike trains that comply with the model assumptions and which have the same parameters as estimated in section 13.2 and the same time resolution and length of the analysis window as in the original data set. Plotting conventions as in Figures 13.4 & 13.7.

<i>ACHs</i>			<i>CCHs</i>		
<i>unit</i>	<i>exp</i>	<i>sim</i>	<i>unit pair</i>	<i>exp</i>	<i>sim</i>
5	4.12	4.07	5 - 8	8.33	7.13
8	3.44	3.39	10 - 11	1.78	1.80
11	1.54	1.50	11 - 14	3.29	3.28

Table 13.1: Sums of squares of residuals ($\cdot 10^5$) between raw coincidence counts and theoretical functions. Left: Comparison of the theoretical ACFs with the experimentally obtained ACHs (column entitled ‘exp’) and with ACHs derived by simulation (column entitled ‘sim’) for the units 5, 8 and 11 (upper row in Fig. 13.11). Right: Comparison of theoretical CCFs with experimentally obtained CCHs (‘exp’) and CCHs derived with simulations (‘sim’) for the unit pairs 5-8, 10-11 and 11-14 (bottom row in Fig. 13.11).

few parameters can account for a high variability in the shape of CCHs. This variability is not arbitrary but follows closely the variability of shapes found in experimental data. Moreover, the model can not only in theory provide an explanation for different shapes, but it can also provide a framework in which several statistics can be interpreted and related in a consistent manner. Among those, single spike trains, but also the variability of counts in both ACHs and CCHs as well as the relation between ACHs of individual units and CCHs representing pairwise interactions have been investigated. Thus, also the predictions that can be derived from the model assumptions agree closely with experimental data.

As a last step, one should note that the present spike train model was developed to provide a mechanism that can explain the origin of phase offsets in central CCH peaks. Since a phase offset that differs from zero can only originate in an asymmetric central peak, the part of the model that deals with sources of asymmetry is of special importance here. Chapter 14 will investigate whether the asymmetry that is taken into account by the present model can also provide an explanation for the existence of non-zero phase offsets as discussed in Part I, as well as for their linear structure, which has been investigated in Part II.

Chapter 14

What then is a phase offset?

Recapitulation Before discussing the relation to the linear structure of phase offsets, the most important results of the Parts I and II will be sketched again shortly. In Part I, predominant spiking delays – so-called ‘phase offsets’ – between pairs of units were estimated by fitting a cosine function to the central peak of the respective CCH. The point at which this cosine function reached its maximum was taken as the estimated phase offset between the two units in question. Phase offsets were determined for a number of unit pairs in the sample data set and were found to have absolute values smaller than 2 milliseconds. These phase offsets could furthermore be estimated with high precision (i.e., < 1 ms), indicating that the deviation from zero of numerous phase offsets was unlikely to be caused by measurement error. Moreover, phase offsets were found to vary systematically with the stimulation condition. These results suggested that phase offsets might be related to information processing.

Therefore, the structure of phase offsets was investigated in Part II. In particular, the idea that phase offsets represent predominant spiking delays motivated the search for an additive, linear structure inherent in a set of phase offsets. By application of an analysis-of-variance approach, experimentally obtained phase offsets were found to be additive to a high degree, i.e., for any triplet of units i, j, k , the sum of phase offsets $\varphi_{ij} + \varphi_{jk}$ corresponded approximately to the direct measurement φ_{ik} . This allowed an $(n - 1)$ -dimensional representation of all units on the time axis in which pairwise distances between units represent measured phase offsets and which, thus, indicates the ‘predominant firing order’ of all units.

The positions of the units 1, 3, 5, 7, 8, 10, 11, and 14 (stimulation condition 1) on the time axis that were derived in Part II are plotted in Figure 14.1 A

(cf. Fig. 8.1 A). The question addressed here is the following: Can the spike train model from chapters 11 and 12 explain how small phase offsets arise between spike train pairs? And if so, why should phase offsets be additive? In other words: What can the spike train model tell us about the relevance of the linear structure of phase offsets for cortical information processing?

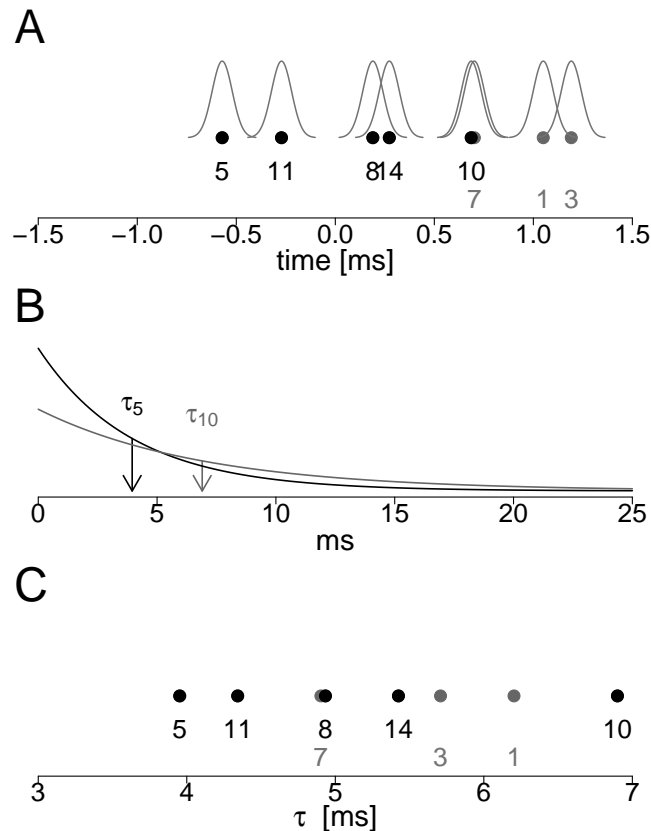


Figure 14.1: Linear configurations obtained from phase offsets and from the spike train model in stimulation condition 1 from the sample data set. A: Linear configuration of units 1, 3, 5, 7, 8, 10, 11 and 14 on the time axis as derived in Part II. B: Exponentially decaying firing intensities after packet onset according to the model assumptions for the units 5 (black) and 10 (gray). C: The parameter estimates of τ_i for all $i \in \{1, 3, 5, 7, 8, 10, 11, 14\}$ as derived in section 13.2.

Phase offsets in the spike train model As discussed earlier, a non-zero phase offset can only be caused by an asymmetric central peak. Thus, in terms of

the present spike train model, only the parameter τ can be relevant for generating phase offsets that differ from zero. As shown in section 12.2.2.3, an asymmetric peak in the CCH of two units i and j is reflected in different parameters τ_i and τ_j . More explicitly, at any height of the central peak, the relation between the width on the right and the width on the left hand side, s_r/s_l , can be approximated by the quotient τ_j/τ_i (cf. Fig. 12.5 and p. 120). Thus, if $\tau_i < \tau_j$, the peak is broader on the right than on the left hand side. As a consequence, a cosine fitted to the central peak is shifted slightly to the right, i.e., to the side with the bigger τ , producing a positive phase offset (Figs. 14.2 A & B). This effect takes place in spite of the fact that the maximal count of coincidences is at delay zero. This is because the edges contribute more information about the location of the peak than the maximum and because the counts at zero are excluded anyway to eliminate artifacts in the recording (cf. Fig. capt. 3.2). As a result, the phase offset extracted from a cosine function should be directly connected to the difference $\tau_j - \tau_i$. Figure 14.2 C illustrates this relation for the parameter set $\sigma = 0.28\mu$ and different combinations of τ_1 and τ_2 by showing the lines where φ is constant. The connection between φ and $\tau_2 - \tau_1$ is nonlinear for $\tau_1 \neq \tau_2$. However, the two quantities are closely related in two respects: First, the sign of φ equals the sign of $\tau_j - \tau_i$, and second, for constant $\tau_1 + \tau_2$, $|\varphi|$ grows with $|\tau_2 - \tau_1|$.

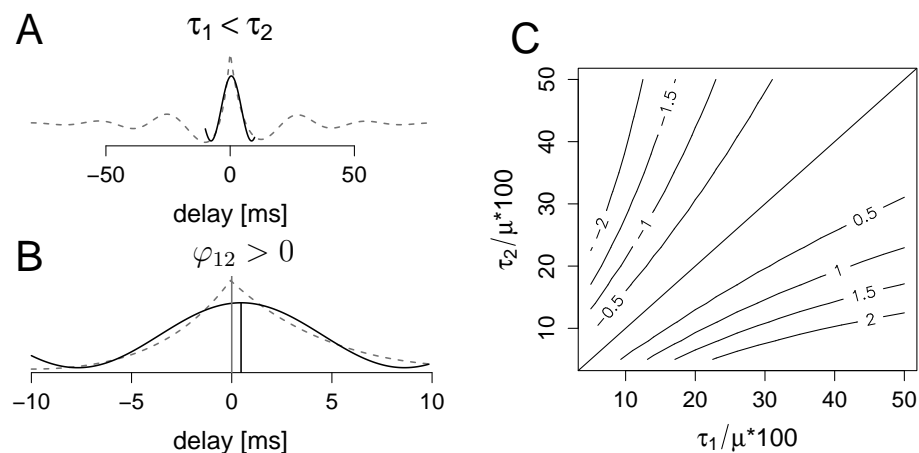


Figure 14.2: Phase offsets of cosine functions fitted to CCFs ($\mu = 25.3$ ms, $\sigma = 7$ ms). A, B: CCF with $\tau_1 = 4$ ms, $\tau_2 = 6$ ms and cosine function fitted to the central part; $|\ell| \leq 10$ ms. Since $\tau_1 < \tau_2$, the phase φ_{12} is positive. C: Phase estimates φ in milliseconds that result from fitting a cosine function to the central peak as shown in A & B.

In addition, a closer look at the raw spike trains supports the idea that the parameter τ_i should be related to the position of unit k on the time axis as extracted with the phase offsets estimated with a cosine function. As pointed out in section 11.2, τ represents the expected delay between a packet onset and the time of a spike in this packet. As a result, the expected time of a spike in unit k relative to packet onset is τ_k . This is shown exemplarily in Figure 14.1 B for the units 5 and 10 from the sample data set. The parameter $\tau_5 \approx 4$ ms indicates the center of mass of $1/\tau_5 \cdot e^{-t/\tau_5}$, and $\tau_{10} \approx 7$ ms indicates the center of mass of $1/\tau_{10} \cdot e^{-t/\tau_{10}}$. As a result, in spite of the fact that the packet onset occurs simultaneously for both units, unit 5 tends to fire earlier than unit 10 because the spikes tend to be closer to the packet onset than the spikes of unit 10. This interpretation of the parameter τ also suggests that the preferred delay between two units i and j should be directly related to the difference $\tau_j - \tau_i$.

Linear Structure By straightforward assignment of one real number τ_i to every unit i , pairwise differences between these real numbers are necessarily additive. Thus, the described spike train model is qualitatively in agreement with the findings in the Parts I and II.

To investigate this relation in the sample data set, the estimates of τ are plotted for the units 1, 3, 5, 7, 8, 10, 11, and 14 in Figure 14.1 C. This group of units is chosen for the comparison because the estimated variability of the parameter estimates is small and because their theoretical CCFs agree with the empirical CCHs (cf. sect. 13.3.1). One can see that for the units 5, 8, 10, 11 and 14, the order on the time axis in panel A is exactly represented by the order of the parameters τ in panel C, i.e., a unit has a bigger τ than another unit if and only if its temporal position derived from the phase offsets is shifted to the right (i.e., to a later position) with respect to the other unit. As mentioned above, the exact distances between the points cannot be replicated with the parameters τ due to the qualitative difference between the cosine function and the CCF peak. However, the order of the units remains the same.

In contrast, the positions of the units 1, 3 and 7 do not agree perfectly across the panels A and C. In particular, the estimates τ_1 , τ_3 and τ_7 are smaller than is suggested by the position on the time axis in panel A. Since the model has been found to agree closely with many statistics extracted from the sample data set particularly for this set of units, deviations from the model assumptions are unlikely to have caused the disagreement with the unit positions extracted with the cosine fit. Therefore, deviations from the linear structure in Figure 14.1 A are

more likely to be caused by a suboptimal estimation of the parameters τ . This is a plausible explanation because these parameters have only been estimated on the basis of the ACHs, which may not provide a data basis for a sufficiently precise estimation of the parameters. In addition, this explanation is also suggested by the goodness of fit of the relevant CCFs. Although, as mentioned in section 13.3.1, all predicted CCFs among the units 1, 3, 5, 7, 8, 10, 11, and 14 agree relatively well with the empirical CCHs, only those among the units 5, 8, 10, 11, and 14 agree perfectly with the smoothed function of the empirical counts in the center of the CCH (cf. Figs. 14.3 A & B). In contrast, those CCHs involving the units 1, 3 and 7 show a suboptimal agreement with respect to the central peak (Figs. 14.3 C & D). In addition, the deeper valleys and higher slopes of the CCF in comparison to the CCH that can be seen on the left of panel C and on the right of panel D indicate that the parameter estimates of τ_3 and τ_7 are too small. The same holds true for all other CCHs involving the units 1, 3 and 7. This suggests that the disagreement between the positions of the units 1, 3 and 7 derived from the estimated τ_i in the spike train model and the positions obtained from the cosine fit may have been caused by suboptimal estimation of the parameters τ_1 , τ_3 and τ_7 .

One should, however, keep in mind that the relation between the parameters τ and the positions on the time axis derived with the cosine fit is not straightforward. The cosine function was chosen more or less arbitrarily to comply with the oscillatory shape of the CCH. One should consider replacing the cosine with a two-sided exponential function when fitting CCHs that comply with the spike train model. On the other hand, the temporal positions extracted from the cosine fit can still be useful for improving the estimates of the parameter τ .

Implications for coding mechanisms In the introduction it was hypothesized that non-zero phase offsets might provide information additional to coincident firing by introducing temporal structure on an extremely fine time scale. As shown in Part II, such a structure can assign to every unit a very precise position on the time axis, which is interpreted to indicate the preferred time at which this unit fires action potentials relative to the other units in the group.

This structure should, however, not be confounded with the proposed mechanism of a temporal order code in which information is encoded in the relative temporal order of spikes of different neurons in a population (cf. App. A.1, p. 158). In contrast, the spike train model from Part III suggests that the temporal order of firing is a phenomenon that can only become visible when delayed

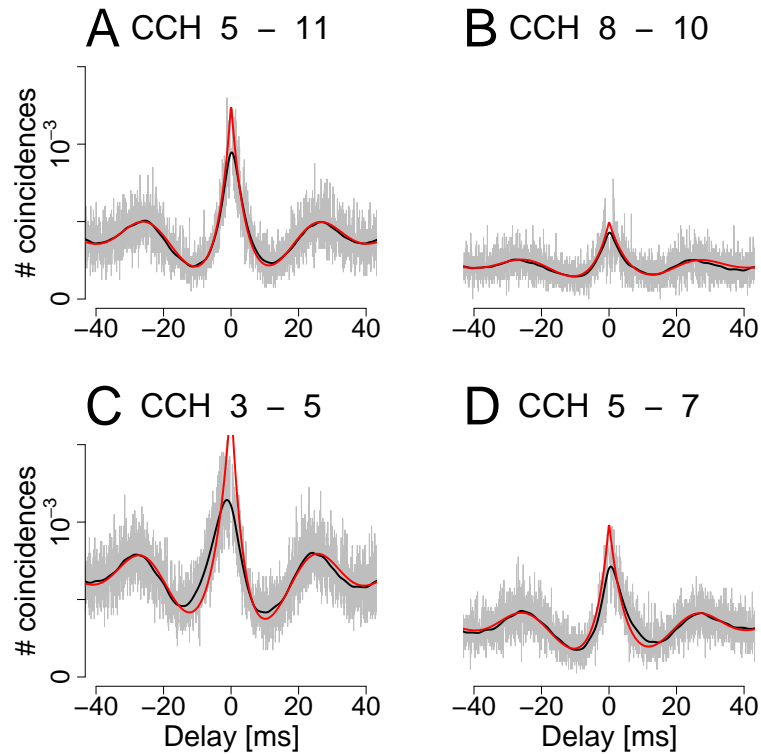


Figure 14.3: Optimal and suboptimal fits of the central CCH peak. Graphs show raw CCH counts (light gray), smoothed counts (black) and predicted CCF (medium gray) for unit pairs with good fits (A: 5-11; B: 8-10) and with less optimal fits (C: 3-5; D: 5-7) around the central peak of the CCH, i.e., in the interval $[-10 \text{ ms}, 10 \text{ ms}]$ in which the cosine function was fitted.

spike pairs are summed across relatively big analysis windows because ‘preferred delays’ simply result from the mean delay between a packet onset and the time of a spike, summed across many packets, and can thus not be observed in single packets.

Essentially, the present spike train model suggests that a unit that has the tendency to fire its spikes more densely at packet onset than the other units is assigned an earlier position on the time axis. Another unit whose spikes are more distributed and less locked to the global oscillation (or to the packet onsets) is assigned a later temporal position. Further implications as well as limitations of the model are discussed in chapter 15.

Chapter 15

Discussion and outlook

Summary In Part III, a spike train model was presented with which multiple spike trains with a common oscillatory rhythm can be analyzed and with which their ACHs and CCHs can be quantified and interpreted. The basic assumptions are derived from common observations in experimental data that have been verbalized qualitatively (Engel *et al.*, 1992; Singer and Gray, 1995). In contrast to earlier approaches in which CCH features have been measured descriptively (e.g., Aertsen and Gerstein, 1985; Melssen and Epping, 1987; König, 1994; Nowak *et al.*, 1995) or in which properties of CCHs were compared to independent renewal processes (Abeles, 1982a; Aertsen and Gerstein, 1985), the model presented here grasps and quantifies important features inherent in coincident oscillatory spiking activity, and all parameters have a direct interpretation.

The present model basically contains two different components: First, a packet onset process produces independent and normally distributed inter packet intervals (IPIs) and determines the simultaneous packet onset times of all units. With this mechanism, a pseudo-oscillation is introduced in which the preferred oscillation period is reflected in the mean of the normal distribution, μ , and in which the variance of IPIs is given by σ^2 . Second, the spike intensities in every unit are assumed to decay exponentially from the times of the packet onsets. In particular, different units may have different decay constants τ , and accordingly, the spikes of some units may on average occur more closely to the packet onset than the spikes of other units.

With the presented model, many different theoretical shapes of ACHs and CCHs can be explained. Furthermore, the model allows the approximation of essential quantities in the CCHs such as the height of the peak or the baseline level. For example, μ roughly determines the position of the first side peak,

and the speed of decay of the coincidence counts towards baseline depends on σ . More importantly, both the height and the width of the central peak relative to baseline vary with τ , and the CCH of two units i and j with different decay constants τ_i and τ_j shows an asymmetric central peak. In particular, on the side with the smaller τ , the counts decay faster, the valley is deeper and the peak is narrower.

The fact that the model is based only on a small number of parameters allows the investigation of whether the model assumptions can be considered plausible. To this end, the parameters were estimated by fitting theoretical auto correlation functions derived with the spike train model to the empirically observed ACHs. The parameters obtained with this procedure were used to predict the shape of the CCHs under the model assumption that packet onsets are synchronized across units. Most of the CCHs obtained with this procedure were in high agreement with the experimentally obtained CCHs. In particular, differences of the parameter estimates τ led to the same combination of features in asymmetric central peaks that can be obtained theoretically.

Thus, the model provides a method with which inferences about pairwise interactions can be made on the basis of single spike trains. In this respect, not only a high agreement between the predicted CCHs and the observed CCHs can provide useful conclusions about pairwise interactions, but also disagreement between the prediction and the observation can indicate the existence of additional mechanisms and can motivate plausible model extensions. In particular, the assumptions of independence and normal distribution of IPIs are sufficiently general to allow the direct incorporation of several model extensions without further technical effort.

Model extensions could involve modifications concerning the perfect coincidence of the packet onsets across units. In the sample data set, unit 13 showed less prominent oscillatory activity in the CCHs, i.e., in the interactions with other units than was predicted on the basis of the ACH. In this case, the packet onsets of this unit might only be partially locked to the global packet onset process. In addition, also the exponentially decaying function that describes the firing intensity within packets might be a candidate for modifications. In chapter 13, mismatches between the predicted and the empirical CCH were mostly assumed to result from a suboptimal estimation of the parameters τ . However, they might also result from a disagreement between the model assumption of exponential decay and the firing intensity within packets.

Future investigations should also approach the question whether the mismatch between the empirical observations and the theoretical predictions of the model can indeed be explained by deficiencies in the parameter estimation. To this end, it should be studied whether different parameter estimates of τ can produce a better agreement between the model and the empirical CCH counts in the cases where this agreement is not yet given. In this respect, the fitting procedure in which only the ACHs were used to estimate the parameters should be extended because the ACHs may be insufficient to determine the parameter estimates precisely enough. One major problem is that the counts in the center of the ACH are missing due to the spike detection algorithm. Thus, in order to estimate the parameters more precisely, also the CCHs could be taken into account.

Another possibility to improve the estimation of the parameters is to use the linear temporal structure of the units as derived in Part II. As discussed in the previous chapter, the position of unit i on the time axis as derived on the basis of pairwise phase offsets should correspond to the size of the parameter τ_i in the spike train model. Therefore, the position of unit i in the linear configuration could help to improve the estimation of the parameter τ_i .

Implications The direct connection between the parameters τ_i and the temporal positions of the units on the time axis can provide a basis for further interpretation of phase offsets and their additive structure. In the spike train model, a positive phase offset in the CCH between units i and j results from the mechanism that the spikes of unit i tend to be more densely clustered at packet onset, whereas the spikes of unit j tend to be distributed more regularly across the oscillation cycle. As a consequence, unit j is interpreted to fire its spikes later than unit i . However, this mechanism works only on average, i.e., when summing up spikes across large analysis windows. In single oscillation cycles, the only coordination that is assumed in the model is the simultaneous start of the packets. Single spikes are not assumed to be coordinated and thus, observable spike delays between units show a high variability across different oscillation cycles.

The impact of the described spike train model on the interpretation of phase offsets and their linear structure depends on whether similar mechanisms can be observed in the activity of single neurons. As described in Appendix A.3, the data set analyzed here contains multi-unit activity, i.e., every recorded channel incorporates the firing activity of 1-5 single neurons. More precise temporal

properties such as a temporal order code (Hopfield, 1995; Van Rullen *et al.*, 1998) might be hidden when the activity of several single units is merged. It is also possible that the tendency of a multi unit to fire spikes more or less locked to packet onset depends on the agreement between the neurons in the composition. For example, if all single neurons respond in a similar way to specific stimulus properties, the spikes in the multi unit might occur closer together than if the units respond in different ways to the same stimulus property. In addition, the tendency to fire spikes more or less locked to the packet onset might also depend on the level of activation (Hopfield, 1995; König *et al.*, 1995; Traub *et al.*, 1997; Wennekers and Palm, 2000).

Another possible connection of the presented model to recently proposed coding mechanisms may be found in the work of Hopfield and Brody (2001), who showed that an input pattern of different decaying currents with different speeds of decay can evoke synchronous activity in the successive neurons. A complete investigation of the degree to which the model presented here may be related to information processing is beyond the scope of the present work. However, the spike train model can be used as a framework for the analysis and interpretation of oscillatory spiking activity.

In conclusion, the present model provides a method with which oscillatory CCHs can be described and quantified and with which their commonly observed features can be related to spike train characteristics. The model provides an interpretation of important temporal properties such as near-zero phase offsets and their linear temporal structure. It can be used to analyze temporal relations between multiple spike trains recorded in parallel and can thus provide a way to reduce the complexity in a highly dimensional data set. As a consequence, it can represent a powerful tool in the analysis of the temporal structure in neuronal spiking activity.

Appendix A

Neurophysiological Background

A.1 Neuronal information processing

The brain Neuroscientists from various disciplines are accumulating evidence about the mechanisms of complex information processing in the brain. It is commonly agreed that information is encoded and processed by the electric discharges of special nerve cells, the neurons. In one single neuron, electric inputs are collected at the dendrites and propagate to the cell body where they are integrated. If the inputs are strong enough to lift the membrane potential above a threshold, the neuron emits an action potential (spike), i.e. the membrane potential rises rapidly, which is followed after about 1 ms by a period of hyperpolarization, the refractory period. The emitted spike is propagated along the axon to the synapses where the release of neurotransmitter evokes a depolarization of the membrane potential at the dendrites of successive neurons (for a detailed description see, e.g., Braitenberg and Schüz, 1991; Kandel *et al.*, 1996).

The significance of this electric communication among neurons has to be interpreted with respect to the connectivity structure. The human neocortex consists of about 10^{14} neurons each of which receives about 10^4 inputs from other cells (Larkman, 1991) (high convergence) and projects this information to about the same number of units (high divergence). Those connections can be feed-forward, feedback as well as intrinsic (DeYoe and Van Essen, 1988).

Coding: Single neurons or assemblies? There is an ongoing debate on how this highly connective structure may be efficiently used in fast and precise coding mechanisms. One of the first ideas was formulated by Barlow (1972) who

proposed that simple feature-detecting neurons from lower brain areas converge onto specific cells that represent more and more complex feature combinations. Information was assumed to be integrated and propagated by an enhancement of the spiking ('firing') rates of the respective neurons. On the highest level, so-called 'cardinal cells' were hypothesized to increase their firing rates in response to entire objects. This place code theory led to insights into fundamental cortical mechanisms. Simple feature detectors have been found in primary sensory areas such as cells with selective orientation or color preferences in primary visual cortex (Hubel and Wiesel, 1962). Additionally, there is evidence for the existence of neurons responding to more complex features such as faces (Perrett *et al.*, 1982). On higher levels, localized lesions in different brain areas cause specific behavioral deficiencies, indicating specialized contributions of different areas such as perception or motor control. Many of these areas are in turn organized in systematic maps such that nearby objects are represented in adjacent cortical structures (see e.g. Kandel *et al.*, 1996).

Barlow's so-called 'single-neuron doctrine' was subject to criticism (von der Malsburg, 1981; Engel *et al.*, 1992; Singer, 1993). It was argued that the number of neurons is too small to allow for the coding of every combination of features and that numerous cells would have to be reserved for new objects. Also, apart from a few exceptions, no evidence had been found for highly specialized cells, which then in turn would not be capable of coordinating complex responses that are represented in the activity of multiple neurons. Therefore, it was proposed that the combined activity of assemblies of neurons may be used to represent complex objects (Hebb, 1949; von der Malsburg, 1981; Abeles, 1982a; Gerstein and Aertsen, 1989). With this mechanism, the combinatorial problem can be solved because assemblies can group in a dynamical way, allowing each neuron to participate at different times in different assemblies (Singer, 1993).

The binding problem and synchrony The use of assembly activity requires mechanisms with which co-active neurons can be identified and related. Additionally, assemblies that represent different but overlapping features need to be reliably distinguished to allow execution of complex tasks. This issue is commonly referred to as the binding problem (Gray *et al.*, 1992). It could not be solved if assemblies were formed on the basis of a coordinated increase in firing rates because this would not allow separating overlapping assemblies and would thus give rise to ambiguities. Furthermore, psychophysical studies showed that complex pattern recognition can be achieved as quickly as 80-100 ms after stim-

ulus presentation (Perrett *et al.*, 1982; Thorpe *et al.*, 1996), leaving too little time per processing stage to allow detecting a firing rate increase. An alternative approach, reviving the Hebbian assumption that coincident activity leads to a strengthening of connections between neurons (Hebb, 1949), proposed that assemblies could be defined by the temporal correlation of discharges (von der Malsburg, 1981; Abeles, 1982a; Singer, 1993). Neurons were hypothesized to synchronize their responses on a fine time scale. This would allow fast processing as well as coexistence and separability of different cell assemblies.

The mechanisms required for the establishment and propagation of precise synchronous spiking activity have been found in the cortex. In the first place, neuronal discharges can occur with high temporal precision (Reinagel and Reid, 2000, 2002). Both spike patterns and membrane potential changes can replicate with a precision of about 1 ms (Mainen and Sejnowski, 1995; Ikegaya *et al.*, 2004). In addition, synchronous firing across groups of neurons as well as temporal patterns in single neurons and pairs of cells was found to occur with a precision of up to a few ms (Strehler and Lestienne, 1988; Lestienne, 1996; Riehle *et al.*, 1997). Second, neurons were found to be able to act as coincidence detectors, i.e., to identify and react to synchronous assembly activity (Abeles, 1982b; König *et al.*, 1996). Moreover, the assumption that precisely synchronized discharges can propagate through the cortex (a concept called ‘synfire chain’ (Abeles, 1982a)) has found support on the theoretical basis (Diesmann *et al.*, 1999) as well as in experimental studies (Abeles *et al.*, 1993; Lindsey *et al.*, 1997; Prut *et al.*, 1998; Ikegaya *et al.*, 2004). Finally, cells were found to form dynamically into assemblies of synchronous firing activity, depending on the nature of the task (Vaadia *et al.*, 1995; Grün *et al.*, 2002b), even in the context of higher level functions such as expectation (Riehle *et al.*, 1997).

Oscillation In addition to synchronous spiking activity, another phenomenon seems to play an important role in the formation of cell assemblies: Especially in the visual cortex of the cat, synchronous firing of multiple neurons is associated with coordinated rhythmic discharges (Gray and Singer, 1989; Engel *et al.*, 1992; Gray *et al.*, 1992). Due to its stimulus specific occurrence (Gray *et al.*, 1989; Kreiter and Singer, 1996), synchronous oscillation has been proposed to serve as a binding mechanism for spatially separate groups of neurons (Gray and Singer, 1989), allowing cells to dynamically combine into different assemblies by changing their phase relationships (Eckhorn *et al.*, 1988). Going one step further, it has been argued that information might be encoded in the temporal order of spikes

of different neurons (Traub *et al.*, 1997; Van Rullen *et al.*, 1998; Delorme and Thorpe, 2001; Delorme, 2003).

Connection: Synchrony and temporal order The two concepts of coding by temporal order and coding by synchronous activity are linked by various conjunctions. First, coincidence detection can be used as a decoding mechanism for precise temporal delays in combination with delay lines (Jeffress, 1948; Carr and Konishi, 1990). Also, in the concept of synfire chains, synchronous activity that propagates through the network produces precise firing patterns across different assemblies (Abeles, 1991). Furthermore, on the temporal micro-level, coincident activity can only be defined with respect to a maximal jitter (Grün *et al.*, 1999) in which spikes may be ordered systematically, such that temporal order could be hidden within activity that is classified as coincident. Similarly, as mentioned before, small phase offsets in oscillatory activity can either be interpreted as virtual zero delays or investigated more closely for systematic variations, which is the principal intention of the present work.

A.2 ‘CCH’ - Terminology

The term ‘cross correlation histogram’ (CCH) is used in accordance with the neurophysiological literature and does not precisely match the mathematical definition. Mathematically, the term ‘cross covariance’ would be more appropriate. For two time series $f(t)$ and $g(t)$ in continuous time, the cross covariance CCV at time lag τ is described as

$$\int f(t)g(t + \tau)dt,$$

which simplifies directly to equation (1.1) for the discrete time case, with $f = S_1$, $g = S_2$ and $\tau \in \mathfrak{L}_\delta^L$. The cross covariance is only identical to the cross correlation if both f and g have mean zero and variance 1. Although this does not hold for spike trains in general, the term ‘cross correlation’, or ‘cross correlogram’, is wide-spread. On the other hand, the terminology in the literature is not strict, and the same name can refer to different quantities. In this work, ‘CCH’ always denotes an empirical quantity computed between two discrete time spike trains as defined in equation (1.1). In Part III, empirical CCHs are distinguished from the theoretically derived ‘cross correlation function’ (‘CCF’).

A.3 The sample data set

To show the practical relevance of the proposed analysis methods, they are demonstrated exemplarily by application to a sample data set obtained from electrophysiological recordings from the visual cortex of an anesthetized cat under visual stimulation. Multi-unit responses that contain the activity of about 1-5 single neurons (König *et al.*, 1995) were recorded extra-cellularly and in parallel at each of 16 electrodes (channels/ units). Fourteen electrodes showed good responses and were selected for the analysis. The original time resolution was given by the sampling frequency of 1/32 ms. Figure A.1 shows an exemplary raster plot of five spike trains recorded in parallel.

Responses were recorded under visual stimulation with six different stimuli (single and conflicting moving bars, Fig. A.2). Each stimulus was presented 20 times, its presentation randomized within the total $120 = 6 \cdot 20$ trials of all stimulation conditions. Each trial lasted for 6 seconds, including spontaneous activity and responses to stimulus onset and stimulus end, but only two seconds in the middle of the trial were chosen for the analysis (Fig. A.3). This time window is characterized by the highest rate responses, and most spike trains showed ‘repetitive burst discharges’ (Singer and Gray, 1995).

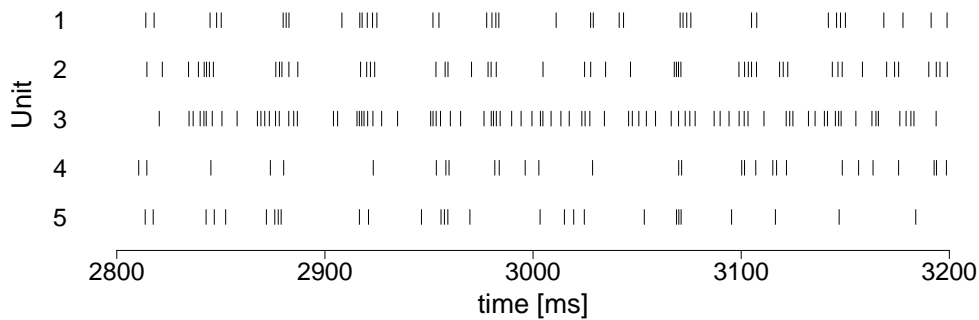


Figure A.1: Raster plot of spike trains recorded simultaneously in 5 electrodes.

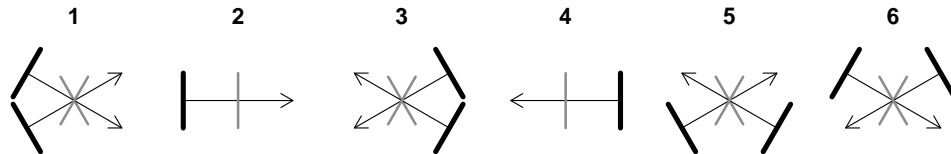


Figure A.2: The six different visual stimuli in the sample data set. Bars (thick black lines) moved into the directions indicated by arrows. Conflicting bars moved simultaneously, crossing at the receptive field (RF). Positions of bars in the center of the RF are indicated by gray bars.

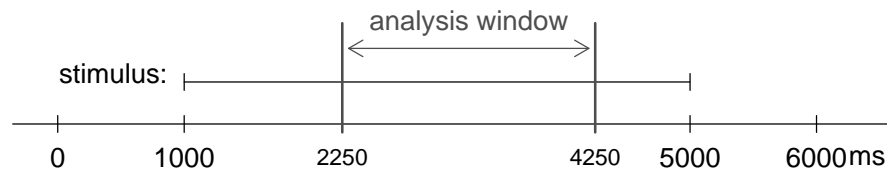


Figure A.3: The time course of a trial. A total duration of 6 seconds was recorded, including 1 s spontaneous activity at the beginning and end of the trial and 4 s stimulus presentation. The time when the stimulus crossed the RF and evoked high rate responses (2250-4250) was chosen as the analysis window.

List of Figures

1.1	Formal representation of a spike train	1
1.2	Schematic representation: Computation of a raw CCH	3
1.3	Data structure: CCHs	3
3.1	Model 1: An example CCH with a Gabor and a cosine function . .	14
3.2	Analysis of residuals between CCHs and fitted cosine functions . .	18
4.1	Illustration of the parameters s and f	28
4.2	Influence of N and σ/A on the estimation precision of φ	28
4.3	Dependence of G on the visible part of the period for $s = 0$	31
4.4	Dependence of G on the visible part of the period for $s \neq 0$	32
4.5	Decrease of $\text{Var}(\hat{\varphi})$ with the size of the analysis window	33
4.6	Distributions of parameter estimates, stimulation condition 1	36
4.7	Distributions of estimates for the typical parameter set	37
4.8	Usefulness of formula and construction of confidence intervals	39
4.9	Limitations of the asymptotic formula for binned data	40
4.10	Experimental and theoretical variability of phase offsets	43
6.1	Model 2: Additivity of phase offsets	50
7.1	Estimation of model distances	58
7.2	Decomposition of Φ by orthogonal projection	60
8.1	Linear configuration in stimulation condition 1	79
8.2	Representation of phase offsets by model distances	80
8.3	Linear configuration extracted from subsets of measurements	81
8.4	Linear configuration: ML-estimates under heteroscedasticity	82
8.5	The model applied to randomly permuted phase offsets	84
8.6	Graphic comparison of configurations	87

10.1	Features of oscillatory CCHs	94
11.1	Firing intensity of spikes within a packet	100
11.2	Doubly stochastic construction of a spike train	102
11.3	Summary of the spike train model	104
12.1	Derivation of the Palm distribution	108
12.2	Decomposition of a CCF	115
12.3	Dependence of the CCF shape on σ	118
12.4	Dependence of the CCF shape on τ	119
12.5	Asymmetric CCFs	120
13.1	Estimation algorithm for IPIs in the sample data set	125
13.2	Distributions of IPIs and of spikes in packets	126
13.3	Firing rates within and across trials	128
13.4	Theoretical ACFs fitted to experimental ACHs	130
13.5	Analysis of residuals	132
13.6	Variability of estimated parameters in the fit	133
13.7	CCHs and theoretically predicted CCFs with good fits	135
13.8	CCHs and theoretically predicted CCFs with suboptimal fits	136
13.9	Effects of rate correction	138
13.10	Comparison of recorded and simulated spike trains	140
13.11	ACHs and CCHs derived from simulated spike trains	142
14.1	Linear configurations of phase offsets vs. parameters in the spike train model	146
14.2	Phase offsets of cosine functions fitted to CCFs.	147
14.3	Optimal and suboptimal fits of the central CCH peak	150
A.1	Raster plot of 5 spike trains recorded simultaneously	159
A.2	The six different visual stimuli in the sample data set	160
A.3	The time course of a trial	160
A.4	Datenstruktur: Spike Trains und CCHs	178
A.5	Modell 1	180
A.6	Modell 2	181
A.7	Modell 3	184

List of Abbreviations

ACF	auto correlation function
ACH	auto correlation histogram
CCF	cross correlation function
CCH	cross correlation histogram
IPI	inter packet interval
PT	preferred firing time
POP	packet onset process

Notation

general

S, S_1, S_2, \dots	spike trains
T	length of spike train in ms
δ	time resolution / bin size in ms
L	maximal analyzed spike delay in CCH
N	number of data points in a CCH
Z, Z_{ij}	standard normally distributed random variables
φ, φ_{ij}	phase offset in a CCH (between units i and j)
$\mathcal{N}(\mu, \sigma^2)$	normal distribution with mean μ and variance σ^2

Part I

A, ω	amplitude and oscillation frequency of a cosine function
β_0	additive constant of a cosine function
s	shift of a cosine in percent of the period
f	visible fraction of the cosine period
σ^2	variance of the noise around the cosine
σ_φ^2	variance of the phase offset φ

Part II

$\mathbf{x} = (x_1, \dots, x_n)$	unit positions on the time axis
$\Delta = (\delta_{ij})_{i < j}$	model distances between unit positions
$\Phi = (\varphi_{ij})_{i < j}$	vector of phase offsets
Q	error sum of squares
\mathcal{M}_n	subspace of \mathbb{R}^m in which model distances are additive
σ^2	global variance of measurement error of phase offsets
σ_{ij}^2	variance of measurement error of phase offset φ_{ij}

Part III

$\mathbb{B} = (B_b)_{b \in \mathbb{Z}}$	packet onset process with $\mathcal{N}(\mu, \sigma^2)$ -distributed IPIs
$X_{\mathbb{B}}$	cluster point process with packets starting at B_b
α_j	expected number of spikes in each packet in unit j
β_j	background intensity in unit j
τ_j	speed of decay of packet spiking intensity in unit j
$D_{0i}(s)$	spike pairs with delay s in packets at B_0 / B_i

Bibliography

- M. Abeles and I. Gat. Detecting precise firing sequences in experimental data. *Journal of Neuroscience Methods*, 107(1-2):141–154, 2001.
- M. Abeles and G. L. Gerstein. Detecting spatiotemporal firing patterns among simultaneously recorded single neurons. *Journal of Neurophysiology*, 60(3):909–924, 1988.
- M. Abeles, H. Bergman, E. Margalit, and E. Vaadia. Spatiotemporal firing patterns in the frontal cortex of behaving monkeys. *Journal of Neurophysiology*, 70(4):1629–1638, 1993.
- M. Abeles. *Local cortical circuits: An electrophysiological study*. Springer, Berlin, Heidelberg, New York, 1982.
- M. Abeles. Role of the cortical neuron: integrator or coincidence detector? *Israel Journal of Medical Sciences*, 18:83–92, 1982.
- M. Abeles. *Corticonics: Neural circuits of the cerebral cortex*. Cambridge University Press, Cambridge, 1991.
- A. M. H. J. Aertsen and G. L. Gerstein. Evaluation of neuronal connectivity: Sensitivity of cross-correlation. *Brain Research*, 340(2):341–354, 1985.
- A. M. H. J. Aertsen, G. L. Gerstein, M. K. Habib, and G. Palm. Dynamics of neuronal firing correlation: Modulation of “effective connectivity”. *Journal of Neurophysiology*, 61(5):900–917, 1989.
- S. Amari, H. Nakahara, S. Wu, and Y. Sakai. Synchronous firing and higher-order interactions in neuron pool. *Neural Computation*, 15(1):127–142, 2003.

- W. Bair, C. Koch, W. Newsome, and K. Britten. Power spectrum analysis of bursting cells in area MT in the behaving monkey. *The Journal of Neuroscience*, 14(5):2870–2892, 1994.
- S. N. Baker and G. L. Gerstein. Improvements to the sensitivity of gravitational clustering for multiple neuron recordings. *Neural Computation*, 12(11):2597–2620, 2000.
- S. N. Baker and G. L. Gerstein. Determination of response latency and its application to normalization of cross-correlation measures. *Neural Computation*, 13(6):1351–1377, 2001.
- S. N. Baker and R. N. Lemon. Precise spatiotemporal repeating patterns in monkey primary and supplementary motor areas occur at chance levels. *Journal of Neurophysiology*, 84(4):1770–1780, 2000.
- H. B. Barlow. Single units and sensation: A neuron doctrine for perceptual psychology? *Perception*, 1(4):371–394, 1972.
- Y. M. M. Bishop, S. E. Fienberg, and P. W. Holland. *Discrete multivariate analysis: theory and practice*. The MIT Press, Cambridge, London, 1975. With the collaboration of Richard J. Light and Frederick Mosteller.
- V. Braitenberg and A. Schüz. *Anatomy of the Cortex. Statistics and geometry*. Springer Verlag, Berlin, Heidelberg, New York, 1991.
- C. D. Brody. Disambiguating different covariation types. *Neural Computation*, 11(7):1527–1535, 1999.
- C. D. Brody. Correlations without synchrony. *Neural Computation*, 11(7):1537–1551, 1999.
- E. N. Brown, R. E. Kass, and P. P. Mitra. Multiple neural spike train data analysis: state-of-the-art and future challenges. *Nature Neuroscience*, 7(5):456–461, 2004.
- C. E. Carr and M. Konishi. A circuit for detection of interaural time differences in the brain stem of the barn owl. *The Journal of Neuroscience*, 10(10):3227–3246, 1990.
- D. R. Cox and P. A. W. Lewis. *The statistical analysis of series of events*. Methuen & Co. Ltd., London, 1966.

- A. Delorme and S. J. Thorpe. Face identification using one spike per neuron: resistance to image degradations. *Neural Networks*, 14(6-7):795–803, 2001.
- A. Delorme. Early cortical orientation selectivity: How fast inhibition decodes the order of spike latencies. *Journal of Computational Neuroscience*, 15(3):357–365, 2003.
- E. A. DeYoe and D. C. Van Essen. Concurrent processing streams in monkey visual cortex. *Trends in Neurosciences*, 115(5):219–226, 1988.
- M. Diesmann, M.-O. Gewaltig, and A. Aertsen. Stable propagation of synchronous spiking in cortical neural networks. *Nature*, 402(6761):529–533, 1999.
- R. Eckhorn, R. Bauer, W. Jordan, M. Brosch, W. Kruse, M. Munk, and H. J. Reitboeck. Coherent oscillations: A mechanism of feature linking in the visual cortex. *Biological Cybernetics*, 60(2):121–130, 1988.
- J. J. Eggermont, G. M. Smith, and D. Bowman. Spontaneous burst firing in cat primary auditory cortex: Age and depth dependence and its effect on neural interaction measures. *Journal of Neurophysiology*, 69(4):1292–1313, 1993.
- A. K. Engel, A. K. Kreiter, P. König, and W. Singer. Interhemispheric synchronization of oscillatory responses in cat visual cortex. *Science*, 252(5009):1177–1179, 1991.
- A. K. Engel, P. König, A. K. Kreiter, T. B. Schillen, and W. Singer. Temporal coding in the visual cortex: New vistas on integration in the nervous system. *Trends in Neurosciences TINS*, 15(6):218–226, 1992.
- W. Feller. *An introduction to probability theory and its applications. Vol. II.* Second edition. John Wiley & Sons Inc., New York, 1971.
- G. L. Gerstein and A. M. H. J. Aertsen. Representation of cooperative firing activity among simultaneously recorded neurons. *Journal of Neurophysiology*, 54(6):1513–1528, 1985.
- G. L. Gerstein and A. M. H. J. Aertsen. Neuronal assemblies. *IEEE Transactions on Biomedical Engineering*, 36(1):4–14, 1989.
- G. L. Gerstein and N. Y.-S. Kiang. An approach to the quantitative analysis of electrophysiological data from single neurons. *Biophysical Journal*, 1:15–28, 1960.

- G. L. Gerstein and D. H. Perkel. Simultaneously recorded trains of action potentials: Analysis and functional interpretation. *Science*, 164(3881):828–830, 1969.
- G. L. Gerstein and D. H. Perkel. Mutual temporal relationships among neuronal spike trains. Statistical techniques for display and analysis. *Biophysical Journal*, 12(5):453–473, 1972.
- G. L. Gerstein, D. H. Perkel, and J. E. Dayhoff. Cooperative firing activity in simultaneously recorded populations of neurons: Detection and measurement. *The Journal of Neuroscience*, 5(4):881–889, 1985.
- G. L. Gerstein. Analysis of firing patterns in single neurons. *Science*, 131(3416):1811–1812, 1960.
- P. M. Gochin, E. K. Miller, C. G. Gross, and G. L. Gerstein. Functional interactions among neurons in inferior temporal cortex of the awake macaque. *Experimental Brain Research*, 84(3):505–516, 1991.
- C. M. Gray and W. Singer. Stimulus-specific neuronal oscillations in orientation columns of cat visual cortex. *Proceedings of the National Academy of Sciences of the United States of America*, 86(5):1698–1720, 1989.
- C. M. Gray, P. König, A. K. Engel, and W. Singer. Oscillatory responses in cat visual cortex exhibit inter-columnar synchronization which reflects global stimulus properties. *Nature*, 338(6213):334–337, 1989.
- C. M. Gray, A. K. Engel, P. König, and W. Singer. Synchronization of oscillatory neuronal responses in cat striate cortex: Temporal properties. *Visual Neuroscience*, 8(4):337–347, 1992.
- S. Grün, M. Diesmann, F. Grammont, A. Riehle, and A. Aertsen. Detecting unitary events without discretization of time. *Journal of Neuroscience Methods*, 94:67–79, 1999.
- S. Grün, M. Diesmann, and A. Aertsen. 'Unitary events' in multiple single-neuron activity. I. Detection and significance. *Neural Computation*, 14(1):43–80, 2002.
- S. Grün, M. Diesmann, and A. Aertsen. 'Unitary events' in multiple single-neuron activity. II. Non-stationary data. *Neural Computation*, 14(1):81–119, 2002.

- D. O. Hebb. *The organization of behavior: A Neuropsychological Theory*. John Wiley & Sons, New York, 1949.
- J. J. Hopfield and C. D. Brody. What is a moment? Transient synchrony as a collective mechanism for spatiotemporal integration. *Proceedings of the National Academy of Sciences of the United States of America*, 98(3):1282–1287, 2001.
- J. J. Hopfield. Pattern recognition computation using action potential timing for stimulus representation. *Nature*, 376(6535):33–36, 1995.
- D. H. Hubel and T. N. Wiesel. Receptive fields, binocular interaction and functional architecture in the cat's visual cortex. *Journal of Physiology*, 160:106–154, 1962.
- Y. Ikegaya, G. Aaron, R. Cossart, D. Aronov, I. Lampl, D. Ferster, and R. Yuste. Synfire chains and cortical songs: Temporal modules of cortical activity. *Science*, 304(5670):559–564, 2004.
- L. A. Jeffress. A place theory of sound localization. *Journal of Comparative and Physiological Psychology*, 41:35–39, 1948.
- R. S. Johansson and I. Birznieks. First spikes in ensembles of human tactile afferents code complex spatial fingertip events. *Nature Neuroscience*, 7(2):170–177, 2004.
- P. Kaluzny, R. Tarnecki, and W. Zmyslowski. Multiple spike-train analysis using mutual interval matrix. *Journal of Neuroscience Methods*, 40(2-3):149–153, 1991.
- E. R. Kandel, J. H. Schwartz, and T. M. Jessell. *Neurowissenschaften. Eine Einführung*. Spektrum akademischer Verlag, Heidelberg, 1996.
- Y. Kaneoke and J. L. Vitek. Burst and oscillation as disparate neuronal properties. *Journal of Neuroscience Methods*, 68:211–223, 1996.
- B. Karmon and H. Bergman. Detection of neuronal periodic oscillations in the basal ganglia of normal and parkinsonian monkeys. *Israel Journal of Medical Sciences*, 29:570–579, 1993.
- R. E. Kass and V. Ventura. A spike-train probability model. *Neural Computation*, 13(8):1713–1720, 2001.

- P. König, A. K. Engel, P. R. Roelfsema, and W. Singer. How precise is neuronal synchronization? *Neural Computation*, 7(3):469–485, 1995.
- P. König, A. K. Engel, and W. Singer. Integrator or coincidence detector? The role of the cortical neuron revisited. *Trends in Neurosciences*, 19(4):130–137, 1996.
- P. König. A method for the quantification of synchrony and oscillatory properties of neuronal activity. *Journal of Neuroscience Methods*, 54(1):31–37, 1994.
- A. K. Kreiter and W. Singer. Stimulus-dependent synchronization of neuronal responses in the visual cortex of the awake macaque monkey. *The Journal of Neuroscience*, 16(7):2381–2396, 1996.
- A. U. Larkman. Dendritic morphology of pyramidal neurones of the visual cortex of the rat: III. Spine distributions. *The Journal of Comparative Neurology*, 306(1):332–343, 1991.
- C. R. Legendy and M. Salcman. Bursts and recurrences of bursts in the spike trains of spontaneously active striate cortex neurons. *Journal of Neurophysiology*, 53(4):926–939, 1985.
- R. Lestienne and H. C. Tuckwell. The significance of precisely replicating patterns in mammalian CNS spike trains. *Neuroscience*, 82(2):315–336, 1998.
- R. Lestienne. Determination of the precision of spike timing in the visual cortex of anaesthetised cats. *Biological Cybernetics*, 74(1):55–61, 1996.
- A. Liemant, K. Matthes, and A. Wakolbinger. *Equilibrium distributions of branching processes*, volume 34 of *Mathematics and its Applications (East European Series)*. Kluwer Academic Publishers Group, Dordrecht, 1988.
- B. G. Lindsey, K. F. Morris, R. Shannon, and G. L. Gerstein. Repeated patterns of distributed synchrony in neuronal assemblies. *Journal of Neurophysiology*, 78(3):1714–1719, 1997.
- Z. F. Mainen and T. J. Sejnowski. Reliability of spike timing in neocortical neurons. *Science*, 268(5216):1503–1506, 1995.
- L. Martignon, H. von Hasseln, S. Grün, A. Aertsen, and G. Palm. Detecting higher-order interactions among the spiking events in a group of neurons. *Biological Cybernetics*, 73(1):69–81, 1995.

- W. J. Melssen and W. J. M. Epping. Detection and estimation of neural connectivity based on crosscorrelation analysis. *Biological Cybernetics*, 57(6):403–414, 1987.
- J. Møller and G. L. Torrisi. Generalised shot noise Cox processes. *Advances in Applied Probability*, 37(1):48–74, 2005.
- G. P. Moore, D. H. Perkel, and J. P. Segundo. Statistical analysis and functional interpretation of neuronal spike data. *Annual Review of Physiology*, 28:493–522, 1966.
- G. P. Moore, J. P. Segundo, D. H. Perkel, and H. Levitan. Statistical signs of synaptic interaction in neurons. *Biophysical Journal*, 10(9):876–900, 1970.
- M. Nawrot, A. Aertsen, and S. Rotter. Single-trial estimation of neuronal firing rates: From single-neuron spike trains to population activity. *Journal of Neuroscience Methods*, 94:81–92, 1999.
- L. G. Nowak, M. H. J. Munk, J. I. Nelson, A. C. James, and J. Bullier. Structural basis of cortical synchronization. I. Three types of interhemispheric coupling. *Journal of Neurophysiology*, 74(6):2379–2400, 1995.
- Q. Pauluis. Statistical signs of common inhibitory feedback with delay. *Neural Computation*, 12(11):2513–2518, 2000.
- D. H. Perkel, G. L. Gerstein, and G. P. Moore. Neuronal spike trains and stochastic point processes I. The single spike train. *Biophysical Journal*, 7(4):391–418, 1967.
- D. H. Perkel, G. L. Gerstein, and G. P. Moore. Neuronal spike trains and stochastic point processes II. Simultaneous spike trains. *Biophysical Journal*, 7(4):419–440, 1967.
- D. H. Perkel, G. L. Gerstein, M. S. Smith, and W. G. Tatton. Nerve-impulse patterns: a quantitative display technique for three neurons. *Brain Research*, 100(2):271–296, 1975.
- D. I. Perrett, E. T. Rolls, and W. Caan. Visual neurones responsive to faces in the monkey temporal cortex. *Experimental Brain Research*, 47(3):329–342, 1982.

- Y. Prut, E. Vaadia, H. Bergman, I. Haalman, H. Slovin, and M. Abeles. Spatiotemporal structure of cortical activity: Properties and behavioral relevance. *Journal of Neurophysiology*, 79(6):2857–2874, 1998.
- P. Reinagel and R. C. Reid. Temporal coding of visual information in the thalamus. *The Journal of Neuroscience*, 20(14):5392–5400, 2000.
- P. Reinagel and R. C. Reid. Precise firing events are conserved across neurons. *The Journal of Neuroscience*, 22(16):6837–6841, 2002.
- P. Reinagel, D. Godwin, S. M. Sherman, and C. Koch. Encoding of visual information by LGN bursts. *Journal of Neurophysiology*, 81:2558–2569, 1999.
- A. Riehle, S. Grün, M. Diesmann, and A. Aertsen. Spike synchronization and rate modulation differentially involved in motor cortical function. *Science*, 278(5345):1950–1953, 1997.
- R. W. Rodieck, Kiang N. Y.-S., and G. L. Gerstein. Some quantitative methods for the study of spontaneous activity of single neurons. *Biophysical Journal*, 2(4):351–368, 1962.
- P. R. Roelfsema, A. K. Engel, P. König, and W. Singer. Visuomotor integration is associated with zero time-lag synchronization among cortical areas. *Nature*, 385(6612):157–161, 1997.
- G. Schneider and S. Grün. Analysis of higher-order correlations in multiple parallel processes. *Neurocomputing*, 52-54:771–777, 2003.
- G. Schneider and D. Nikolić. Detection and assessment of near-zero delays in neuronal spiking activity. *Journal of Neuroscience Methods*, 152:97–106, 2006.
- G. Schneider, M. N. Havenith, and D. Nikolić. Spatio-temporal structure in large neuronal networks detected from cross correlation. *Neural Computation*, accepted for publication, 2006.
- W. Singer and C. M. Gray. Visual feature integration and the temporal correlation hypothesis. *Annual Review of Neuroscience*, 18:555–586, 1995.
- W. Singer. Synchronization of cortical activity and its putative role in information processing and learning. *Annual Review of Physiology*, 55:349–374, 1993.

- D. R. Smith and G. K. Smith. A statistical analysis of the continual activity of single cortical neurones in the cat unanaesthetized isolated forebrain. *Biophysical Journal*, 5(1):47–74, 1965.
- D. Stoyan, W. S. Kendall, and J. Mecke. *Stochastic geometry and its applications*. Wiley Series in Probability and Mathematical Statistics: Applied Probability and Statistics. John Wiley & Sons Ltd., Chichester, 1987.
- B. L. Strehler and R. Lestienne. Evidence on precise time-coded symbols and memory of patterns in monkey cortical neuronal spike trains. *Proceedings of the National Academy of Sciences of the United States of America*, 83(24):9812–9816, 1988.
- D. C. Tam, T. J. Ebner, and C. K. Knox. Conditional cross-interval correlation analyses with applications to simultaneously recorded cerebellar purkinje neurons. *Journal of Neuroscience Methods*, 23:23–33, 1988.
- S. Thorpe, D. Fize, and C. Marlot. Speed of processing in the human visual system. *Nature*, 381(6582):520–522, 1996.
- K. Toyama, M. Kimura, and K. Tanaka. Cross-correlation analysis of interneuronal connectivity in cat visual cortex. *Journal of Neurophysiology*, 46(2):191–201, 1981.
- R. D. Traub, M. A. Whittington, and J. G. R. Jefferys. Gamma oscillation model predicts intensity coding by phase rather than frequency. *Neural Computation*, 9(6):1251–1264, 1997.
- D. Y. Ts'o, C. D. Gilbert, and T. N. Wiesel. Relationships between horizontal interactions and functional architecture in cat striate cortex as revealed by cross-correlation analysis. *The Journal of Neuroscience*, 6(4):1160–1170, 1986.
- W. M. Usrey and R. C. Reid. Synchronous activity in the visual system. *Annual Review of Physiology*, 61:435–456, 1999.
- E. Vaadia, I. Haalman, M. Abeles, H. Bergman, Y. Prut, H. Slovin, and A. Aertsen. Dynamics of neuronal interactions in monkey cortex in relation to behavioural events. *Nature*, 373(6514):515–518, 1995.
- R. Van Rullen and S. J. Thorpe. Rate coding versus temporal order coding: What the retinal ganglion cells tell the visual cortex. *Neural Computation*, 13(6):1255–1283, 2001.

- R. Van Rullen, J. Gautrais, A. Delorme, and S. J. Thorpe. Face processing using one spike per neurone. *BioSystems*, 48(1-3):229–239, 1998.
- V. Ventura. Testing for and estimating latency effects for poisson and non-poisson spike trains. *Neural Computation*, 16(11):2323–2349, 2004.
- C. von der Malsburg. The correlation theory of brain function. *Internal Report 81-2. Max-Planck-Institute for Biophysical Chemistry. online at: <http://www.neuroinformatik.ruhr-uni-bochum.de/ini/VDM/PUBLIST/1981/>*, 1981.
- T. Wennekers and G. Palm. Cell assemblies, associative memory and temporal structure in brain signals. In R. Miller, editor, *Time and the brain. Conceptual Advances in Brain Research*, volume 3, pages 251–273. Harwood Academic Publishers, 2000.
- A. W. Wiegner and M. M. Wierzbicka. A method for assessing significance of peaks in cross-correlation histograms. *Journal of Neuroscience Methods*, 22(2):125–131, 1987.
- R. Wyman. Probabilistic characterization of simultaneous nerve impulse sequences controlling dipteran flight. *Biophysical Journal*, 5(4):447–471, 1965.

Zusammenfassung

Überblick

Spike Trains - Punktprozesse Eine zentrale Frage auf dem Gebiet der Neurowissenschaften betrifft die Mechanismen bei der Verarbeitung und Integration komplexer Informationen. Daran ist eine hohe Anzahl an Nervenzellen beteiligt, die mit Hilfe von kurzfristigen Ausschlägen des Membranpotentials ('Spikes') kommunizieren. Bei der experimentellen Gewinnung von Spikezeitpunkten kann nur auf einem Gitter bestimmt werden, ob im betroffenen Intervall $[j\delta, (j+1)\delta)$ mindestens ein Spike aufgetreten ist. Daher werden die experimentell beobachteten Feuerzeiten einer Zelle als zeitdiskrete binäre Zeitreihen ('Spike Trains') dargestellt:

$$S(j\delta) = \begin{cases} 1 & \text{falls mindestens 1 Spike in } [j\delta, (j+1)\delta), \\ 0 & \text{sonst.} \end{cases}$$

Zeitliche Korrelationen Aufgrund der hohen Vernetzung der Nervenzellen im Kortex wird der zeitlichen Koordination der Feueraktivität eine besondere Rolle zugemessen. Um diese zu untersuchen, gewinnt man parallel die Spike Trains S_1, \dots, S_n von n Zellen (vgl. Fig. A.4 A, $n = 2$). Zur Analyse zeitlicher Korrelationen zwischen zweien solcher Prozesse S_1, S_2 wird in der Praxis häufig das sogenannte Kreuzkorrelations-Histogramm ('CCH') eingesetzt. Es stellt für alle Zeitdifferenzen $\ell \in \{k\delta \mid k \in \mathbb{Z}, |k\delta| \leq L\}$ mit $L > 0$ die Häufigkeiten dar, mit denen auf einen Spike in S_1 nach ℓ Zeiteinheiten ein Spike in S_2 folgt:

$$H_{S_1 S_2}(\ell) := \sum_j S_1(j\delta) S_2(j\delta + \ell).$$

Figur A.4 B zeigt ein Beispiel eines CCHs für zwei experimentell gewonnene Spike Trains ($L = 80$ ms).

Programm Da CCHs in den Anwendungen sehr verbreitet sind, sollen in dieser Arbeit verschiedene Aspekte dieser Statistik beleuchtet werden. Um die relevanten Parameter zu schätzen, werden an die in der Regel verrauschten Daten geeignete Kurven angepasst.

Im ersten Teil wird insbesondere die Position des Maximums im CCH untersucht, die auch als ‘Phase’ bezeichnet wird. Oft nimmt das CCH sein globales Maximum nahe $\ell = 0$ an, was darauf hindeutet, dass die Spikes beider Zeitreihen tendenziell zeitgleich auftreten. Wie in Figur A.4 C zu sehen ist, kann die Phase von 0 abweichen. Kleine Abweichungen der Phasenschätzung vom Wert 0 wurden bisher der Messungenauigkeit zugeschrieben und in der Regel nicht weiter analysiert. In den letzten Jahren häufen sich jedoch die Hinweise darauf, dass die Informationsverarbeitung mit hoher zeitlicher Präzision geschieht und damit auch kleine Zeitverzögerungen von Belang sein könnten. Daher ist es wichtig, die Varianz der Phasenschätzung so genau wie möglich zu bestimmen, um entscheiden zu können, ob kleine Abweichungen durch Messfehler zustande kommen könnten. Dazu wird im ersten Teil dieser Arbeit eine Methode entwickelt, mit der sowohl die Phase geschätzt als auch die Varianz dieser Schätzung bestimmt werden kann.

Die entwickelten Methoden werden auf einen Datensatz aus $n = 14$ experimentell gewonnenen Spike Trains angewendet. Auch sehr kleine Phasenverschiebungen von wenigen Millisekunden sind im analysierten Datensatz kaum durch Messungenauigkeiten zu erklären, da die Standardabweichung $\sigma_{\hat{\varphi}}$ der Phasenschätzung meist deutlich kleiner ist als die geschätzte Phase $|\hat{\varphi}|$ selbst. Zusätzlich scheinen die Phasen in systematischer Weise zwischen verschiedenen Stimulationsbedingungen zu variieren, was auf eine präzise zeitliche Koordination zwischen den Neuronen hindeutet. Um diese zu analysieren, wird in Teil II der Arbeit versucht, die in $\binom{n}{2}$ Phasen zwischen n Spike Trains enthaltene paarweise Information zu komprimieren. Dies geschieht auf der Basis der Annahme, dass für alle Triplets von Spike Trains S_i, S_j, S_k die entsprechenden Phasen annähernd additiv sind, d.h. dass $\varphi_{ik} \approx \varphi_{ij} + \varphi_{jk}$. Ist die Additivitätsannahme erfüllt, kann die Menge der $\binom{n}{2}$ Phasen in einer $(n - 1)$ -dimensionalen Darstellung erfasst werden, bei der jedem Spike Train S_i ein Wert $x_i \in \mathbb{R}$ zugeordnet wird, so dass jede Phase φ_{ij} der paarweisen Differenz $x_j - x_i$ entspricht. In Teil II wird ein stochastisches Modell entwickelt, mit dem die x_i auch für einen Satz nicht perfekt additiver Phasen geschätzt werden können, um die Phasen so gut wie möglich durch paarweise Differenzen innerhalb der ‘linearen Konfiguration’ $\mathcal{C} = \{\hat{x}_1, \dots, \hat{x}_n\}$ zu repräsentieren. Bei der Anwendung dieses Modells auf den experimentellen Datensatz zeigt sich ein starker Anteil additiver Struktur in den gemessenen Phasen: Die Abweichungen der Phasen φ_{ij} von den geschätzten Modelldistanzen $\hat{x}_j - \hat{x}_i$ in der linearen Konfiguration sind minimal. Zusätzlich sind im analysierten Datensatz zwischen Konfigurationen $\mathcal{C}_1, \mathcal{C}_2$ aus Phasenmengen unterschiedlicher Stimulationsbedingungen deutliche Unterschiede zu erkennen.

Die in den ersten beiden Teilen vorgestellten Methoden sind für die experimentelle Neurophysiologie aus zweierlei Gründen besonders interessant. Zum einen bauen sie auf der verbreiteten paarweisen Analysetechnik der CCHs auf, und zum anderen erlauben sie, Aspekte der zeitlichen Koordination einer hohen Anzahl paralleler Spike Trains auf effiziente Weise zu analysieren. Da die Methoden jedoch ausschließlich auf wenigen Parametern der paarweisen CCHs beruhen, erlauben ihre Ergebnisse nur begrenzt, Rückschlüsse auf die Natur der zugrunde liegenden Prozesse zu ziehen. Insbesondere bleibt unklar, welche Eigenschaften der Spike Trains die extrahierten Phänomene kleiner Phasen und ihrer additiven Struktur verursachen könnten. Daher wird im dritten Teil ein parametrisches stochastisches Modell für n Spike Trains angegeben, mit dem untersucht werden kann, welche Eigenschaften der Prozesse zur Ausprägung verschiedener Formparameter oszillatorischer CCHs beitragen können. Dazu werden n Spike Trains S_1, \dots, S_n im Rahmen eines doppelt stochastischen Modells durch parallele Punktprozesse X_1, \dots, X_n modelliert. Das Modell generiert im ersten Schritt einen stationären Punktprozess $\mathbb{B} = (\dots, B_{-1}, B_0, B_1, \dots)$ mit bevorzugter Intervalllänge μ . Gegeben \mathbb{B} , werden n unabhängige, inhomogene Poissonprozesse betrachtet mit Intensitäten

$$\rho_{\mathbb{B}}^j(t) := \frac{\alpha_j}{\tau_j} \sum_{b \in \mathbb{Z}, B_b \leq t} e^{-\frac{(t-B_b)}{\tau_j}} + \beta_j, \quad j = 1, \dots, n.$$

Man stellt sich die B_b als globale Paketanfangszeiten vor, die in allen Prozessen simultane Pakete mit exponentiell abfallender Intensität auslösen. Anhand dieses Modells können relevante geometrische Eigenschaften des CCHs zweier Punktprozesse X_i, X_j in Beziehung zu den zugrunde liegenden Parametern α, β, τ, μ und σ gesetzt werden. Der Parameter μ beeinflusst vor allem die Position des ersten Seitenpeaks. Die Geschwindigkeit, mit der die Höhe der Seitenpeaks abfällt, wächst mit σ , und kleine Werte von τ produzieren hohe und schmale Peaks. Insbesondere erklärt sich eine von Null abweichende Phase im CCH zwischen X_i und X_j durch eine Differenz der Parameter $\tau_j - \tau_i$: Für $\tau_i < \tau_j$ fällt die Intensität ρ^i nach jedem Paketanfang B_b schneller ab als die Intensität ρ^j , so dass die Spikes von X_i im Mittel früher kommen als die von X_j . Additivität lässt sich im Rahmen dieses Modells direkt durch die lineare Anordnung der Werte $\tau_i \in \mathbb{R}$ erklären.

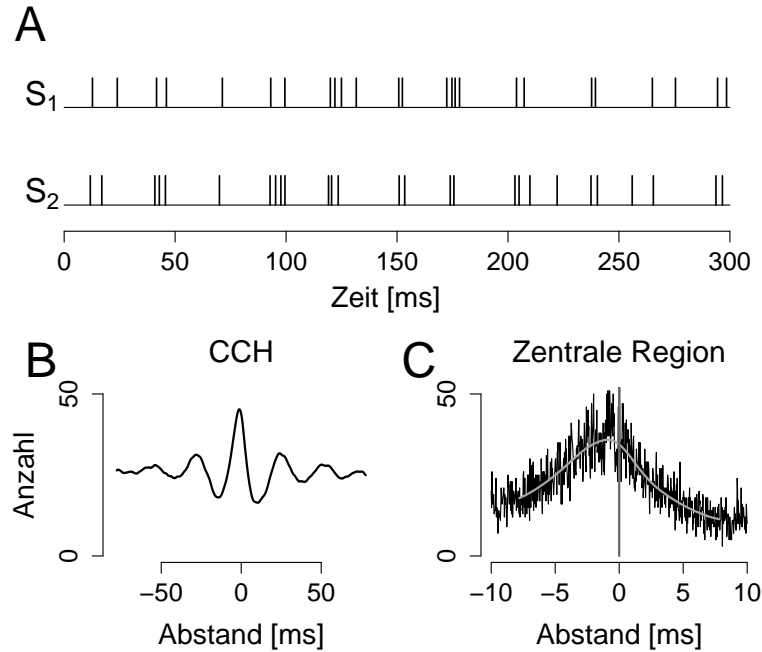


Figure A.4: Datenstruktur. A: Zwei parallele binäre Zeitreihen (Spike Trains) in diskreter Zeit. B: Ein CCH zweier Prozesse zählt für jedes $\ell \leq L$ die Anzahl der Spikepaare mit Abstand ℓ (hier: $L = 80$ ms). Das dargestellte CCH ist geglättet und hat eine oszillatorische Form: Differenzen $\ell \approx 0, \pm 25$ ms, ... werden bevorzugt; zwischenliegende Zeitdifferenzen treten seltener auf. C: Zentrale Region ($L = 10$ ms, $\delta = 1/32$ ms) mit geglätteter Kurve in grau.

Teil I

Modell 1: Kosinus mit unabhängigen, normalverteilten Rauschen

Zur Schätzung der Phase in verrauschten CCHs wird wegen der oszillatorischen Gestalt vieler experimenteller CCHs folgendes stochastische Modell zugrunde gelegt: Es wird angenommen, dass die Werte $H(\ell)$ in der zentralen Region des CCHs einer Kosinusfunktion folgen und mit unabhängigen, normalverteilten Fehlern σZ_ℓ behaftet sind:

$$H(\ell) = A \cos(\omega(\ell - \varphi)) + \beta_0 + \sigma Z_\ell, \quad (\text{Fig. A.5 A}) \quad (\text{A.1})$$

für $\ell \in \{k\delta \mid k \in \mathbb{Z}, |k\delta| \leq L\}$ mit $L > 0$. Ausgehend von diesen Annahmen wird mit einem nichtlinearen Kleinste-Quadrate-Algorithmus mit standardisierten Startwerten eine Kosinusfunktion an den zentralen Peak angepasst, um die Parameter A , ω , β_0 und die Phase φ zu schätzen. Die bei Anwendung auf einen Datensatz mit 14 parallelen Spike Trains resultierenden 91 Phasenschätzer nahmen sehr kleine Werte zwischen ± 2 Millisekunden an.

Varianz von $\hat{\varphi}$: Approximative Formel Die Varianz der Phasenschätzung lässt sich im Rahmen des Modells approximieren. Unter der Annahme, dass ω bekannt ist, folgt mit der δ -Methode, dass der Schätzer $\hat{\varphi}$ approximativ normalverteilt ist mit approximativer Varianz

$$\hat{\sigma}_{\hat{\varphi}}^2 = V(\omega, A/\sigma, N) \cdot G(s, f), \quad (\text{vgl. (4.29)-(4.33)})$$

wobei $N := \#\{k\delta \mid k \in \mathbb{Z}, |k\delta| \leq L\}$. Da V monoton fallend in jedem seiner Argumente ist, wächst die Genauigkeit der Schätzung von φ mit jedem dieser Werte. Der Term G erlaubt eine geometrische Interpretation; er hängt ab von der Verschiebung $s = \varphi/p$ des Kosinus im Verhältnis zur Periodenlänge p und vom relativen Anteil der Periodenlänge $f = 2L/p$, an den die Kosinusfunktion angepasst wird. Das wichtigste geometrische Prinzip, das aus diesen Parametern abgeleitet wird, besagt, dass die Werte $H(\ell)$ für solche ℓ , an denen die Steigung des Kosinus maximal ist, viel Information beitragen, wohingegen die Werte in der Nähe der Extrema wenig informativ sind. Daher ist der Anteil der Punkte an den Kanten im Verhältnis zum Anteil an den Extrema eine entscheidende Größe. Sie hängt von der Phase s selbst ab sowie vom analysierten Anteil der Periode, f .

Anwendbarkeit der Formel in der Praxis Um die Güte der approximativen Formel für $\hat{\sigma}_{\hat{\varphi}}$ für unbekanntes ω und für praxisrelevante Werte von N zu untersuchen, werden verrauschte Kosinusfunktionen mit realistischen Parametersätzen simuliert und ihre Phasen geschätzt. Die empirische Streuung der Phasenschätzungen $\sigma_{\hat{\varphi}}$ wird mit der Verteilung der in den Simulationen durch die Formel geschätzten Werte $\hat{\sigma}_{\hat{\varphi}}$ verglichen (Fig. A.5 B). Für einen typischen Parametersatz beträgt $\sigma_{\hat{\varphi}}$ knapp 0.2 ms oder 1% einer Periode. Die approximativen Werte $\hat{\sigma}_{\hat{\varphi}}$ haben von $\sigma_{\hat{\varphi}}$ eine typische Abweichung von nur etwa 6.5% von $\sigma_{\hat{\varphi}}$. Sowohl diese Abweichung als auch die Werte $\sigma_{\hat{\varphi}}$ selbst wachsen mit σ/A . Für alle Parametersätze ist die mit $\hat{\sigma}_{\hat{\varphi}}$ normierte Phasenschätzung approximativ normalverteilt, was die Konstruktion von Konfidenzintervallen

erlaubt. Für ein typisches $\sigma_{\hat{\varphi}}$ umfasst ein 95%-Konfidenzbereich weniger als eine Millisekunde, so dass Abweichungen der Phase im Millisekundenbereich kaum durch Messfehler zu erklären sind.

Zusätzlich wurde die Variabilität der Phasenschätzungen im experimentell gewonnenen Datensatz mit der approximativen Formel verglichen. Dazu wurde durch Teilung des Datensatzes jede Phase zwei Mal unabhängig geschätzt. Die Verteilung der Differenzen der Schätzungen, normiert an der geschätzten Standardabweichung, $Z := (\hat{\varphi}_1 - \hat{\varphi}_2) \cdot (\hat{\sigma}_{\hat{\varphi}_1}^2 + \hat{\sigma}_{\hat{\varphi}_2}^2)^{1/2}$, zeigte keine nennenswerte Abweichung von der Standardnormalverteilung, was darauf schließen lässt, dass die approximative Formel die Variabilität der Phasenschätzung im experimentellen Datensatz beschreiben kann. Daher wurden mit Hilfe der Formel zwei Mengen gepaarter Phasen aus dem experimentellen Datensatz statistisch miteinander verglichen. Dabei zeigten sich signifikante Unterschiede zwischen Mengen von Phasen, die unter verschiedenen Stimulationsbedingungen abgeleitet wurden, wohingegen Unterschiede zwischen mehrfachen Präsentationen desselben Stimulus statistisch nicht signifikant ausfielen. Diese Ergebnisse legen nahe, dass auch sehr kleine Phasenverschiebungen im Bereich weniger Millisekunden in systematischer Weise variieren können.

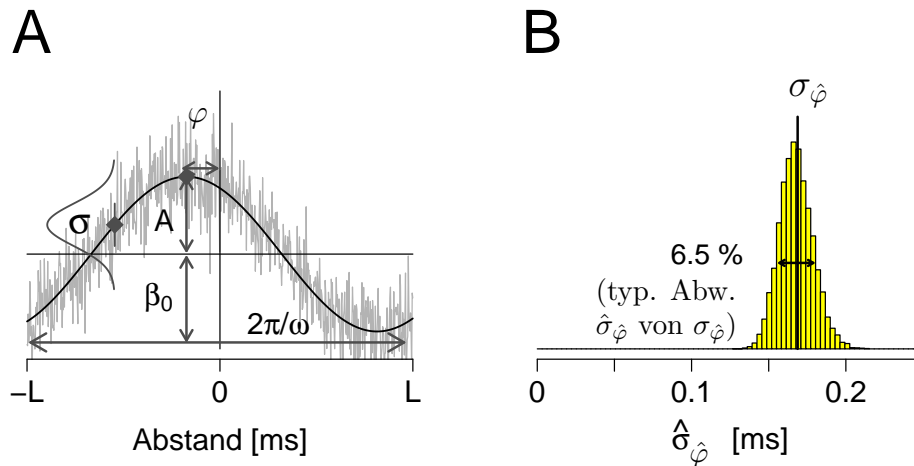


Figure A.5: Modell 1. A: Es wird angenommen, dass sich die Datenpunkte eines zentralen CCHs additiv zusammensetzen aus einer Kosinusfunktion und unabhängigen, normalverteilten Fehlern. B: Die durch Simulationen ermittelte Variabilität von $\hat{\varphi}$ wird durch die Verteilung der in den Simulationen mit der Formel geschätzten Werte $\hat{\sigma}_{\hat{\varphi}}$ gut approximiert, mit einer typischen Abweichung von 6.5% von $\sigma_{\hat{\varphi}}$.

Teil II

Modell II: Verrauschte paarweise Distanzen auf der Geraden

Um zu untersuchen, in wiefern ein Datensatz aus $\binom{n}{2}$ Phasenmessungen zwischen n Prozessen in einer additiven Struktur erfasst werden kann, wird ein lineares Modell verwendet: Jede Phase φ_{ij} sei die Messung einer Distanz $\delta_{ij} = x_j - x_i$ zwischen Punkten $x_i, x_j \in \mathbb{R}$, die mit unabhängigem, normalverteiltem Fehler mit Erwartungswert 0 und Varianz σ^2 behaftet ist:

$$\varphi_{ij} = \delta_{ij} + \sigma Z_{ij} \quad \forall 1 \leq i < j \leq n. \quad (\text{Fig. A.6 B}) \quad (\text{A.2})$$

Aus Gründen der Eindeutigkeit wird normiert auf $\sum_i x_i = 0$. Analog zur Interpretation der Phasenverschiebungen als bevorzugte Differenzen zwischen den Spikezeitpunkten zweier Prozesse werden die Positionen x_i als bevorzugte Feuerzeiten der Prozesse relativ zueinander betrachtet. Eine Menge $\mathcal{C} = \{x_1, \dots, x_n\}$ solcher Punkte auf der Zeitachse wird als lineare Konfiguration bezeichnet.

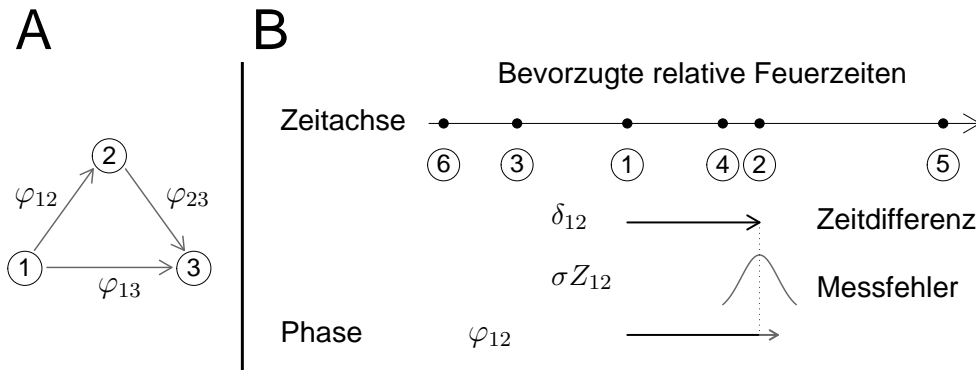


Figure A.6: Modell 2: Additivität von Phasen in einem linearen Modell. A: Drei Phasen zwischen drei Spike Trains. B: Jede Phase φ_{ij} sei eine verrauschte Messung der Differenz $\delta_{ij} = x_j - x_i$ zweier Punkte auf der Zeitachse (\mathbb{R}). Alle Messfehler seien unabhängig und normalverteilt mit Erwartungswert 0 und gleicher Varianz σ^2 .

Schätzer Der Maximum-Likelihood-Schätzer für die Position x_k hat die einfache Form

$$\hat{x}_k = \frac{1}{n} \sum_{i \neq k} \varphi_{ik}.$$

Dieser Schätzer ist auch erwartungstreu. Die daraus resultierenden Schätzer für die Modelldistanzen

$$\hat{\delta}_{ij} = \hat{x}_j - \hat{x}_i = \frac{1}{n} \left(2\varphi_{ij} + \sum_{\ell \neq i,j} (\varphi_{i\ell} + \varphi_{\ell j}) \right)$$

sind interpretierbar als gewichtete Summen aus direkten Messungen φ_{ij} und indirekten Messungen $\varphi_{i\ell} + \varphi_{\ell j}$. Sie minimieren die Fehlerquadratsumme $Q := \sum_{i < j} (\varphi_{ij} - \hat{\delta}_{ij})^2$, die die Abweichungen der Phasen von der additiven Struktur angibt und mit deren Hilfe σ erwartungstreu geschätzt werden kann mit $\hat{\sigma} = Q / \binom{n-1}{2}$. Geometrisch ist der Vektor der Schätzer der Modelldistanzen $\hat{\Delta}$ die orthogonale Projektion des Phasenvektors $\Phi \in \mathbb{R}^{\binom{n}{2}}$ auf einen $(n-1)$ -dimensionalen Unterraum, den Modellraum \mathcal{M}_n . Bei dieser Projektion wird $\hat{\Delta}$ so bestimmt, dass das Abstandsquadrat Q zwischen $\hat{\Delta}$ und Φ minimal wird.

Die im untersuchten experimentellen Datensatz gemessenen 91 Phasen konnten gut durch die geschätzten Modelldistanzen δ_{ij} repräsentiert werden (vgl. Figur 8.2 A, und entsprechend Figur 8.5 B für permutierte Phasen).

Varianzanalyse Um k lineare Konfigurationen $\mathcal{C}_1, \dots, \mathcal{C}_k$ auf Unterschiede zu testen, wird das lineare Modell erweitert. Dabei wird der Vektor der Phasen $(\Phi_1, \dots, \Phi_k) \in \mathbb{R}^{k \binom{n}{2}}$ durch wiederholte orthogonale Projektion zerlegt: Die erste Projektion auf einen $k(n-1)$ -dimensionalen Unterraum erzeugt individuelle Schätzer $(\hat{x}_i^{(\ell)})_{i=1, \dots, n}$ für jede der k Konfigurationen ($\ell = 1, \dots, k$). Eine weitere Projektion auf einen $(n-1)$ -dimensionalen Unterraum erzeugt globale Schätzer der x_i , mit denen die Nullhypothese repräsentiert wird, dass sich die zugrundeliegenden Konfigurationen nicht unterscheiden. Für eine solche Zerlegung ist die Verteilung des Quotienten der Längenquadrate bestimmter Vektoren bekannt und wird verwendet, um Unterschiede zwischen den Konfigurationen statistisch zu untersuchen. Dabei fallen Unterschiede zwischen linearen Konfigurationen aus mehrfacher Präsentation desselben Stimulus gering aus, wohingegen sich Konfigurationen aus verschiedenen Stimulationsbedingungen deutlich unterscheiden.

Eine weitere Modellerweiterung betrifft den für die Praxis wichtigen Fall, in dem nicht alle $\binom{n}{2}$ Phasen gemessen werden können. Es wird ein Gleichungssystem bereitgestellt, mit dessen Hilfe die ML-Schätzer berechnet werden können, und eine notwendige und hinreichende Bedingung für ihre Eindeutigkeit gezeigt.

Teil III

Motivation Um die Frage nach der Ursache kleiner Phasen und ihrer additiven Struktur anzugehen, wird zunächst eine grundlegendere Frage formuliert, die Eigenschaften paralleler Punktprozesse in Beziehung zu der Form ihres CCHs setzt: Mit welchen Parametern sollte man einen Punktprozess beschreiben, um die essentiellen Eigenschaften eines oszillatorischen CCHs vorhersagen zu können? Zu diesen Eigenschaften gehören nicht nur die Asymmetrie des zentralen Peaks, dargestellt durch das mittelgraue Dreieck in Figur A.7 A, sondern auch seine Höhe und Breite sowie die mit abnehmender Amplitude periodisch auftretenden lokalen Maxima.

ACHs Da das CCH primär Interaktionen zwischen zwei Prozessen beschreibt, kann es nur indirekte Informationen über die Eigenschaften der einzelnen Prozesse liefern. Aussagekräftiger ist das Autokorrelations-Histogramm ('ACH'), ein CCH eines Prozesses mit sich selbst, das ausschließlich Eigenschaften eines einzelnen Prozesses beleuchtet. Ein ACH ist im Unterschied zum CCH per Definition symmetrisch. Jedoch können die beiden anderen wichtigen Eigenschaften des CCHs auch im ACH sichtbar werden: Zum einen können sich die Anzahlen um $\ell = 0$ häufen, was darauf hindeutet, dass die Spikes sich in Paketen sammeln, und zum anderen lässt sich eine regelmäßige oszillatorische Form mit abnehmender Amplitude ausmachen, die Hinweise darauf liefert, dass die Pakete mit einer gewissen Periodizität auftreten.

Modell III: Doppelt stochastische Punktprozesse

In Teil III werden n Spike Trains S_1, \dots, S_n durch Punktprozesse X_1, \dots, X_n modelliert. Um einen Prozess X mit quasi-periodisch auftretenden Paketen zu beschreiben, wird ein doppelt stochastisches Modell verwendet: Zunächst erzeugt eine Irrfahrt auf \mathbb{R} mit unabhängigen und $\mathcal{N}(\mu, \sigma^2)$ -verteilten Intervallen ($\sigma > 0$) einen stationären Punktprozess $\mathbb{B} := (\dots, B_{-2}, B_{-1}, B_0, B_1, B_2, \dots)$. Jeder Punkt B_b löst einen Poissonschen Punktschauer mit exponentiell abfallender Rate aus. Gegeben \mathbb{B} , ist damit $X_{\mathbb{B}}$ ein inhomogener Poissonprozess mit Intensität

$$\rho_{\mathbb{B}}(t) := \frac{\alpha}{\tau} \sum_{b \in \mathbb{Z}, B_b \leq t} e^{-\frac{(t-B_b)}{\tau}} + \beta.$$

Zur Modellierung von n parallelen Punktprozessen X_1, \dots, X_n wird angenommen, dass alle Prozesse vom selben stationären Mutterprozess \mathbb{B} kommen

(Fig. A.7 B, $n = 2$). Die Parameter μ und σ sind damit global; die Parameter α , τ und β können zwischen den Prozessen variieren. Der Parameter α_j beschreibt die erwartete Anzahl an Ereignissen pro Paket in Prozess X_j , τ_j die Geschwindigkeit des exponentiellen Abfalls der Intensität sowie das mittlere Intervall zwischen Paketstart B und einem Spike, und β_j ist eine konstante, von den Paketen unabhängige Hintergrundintensität. Für gegebenes \mathbb{B} sind alle Prozesse X_j unabhängige Poissonprozesse, und die einzige Form der Korrelation entspringt den simultanen Paketanfängen.

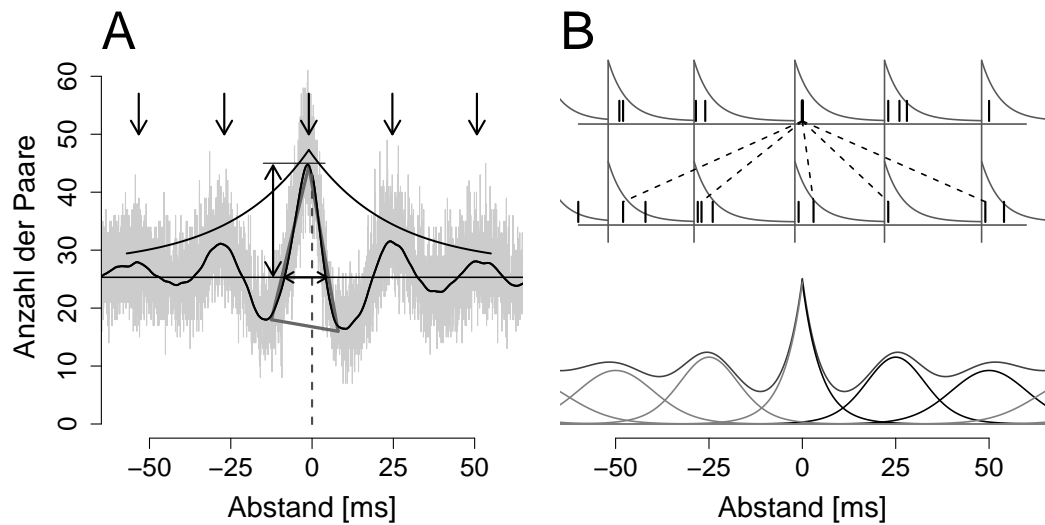


Figure A.7: Modell 3: Beziehung zwischen Eigenschaften paralleler Prozesse und Form ihres CCHs. A: Formparameter eines oszillatorischen CCHs: Höhe, Breite und Asymmetrie der zentralen Region sowie periodisch auftretende Peaks mit fallender Amplitude. B: Doppelt stochastisches Modell: Simultane Pakete werden erzeugt von einer Irrfahrt auf \mathbb{R} mit $\mathcal{N}(\mu, \sigma^2)$ -verteilten Intervallen. Für gegebene Paketzeiten ist jeder Prozess ein Poissonprozess, dessen Intensität nach den Paketzeiten exponentiell abfällt. Das zugehörige CCH setzt sich zusammen aus verschiedenen Summanden, die die erwartete Intensität der Spikepaare aus verschiedenen Paketpaaren beschreiben (zentrale Region: gleichzeitige Pakete, Region um 25 ms: nebeneinander liegende Pakete, etc.).

ACF und CCF Im Rahmen dieses Modells wird eine Formel hergeleitet für die Intensität der Ereignispaare mit Abstand s . In Analogie zur vorherigen Nomenklatur wird diese bezeichnet als die Auto- bzw. Kreuzkorrelations-Funktion ('ACF'/'CCF') an der Stelle s (vgl. (12.1) & (12.2)). Die ACF eines Prozesses X wird berechnet als die umskalierte bedingte Intensität der Spikes in X , gegeben

einen Spike zur Zeit t , und damit als die umskalierte Intensität der Palmischen Verteilung von X . Für die gegebenen doppelt stochastischen Prozesse setzt sich diese Funktion aus verschiedenen Summanden zusammen, die in Figur A.7 B unten durch Kurven dargestellt sind. Der zentrale Teil beinhaltet die Verteilung der ‘Geschwister’ des Ausgangsspikes, die aus demselben Paket stammen wie der Spike bei t ; der Teil um 25 ms reflektiert die Intensität der Paare, die aus aufeinander folgenden Paketen stammen, etc.

Bedeutung der Parameter Mit Hilfe der hergeleiteten Formel wird untersucht, wie die Formen von ACF und CCF von den Parametern abhängen. Der Parameter μ beschreibt approximativ die Position des ersten Seitenpeaks, und die Stärke der Oszillation fällt mit wachsendem σ . Der Parameter τ bestimmt sowohl Höhe als auch Breite der zentralen Region, wobei mit fallendem τ die Höhe zu- und die Breite abnimmt. Die Differenz zwischen den Parametern τ_i und τ_j ist die einzige Quelle für Asymmetrie in der CCF zwischen den Prozessen i und j : Ist $\tau_i < \tau_j$, so fällt der Peak schneller, erreicht kleinere Werte und ist schmaler auf der linken als auf der rechten Seite der zentralen Region. Damit können mit wenigen, direkt interpretierbaren Parametern die prinzipiellen Eigenschaften eines CCHs beschrieben und gleichzeitig in Beziehung gesetzt werden zu den Parametern der Punktprozesse.

Datenanalyse Um zu untersuchen, ob das vorgeschlagene doppelt stochastische Modell sich für die Analyse experimenteller Daten eignet, werden theoretische ACFs an empirisch gewonnene ACHs angepasst und so die Parameter geschätzt. Die Formen aller ACHs werden durch die ACFs gut beschrieben, mit globalen Parametern μ und σ . Aus den geschätzten Parametersätzen werden Vorhersagen über die CCFs abgeleitet und mit den Formen der empirisch gewonnenen CCHs verglichen. Meist können diese Interaktionen zwischen Paaren von Prozessen mit Hilfe der Modellannahmen, dass die Prozesse vom selben Mutterprozess \mathbb{B} erzeugt werden und, darauf bedingt, unabhängige Poissonprozesse sind, präzise vorhergesagt werden. Auch ein Vergleich mit simulierten parallelen Prozessen zeigt eine hohe Übereinstimmung der Variabilität der Datenpunkte im CCH um die theoretische CCF. Diese Befunde legen nahe, dass das doppelt stochastische Modell eine sinnvolle Beschreibung essentieller Charakteristiken der beobachteten Spike Trains und CCHs liefern kann.

Fazit: Die Bedeutung additiver kleiner Phasen im Modell Anhand des Modells wird schließlich untersucht, in welcher Weise die additive Struktur kleiner Phasen für Kodiermechanismen eingesetzt werden kann. Durch Anpassen einer Kosinusfunktion wird genau dann eine Phasenverschiebung im CCH identifiziert, wenn sich die Parameter τ_i und τ_j der Prozesse X_i und X_j unterscheiden. Dabei wird anhand von zwei Argumenten der Zusammenhang zwischen der Differenz $\tau_j - \tau_i$ und der Phase φ_{ij} deutlich: Zum einen ist φ_{ij} aufgrund der asymmetrischen Form des Peaks genau dann positiv, wenn $\tau_i < \tau_j$, d.h. wenn $\tau_j - \tau_i > 0$. Zum anderen beschreibt τ_i die erwartete Position eines typischen Punktes in Prozess X_i relativ zum Paketanfang, so dass die mittlere Differenz solcher Positionen zwischen den Prozessen X_i und X_j mit der Differenz $\tau_i - \tau_j$ zusammenhängt. Wenn man auf diese Art jedem Prozess X_i als ‘bevorzugten Feuerzeitpunkt’ seinen Wert τ_i zuschreibt, erhält man eine temporale Karte, die mit der in Teil II entwickelten linearen Konfiguration verwandt ist. Additivität der paarweisen Differenzen $\tau_j - \tau_i$ erklärt sich dann in natürlicher Weise durch die lineare Struktur von \mathbb{R} .

Im Rahmen des Modells werden kleine Phasenverschiebungen zwischen Paaren von Punktprozessen nicht auf kurzen Zeitskalen erkennbar. Erst durch Integration über lange Analysefenster können kleine Phasenverschiebungen oder Differenzen in den τ_i deutlich werden. Aufgrund der hohen Geschwindigkeit der Informationsverarbeitung im Gehirn sind daher im Modell Kodiermechanismen, die auf Differenzen der τ_i basieren, nicht plausibel. Es ist jedoch denkbar, dass die Modellstruktur weniger zwischen einzelnen Paaren von Prozessen als vielmehr im Rahmen großer Netzwerke eingesetzt werden kann.

Lebenslauf

Gaby Schneider
Kiesstr. 10
60486 Frankfurt am Main

Geburtsdatum: 05. August 1977
Geburtsort: Frankfurt am Main
Staatsangehörigkeit: deutsch

- 1987 - 1996 LIEBIGGYMNASIUM, FRANKFURT AM MAIN
Abiturnote: 1.0
Buchpreis der chemischen Industrie
- Okt. 1996 - Okt. 2002 J. W. GOETHE-UNIVERSITÄT FRANKFURT AM MAIN
Studium der Mathematik auf Diplom, Nebenfach Informatik
Vordiplom: Aug. 1998, 'sehr gut'
Professoren R. Bieri, O. Drobnik, G. Kersting, J. Wolfart
Diplom: Okt. 2002, 'mit Auszeichnung'
Professoren M. Reichert-Hahn, A. Wakolbinger, D. Wotschke
- Okt. 1997 - Juli 2003 J. W. GOETHE-UNIVERSITÄT FRANKFURT AM MAIN
Studium der Psychologie auf Diplom
Vordiplom: Feb. 2002, 'sehr gut'
Professoren W. Bauer, H. Gögelein, V. Hodapp, H. Moosbrugger, M. Knopf, V. Sarris, E. Schwanenberg
Diplom: Jul. 2003, 'sehr gut'
Professoren G. Büttner, V. Hodapp, K. Maurer, H. Moosbrugger, R. Sireteanu, U. Stangier, D. Zapf
- Diplomarbeit
(Math. & Psych.) Analysis of Higher-Order Coincident Activity in Multiple Parallel Processes
Ausgezeichnet mit dem Preis der Zürich-Gruppe
Betreuer: Dr. Sonja Grün, Max-Planck-Institut für Hirnforschung, Abt. Neurophysiologie, Dr. Brooks Ferebee, JWG-Universität Frankfurt, FB Mathematik
Gutachter: Prof. Dr. Anton Wakolbinger, JWG-Universität Frankfurt, FB Mathematik, Prof. Dr. Wolf Singer, Max-Planck-Institut für Hirnforschung, Abt. Neurophysiologie
- Dez. 2002 - Aug. 2003 COVIDENCE GMBH, ESCHBORN
Anstellung als Biostatistikerin
- seit Sept. 2003 J.W. GOETHE-UNIVERSITÄT FRANKFURT AM MAIN
Promotionsstudentin und wissenschaftliche Mitarbeiterin bei Prof. Dr. A. Wakolbinger
Fachbereich Informatik und Mathematik
Institut für Stochastik und Mathematische Informatik
-